The Role of Charge and Orbital Ordering in Quadruple Perovskite Materials with Multiferroic Potential

Natasha J. Perks

Brasenose College

University of Oxford

A thesis submitted for the degree of Doctor of Philosophy

Trinity Term 2015

The Role of Charge and Orbital Ordering in Quadruple Perovskite Materials with Multiferroic Potential

Natasha J. Perks

Brasenose College, University of Oxford
A thesis submitted for the degree of Doctor of Philosophy
Trinity Term 2015

With the overriding goal of developing functional multiferroic systems with technological potential, this thesis focuses on the role of orbital and charge ordering in coupling magnetism and ferroelectricity in synthetic quadruple perovskites. Using x-ray diffraction as the primary characterisation tool, modulations to crystal ordering have been interpreted in terms of orbital occupation and charge variation.

Expanding on previous magnetic structure studies and polarisation measurements, structural analysis of $CaMn_7O_{12}$ has led to the experimental realisation of a new mechanism for multiferroicity, resulting from a "magneto-orbital helix". Motivated by the idea of tuning multiferroic properties through varying manganese valence, the doped system $CaCu_{0.15}Mn_{6.85}O_{12}$ has been studied. Structural models considering the possibility of domain formation and multiple coexisting modulations have been tested against x-ray diffraction data. Finally, motivated by theoretical predictions of ferroelectric phases and multiferroicity in doped, simple, manganite perovskites, a structural model for the low temperature phase of $NaMn_7O_{12}$ has been developed, based upon theoretical predictions for orbital ordering and the experimentally determined magnetic structure. This model has been tested against previously measured neutron diffraction data. The importance of understanding crystal formation and domain structures when applying theoretical models has been highlighted, and has prompted the consideration of future work involving viewing and manipulating twin formation.

Acknowledgements

I owe a great deal of thanks to my supervisor Paolo Radaelli for providing me with invaluable teaching, direction and encouragement throughout my DPhil. I am lucky to have been part of a fantastic research group, and in particular, I would like to thank Roger Johnson for his support, and for sharing many ideas that have contributed a great deal to my work over the past four years. Alex Hearmon provided me with valuable advice at the start of my DPhil, and the enthusiasm of Noah Waterfield Price, James Beilsten-Edmands and Francis Chmiel has been a great source of motivation over the past few months.

I am fortunate to have had the opportunity to perform experiments at Diamond and ISIS, and I am particularly grateful to the I16 beamline scientists; Steve Collins, Gareth Nisbet, and especially Alessandro Bombardi, for all of his efforts to ensure that my experiments were successful.

My work has benefitted from many useful discussions outside of Oxford. I would like to thank Laurent Chapon and Maxim Mostovoy for their valuable contributions, Dmirty Khalyavin and Pascal Manuel at WISH, for taking an interest in my research and giving me new ideas, and Matthias Gutmann at SXD, for sharing his knowledge, and patiently teaching me the many quirks of the SXD software.

My experiments would not have been possible without the brilliant work of Dharmalingam Prabhakaran and Christine Martin, growing many high quality crystals. I also owe thanks to Andrea Prodi for providing me with SXD data and to Susannah Speller, for her assistance with electron microscopy measurements.

Brasenose College have provided me with helpful support, and I would like to acknowledge their financial generosity; funding my attendance at several conferences, and awarding me a Senior Hulme Scholarship.

Many people in the Clarendon have helped me along the way. Ben Williams has helped avert several experimental disasters, and Danielle Kaminski, Jordan Thompson, and all those in Office 105 have made the Clarendon an enjoyable place to work. Great thanks are also due to Corinna Dahnke, for her valiant efforts to keep me organised.

I am incredibly grateful for the support and encouragement I have had from my friends and family. I owe thanks to my father, who enthusiastically reads all of my research, and to my mother and sister, who provide me with welcome distractions from work. Friends in Cambridge have been incredibly supportive during my time at University, particularly Robert Cole and Simon Wright, without whom I may not have survived my first year exams, let alone managed to write a thesis. Finally, I want to thank all those who have made my time in Oxford so memorable, especially Sam, who has been my greatest friend and support over the past few years.

Contents

1 Introduction **1**
- 1.1 Order and Disorder . . . 1
- 1.2 The Theory of Multiferroic Materials . . . 3
  - 1.2.1 Ferroicity . . . 3
  - 1.2.2 Ferromagnetism . . . 3
  - 1.2.3 Ferroelectricity . . . 7
  - 1.2.4 Ferroelasticity and Ferrotoroidicity . . . 10
  - 1.2.5 Multiferroicity . . . 10
- 1.3 Progress in the Field of Multiferroics . . . 14
  - 1.3.1 Breakthrough Materials . . . 14
  - 1.3.2 Technological Potential . . . 23
- 1.4 Thesis Plan . . . 24

2 Characterisation Techniques **26**
- 2.1 Electron Microscopy . . . 27
  - 2.1.1 Interaction of electrons with the sample . . . 27
  - 2.1.2 The SEM microscope . . . 30
  - 2.1.3 Energy Dispersive Spectroscopy (EDX) . . . 34
- 2.2 X-ray Diffraction . . . 34
  - 2.2.1 The theory of x-ray scattering . . . 35
  - 2.2.2 X-ray sources and facilities . . . 47
- 2.3 Neutron Diffraction . . . 59
  - 2.3.1 Interaction of neutrons with atoms . . . 60
  - 2.3.2 Neutron sources and facilities . . . 61

3 $CaMn_7O_{12}$ **65**
- 3.1 Introduction . . . 65
  - 3.1.1 Motivation for studying $CaMn_7O_{12}$ . . . 65
  - 3.1.2 The crystal structure . . . 70
  - 3.1.3 The magnetic structure . . . 71
  - 3.1.4 The ferroelectric polarisation . . . 73
- 3.2 X-ray Diffraction Experiments . . . 74
  - 3.2.1 Sample characterisation . . . 74
  - 3.2.2 I16 Diamond Light Source - Observation of the incommensurate structural modulation . . . 75
  - 3.2.3 I19 Diamond Light Source and Supernova - Collection of satellite peaks . . . 79
  - 3.2.4 Powder diffraction - Determination of lattice parameters . . . 80

3.3 Results . . . 81
3.3.1 Structural refinement . . . 81
3.3.2 Interpreting the modulation - the orbital helix . . . 84
3.3.3 Magnetic coupling - the magneto-orbital Helix . . . 89
3.3.4 The ferroelectric polarisation . . . 92
3.4 Conclusions . . . 96

4 $CaCu_{0.15}Mn_{6.85}O_{12}$ 98
4.1 Introduction . . . 98
4.1.1 Motivation for studying $CaCu_{0.15}Mn_{6.85}O_{12}$ . . . 98
4.1.2 The impact of copper doping . . . 98
4.2 Crystal Characterisation . . . 100
4.2.1 Preliminary x-ray diffraction . . . 100
4.2.2 SEM microscopy . . . 101
4.3 Results . . . 105
4.3.1 Single crystal x-ray diffraction on $CaCu_{0.15}Mn_{6.85}O_{12}$ SuperNova experiment . . . 105
4.3.2 Testing the models . . . 112
4.3.3 Analysis of SuperNova data . . . 117
4.4 Conclusions and Further Investigations . . . 132
4.4.1 The role of twinning . . . 132
4.4.2 The magnetic structure . . . 134
4.4.3 Ferroelectric polarisation and multiferroicity . . . 134

5 $NaMn_7O_{12}$ 135
5.1 Introduction . . . 135
5.1.1 Motivation for studying $NaMn_7O_{12}$ . . . 135
5.1.2 The crystal structure . . . 136
5.1.3 The magnetic structure . . . 138
5.1.4 Orbital ordering . . . 139
5.1.5 The purpose of this work . . . 140
5.2 Building a Model for the Low Temperature Structure . . . 141
5.2.1 Constructing the model using ISODISTORT . . . 141
5.2.2 Testing consistency with the magnetic structure . . . 146
5.2.3 Alternative models for the low temperature structure . . . 147
5.3 Testing the Model - Refinement Against Experimental Data . . . 150
5.3.1 Analysis of the single crystal neutron diffraction data . . . 150
5.3.2 Refinement of the single crystal neutron diffraction data . . . 151
5.4 Further Work . . . 156

6 Concluding Remarks 158

References 159

A The Structure Factor for Modulated Crystals **168**

B Refinement of X-ray Diffraction Data **171**
B.1 Powder Diffraction Data
Rietveld Refinement and the LeBail Method 171
B.2 Single Crystal Diffraction Data
Structural Optimisation and Refinement 173
B.2.1 The phase problem 173
B.2.2 The Patterson function 174
B.2.3 Direct methods 175
B.2.4 Structural optimisation 175

C Four Dimensional Space Group Analysis **178**

List of Figures

1.1 The atomic magnetic moment . . . 3
1.2 Magnetic ordering of a 2-d spin array . . . 6
1.3 Magnetic domains . . . 7
1.4 Ferroelectric hysteresis loop . . . 9
1.5 The cubic to tetragonal transition in a proper ferroelectric perovskite . . 10
1.6 Spatial and time inversion properties of magnetic and electric dipole moments . . . 12
1.7 The cycloidal magnetic spin structure of $TbMnO_3$ . . . 15
1.8 Comparison of a clockwise and anticlockwise cycloid . . . 15
1.9 The effect of the Dzyaloshinskii-Moriya interaction . . . 17
1.10 Cycloidal multiferroic: The crystal and magnetic structure of $TbMn_2O_5$. 18
1.11 Quasi-collinear multiferroic: The magnetic structure of $HoMnO_3$ . . . 19
1.12 Helical multiferroic: The crystal structure of $RbFe(MoO_4)_2$ . . . 21
1.13 The antiferromagnetic kagome magnetic structure . . . 22

2.1 Secondary electron generation . . . 29
2.2 Characteristic x-ray generation . . . 29
2.3 SEM electromagnetic lens . . . 31
2.4 The SEM set up . . . 32
2.5 Interaction volume for different SEM signals . . . 33
2.6 Layout of an x-ray scattering experiment . . . 36
2.7 Classical scattering of an x-ray by an electron . . . 37
2.8 Reference directions for the polarisation factor . . . 39
2.9 Bragg's Law . . . 41
2.10 Debye-Scherrer cones from powder diffraction . . . 46
2.11 An x-ray tube source . . . 49
2.12 The set up of the SuperNova x-ray diffractometer . . . 50
2.13 Diffractometer angles used for positioning samples in SuperNova . . . 51
2.14 The layout of the Diamond Light Source . . . 54
2.15 The undulator insertion device . . . 55
2.16 The Lorentz force . . . 56
2.17 Comparison between the neutron Fermi length and x-ray atomic form factor 60

3.1 The perovskite unit cell . . . 65
3.2 Ferroelectric phase transitions in $BiTiO_3$ . . . 66
3.3 Charge, orbital and magnetic ordering in $La_{0.5}Ca_{0.5}MnO_3$ . . . 67
3.4 The CE and SOS magnetic structures predicted for quarter doped manganite perovskites . . . 68
3.5 The high temperature $Im\bar{3}$ structure of $CaMn_7O_{12}$ . . . 70

3.6 The $R\bar{3}$ structure of $CaMn_7O_{12}$ viewed as three inequivalent triangular layers along the hexagonal c axis, and in the pseudo-cubic cell 71
3.7 The magnetic structure of $CaMn_7O_{12}$ below T_{N1} 72
3.8 A $CaMn_7O_{12}$ crystal mounted for an x-ray diffraction experiment 74
3.9 SuperNova x-ray diffraction data: Room temperature Bragg peaks in the hk plane for $CaMn_7O_{12}$ 75
3.10 I16 x-ray diffraction data: Variation in intensity and propagation vector of a structural satellite peak and second harmonic in $CaMn_7O_{12}$ 77
3.11 Magnetic satellite peak 79
3.12 Satellite peaks associated with an incommensurate structural modulation in $CaMn_7O_{12}$ 80
3.13 Powder diffraction fits for $CaMn_7O_{12}$ 81
3.14 Lattice parameters for $CaMn_7O_{12}$ obtained from powder diffraction . . . 82
3.15 Variation in Mn-O bond lengths resulting from the structural modulation in $CaMn_7O_{12}$ 85
3.16 Interpreting Mn-O bond length variations of Jahn-Teller active octahedra in terms of orbital occupation 86
3.17 Periodically varying orbital occupation along the c axis in $CaMn_7O_{12}$ . . 86
3.18 Orbital occupation plotted as an orbital mixing angle 87
3.19 Variation in bond valence in $CaMn_7O_{12}$ 88
3.20 The implications of orbital occupation for magnetic exchange constants in $CaMn_7O_{12}$ 90
3.21 Phase diagram for the magnetic structure of $CaMn_7O_{12}$ 92
3.22 The global structural rotation in $CaMn_7O_{12}$ 93
3.23 The Dzyaloshinskii-Moriya interaction in $CaMn_7O_{12}$ 94
3.24 Generation of a local polarisation in $CaMn_7O_{12}$ 95

4.1 Room temperature and 85 K diffraction data for $CaCu_xMn_{7-x}O_{12}$ with x = 0.1 and x = 0.6 101
4.2 Room temperature and 85 K diffraction data for $CaCu_xMn_{7-x}O_{12}$ samples, highlighting multiple families of satellite peaks 102
4.3 SEM images and EDX spectrums for $CaCu_xMn_{7-x}O_{12}$with nominal composition $x = 0.1$ 103
4.4 Small impurity region identified using using backscattered electron signals and topographic imaging in a crystal of $CaCu_{0.15}Mn_{6.85}O_{12}$ 104
4.5 q_c, q_1, q_2 and q_3 satellites observed in $CaCu_{0.15}Mn_{6.85}O_{12}$ at 85 K 106
4.6 Four structural models that could explain the appearance of four sets of satellites in $CaCu_{0.15}Mn_{6.85}O_{12}$ 108
4.7 Comparison of Mn-O bond lengths in the modulated structure of $CaMn_7O_{12}$ and $CaCu_{0.15}Mn_{6.85}O_{12}$ 111
4.8 Variation in satellite intensity with x-ray beam probe size 114
4.9 Comparing intensities of all four satellites for a minimum x-ray beam probe size 115
4.10 Temperature dependencies of the four satellites of the (0,4,2) Bragg peak, measured at I16 116

4.11 Comparisons of intensities for equivalent pairs of q_1, q_2 and q_3 satellites, taken from SuperNova data at 85 K . . . 118
4.12 The refined model incorporating q_1, q_2 and q_3 . . . 121
4.13 Bond valence calculations for one Mn2 site in the unit cell, plotted in the hexagonal ab plane . . . 122
4.14 Bond valence variation for Mn2 sites related by 3-fold symmetry in the ab plane . . . 122
4.15 Bond valence variation for Mn2 sites related by R-centring in the ab plane. 123
4.16 Bond valence variation for all inequivalent Mn2 sites . . . 123
4.17 Mn2 Bond valence variation in the ab plane for $l_z = 7$ . . . 124
4.18 The four cubic diagonals that can correspond to the hexagonal c axis in $CaCu_{0.15}Mn_{6.85}O_{12}$ . . . 126
4.19 Obverse/reverse settings of the hexagonal cell . . . 127
4.20 Comparison of intensities for equivalent satellite peaks associated with four twins . . . 129
4.21 Refined Mn-O bond lengths for $CaCu_{0.15}Mn_{6.85}O_{12}$ incorporating a twin model and a single propagation vector . . . 131
4.22 Observed and calculated structure factors for the twin model . . . 131
4.23 A mechanism for manipulating domain distribution in $CaCu_{0.15}Mn_{6.85}O_{12}$ crystals through applied stress . . . 133

5.1 The room temperature crystal structure of $NaMn_7O_{12}$ . . . 136
5.2 The charge ordered $I2/m$ structure of $NaMn_7O_{12}$ . . . 137
5.3 The antiferromagnetic CE structure of $NaMn_7O_{12}$ . . . 138
5.4 Building a low temperature model for $NaMn_7O_{12}$ - Assigning inequivalent Mn sites . . . 141
5.5 The proposed pattern of orbital ordering for the low temperature model . 142
5.6 The primitive monoclinic cell for the proposed distorted low temperature model . . . 143
5.7 The $Mn4O_6$ octahedra allowed to displace in ISODISTORT . . . 144
5.8 The symmetry allowed mode for Mn4 displacement . . . 144
5.9 Symmetry allowed modes for oxygen anions forming the octahedra surrounding the Mn4 site . . . 145
5.10 The distorted, low temperature structure of $NaMn_7O_{12}$ obtained from ISODISTORT . . . 146
5.11 Checking the consistency of the model for the low temperature structure against the experimentally determined magnetic structure . . . 147
5.12 Room temperature refinement of SXD $NaMn_7O_{12}$ data . . . 152
5.13 The refined low temperature structure of $NaMn_7O_{12}$ . . . 155
5.14 Refinement of the low temperature model for $NaMn_7O_{12}$ . . . 156

A.1 A 1-d sinusoidal modulation to a 2-d lattice . . . 168

List of Tables

3.1 Average fractional coordinates, occupancies and thermal parameters for $CaMn_7O_{12}$ at 150 K . . . 83
3.2 Refined Fourier coefficients for the modulation in $CaMn_7O_{12}$ at 150 K. . 84

4.1 Compositions of $CaCu_xMn_{7-x}O_{12}$ samples obtained from SEM microscopy with EDX analysis . . . 104
4.2 Refining q_c - Average fractional coordinates for $CaCu_{0.15}Mn_{6.85}O_{12}$ at 85 K . . . 110
4.3 Refining q_c - Anisotropic thermal parameters for $CaCu_{0.15}Mn_{6.85}O_{12}$ at 85 K . . . 110
4.4 Refined Fourier coefficients for the q_c modulation in $CaCu_{0.15}Mn_{6.85}O_{12}$ at 85 K . . . 110
4.5 Propagation vectors q_c, q_1, q_2 and q_3 measured at I16 . . . 113
4.6 Refining q_1, q_2 and q_3 - Occupancies and average fractional coordinates for $CaCu_{0.15}Mn_{6.85}O_{12}$ at 85 K . . . 120
4.7 Refining q_1, q_2 and q_3 - Refined thermal parameters for $CaCu_{0.15}Mn_{6.85}O_{12}$ at 85 K . . . 120
4.8 Refined Fourier coefficients for q_1 . . . 120
4.9 Refined Fourier coefficients for q_2 . . . 120
4.10 Refined Fourier coefficients for q_3 . . . 121
4.11 Refining a twin model for $CaCu_{0.15}Mn_{6.85}O_{12}$ - Occupancies and average fractional coordinates . . . 130
4.12 Refining a twin model for $CaCu_{0.15}Mn_{6.85}O_{12}$ - Refined Fourier coefficients for the q_c modulation . . . 130
4.13 Refined twin fractions for $CaCu_{0.15}Mn_{6.85}O_{12}$ . . . 130

5.1 The combination of distortion modes that reproduces our low temperature model for $NaMn_7O_{12}$, generated using ISODISTORT . . . 145
5.2 Streltsov's low temperature model - Gamma point distortion modes . . . 148
5.3 Streltsov's low temperature model - A point distortion modes . . . 149
5.4 Comparing distortion modes for our low temperature $NaMn_7O_{12}$ model and Streltsov's model . . . 149
5.5 Refined $NaMn_7O_{12}$ oxygen fractional coordinates and thermal parameters for the room temperature structure . . . 151
5.6 Refined $NaMn_7O_{12}$ fractional coordinates and thermal parameters for the 150 K low temperature structure . . . 154
5.7 Refined $NaMn_7O_{12}$ Fourier coefficients for the low temperature (150 K) modulation . . . 154

Chapter 1

Introduction

1.1 Order and Disorder

Condensed matter physics focuses on understanding physical properties of materials, whether this be natural or synthetic materials, crystals or glasses. A prominent theme that makes these materials interesting and often dominates their physical properties is order, or lack of order, of atoms and spins. Many different avenues can be explored to characterise orderings in solid state materials:

Firstly, basic microscopic orderings can be considered. Presence or absence of atomic periodicity, defined in terms of a lattice and a unit cell, determines whether a material is a crystal or a glass. Basic atomic periodicities may be modulated, changing the crystal symmetry, and often leading to complex physical properties and cross coupling to other orderings. Ordering of unpaired electronic spins, on some, or all atoms in a crystal can either lead conventional ferromagnetic materials, antiferromagnetism or ferrimagnetism, or novel cycloidal and helical magnetic structures. Increasingly, orbital and charge order are emerging as an important characteristics in the development of technologically useful and functional solid state materials [1, 2]. Electronic correlations, for example, anisotropic orbital ordering emerging from a high temperature isotropic state may provide routes to coupling other order parameters in solid state materials, such as structural and magnetic order [3].

The driving force behind a specific crystallographic ordering is minimisation of free

energy. The most energetically favourable arrangement of atoms, magnetic moments or electronic moments may vary under different external conditions; temperature, pressure, stress, magnetic or electrical fields. Phase transitions between disordered and ordered states, or between ordered states of different symmetry frequently occur. Manipulation of orderings in crystals through control and application of external stimuli is a vast area of study. Phase mappings for materials under different stimuli can be produced and again, are often valuable when considering how crystal properties can be tuned for technological application.

When characterising orderings in crystalline materials, the correlation length scales should be considered. Whilst orderings may be homogeneous and long range, spanning the range of the crystal, it is common for crystals to be divided into domains, with each domain possessing the same orderings, but in different orientations related by symmetry. This domain formation may be as a result of crystal growth techniques, in response to a phase transition or to minimise a specific crystal energy. Domain formation may be unavoidable but may be controllable through application of external stimuli, and it may be possible to manipulate domain arrangement to tune physical properties. In the case of a crystal with domains, it is important to consider the summed contribution of different domains when analysing the overall characteristics of the crystal. Not only is the domain pattern of importance, domain boundaries can be of interest, sometimes possessing novel physical properties themselves, and having substantial effects on overall crystal properties [4].

In this thesis, many of the considerations outlined above will be used to characterise and understand the structural, magnetic and electrical properties of synthetic crystals that have multiferroic potential. The overriding focus is on how different order parameters may couple together, and how external stimuli may thus influence net crystal properties. At the forefront of this research is the strive towards developing functional devices from crystals that are not only physically novel and exciting, but that could be of interest and benefit to the wider community, having technical and commercial potential.

1.2 The Theory of Multiferroic Materials

1.2.1 Ferroicity

Ferroic materials undergo a spontaneous phase transition at a critical temperature (T_C), involving breaking of point symmetry. Below T_C, the material possesses macroscopic order, at least up to the level of domains, that can be described by an order parameter (Q). Q evolves from a value of zero in the high temperature phase, and is coupled to an external field below T_C. Application of the relevant external field may switch Q.

Four primary classes of ferroic ordering that can arise; ferromagnetism, ferroelectricity, ferrotorroidicity and ferroelasticity.

1.2.2 Ferromagnetism

Ferromagnetism was the first type of ferroic ordering to be discovered. Fundamentally, magnetism arises from the inherent magnetic dipole moment possessed by electrons, coupled with an orbital contribution from the electrons orbiting the nucleus, as shown in Figure 1.1.

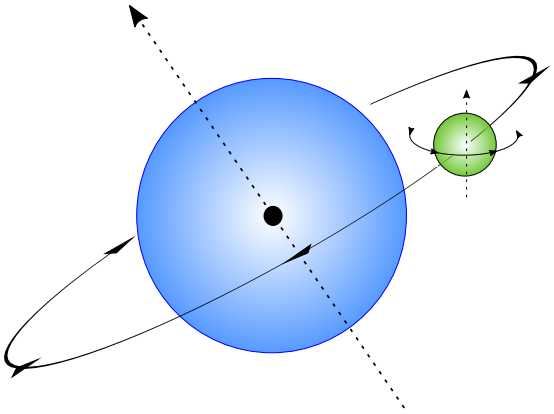


Figure 1.1: The atomic magnetic moment, arising from coupling between the magnetic moment associated with the intrinsic electronic spin and the moment resulting from the electron orbiting the nucleus.

Atoms with unpaired electrons possess net magnetic dipoles, and through the phenomena of quantum mechanical exchange, these magnetic moments can align, giving rise to net magnetic order in crystals.

The exchange interaction arises from the Pauli exclusion principle: For a system of electrons (fermions), the total wave function must change sign but be otherwise unchanged under the exchange of two particles, in order to preserve the physical properties of the system. Following the formalism of Ref. [5], considering two electrons at positions $\mathbf{r}_1$ and $\mathbf{r}_2$: The total wave function for the system can be written in terms of the single electron states $\psi_a(\mathbf{r_1})$ and $\psi_b(\mathbf{r_2})$, in one of the following forms[1]:

$$\Psi_S = \frac{1}{\sqrt{2}}[\psi_a(\mathbf{r}_1)\psi_b(\mathbf{r}_2) + \psi_a(\mathbf{r}_2)\psi_b(\mathbf{r}_1)]\chi_S \tag{1.2.1}$$

or

$$\Psi_T = \frac{1}{\sqrt{2}}[\psi_a(\mathbf{r}_1)\psi_b(\mathbf{r}_2) - \psi_a(\mathbf{r}_2)\psi_b(\mathbf{r}_1)]\chi_T. \tag{1.2.2}$$

The energies of these two possible states can be written in terms of the system Hamiltonian $\hat{H}$:

$$E_S = \int \Psi_S^* \hat{H} \Psi_S d\mathbf{r}_1 d\mathbf{r}_2 \tag{1.2.3}$$

or

$$E_T = \int \Psi_T^* \hat{H} \Psi_T d\mathbf{r}_1 d\mathbf{r}_2. \tag{1.2.4}$$

The difference between these two states is given by

$$E_S - E_T = 2 \int \psi_a^*(\mathbf{r}_1)\psi_b^*(\mathbf{r}_2)\hat{H}\psi_a(\mathbf{r}_2)\psi_b(\mathbf{r}_1) d\mathbf{r}_1 d\mathbf{r}_2. \tag{1.2.5}$$

It can be shown that the difference between singlet and triplet states can be parameterised in terms of the product of the electronic spins on adjacent atoms ($\mathbf{S_1} \cdot \mathbf{S_2}$).

[1] Antisymmetric singlet state χ_S for the case of a symmetric spatial state, and symmetric triple state. χ_T for the case of an antisymmetric spatial state.

For the singlet state: $\mathbf{S}_1 \cdot \mathbf{S}_2$ = -0.75 and for a triplet state, $\mathbf{S}_1 \cdot \mathbf{S}_2 = 0.25$.

$\hat{H}$ can then be written in the form of an effective Hamiltonian:

$$\hat{H} = \frac{1}{4}(E_S + 3E_T) - (E_S - E_T)\mathbf{S_1} \cdot \mathbf{S_2}. \tag{1.2.6}$$

The first term in this expression is a constant that can be absorbed into other constant energy terms, but the second term is spin dependent.

Defining an exchange constant J:

$$J = \frac{E_S - E_T}{2} = \int \psi_a^*(\mathbf{r}_1)\psi_b^*(\mathbf{r}_2)\hat{H}\psi_a(\mathbf{r}_2)\psi_b(\mathbf{r}_1)d\mathbf{r}_1 d\mathbf{r}_2 \tag{1.2.7}$$

prompts a spin dependent exchange term in the Hamiltonian:

$$\hat{H}_{spin} = -2J\mathbf{S}_1 \cdot \mathbf{S}_2. \tag{1.2.8}$$

Whilst this equation has been derived for two electrons, it can be generalised and motivates the Hamiltonian of the Heisenberg model:

$$\hat{H} = -\sum_{ij} J_{ij}\mathbf{S}_i \cdot \mathbf{S}_j \tag{1.2.9}$$

where J_{ij} is the exchange constant between the i^{th} and j^{th} spins. Considering unpaired electronic spins on neighbouring atoms, $J_{ij} > 0$ favours a ferromagnetic arrangement with spins aligned parallel to one another, whilst $J_{ij} < 0$ favours an antiferromagnetic, antiparallel arrangement of spins. A phase transition from a paramagnetic state, with a random arrangement of spins to an (anti)ferromagnetically ordered state, as shown for a 2-d lattice in Figure 1.2, can be realised through consideration of the exchange between nearest neighbour spins, taking all exchange interactions for non-nearest neighbours to be zero. Below $\mathrm{T_C}$, a lattice of spins will align along a specific direction, and this direction can be switched through application of an external magnetic field. In more complex magnetically ordered systems such as helical and cycloidal magnetic

states, it is often necessary to consider magnetic exchange interactions beyond nearest neighbour atoms.

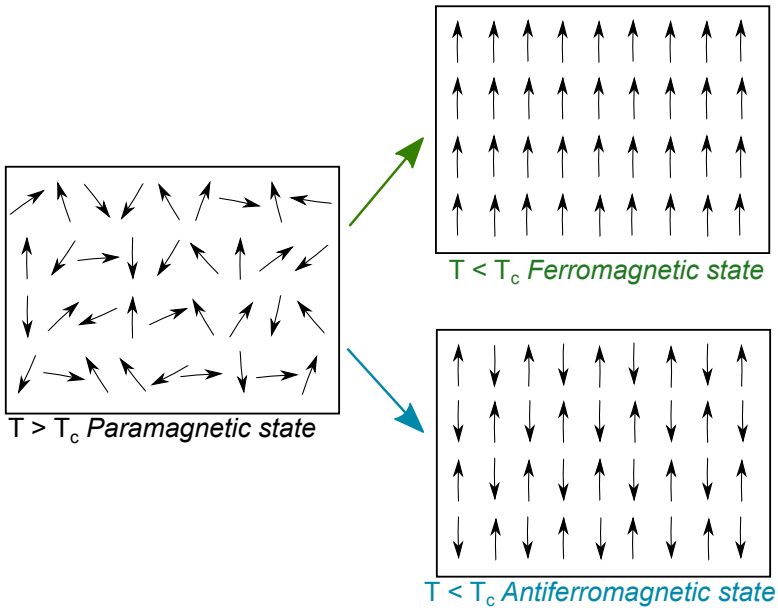


Figure 1.2: A 2-d array of magnetic spins, undergoing a transitions from a paramagnetic state to ferro and antiferromagnetically ordered states below a critical temperature T_C, governed by the exchange constant J_{ij} between nearest neighbour spins i and j.

The direct exchange formalism outlined above is applicable to electrons interacting on neighbouring magnetic ions, and requires spatial overlap of the occupied orbitals. In reality, sufficient orbital overlap of adjacent magnetic cations is rare, both for transition metal and rare earth systems. More commonly, strong magnetic interactions occur via interaction via a non-metal intermediary; a phenomenon referred to as superexchange. Typically an unpaired electron in a transition metal cation may occupy a d orbital that overlaps with a vacant p orbital on a neighbouring oxygen anion. This neighbouring p orbital in turn overlaps with another partially occupied transition metal d orbital. For superexchange, the underlying crystal structure, specifically the bond lengths and bond angles between anions and cations determine the extent of overlap between orbitals, thus influencing the sign and size of exchange constants and the magnetic structure and phase transitions.

Magnetic exchange interactions are responsible for the relative alignment of atomic

spins, but in the absence of a magnetic field, magnetic anisotropy determines the direction of alignment of a net magnetic moment in a ferromagnetically ordered crystal. Several types of magnetic anisotropy are applicable, all promoting lowering of internal crystal energy through a specific direction of magnetic orientation. In bulk ferromagnetic materials, the lowest energy configuration of magnetic spins results from the formation of magnetic domains. Spins within a given domain align, but the net magnetic moment summed across all domains will be zero, as shown in Figure 1.3(a). Under the application of an external magnetic field **H** energetically favourable domains will grow (Figure 1.3(b)), giving rise to a net magnetisation parallel to the direction of **H**, and eventually leading to a single domain (Figure 1.3(c)).

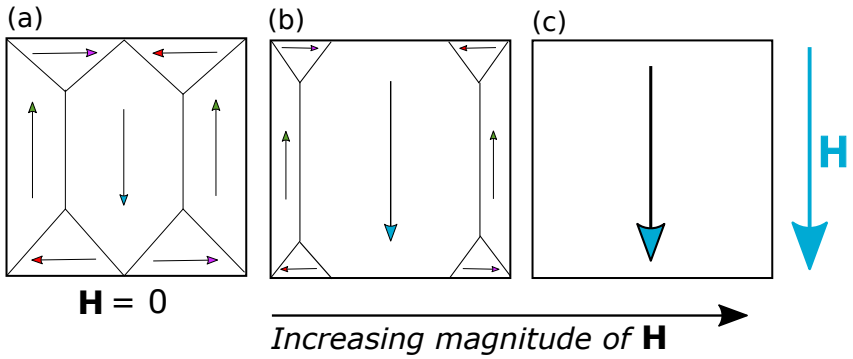


Figure 1.3: (a) The formation of a domains in a ferromagnetic material in order to minimise magneto-static energy. (b) Energetically favourable domains with a magnetic moment parallel to **H** grow, giving rise to a net magnetic moment. (c) Under a sufficient large magnetic field, a single domain will result.

1.2.3 Ferroelectricity

Internal electric dipoles in crystals are inherently coupled to the geometry of the crystal lattice, and there are a variety of ways in which the electrical properties of crystals can change under application of external stimuli. In piezoelectric materials, a mechanical stress results in the onset of a polarisation, whilst in pyroelectric materials polarisation varies with temperature. Ferroelectrics are unique in that the develop-

ment of a net dipole moment and electrical polarisation is spontaneous below a critical temperature T_C, and can be switched directly through application of external electric field.

Below T_C, specific charged atoms will be displaced, often along crystallographic axes, giving rise to the internal dipole moments. The net dipole moment in a ferroelectric material is the vector sum of the dipole moments ($\boldsymbol{\mu} = q.\boldsymbol{r}$) in each unit cell, $\sum \boldsymbol{\mu}$, and crystal polarisation ($\mathbf{P}$) is defined as the net dipole moment per unit volume $\left(\mathbf{P} = \frac{\sum \boldsymbol{\mu}}{V}\right)$. The emergence of $\mathbf{P}$ in a centrosymmetric, charge neutral crystal is a complex issue, discussed in Ref. [6], however, in the case of an acentric crystal, depending on the specific crystallographic symmetry, there may be multiple equivalent crystallographic directions for displacement, and this may lead to the formation of ferroelectric domains. Analogously to the case of ferromagnetic domains (cf. Figure 1.3), within each ferroelectric domain, all dipole moments will be aligned, but the net dipole moment will be different for different domains. A ferroelectric crystal may or may not possess a polarisation in the absence of an electric field, depending on whether a domain structure exists and whether the vector sum of individual domain polarisations is zero.

A characteristic feature of ferroelectric materials under applied electric field is the hysteresis loop shown in Figure 1.4(a). Under the application of an electric field $\mathbf{E}$ the polarisation of individual domains can switch, with the electric field biasing the free energy profile, making it energetically favourable for individual dipoles to align parallel to $\mathbf{E}$. The larger the applied field, the greater the energy gain from switching dipole moments, and above a critical, coercive field ($\mathbf{E_C}$), all dipole moments will switch, leading to a fully polarised, single domain state (Figure 1.4(b)). If a reversed electric field is then applied to an already fully polarised state, new domains with reversed dipole moments will nucleate, sweeping out the old polarisation (Figure 1.4(c) and (d)), but with appreciable time and field lag due to the nucleation process of the individual poled domains.

There are various mechanisms that can give rise to ferroelectric ordering in crystals,

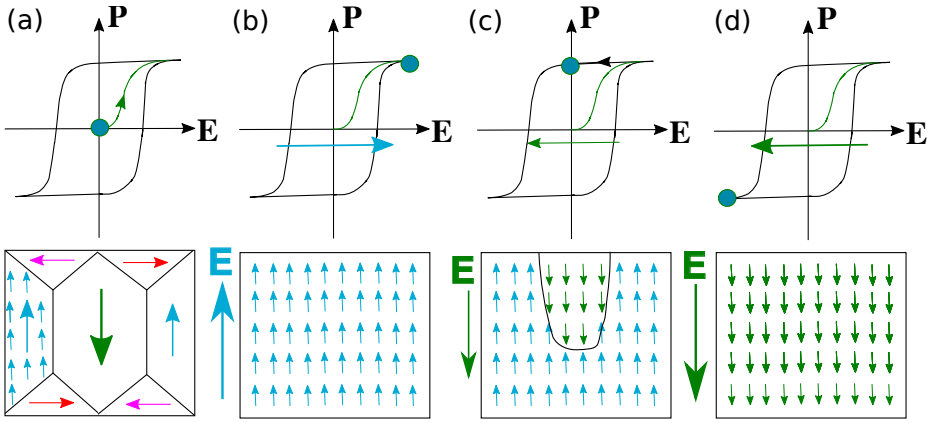


Figure 1.4: The characteristic hysteresis loop for a ferroelectric under applied field **E**. (a) A multidomain ferroelectric with zero net polarisation in the absence of an applied field (b) Under application of a coercive field $\mathbf{E_C}$, all domains will switch to form a single domain polarised state. (c) New domains will nucleate as the field is reversed, and (d) under sufficient reversed field, the net polarisation will be reversed.

divided into two classes, which differ in the primary driving force that leads to a polarisation [7]: Proper and improper ferroelectrics.

1.2.3.1 Proper ferroelectrics

In proper ferroelectric crystals, polarisation is a direct consequence of a structural transition, driven by a reduction in energy and resulting in a polar state. Often in perovskite ferroelectrics, the polar distortion is B site displacement relative to an octahedral oxygen cage, as shown in Figure 1.5. This displacement is reliant upon transfer of electrons from filled oxygen p orbitals to vacant metal cation orbitals, and thus a requirement for proper ferroelectricity is a B site with vacant orbitals (commonly a transition metal with vacant $3d$ orbitals).

1.2.3.2 Improper ferroelectrics

An order parameter that results in a ferroelectric polarisation may in fact be primarily driving a different macroscopic ordering. Polar lattice distortions may occur as a by product of charge or magnetic ordering. The magnitudes of polarisations arising as secondary order parameters are generally smaller than those for proper fer-

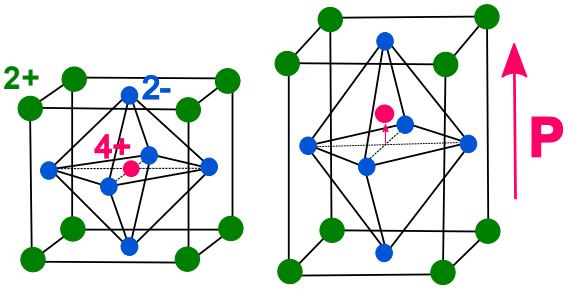


Figure 1.5: An example of a cubic to tetragonal phase transition resulting in the onset of a ferroelectric polarisation in a perovskite. The B site cation shown in pink is displaced relative to the surrounding oxygens (blue), resulting in a dipole moment.

roelectrics, but coupling can exist between the order parameters, and any changes in magnetic or charge ordering may influence the magnitude or direction of ferroelectric polarisation.

1.2.4 Ferroelasticity and Ferrotoroidicity

To an extent, ferroelasticity can be regarded as the mechanical equivalent to ferroelectricity and ferromagnetism. Below T_c ferroelastic materials exhibit spontaneous strain, which can switch between different structures and phases in response to an applied stress. In an analogous manner to the ferroelectric hysteresis loop, ferroelastic materials show hysteresis effects under applied stress, due to non-linear strain responses

Ferrotoroidic materials possess a vector toroidal moment ($\mathbf{T}$), characterising a vortex of spins below T_c. The vector ($\mathbf{T}$) can be manipulated by source vectors ($\mathbf{S}$), where $\mathbf{S} = \mathbf{E} \times \mathbf{H}$. Ferrotoroicity is discussed further in Ref. [8] and Ref. [9].

1.2.5 Multiferroicity

Ferroelectric, ferromagnetic and ferroelastic orderings have been extensively studied, and microscopic mechanisms governing the ordering across a vast array of materials are well understood [10, 11]. Of increasing interest and importance is the interplay

between ferroic orderings, uncovering materials in which two or more ferroic orders exist simultaneously and are coupled [12]. Taking the broadest definition, a multiferroic is a crystal that possesses any two or more of the four ferroic orderings in the same phase. Specifically, in this thesis, the focus is on crystals that are simultaneously ferroelectric and ferromagnetic. These multiferroics can be divided into two classes. For *Type I* multiferroics, the ferroelectric and ferromagnetic transitions occur independently, at different critical temperatures. Often the dipole and magnetic moments are associated with different cations, due to mutually exclusive requirements of vacant valence orbitals for proper ferroelectricity, but partially occupied valence orbitals for ferromagnetic exchange. Type I multiferroics with large polarisations and high critical temperatures have been uncovered [13], but since the ferroelectric polarisation and magnetism are governed by independent order parameters, coupling between the two is weak, and little possibility exists to influence the magnetic order though electric fields or vice versa. *Type II* ferroelectric/ferromagnetic multiferroics show improper ferroelectric ordering below T_C , with antiferromagnetism being the primary order parameter. Inversion symmetry is broken by a phase transition to a polar magnetic phase, and magneto-structural coupling to the crystal structure enables the formation of an electrically polar state. Since ferroelectric polarisation is a direct consequence of a specific magnetic ordering, there is potential for strong coupling between the two order parameters [14]. However, polar magnetic phases are often geometrically frustrated with suppressed transition temperatures, and hence the onset of type II multiferroicity typically occurs well below room temperature. Magnetically induced improper ferroelectric polarisations also tend to be several orders of magnitude weaker than typical proper ferroelectric polarisations.

In this thesis, type II multiferroic materials are explored, working towards the goal of uncovering a strongly coupled, room temperature multiferroic with a large ferroelectric polarisation.

Coupling between ferroelectric and magnetic order parameters in type II multiferroics can be understood by considering how magnetic and electric dipole moments trans-

form under two symmetry operators; time inversion ($\hat{\boldsymbol{T}}$) and spatial inversion ($\hat{\boldsymbol{I}}$). The direction of a magnetic moment is determined by electronic angular momentum, hence magnetic dipoles are represented by axial vectors. Under spatial inversion, axial vectors are invariant, but change sign under time inversion. In contrast, since electrical dipole moments are generated by static charges, they are invariant under time inversion, but change sign under spatial inversion. This is summarised in Figure 1.6.

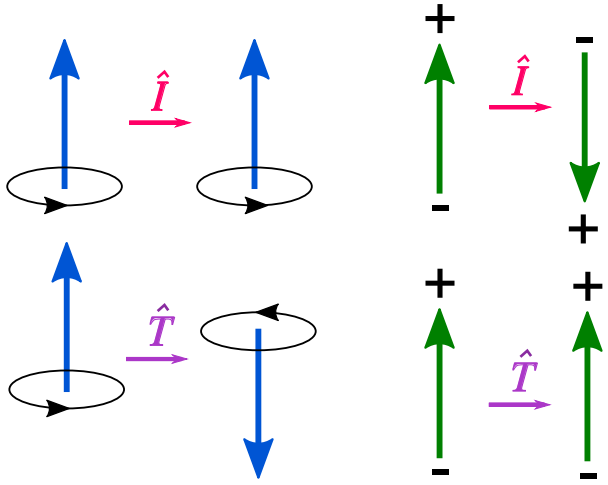


Figure 1.6: The opposite transformation properties of a magnetic moment (blue), and electric dipole (green) under spatial ($\hat{\boldsymbol{I}}$) and time ($\hat{\boldsymbol{T}}$) operators.

The opposite transformation properties of $\mathbf{P}$ and $\mathbf{M}$ forbids linear coupling. Forth order coupling proportional to $\mathbf{P}^2\mathbf{M}^2$ is generally allowed by symmetry, but is typically weak, giving rise to small anomalies in the dielectric constant at magnetic transitions.

However, third order couplings of the form $\mathbf{PM}d\mathbf{M}$ that are linear in $\mathbf{P}$ can have interesting consequences [15, 16], and for the case of a system with inhomogeneous magnetic ordering, can induce a ferroelectric polarisation:

The free energy (F_p) that describes the coupling between a polarisation and a non-uniform distribution of magnetisation can be determined. In a cubic environment, the free energy has the form [17]

$$F_p = \frac{\mathbf{P}^2}{2\chi^e} - \lambda \mathbf{P}[\mathbf{M}(\Delta.\mathbf{M} - (\mathbf{M}.\Delta)\mathbf{M}] \tag{1.2.10}$$

where χ^e is the dielectric susceptibility and λ is a coupling constant.

The induced polarisation can be found by differentiating F_p with respect to $\mathbf{P}$

$$\mathbf{P} = \lambda \chi_e [\mathbf{M}(\Delta.\mathbf{M} - (\mathbf{M}.\Delta)\mathbf{M}]. \tag{1.2.11}$$

The actual form is dependent upon the symmetry of the crystal lattice.

Various forms of magnetic order can induce a polarisation, for example, a spiral spin density wave with wave vector $\mathbf{Q}$, described by

$$\mathbf{M} = M_1 \mathbf{e}_1 cos\mathbf{Q} \cdot \mathbf{x} + M_2 \mathbf{e}_2 sin\mathbf{Q} \cdot \mathbf{x} + M_3 \mathbf{e}_3 \tag{1.2.12}$$

where $\mathbf{e}_i$ forms an orthogonal basis. In the case that both M_1 and M_2 are non-zero (in which case a helix is formed with spin rotation axis $\mathbf{e}_3$) , substituting this form into Eq. (1.2.11):

$$\mathbf{P} = \frac{1}{V} \int d^3x \mathbf{P} = \lambda \chi_e M_1 M_2 [\mathbf{e}_3 \times \mathbf{Q}]. \tag{1.2.13}$$

This leads to an average polarisation that is transverse both to $\mathbf{e}_3$ and $\mathbf{Q}$, and is independent of M_3.

It is noted that whilst the case above for a spiral spin density wave does allow for the onset of a ferroelectric polarisation, a sinusoidal spin density wave (M_1 or $M_2 = 0$), would not give rise to a polarisation, since M_n would be left invariant under spatial inversion.

Searching for candidate type II multiferroic materials involves determining magnetic orders that can lead to improper ferroelectric polarisations. Many breakthroughs have been made in uncovering unconventional magnetic orders and different microscopic mechanisms coupling the ferroelectric polarisation. Several key materials are outlined below:

1.3 Progress in the Field of Multiferroics

1.3.1 Breakthrough Materials

Coupling between magnetic and electrical degrees of freedom is a concept that dates back a long way, beginning with the formalism of Maxwell's equations in the 19^{th} century [18]. The linear magneto-electric effect, in which an electrical polarisation is induced through application of a magnetic field, was initially theoretically predicted by Dzyaloshinskii [19]. Experimental observation of this phenomena by Ref. Astrov [20], sparked rapid discovery of family of magneto-electric compounds, along with a classification of possible symmetry groups that allow for this effect. Schmid [21] extended the formalism for the magneto-electric effect and proposed that systems could arise that have not only cross coupled electric and magnetic responses, but coexisting magnetic and electric orderings in the absence of magnetic and electric fields.

The start of the century marked a surge of interest in the development of functional multiferroic systems. In 2000, Hill addressed the difficulty of finding materials in which magnetism and ferroelectricity coexist [22], and Khomskii summarised possible theoretical mechanisms to overcome this [23]. A major experimental breakthrough was the discovery of room temperature, type I multiferroicity in $BiFeO_3$ [13]. The large polarisation, and enhanced magneto-electric coupling in thin films has resulted in $BiFeO_3$ continuing to be one of the most studied multiferroic systems [24, 25]. In 2003, Kimura [14] characterised a type II multiferroic system; $TbMnO_3$, in which ferroelectric polarisation is induced by a cycloidal magnetic structure. This prompted the search for a vast range of novel magnetic orders that can lead to polar structures. Whilst a thorough explanation of all microscopic mechanisms that can result in type II multiferroicity is beyond the scope of this thesis, key examples that are relevant to the systems characterised in this thesis are outlined below:

1.3.1.1 Cycloidal multiferroic - $TbMnO_3$

$TbMnO_3$ magnetically orders as an antiferromagnetic spin density wave below 40 K with an incommensurate modulation that locks in with propagation vector $\boldsymbol{q}$ = (0, 0.28, 0) below T_{lock} = 30 K [26]. Below T_{lock}, Mn magnetic moments rotate to form a transverse cycloid in the bc plane, and this is coincident with the emergence of a ferroelectric polarisation parallel to the c axis, as shown in Figure 1.7. The direction of polarisation can be flopped to the a axis through application of a magnetic field parallel to b.

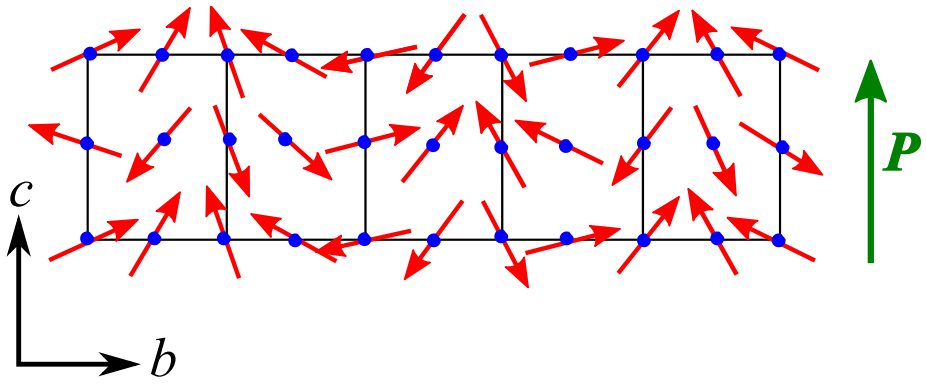


Figure 1.7: Mn magnetic spins below T_{lock} in $TbMnO_3$. The spins rotate to form a cycloidal structure in the bc plane. This coincides with the emergence of a polarisation parallel to c.

Cycloidal magnets are intrinsically polar, such that an absolute up and down direction can be defined, as shown in Figure 1.8.

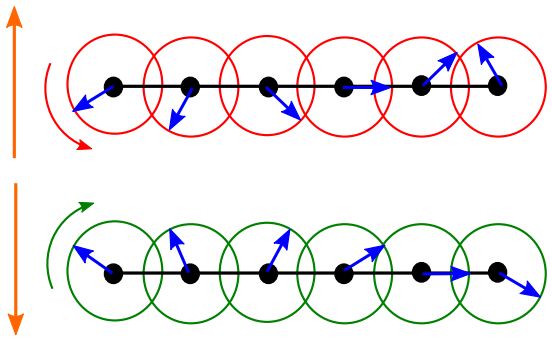


Figure 1.8: Comparison of an "anticlockwise" (red) and "clockwise" (green) cycloid, highlighting the difference in up/down direction, as defined by the orange arrows.

Centrosymmetric crystal structures will become electrically polar in coincidence with cycloidal magnetic ordering provided that a coupling term exists between the magnetic polarity and an order parameter for a structural or electrical polar distortion. This coupling can be understood in terms of the antisymmetric Dzyaloshinskii-Moriya (DM) interaction:

This interaction contributes to the magnetic exchange between two neighbouring spins $\mathbf{S}_i$ and $\mathbf{S}_j$. It was initially postulated by Dzyaloshinskii, using phenomenological considerations based upon Landau theory [27], and the microscopic mechanism of spin orbit coupling was identified by Moriya [28]. The associated term in the Hamiltonian can be written as

$$H_{DM} = \mathbf{D}_{ij} \cdot (\mathbf{S}_i \times \mathbf{S}_j). \tag{1.3.1}$$

where $\mathbf{D}_{ij}$ is a vector constrained by symmetry. For the the case of two magnetic ions connected to a non-magnetic ligand by the vectors $\mathbf{r}_i$ and $\mathbf{r}_j$,

$$\mathbf{D}_{ij} \propto \mathbf{r}_i \times \mathbf{r}_j \tag{1.3.2}$$

$$\Rightarrow \mathbf{D}_{ij} = \lambda \mathbf{r}_{ij} \times \mathbf{x} \tag{1.3.3}$$

where $\mathbf{r}_{ij}$ is the vector that connects the spins $\mathbf{S}_i$ and $\mathbf{S}_j$. Thus $\mathbf{D}_{ij}$ is oriented perpendicular to the triangular arrangement shown in Figure 1.9.

In an antiferromagnetic structure, this interaction favours canting of the two spins, leading to weak ferromagnetic contributions.

When considering the induction of a ferroelectric polarisation in cycloidal magnetic structures, it is the *inverse* DM interaction that takes effect, resulting from exchange striction (lattice relaxation into a magnetically ordered state). Small shifts in connecting oxygen ligands (in this case, forming bonds between between two Mn spins) along the line $\mathbf{x}$ in Figure 1.9, are energetically favourable.

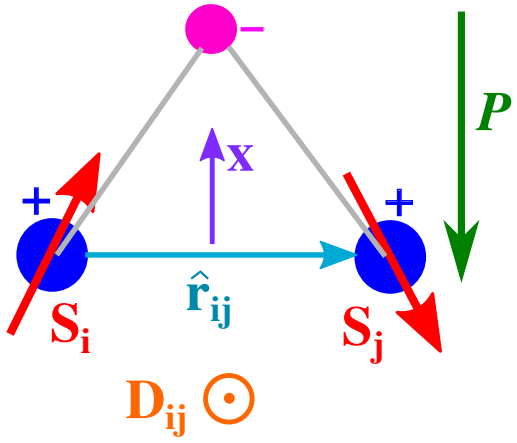


Figure 1.9: The effect of the DM interaction. $\mathbf{D}_{ij}$ is proportional to the spin orbital coupling constant λ, and is dependent upon the position of the ligand (pink) connecting two transition metal cations ($\mathbf{S}_i$ and $\mathbf{S}_j$), defined by the vector $\mathbf{x}$.

Displacement of the ligand results in a polarisation of the form:

$$\mathbf{P} \propto \mathbf{r}_{ij} \times (\mathbf{S}_i \times \mathbf{S}_j). \tag{1.3.4}$$

In a cycloidal magnetic structure, the relative canting of adjacent spins means that the product $\mathbf{S}_i \times \mathbf{S}_j$ has the same sign for all pairs of spins. This results in all ligands being displaced in the same direction, perpendicular to the spin chains, and a net polarisation results.

An alternative model for the coupling mechanism in $TbMnO_3$ and other cycloidal magnetic structures is the KNB (Katsura, Nagoya, Balatsky) spin current model [29]. This describes an electronic contribution to the ferroelectric polarisation, but produces an equivalent result to the DM model, with spin-charge transfer across the Mn-O-Mn bond resulting in a net displacement of charge perpendicular to the vector connecting the two Mn sites.

In reality both models contribute, equivalently resulting in a net polarisation that is constrained to lie within the plane of rotation of the spins, and has a direction determined by the sense of rotation of the cycloid. $TbMnO_3$ was the first cycloidal magnetic multiferroic to be characterised, but is now one of an extensive class, most

of which share the same microscopic coupling mechanism, but differ in the subtleties of the magnetic structure and contribution of secondary magnetic ions (significant for $RMnO_3$ compounds $GdMnO_3$ [30] and $DyMnO_3$ [31, 32, 33, 34]).

1.3.1.2 Quasi-collinear multiferroics - $TbMn_2O_5$ and $HoMnO_3$

$TbMn_2O_5$ The RMn_2O_5 family with R = La,Y,Bi or a rare earth element crystallise in the space group *Pbam*. Edge sharing $Mn^{4+}O_6$ octahedra form chains along the c axis, coupled by $Mn^{3+}O_5$ pyramids as shown in Figure 1.10(a). Magnetic ordering throughout the family shares many similarities [35], but is outlined for $TbMn_2O_5$ below.

$TbMn_2O_5$ forms an incommensurate magnetic structure below $T_N = 44$ K with propagation vector $q = (0.480, 0, 0.245)$. A second transition to a commensurate magnetic structure with $q = (0.5, 0, 0.25)$ occurs at 38 K, accompanied by the onset of a ferroelectric polarisation. The magnetic structure in the ab plane consists of staggered, zig-zag antiferromagnetic chains running along the a axis, with slightly canted spins, as indicated by the pink line in Figure 1.10(b).

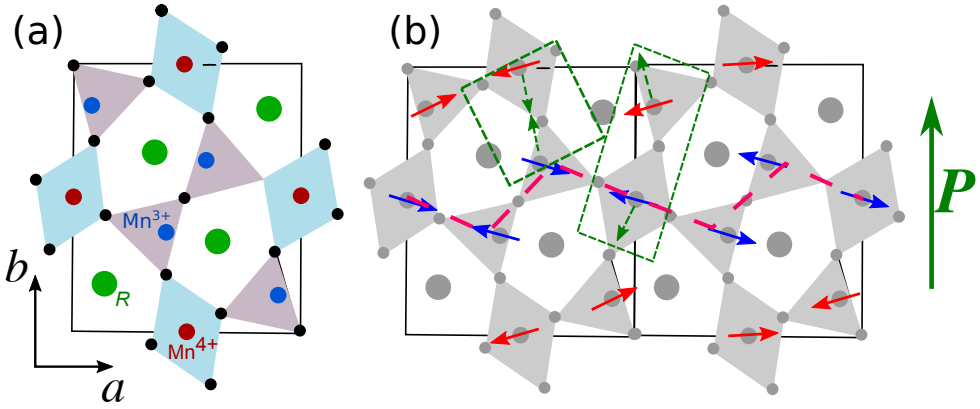


Figure 1.10: Adapted from Ref. [35]. (a) The crystal structure of the RMn_2O_5 compounds in the ab plane. $Mn^{3+}O_5$ pyramids couple $Mn^{4+}O_6$ octahedra, which form edge sharing chains along the c axis. (b) The magnetic structure of $TbMn_2O_5$ below 38 K. Across antiferromagnetic chains (red dashed line), antiparallel spins are shifted closer together whilst parallel spins move apart (green boxes), inducing a polarisation along the b axis.

Looking across the zig-zag chains, approximately half the Mn^{3+} - Mn^{4+} pairs have parallel spins, whilst the other half have antiparallel spins. Cations are shifted to minimise the spin-exchange energy, which is expected to promote an antiferromagnetic structure in $TbMn_2O_5$. Cations with antiparallel spins are pulled together, whilst those with parallel spins move apart, as indicated by the green boxes in Figure 1.10(b), producing a distortion pattern that breaks inversion symmetry, inducing a net polarisation along the b axis.

The mechanism driving ferroelectricity relies on symmetric Heisenberg exchange, which is much stronger than the antisymmetric DM interaction that is dominant in cycloidal type II mutliferroics. Consequently the magnitude of the magnetically induced ferroelectric polarisation is larger than in $TbMnO_3$.

$HoMnO_3$ In a similar manner to $TbMnO_3$, Mn spins in $HoMnO_3$ order with an antiferromagnetic spin density wave below $T_N = 41$ K [36, 37]. However, in contrast to the low temperature cycloidal magnetic structure of $TbMnO_3$, $HoMnO_3$ locks into a quasi-collinear, commensurate E-type antiferromagnetic phase below 26 K, as shown in Figure 1.11 [38].

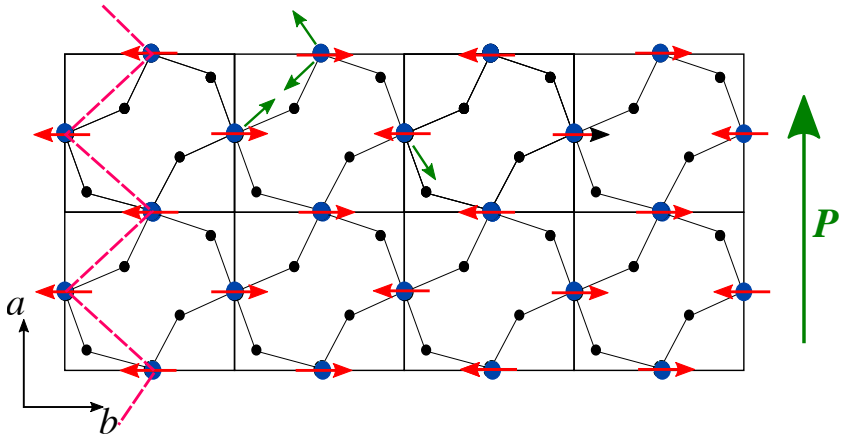


Figure 1.11: Adapted from Ref. [38]. The E-type antiferromagnetic structure of $HoMnO_3$. Mn spins form ferromagnetic chains (pink dotted line) along the a axis. A reduction in the Mn-O-Mn bond angle gives rise to a polarisation along the a axis, as indicated by the green arrow.

Lorenz *et al.* explained that ferroelectricity results from competition between elastic

energy and the gain in electronic energy due to hopping of Mn electrons along ferromagnetic zigag chains [38]. This electronic model is complemented by an ionic picture, similar to that for $TbMn_2O_5$, based upon Goodenough-Kanamori-Anderson (GKA) rules [39, 40, 41, 42]. Favourable ferromagnetic exchange results in parallel Mn spins shifting closer together, whilst antiparallel spins shift further apart. This increases Mn-O-Mn bond angles, displacing oxygen anions, and leading to a net polarisation along the a axis.

It should be noted that below 12 K, an additional contribution to the polarisation occurs in $HoMnO_3$ [38]. The Ho sublattice forms a rotating cycloidal structure in the ab plane, and as a result of the antisymmetric DM interaction, contributes to net polarisation along the a axis.

1.3.1.3 Helical multiferroics - $RbFe(MoO_4)_2$

Unlike cycloidal magnetic structure, helical magnetic structures, in which spins rotate perpendicular to the direction of propagation, are not intrinsically polar, and would not normally induce a ferroelectric polarisation through either of the mechanism outlined above. However, if crystal structures have axial symmetry, coupling between the magnetic ordering and a structural rotational distortion may support a ferroelectric polarisation [43].

An axial vector $\mathbf{A}$, that describes a structural rotational distortion, can couple to a magnetic chirality (σ), giving rise to a polar vector of the form $\mathbf{P} \propto \sigma\mathbf{A}$, and an associated term in the free energy $F_{\text{ax}} = c\sigma\mathbf{A} \cdot \mathbf{P}$. Under application of an electric field, $\mathbf{P}$ will switch, and the magnetic structure may switch chirality in order to keep free energy at a minimum, providing a possibility to directly couple the electric and magnetic order parameters. An example of ferroaxial coupling in $RbFe(MoO_4)_2$ is outlined below.

At room temperature, $RbFe(MoO_4)_2$ is trigonal, $P\bar{3}m1$. Iron cations form 2-d triangular layers that stack along the c axis separated by triangular Rb layers. Within

each unit cell, one MoO_4 tetrahedra points up, and another points down, as shown in Figure 1.12(a). The tetrahedra align exactly with the Fe triangular lattice, but below 190 K the tetrahedra cooperatively rotate, lowering the symmetry to $P\bar{3}$. This structural distortion can be defined as a global rotation of oxygen anions about an axial vector **A**. There are two energetically equivalent directions for oxygen rotation, and thus two axial domains may form with equal population.

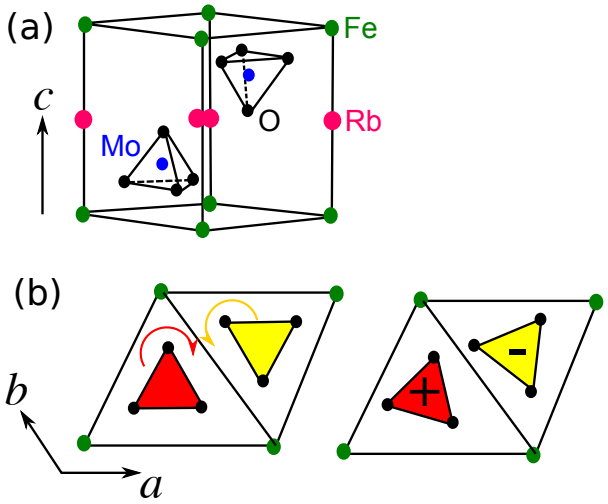


Figure 1.12: Adapted from Ref. [43]. (a) A unit cell of $RbFe(MoO_4)_2$, with one MoO_4 pointing up, and another pointing down. The tetrahedra separate triangular layers of Rb (pink) and Fe (green) that form within the *ab* plane. (b) Cooperative rotation of the tetrahedra around **A**, leading to the formation of two domains (red and yellow).

Below $T_N = 4$ K, Fe^{3+} moments order, forming a classic 120° antiferromagnetic structure within the *ab* plane, shown in Figure 1.13 [44].

Moments are rotated in adjacent plans, leading to a helical magnetic structure with propagation vector $q = (1/3,\ 1/3,\ 0.44)$. For each of the axial domains shown in Figure 1.12(b), there are two degenerate magnetic structures, hence four domains coexist, with propagation vectors; $q = (\pm 1/3,\ \pm 1/3,\ \pm 0.44)$. These domains are characterised by their helical chirality σ_h, which determines the sense of spin rotation along the *c* axis, and triangular chirality σ_t, which determines the rotation direction of the in plane spin arrangement [43]. A ferroaxial coupling term of the form

$$F_{ax} = c_t \sigma_t \mathbf{P} + c_h \sigma_h \mathbf{P} \tag{1.3.5}$$

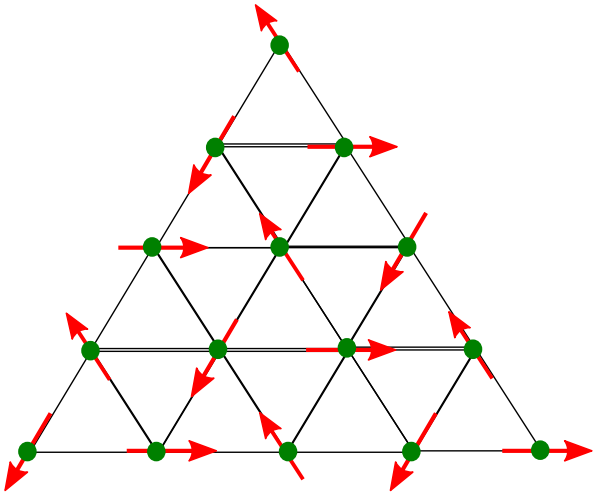


Figure 1.13: The 120° antiferromagnetic kagome magnetic structure, exhibited in Fe layers below T_{N}.

or equivalently,

$$F_{ax} = c\mathbf{A}\sigma_h\mathbf{P} = -c\mathbf{A}\sigma_t\mathbf{P} \tag{1.3.6}$$

can be incorporated into the free energy, where c is a coupling constant and F_{ax} is one of the terms that sums to give the total free energy. Under application of an electric field, the degeneracy of the four magnetic domains is lifted, driving a ferroelectric polarisation. In the absence of an electric field, all four domains are expected to exist in equal proportions, hence $RbFe(MoO_4)_2$ is not expected to behave as a true multiferroic with a spontaneous ferroelectric polarisation. It does however, exhibit magneto-electric coupling, and may provide valuable clues as to microscopic mechanisms for type II multiferroicity in other helical magnetic systems.

Three classes of type II multiferroics have been described above, giving some insight as to the variety of coupling mechanisms that can give rise to the emergence of ferroelectric polarisation from complex magnetic orders. Understanding these coupling mechanisms is key to uncovering multiferroic systems with enhanced functionality; strong, switchable magneto-electric coupling and the emergence of polarisation close to ambient conditions. It is these characteristics that will unlock the technological potential of multiferroics.

1.3.2 Technological Potential

A vital factor in ensuring that interest in multiferroic materials is maintained, is to keep focus on striving towards materials that are not only physically novel and interesting but technologically useful for functional devices with commercial potential.

The primary technological interest in multiferroic materials lies in their application in data storage devices, specifically non-volatile random-access-memory (RAM). Ferroelectric RAM (F-RAM) and magneto-resistive RAM (M-RAM) have been developed as methods to overcome the shortcomings of flash and EEPROM based non-volatile memory; limited read-write cycles, and high power requirements. F-RAM devices are similar in construction to traditional, volatile DRAM which stores data bits as electrical charge on capacitors. F-RAM relies upon thin ferroelectric, rather than dielectric layers. Unlike capacitor charge, ferroelectric layers retain polarity when power is lost, hence the data storage is non-volatile. F-RAM has shown promising potential, with high storage density and fast access speeds, but has several crucial drawbacks: Owing to the stability of the polarisation on ferroelectric layers, a destructive read and reset operation is required. M-RAM writes data to magnetic ordering on a surface, generating the magnetic fields through currents in solenoid coils. This offers a non-destructive, robust storage mechanism, but requires considerable currents in relatively large coils in order to write the data, limiting the storage efficiency. An ideal compromise for the development of non-volatile RAM would be a device that could be written electrically, and read magnetically. Easily localised electrical fields would allow for efficient, dense data writing, without the involvement of large currents, and data would be robustly stored magnetically, and easily reset non-destructively.

Type II ferromagnetic/ferroelectric materials are ideal candidates for such devices, as the coupling between ferroelectric polarisation and magnetic ordering may open up the possibility of manipulating the magnetic order parameter through external electrical fields (and vice versa). In order for this potential to be realised, candidate multiferroics must be functional under ambient conditions. It is an ongoing challenge to uncover

candidate materials in which inhomogeneous magnetic ordering and hence the induced ferroelectricity is not suppressed significantly below room temperature. Additionally, candidate materials must develop large ferroelectric polarisations, comparable to those observed for proper ferroelectrics. Finally, to generate efficient, robust functional devices, the coupling between ferroelectricity and magnetic order will need to be strong, enabling easy switching.

Significant progress has already been made in improving functionality. Coupling between the order parameters in type II multiferroics is significantly stronger than for the earliest studied type I systems. Continued discovery of new magnetic orderings that allow for polar electronic distortions is increasing the likelihood of observing magnetically induced polarisations at higher temperatures. However, current magnetically induced polarisations are typically several orders of magnitude below those of type I multiferroics, and typical onset temperatures for inhomogeneous magnetic ordering are below liquid nitrogen temperature. Thus there is evidently still a great deal of scope for progress in the field.

1.4 Thesis Plan

In accordance with the aims outlined above, this thesis focuses on characterising structural, charge and orbital ordering in quadruple perovskite structures that have multiferroic potential. Three systems have been studied: Firstly, $CaMn_7O_{12}$, a type II multiferroic with a helical magnetic structure that gives rise to ferroelectric polarisation through ferroaxial coupling. Single crystal x-ray diffraction studies have revealed an unprecedented magnet-orbital coupling, yielding one of the largest magnetically induced ferroelectric polarisations measured to date.

Doping of well understood systems is a common technique used to tune structural, magnetic and electrical properties. Bearing this in mind, with the goal of tuning multiferroic functionality, the related system $CaCu_{0.15}Mn_{6.85}O_{12}$ has been studied. SEM and EDX microscopy have been used to confirm crystal compositions, and single

crystal x-ray diffraction studies have allowed a structural comparison to $CaMn_7O_{12}$. Various physical interpretations of structural modulations incorporating twin models, orbital, and charge ordering have been considered and tested. Further work incorporating optical observation of twins, magnetic structure studies and polarisation measurements is proposed.

Finally, charge and orbital ordering in the quadruple perovskite, $NaMn_7O_{12}$ has been studied. A low temperature structural model that reconciles a previous orbital ordering model with experimental x-ray powder diffraction data has been proposed, and is tested against single crystal neutron diffraction data. Further investigation of the magnetic structure and polarisation in $NaMn_7O_{12}$ may reveal multiferroic potential, similar to that theoretically predicted in related half and quarter doped manganite compounds.

In Chapter 2, the experimental characterisation techniques exploited in the structural studies of $CaMn_7O_{12}$, $CaCu_{0.15}Mn_{6.85}O_{12}$ and $NaMn_7O_{12}$ are outlined and explained. This is followed by characterisation studies of each system in turn. Finally, concluding remarks will address the outlook for multiferroic technology, suggesting further experimental and theoretical work, and routes to consider when searching for new multiferroic materials.

Chapter 2

Characterisation Techniques

The theme of this thesis is characterisation of quadruple perovskites with multiferroic potential, incorporating compositional and structural studies to gain insight into charge and orbital orderings, and considering microscopically the mechanisms that couple these orderings to magnetic structures. As is often the case when characterising emerging materials, x-ray and neutron diffraction techniques have been employed as preliminary probes of atomic ordering in this thesis. These techniques exploit an interaction of incoming radiation and the sample, and are sensitive to atomic displacements that occur in systems as a result of symmetry breaking, making them particularly valuable techniques for studying phase transitions in crystalline materials. Additionally, in this thesis, electron microscopy techniques, specifically scanning electron microscopy (SEM) and energy dispersive spectroscopy (EDX) have been used for compositional studies. As with x-ray and neutron diffraction, these techniques exploit the interaction of incident radiation with the sample, but while x-rays and neutrons probe bulk material properties, incident electrons are surface sensitive probes. Several signals are generated from incident electron beams: Detailed surface imaging can be produced from information contained in secondary electrons emitted from the sample, whilst backscattered incident electrons and x-rays yield precise surface compositions.

The fundamental principals of SEM and EDX, x-ray diffraction and neutron diffraction will be outlined below. Practical considerations for experimental studies will be discussed, including sample preparation, instrumentation and facilities available and

control of sample environments such as temperature.

2.1 Electron Microscopy

2.1.1 Interaction of electrons with the sample

Conventional microscopes use visible light photons as a source of illumination. Image resolution (δ) is defined by the Rayleigh criterion:

$$\delta = \frac{0.61\lambda}{\mu \sin\beta} \tag{2.1.1}$$

where μ is the refractive index of the viewing medium, and β is the semi-angle of collection of the magnifying lens. These vary very little, and resolution is primarily determined by the wavelength of the light (λ). Typical wavelengths of visible light give rise to a resolution of $\sim$300 nm, insufficient for imaging an atomic scale, which requires a resolution of $\sim$0.2 nm.

The wavelength of electrons can be determined from the de Broglie equation:

$$\lambda = \frac{h}{p} \tag{2.1.2}$$

where h is Plank's constant and p is the relativistic momentum of the electron. In scanning electron microscopes, electrons are accelerated up to $\sim$10 kV , and travel at appreciable fractions of the speed of light. Taking relativistic effects into account, the relationship between energy and momentum for the electron is given by

$$E^2 = c^2(p^2 + m_0^2 c^2) \tag{2.1.3}$$

where m_0 is the electronic mass.

For an electron accelerated with an energy change ΔE, taking a classical description,

it can be shown that

$$p = \sqrt{2m_0\Delta E}\sqrt{1 + \frac{\Delta E}{2m_0c^2}}. \tag{2.1.4}$$

Thus from Eq. (2.1.2), the relativistic formula for the electron wavelength then becomes

$$\lambda = \frac{h}{\sqrt{2m_0\Delta E}}\frac{1}{\sqrt{1 + \frac{\Delta E}{2m_0c^2}}}. \tag{2.1.5}$$

Considering an accelerating voltage of 10 kV, the resulting electron wavelength will be 1.2 nm. This is a significant improvement on the resolution of conventional visible light microscopy, and can allow for atomic scale resolution.

An SEM generates an image by scanning a focused beam of electrons across the sample surface. Upon interaction with the sample surface, the incident electrons lose energy by several mechanisms, all of which provide signals that carry information relating to the surface composition or topography of the sample:

- **Backscattered Electrons** High energy electrons originating from the incident electron beam can be reflected, or backscattered elastically at high angle via interaction with atomic nuclei in the sample. Heavy atoms (high atomic number) backscatter electrons more strongly than light atoms, and hence sample regions that contain heavy atoms appear brighter. Backscattered electron signals can be used to qualitatively detect compositional contrast in a sample.

- **Secondary Electrons** Incident electrons can also scatter inelastically from the sample. This results in the emission of secondary electrons from the K-shells of atoms in the sample, see Figure 2.1(a). These secondary electrons are low energy (typically <50 eV), and originate from close to the sample surface. Irregularities in the surface texture affect the probability of secondary electron emission, and thus secondary electron detection provides details of surface contrast and topography in samples (Figure 2.1(b)).

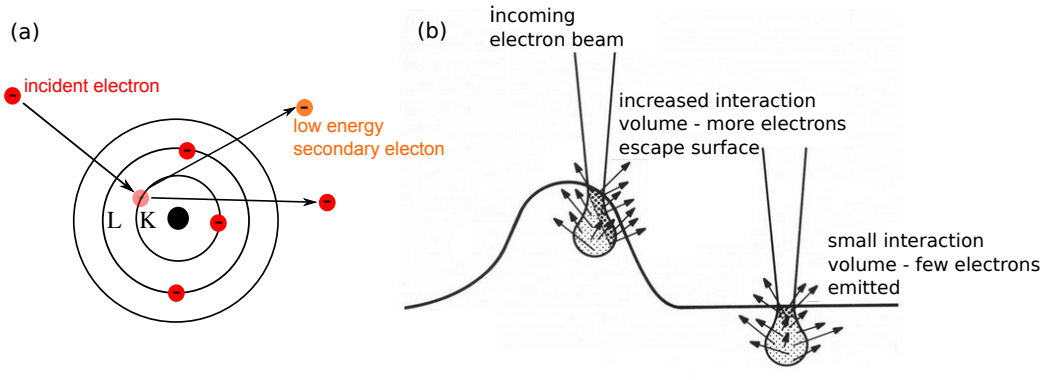


Figure 2.1: (a) The emission of a low energy K-shell electron as a result of inelastic scattering between the incident electron and the atom. (b) Adapted from Ref. [45]. The probability of these low energy electrons being emitted from the sample surface is dependent upon the surface topography, and specifically, the angle between the incident radiation and the sample surface. Surface irregularities will increase secondary electron emission.

- **X-rays** Inelastic scattering of incident electrons will also result in emission of characteristic x-rays. Vacancies arising from the ejection of secondary electrons will be filled by electrons from higher energy states, and the excess energy will be lost as x-rays. The precise x-ray energy corresponds to the energy gap between the electronic states, and will be characteristic of a specific element as shown in Figure 2.2. Hence analysis of emitted x-rays can be used for quantitative compositional studies of the sample surface.

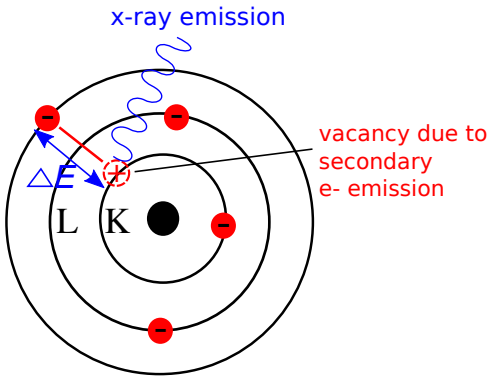


Figure 2.2: An energy change resulting from an electron filling a vacancy created during secondary electron emission. This energy change results in emission of an x-ray of the same energy, which will be characteristic of a specific atom.

2.1.2 The SEM microscope

2.1.2.1 Electron beam generation

The first stage in producing an image from an electron microscope is the generation of a high energy incident electron beam. This is most commonly achieved through thermionic emission from a V-shaped tungsten wire. The wire is heated until electrons have sufficient thermal energy to overcome the work function. Electrons are then emitted and accelerated towards an anode, typically using accelerating voltages of ∼10 kV to produce electron energies ranging from 100 eV to 30 keV, depending upon the evaluation objectives of the experiment.

2.1.2.2 Focusing the beam

The electron beam emerging from the anode will be divergent, and must be converged to a fine probe size before being rastered across the sample surface. This focusing is achieved using electromagnetic condenser lenses, which use copper solenoid coils to apply a Lorentz force to the electrons, as shown in Figure 2.3.

Upon passing through the condenser lens, electrons travelling furthest from the optical axis experience the largest inward force, whereas those travelling along the optical axis feel zero force. This converges the beam, typically to a diameter of around 10 Å.

2.1.2.3 Interaction with the sample and signal detection

The focused electron beam will then be positioned onto the sample surface using further electromagnetic coils. The electron beam strikes the surface, and multiple signals are generated, as described in section 2.2.1.1. These signals are recorded as the electron beam is rastered across the sample surface. Backscattered electron detectors are typically mounted directly above the sample, forming concentric circles around the incident electron beam, as shown in Figure 2.4.

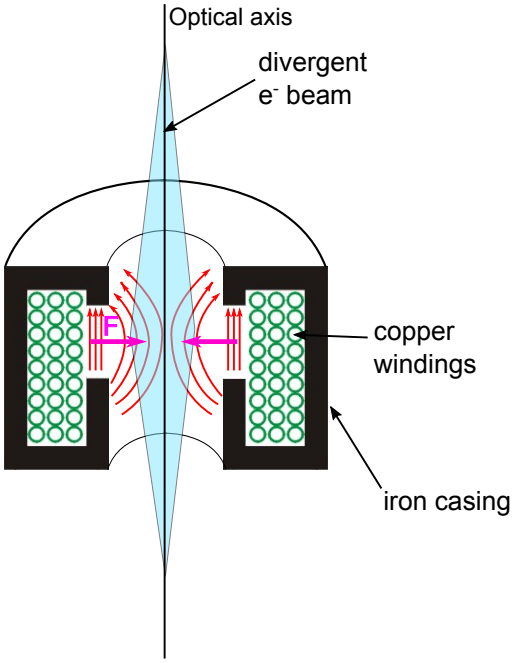


Figure 2.3: Electromagnetic condenser lenses consist of coils of copper wire which form a cylindrical arrangement within an iron casing. A Lorentz force is exerted on electrons as they pass through the cylinder, converging the electrons to form a fine probe.

Backscattered electron detectors are typically scintillators (photomultiplier devices that convert electrons to photons) or semi-conductor devices. Low energy secondary electrons detecters are typically located off to one side of the SEM. Secondary electrons need to be accelerated in order to be sufficiently energetic to generate photons for detection. This is achieved by attracting the emitted electrons towards a electrically biased grid, typically held at ∼400 V, and producing further acceleration by positively biasing the scintillator to voltages of ∼2000 V. In a standard SEM set up, detection of emitted x-rays is not of primary concern. However, SEM's can be equipped with EDX for detection and analysis of x-rays. This is discussed in more detail below.

2.1.2.4 Image formation

The secondary electron signal is most commonly used for image formation. The signal recorded at the detector is amplified and can be displayed as a two dimensional intensity distribution. This can either be photographed as an analogue display or

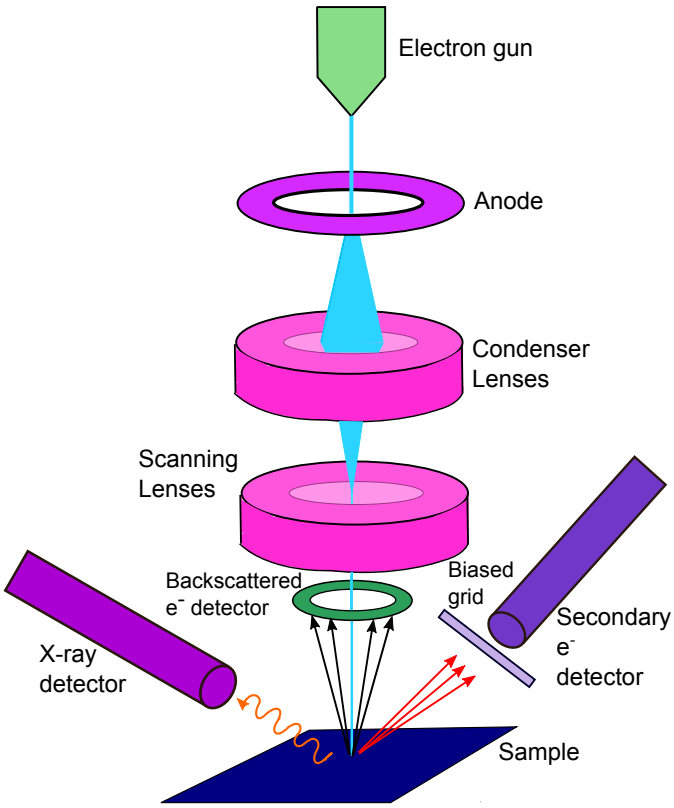


Figure 2.4: The setup of a typical SEM. Electrons are accelerated by an anode, and pass through a series of electromagnetic condenser and scanning lenses, which position a fine probe electron beam onto the sample surface. Backscattered electron detectors are mounted directly above the incident beam position, whilst secondary electron and x-ray detectors are offset to either side.

converted and saved as a digital image. By synchronising the position in the image scan to a scan of the incident electron beam, the display can represent the topography of the sample surface area. The resulting image can be magnified to any given ratio between the display size and the sample area scanned by the electron beam.

2.1.2.5 Sample preparation and resolution

As SEM is a reflection technique, sample preparation is relatively simple compared to that for transmission microscopy techniques. Samples must fit within the sample chamber, with sizes up to ∼15 cm typically being accommodated. Compositional, backscattered electron analysis can be performed on conductive, or non-conductive samples, but for secondary electron imaging, the surface of samples must be electri-

cally conductive, and samples must be grounded to prevent accumulation of static charge. Non-conductive materials can be coated with gold or carbon by sputtering or high vacuum evaporation. To produce high quality backscattered images for compositional mapping, without the need for x-ray analysis, samples may need to be polished. Additionally, samples must be compatible with moderate vacuum, typically under pressures of $\sim$1x10^{-5} Torr.

Spatial resolution of SEM microscopy is dependent upon the interaction volume, as summarised in Figure 2.5. Secondary electrons are generated from a small volume region close to the sample surface, allowing for good resolution, limited by the beam diameter and broadened by the escape depth of the electrons. X-rays emerge from a wider, deeper volume, limiting spatial resolution at the sample surface.

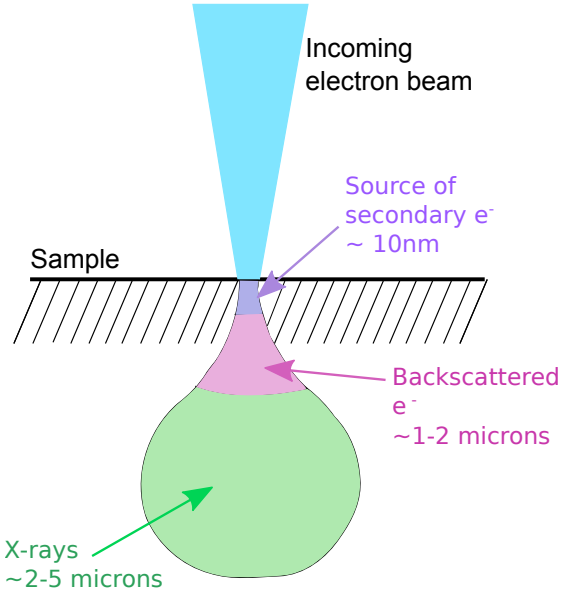


Figure 2.5: The contrast in interaction volumes for the different signals generated in an SEM experiment. X-rays are generated from the largest/deepest volume, and hence provide good compositional information, but are limited in resolution. In contrast, secondary electrons are generated from a small volume and hence provide higher resolution mapping of the surface.

Whilst the wavelength of the electrons should allow for atomic scale resolution in the SEM, the beam spot size and interaction volume are significantly larger than typical atomic spacings. Thus, whilst the resolution is significantly better than that of conventional visible light microscopy and even x-ray diffraction, practical resolution

limits are generally ∼1-20 nm.

2.1.3 Energy Dispersive Spectroscopy (EDX)

Quantitive compositional analysis is not always required in a standard SEM experiment, but it is possible to equip an SEM with an EDX spectrometer to quantitively analyse characteristic x-rays. EDX detectors will measure the relative abundance of emitted x-rays versus their energy, and are typically lithium/silicon solid state devices. When x-rays strike the detector, a charge pulse is generated in proportion to the x-ray energy. This is converted into a voltage pulse, and transmitted to a multichannel analyser. The analyser sorts the pulses by their voltage, and voltages are converted back into characteristic energies. The output is a spectrum of counts versus energy, which can be compared to standards to determine quantities of specific elements present.

In the simplest case, results can be purely qualitative; determining the presence or absence of an element in a sample from detection of x-rays of a specific energy. Semi-quantitative results can be obtained by comparing relative proportions of each single to determine compositions, using mathematical corrections based on expected compositions if necessary. Spatial elemental mapping can be generated by measuring x-ray intensity relative to lateral sample position, combining results with higher resolution, backscattered electron signals. Resolution of ∼0.1 μm can be obtained for these elemental maps. With a good knowledge of predicted composition and a complete set of standard samples, compositional analysis can be accurate to within 0.1 atomic percent.

2.2 X-ray Diffraction

Electron microscopy provides a valuable probe for analysing surface composition, giving insight into impurities, inhomogeneity or any deviations from expected composi-

tions. In this thesis, this has been a useful tool for preliminary characterisation of samples, particularly in the case of doped $CaMn_7O_{12}$ crystals, where precise composition may be uncertain from the crystal growth method. Moving beyond initial crystal characterisation, the structural and magnetic studies necessary to understand microscopic mechanisms for multiferroicity require bulk structure studies.

X-rays are good probes for probing crystalline materials, because their typical wavelengths of 0.1-100 Å are of a similar scale to interatomic spacings. Crystal structures therefore readily diffract x-rays, and the diffraction is sensitive both to periodic atomic orderings, and modulations to ordering such as changes in cell parameters, changes in symmetry, and small atomic displacements such as those associated with ferroelectricity.

The scope of x-ray scattering experiments is vast, incorporating single crystal, powder studies, magnetic diffraction, and resonant elastic and inelastic scattering. In this thesis, single crystal elastic scattering is the primary technique used, and the theoretical basis for this will be outlined below. Initially, the interaction of x-rays with electronic charges will be considered. This will then be extended to the interaction with a periodic crystal structure. Since some results from powder and magnetic diffraction are also presented in this thesis, these techniques will also be briefly discussed.

2.2.1 The theory of x-ray scattering

2.2.1.1 Interaction with an electron

Here a classical description of x-ray scattering is outlined based upon the **Thomson scattering** formalism (which assumes free electrons) following Refs. [46] and [47]. This description is sufficient for the elastic x-ray scattering experiments discussed in this thesis, but it is noted, that for the case of x-ray absorption experiments, a quantum mechanical formalism would be necessary.

The layout of a typical x-ray scattering experiment is shown in Figure 2.6.

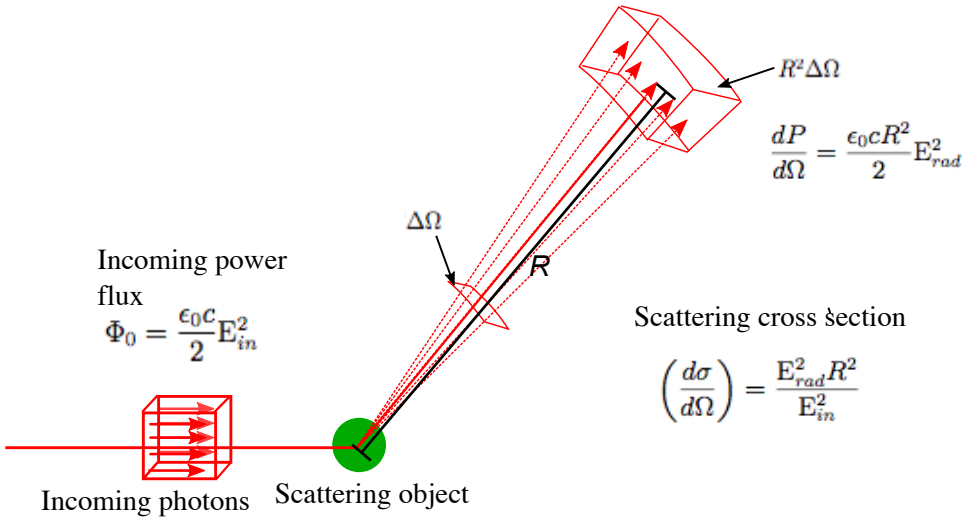


Figure 2.6: Adapted from Ref. [46]. The incident beam, with power flux Φ_0 interacts with a target object to produce a scattered radiation. A detector, situated at a distance R from the sample, subtends an angle $\Delta\Omega$ and detects scattered photons.

When the electric field associated with an x-ray interacts with a free electron, it causes the electron to accelerate, and scattered radiation is emitted. Here, an non-relativistic approximation is made, assuming that the electron charge is observed in a reference frame where its velocity is small compared to the velocity of light.

The fundamental quantity determined is the differential scattering cross section $\left(\frac{d\sigma}{d\Omega}\right)$, defined as the power radiated per unit of solid angle subtended by the detector $\left(\frac{dP}{d\Omega}\right)$, divided by the average power flux of the incident beam (Φ_0). Φ_0 and $\frac{dP}{d\Omega}$ can be rewritten in terms of the electric fields of the incident and scattered x-ray beams ($\mathbf{E}_{in}$ and $\mathbf{E}_{rad}$ respectively).

The energy density of incoming photons is proportional to $\mathbf{E}_{in}^2$, and Φ_0 is given by

$$\Phi_0 = \frac{\epsilon_0 c}{2} \mathbf{E}_{in}^2 \tag{2.2.1}$$

where c is the velocity of light and ϵ_0 is the permittivity of free space. Similarly the energy density of the scattered beam is proportional to $\mathbf{E}_{rad}^2$

$$\frac{dP}{d\Omega} = \frac{\epsilon_0 c R^2}{2} \mathbf{E}_{rad}^2 \tag{2.2.2}$$

where R is the distance from the sample to the detector. The scattering cross section can be written as

$$\left(\frac{d\sigma}{d\Omega}\right) = \frac{\mathbf{E}_{rad}^2 R^2}{\mathbf{E}_{in}^2}. \tag{2.2.3}$$

Considering the scattered field in more detail:

$\mathbf{E}_{in}$ exerts a force on a single electron, causing it to vibrate and radiate a spherical electric field, as shown in Figure 2.7.

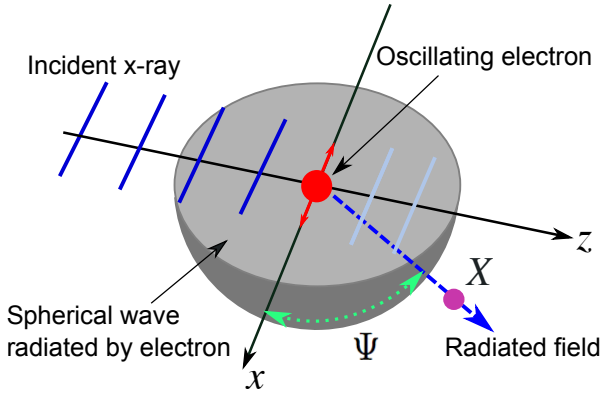


Figure 2.7: Adapted from Ref. [46]. Classical scattering of an x-ray by an electron: The electric incident radiation causes the electron to oscillate and radiate a spherical wave (here, an isotropic, spherical wave with constant phase and amplitude is shown). The incident wave has electric field polarised along x and propagates along z.

This radiated field can be calculated for an observation point X, and will be dependent upon the polarisation of the incident radiation ($\boldsymbol{\epsilon}$), and on the scattering angle (90-2Ψ).

Initially, considering the situation shown in Figure 2.7, where X lies in the plane spanned by $\boldsymbol{\epsilon}$ (parallel to x) and the propagation vector of the incident radiation (z). $\mathbf{E}_{rad}$ will be proportional to electronic charge -e, and to the acceleration (a_X) at a time t' earlier than the observation time t, due to the finite speed at which the radiation propagates.

The radiated field is given by

$$\mathbf{E}_{rad}(R,t) = -\left(\frac{1}{4\pi\epsilon_0 c^2}\right)\frac{e}{R}a_X(t')\sin\Psi \tag{2.2.4}$$

where $t' = t - \frac{R}{c}$.

The factor $\sin\Psi$ accounts for variation of acceleration with the observation angle. For an observer in the xz plane, as shown in Figure 2.7, acceleration will be a maximum for $\Psi = 90°$, and zero for $\Psi = 0°$.

The acceleration a_X can be evaluated from the force exerted on the electron, divided by the electronic mass ($a_X(t') = \frac{F}{m} = \frac{eE}{m}$). Writing the time dependent electric field of the incident wave as

$$\mathbf{E}_{in} = \mathbf{E}_0 \mathrm{e}^{-iwt}. \tag{2.2.5}$$

The acceleration is evaluated as

$$a_X(t') = \frac{-e\mathbf{E}_0 \mathrm{e}^{-iwt'}}{m} = \frac{-e}{m}\mathbf{E}_{in}\mathrm{e}^{i\omega(Rc-t)} = \frac{-e}{m}\mathbf{E}_{in}\mathrm{e}^{i(kR-\omega t)} \tag{2.2.6}$$

thus Eq. (2.2.4) can be rewritten as

$$\frac{\mathbf{E}_{rad}(R,t)}{\mathbf{E}_{in}} = \left(\frac{e^2}{4\pi\epsilon_0 c^2 m}\right)\frac{\mathrm{e}^{i(kR-\omega t)}}{R}\sin\Psi. \tag{2.2.7}$$

The **Thomson Scattering Length** is defined as

$$r_0 = \left(\frac{e^2}{4\pi\epsilon_0 c^2 m}\right) = 2.82 \times 10^{-15}\mathrm{m} \tag{2.2.8}$$

and can be incorporated into Eq. (2.2.7), giving

$$\frac{\mathbf{E}_{rad}(R,t)}{\mathbf{E}_{in}} = r_0\frac{\mathrm{e}^{i(kR-\omega t)}}{R}\sin\Psi. \tag{2.2.9}$$

Generalising for an observation point X, at an arbitrary angle with respect to the incident beam, the $\sin\Psi$ term is reevaluated such that if $\boldsymbol{\epsilon}$ is the polarisation of the incident field, and $\boldsymbol{\epsilon}'$, that of the radiated field, $[\boldsymbol{\epsilon}\cdot\boldsymbol{\epsilon}'] = \cos 90° + \Psi$ = -$\sin\Psi$.

Rewriting Eq. (2.2.9):

$$\frac{\mathbf{E}_{rad}(R,t)}{\mathbf{E}_{in}} = -r_0 \frac{\mathrm{e}^{i(kR-\omega t)}}{R}[\boldsymbol{\epsilon}\cdot\boldsymbol{\epsilon}']. \tag{2.2.10}$$

The factor of -1 represents the 180° phase shift between the incident and scattered waves. The differential cross section becomes

$$\left(\frac{d\sigma}{d\Omega}\right) = r_0^2[\boldsymbol{\epsilon}\cdot\boldsymbol{\epsilon}']^2. \tag{2.2.11}$$

The factor $[\boldsymbol{\epsilon}\cdot\boldsymbol{\epsilon}']$ should be considered when determining the optimal geometry for x-ray diffraction experiments. Laboratory sources typically have unpolarised x-ray beams, whilst synchrotron sources produce x-rays that are linearly polarised. Two linear polarisation directions are defined; σ (perpendicular to the scattering plane), and π (parallel to the scattering plane), as shown in Figure 2.8. Then, if Ψ is the scattering angle, a polarisation factor is defined, dependent upon the x-ray source:

$$[\boldsymbol{\epsilon}\cdot\boldsymbol{\epsilon}']^2 = \begin{cases} 1 & \text{synchrotron: } \sigma \rightarrow \sigma \text{ scattering} \\ \cos^2\Psi & \text{synchrotron: } \pi \rightarrow \pi \text{ scattering} \\ \frac{1}{2}(1+\cos^2\Psi) & \text{unpolarised source} \end{cases}$$

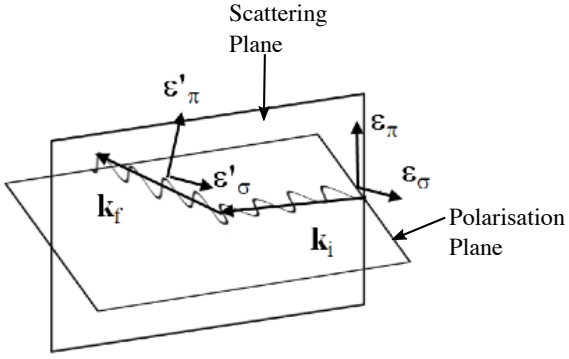


Figure 2.8: Adapted from Ref. [48]. σ and π reference directions for linearly polarised incident and scattered x-ray beams with propagation vectors $\mathbf{k}_i$ and $\mathbf{k}_f$ respectively.

2.2.1.2 Interaction with an atom

The formalism presented above can be extended to consider multiple scattering centres. Again, a classical description is presented here, and elastic scattering is assumed. The spherical waves emitted by each electron will interfere, and the combined effects of these waves can be calculated, using the following assumptions:

- The amplitude of electron oscillation is much smaller than the wavelength of the scattered radiation.
- The distance at which scattering is observed is much larger than the distance between electrons (this is the **Fraunhofer or far field diffraction limit**).
- The distribution of electrons is continuous, with number density $\rho(\mathbf{x}_i)$.

The radiation emitted by an electron at each position $\mathbf{x}_i$ is characterised by a phase factor $\mathrm{e}^{-i\mathbf{k}\cdot\mathbf{x}_i}$ (where $\mathbf{k}$ is the wave vector of the incident radiation) and will contribute $-r_0\rho(\mathbf{x}_i)\mathbf{dx}_i$ to the scattered field.

The total scattered field (scattering amplitude) can be written (cf. Eq. (2.2.10)) as

$$\mathbf{E}_{rad}(R,t) = -r_0 E_0 \frac{\mathrm{e}^{i(kR-\omega t)}}{R} \int_i \rho(\mathbf{x}_i)\mathrm{e}^{-i\mathbf{Q}\cdot\mathbf{x}}\mathbf{dx} \tag{2.2.12}$$

where $\mathbf{Q} = \mathbf{k}_f - \mathbf{k}_i$ is the scattering vector, and $\mathbf{k}_f$ and $\mathbf{k}_f$ are the incident and scattered wave vectors. In the case of elastic scattering,

$$Q = |\mathbf{Q}| = \frac{4\pi\sin\theta}{\lambda}. \tag{2.2.13}$$

The integral

$$f_0(\mathbf{Q}) = \int_i \rho(\mathbf{x}_i)\mathrm{e}^{-i\mathbf{Q}\cdot\mathbf{x}}\mathbf{dx} \tag{2.2.14}$$

is known as the **atomic form factor**. The scattering amplitude is proportional to the Fourier transform of the charge distribution. In the limit that $\mathbf{q} \to 0$, all volume elements scatter in phase and $f^0(\mathbf{Q}) \to \mathbf{Z}$, whereas if $\mathbf{Q} \to \infty$, $f^0(\mathbf{Q}) \to \mathbf{0}$. For

a broader charge distribution surrounding an atom, $f(\mathbf{Q})$ will decay faster for high $\mathbf{Q}$.

2.2.1.3 Interaction with a crystal

Crystals generally comprise a periodic array of atoms. Thus, in order to extend the formalism above for scattering from a crystal, scattering from multiple atoms, coupled with the effect of periodicity must be considered.

In basic explanations of x-ray scattering, Bragg's law is derived:

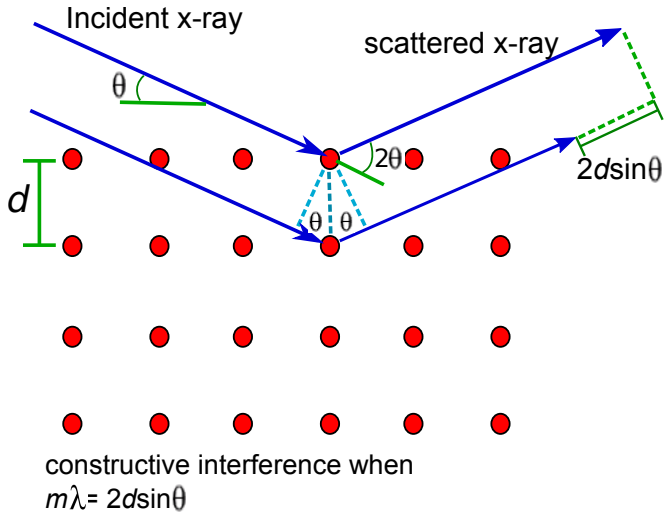


Figure 2.9: The geometry of Bragg's law, defining the condition for constructive interference of diffracted waves with wavelength (λ) from a set of crystallographic planes, with interplanar spacing d_{hkl}

$$m\lambda = 2d_{hkl}\sin\theta. \tag{2.2.15}$$

This equation defines the condition for constructive interference of x-ray waves with wavelength λ, having an angle of incidence θ to sets of lattice planes separated by a distance d_{hkl}. Constructive interference and hence diffraction occurs for integer value of m, as shown in Figure 2.9. Whilst this formalism is useful in understanding diffraction geometry, it is limited in that it cannot be used to calculate scattering

intensity. The formalism presented below, which is an extension of section 2.2.1.2, gives equivalent results to Bragg's Law.

To calculate the scattering cross section, here it is assumed that the crystal is small, such that multiple scattering events do not need to be considered. Additionally, as in section 2.2.1.2, the Fraunhofer (far field) approximation is used.

The scattering amplitude is obtained from integrating over the crystal (c.f. Eq. (2.2.12)):

$$A(\mathbf{Q}) = r_0 \int_{Crystal} \rho(\mathbf{r}) \mathrm{e}^{-i\mathbf{Q}\cdot\mathbf{r}} \mathbf{dr}. \tag{2.2.16}$$

Exploiting the periodicity of a crystal lattice, if $\mathbf{x}$ is a site within the unit cell at the origin, and $\mathbf{r}_i$ is a lattice translation, then

$$\rho(\mathbf{r}) = \rho(\mathbf{r}_i + \mathbf{x}) = \rho(\mathbf{x}). \tag{2.2.17}$$

The scattering amplitude then becomes:

$$A(\mathbf{Q}) = r_0 \sum_i \int_{Unitcell} \rho(\mathbf{x}) \mathrm{e}^{-i\mathbf{Q}\cdot(\mathbf{r}_i+\mathbf{x})} \mathbf{dx} = r_0 \sum_i \mathrm{e}^{-i\mathbf{Q}\cdot(\mathbf{r}_i)} \int_{Unitcell} \rho(\mathbf{x}) \mathrm{e}^{-i\mathbf{Q}\cdot\mathbf{x}} \mathbf{dx} \tag{2.2.18}$$

with the summation running over all unit cells in the crystal.

The integral

$$F(\mathbf{Q}) = r_0 \sum_i \int_{Unitcell} \rho(\mathbf{x}) \mathrm{e}^{-i\mathbf{Q}\cdot\mathbf{x}} \mathbf{dx} \tag{2.2.19}$$

is the **Structure factor**, bearing close analogy to Eq. (2.2.14), and is proportional to the Fourier transform of the charge density, integrated over the unit cell.

If the electron density $\rho(\mathbf{r})$ is a superstition of atomic electron densities, $F(\mathbf{q})$ can be written as

$$F(\mathbf{Q}) = r_0 \sum_n f_n(\mathbf{q}) \mathrm{e}^{-i\mathbf{Q}.\mathbf{x}_n} \tag{2.2.20}$$

where f_n are the atomic form factors for individual atoms, and the sum runs over all atoms in the crystal, at positions $\mathbf{x}_n$.

The scattering cross section can be calculated as

$$\frac{d\sigma}{d\Omega} = A(\mathbf{q})A^*(\mathbf{q}) = \left(\sum_j \sum_i e^{-i\mathbf{q}\cdot(\mathbf{r}_i - \mathbf{r}_j)}\right) |F(\mathbf{q})|^2. \tag{2.2.21}$$

For an infinite lattice, the summation over j can be replaced by a multiplication by the number of unit cells in the crystal N_c. The remaining summation over i is non-zero only for the case where $\mathbf{Q}$ is equal to a reciprocal lattice vector. This can be expressed as a delta function, and it can be shown that the scattering cross section can be written as

$$\frac{d\sigma}{d\Omega} = N_c \frac{(2\pi)^3}{v_0} \sum_\tau \delta(\mathbf{Q} - \boldsymbol{\tau})|F(\boldsymbol{\tau})|^2 \tag{2.2.22}$$

where v_0 is the unit cell volume, and the sum is made over delta functions situated at reciprocal lattice nodes.

It should be noted that in section 2.2.1.2 and in the formalism above, the polarisation factor introduced in section2.2.1.1 has been omitted for simplicity. As discussed in section 2.2.1.1 this would give rise to a term $[\boldsymbol{\epsilon}.\boldsymbol{\epsilon}']^2$ in the scattering cross section, which is averaged over all incident and scattered polarisations, and depends upon the scattering geometry.

The Laue equations

The equation (2.2.22) is only non-zero for the case that $\mathbf{Q}$ is equal to a reciprocal lattice vector. This condition can also be expressed using **Laue Equations**, from which Bragg's law is derived [49].

In this formalism, scattering vectors fulfil the condition

$$\mathbf{Q} \cdot \mathbf{R}_n = 2\pi \times \text{integer} \tag{2.2.23}$$

where lattice vectors $\mathbf{R}_n$ are of the form

$$\mathbf{R}_n = n_1\mathbf{a}_1 + n_2\mathbf{a}_2 + n_3\mathbf{a}_3 \tag{2.2.24}$$

and where $\mathbf{a_1}$, $\mathbf{a_2}$ and $\mathbf{a_3}$ are basis vectors of the lattice, and n_1, n_2 and n_3 are integers.

For reciprocal lattice vectors, defined as

$$\mathbf{a}_1^* = 2\pi \frac{\mathbf{a}_2 \times \mathbf{a}_3}{\mathbf{a}_1 \cdot (\mathbf{a}_2 \times \mathbf{a}_3)} \; \mathbf{a}_2^* = 2\pi \frac{\mathbf{a}_3 \times \mathbf{a}_1}{\mathbf{a}_1 \cdot (\mathbf{a}_2 \times \mathbf{a}_3)} \; \mathbf{a}_3^* = 2\pi \frac{\mathbf{a}_1 \times \mathbf{a}_2}{\mathbf{a}_1 \cdot (\mathbf{a}_2 \times \mathbf{a}_3)}. \tag{2.2.25}$$

Any lattice site in the reciprocal lattice is given by

$$\mathbf{G} = h\mathbf{a}_1^* + k\mathbf{a}_2^* + l\mathbf{a}_3^* \tag{2.2.26}$$

where h, k and l are all integers.

The product of a lattice vector in real and reciprocal space is given by

$$\mathbf{G} \cdot \mathbf{R}_n = 2\pi(hn_1 + kn_2 + ln_3) = 2\pi \times \text{integer}. \tag{2.2.27}$$

$F(\mathbf{Q})$ is non-vanishing only for the condition that $\mathbf{Q} = \mathbf{G}$. This is the Laue condition for crystalline diffraction. A peak in scattered intensity can thus be observed if the scattering geometry is position for the correct $\mathbf{Q}$. This defines a Bragg peak. For the case of an ideal crystal, the delta function given in Eq. (2.2.22) would suggest infinitely sharp Bragg peaks. In practice, crystal imperfections, deviations from a perfectly monochromatic team, finite crystal size and other factors lead to peak broadening in experimental diffraction data.

The effect of atomic vibrations

Atoms are displaced away from "ideal" periodic positions due to thermal vibrations. Returning to the formalism for the scattering cross section, this gives rise to an additional term in the scattering amplitude [47]:

$$A(\mathbf{Q}) = r_0 \sum_i \mathrm{e}^{-i\mathbf{Q}\cdot\mathbf{r}_i} \sum_n f_n(\mathbf{Q}) \mathrm{e}^{-i\mathbf{Q}\cdot(\mathbf{x}_n + \mathbf{u}_{n,i})} \tag{2.2.28}$$

where $\mathbf{u}_{n,i}$ is the displacement vector for the atom labelled n in the ith unit cell.

Time averaging for the scattering amplitde can be expressed as

$$A(\mathbf{Q}) = r_0 \sum_i \mathrm{e}^{-i\mathbf{Q}\cdot\mathbf{r}_i} \sum_n f_n(\mathbf{Q}) \mathrm{e}^{-i\mathbf{Q}\cdot\mathbf{x}_n} \langle \mathrm{e}^{-i\mathbf{Q}\cdot\mathbf{u}_{n,i}} \rangle. \tag{2.2.29}$$

The expression contained within $\langle\rangle$ does not depend upon the reference i, because once time averaging has been performed, the position of each unit cell will average to identical values. Using the **Bloch Identity**

$$\langle \mathrm{e}^{-i\mathbf{Q}\cdot\mathbf{u}_{n,i}} \rangle = \mathrm{e}^{-W(\mathbf{Q},n)} \tag{2.2.30}$$

where W is known as the **Debye-Waller factor**. For the case of isotropic thermal vibrations

$$W(\mathbf{Q}, n) = U_n q Q^2 \tag{2.2.31}$$

(in the anisotropic case, U_n is a tensor).

Incorporating this result into the expression for the X-ray structure factor, in the isotropic case:

$$F(\mathbf{Q}) = r_0 \sum_n f_n(Q) \mathrm{e}^{-i\mathbf{Q}\cdot\mathbf{x}_n} \mathrm{e}^{-U_n Q^2}. \tag{2.2.32}$$

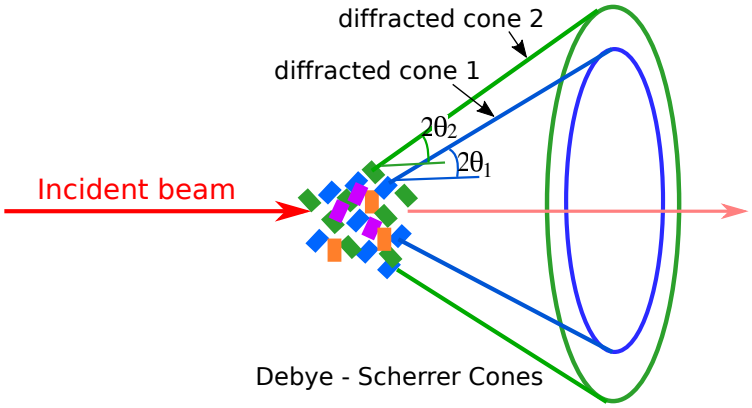
To summarise this section, x-ray scattering from a crystal is confined to specific points in reciprocal space. The intensity at each point is modulated by the square of the structure factor. From a large set of diffraction intensities, it is possible to determine atomic positions within a unit cell. This will be explored further in Chapter 3 and Appendix B.

2.2.1.4 Powder diffraction

Single crystal x-ray diffraction is a powerful, well established technique for crystal structure solution, exploiting information contained in diffraction peak intensities

and positions to determine atomic positions, unit cell parameters and crystal symmetry.

A good powder sample will consist of thousands of crystallites oriented randomly. For any given x-ray incident wave vector $\mathbf{k}$, and reciprocal lattice vector $\mathbf{G}$, multiple crystallites will be in the required orientation to diffract, as illustrated in Figure 2.2.1.4 [46].



The geometry of x-ray powder diffraction. For an incident x-ray beam with wave vector $\mathbf{k}$, diffracted waves from sites associated with a given reciprocal lattice vector $\mathbf{G}_{hkl}$ form a cone, due to the random orientation of crystallites in the powder sample.

Figure 2.10: In an ideal powder sample, there is a random distribution of all possible crystallite orientations such that each orientation is equally represented. Diffracted x-ray beams form cones (Debye-Scherrer cones) with each cone corresponding to diffraction intensity from a different set of lattice planes. Traditionally, these cones would be detected as circular arcs on x-ray film.

In this thesis, powder diffraction has been used for determination of lattice parameters. Each diffraction peak will contain intensity from multiple crystallites and will have a peak position determined from the average interplanar spacing of these crystallites. Powder diffraction benefits from easy sample preparation, rapid data acquisition time, and is a valuable structure solution method when single crystals of sufficient size or quality are not available. Further details of refinement of powder x-ray diffraction data are given in Appendix B.

2.2.1.5 Magnetic x-ray scattering

Magnetic x-ray scattering will only be discussed very briefly in this thesis, and will be limited to non-resonant magnetic diffraction. Since x-rays are electromagnetic waves, the magnetic component of incident radiation can interact with electronic spin, analogously to the electric component interacting with electronic charge. Thus, magnetic scattering can give rise to additional terms in the scattering cross section. Magnetic x-ray scattering is significantly weaker than charge x-ray scattering, with an amplitude ratio between the two given by

$$\left(\frac{A_{magnetic}}{A_{charge}}\right) = \left(\frac{\hbar\omega}{mc^2}\right). \tag{2.2.33}$$

For laboratory x-ray sources, this results in magnetic peaks being $\sim 10^{-4}$ times weaker than charge peaks, hence x-ray scattering is not widely used for magnetic structure determination. In recent years, however, increased availability of high intensity synchrotron radiation, as discussed below, has opened up the possibility of exploiting x-ray diffraction as a practical tool for probing magnetic ordering.

2.2.2 X-ray sources and facilities

The theory presented above explains how information contained in x-ray scattering data relates to atomic positions in crystalline materials. This section considers how this relationship can be used in practice, outlining how x-rays can be generated, how scattering experiments are performed and how data can be analysed to deduce atomic structures. Again, discussion will be limited to the case of elastic, non-resonant, single crystal scattering; the primary technique that has been used throughout this thesis.

There are two primary sources for x-rays used in elastic scattering experiments, laboratory sources based on x-ray tubes, and synchrotron sources. These differ in the brilliance of x-rays generated. X-ray brilliance is a quality factor incorporating the

number of photons emitted per second by the source, the source area (in mm^2), the divergence (collimation) of the beam (measured vertically and horizontally in milliradians), and the range of photon energies contributing to the beam intensity (defined as an energy bandwidth BW).

$$\text{Brilliance} = \frac{\text{photons}}{(\text{mrad}^2)(\text{mm}^2)(\text{second})(0.1\%\text{BW})}. \tag{2.2.34}$$

Higher brilliance allows observation of weaker scattering peaks, allowing finer details to be observed in the structure being studied. Synchrotron sources may have a brilliance more than a billion times higher than laboratory sources, but laboratory sources have significant use in initial characterisation and simple structure solutions due to their wider availability, lower cost, and ease of operation. Both laboratory and synchrotron scattering experiments have been used to produce the results presented in this thesis, and a description the specific facilities used is given below:

2.2.2.1 Laboratory sources

The Agilent Technologies "SuperNova" X-ray Diffractometer

In this thesis, the SuperNova diffractometer has been used to assess crystal quality and orient crystals, prior to synchrotron and electron microscopy experiments. Results obtained using the SuperNova have also been crucial in measuring and characterising the details of structural modulations.

SuperNova uses an x-ray tube source, as shown in Figure 2.11; electrons are accelerated from a cathode by a high voltage source, and strike an anode, causing x-rays to be emitted in a direction perpendicular to the electron trajectory. The anode is a high flux, 50 W molybdenum source which produces an unpolarised x-ray beam ∼300 μm in diameter.

Single crystal samples are mounted onto a four circle, kappa geometry goniometer, and the crystal can be positioned in the gas stream of either a nitrogen or helium

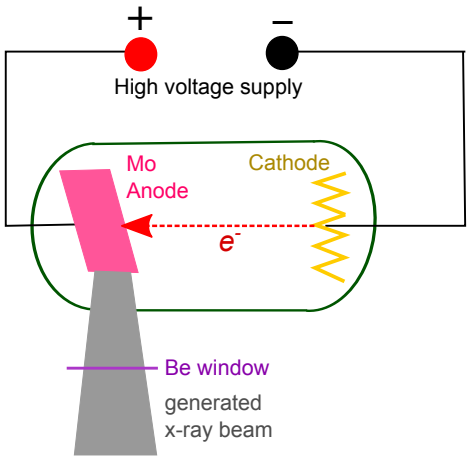


Figure 2.11: X-ray generation from a tube source. Within an evacuated tube, electrons are emitted from a heated filament and are accelerated by an electric potential, to strike an anode (Molybdenum in this case). X-rays are emitted and pass out of the tube via a Beryllium window. A monochromator is used to select a specific x-ray wavelength for use in experiments.

jet for cooling. A camera is mounted above the sample for accurate alignment in the x-ray beam. Scattered x-rays are detected using an ATLAS area detector, consisting of a phosphorescent screen that emits light in response to x-rays. A fiber optic taper then transmits this light to a CCD chip. The detector is mounted onto a moveable arm, which allows it to move away from the goniometer whilst sample orientation is adjusted, but enabling it to move inwards and span a wide angle around the sample during data collection. This set up is shown in Figure 2.12.

In order to index scattered x-rays, and attribute them to specific crystallographic hkl planes, the diffractometer angles and the scattering vector $\mathbf{Q} = \mathbf{k}_f$ - $\mathbf{k}_i$ must be known. Conventionally, three angles, ϕ, ω and χ are used to position samples, as depicted in Figure 2.13(a). In SuperNova, the sample stage can rotate through an angle ϕ about its axis. Whilst in a four circle geometry, the sample stage would move around the χ circle, tilted at an angle of $\omega + \theta$ to the incoming beam direction, in Supernova, this is replaced by a κ rotation, inclined at an angle of $\alpha = 50°$ to the horizontal, and coupled to ω, as shown in Figure 2.13(b).

The scattering vector $\mathbf{q}$ is related to the (hkl) index of the scattered peak by the equation

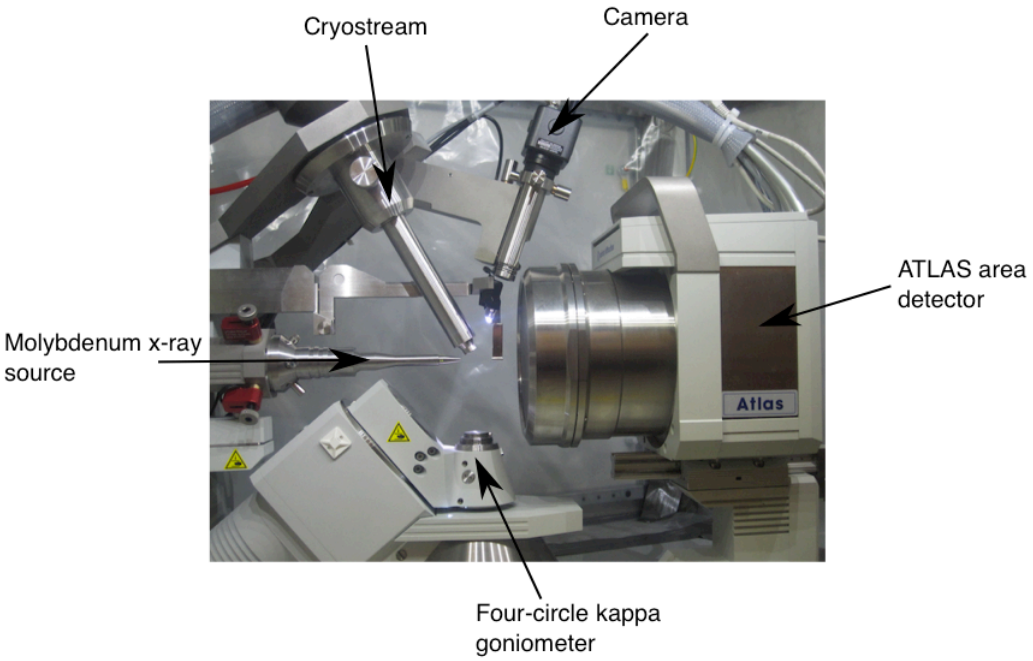


Figure 2.12: The set up of the SuperNova diffractometer. Single crystals are mounted on the goniometer, and scattered x-rays are detected using the area detector. The cryostream can be used to control sample temperature, whilst the camera is used to position and align the sample in the x-ray beam.

$$\begin{pmatrix} |\mathbf{Q}| \\ 0 \\ 0 \end{pmatrix} = \Omega\ \mathbf{K}\ \Phi\ \mathbf{UB} \begin{pmatrix} h \\ k \\ l \end{pmatrix}. \tag{2.2.35}$$

For a peak index $(h, k, l) = h\mathbf{a}^* + k\mathbf{b}^* + l\mathbf{c}^*$, the matrix $\mathbf{B}$ converts the reciprocal basis vectors $\mathbf{a}^*, \mathbf{b}^*, \mathbf{c}^*$ into Cartesian axes attached to the crystal, and the matrix $\mathbf{U}$ then rotates the sample from this Cartesian set onto an equivalent set, attached to the goniometer head. This accounts for the fact that the crystal may be mounted in an arbitrary orientation. Matrices Φ, $\mathbf{K}$ and Ω then rotate about the ϕ, κ and ω axes, such that the scattering vector bisects the angle between the straight through beam and the centre of the detector.

Generally, the $\mathbf{UB}$ matrix is not known in advance of the experiment. CrysAlis PRO [51] software is used for data analysis in conjunction with SuperNova. CrysAlis

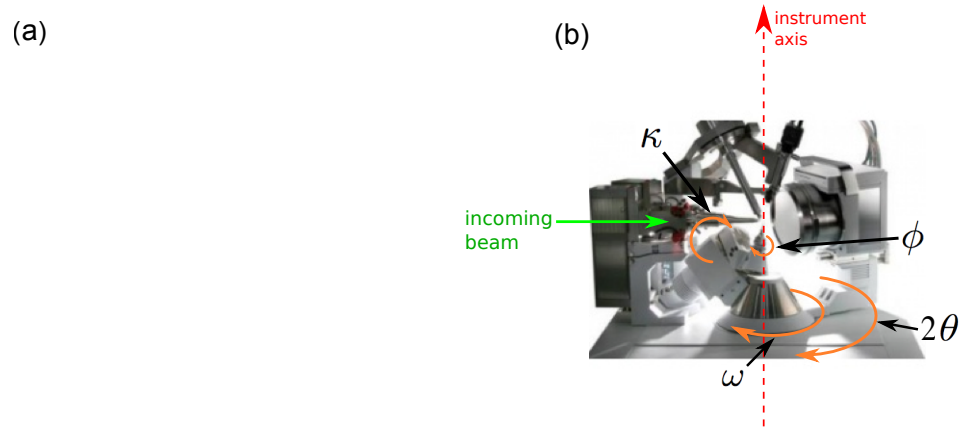


Figure 2.13: (a) The angles used to position samples within conventional four circle geometry, taken from Ref. [50] (© Union of Crystallography). (b) Specific angles used for positioning samples using SuperNova. κ is inclined at 50° to the horizontal and is coupled to ω.

PRO continually processes data during collection, using a least squares refinement technique to determine the **UB** matrix that indexes the greatest number of reflections consistently. In the simplest case, the basic output from CrysAlis PRO is a list of indexed (hkl) peaks and corresponding intensities that can be used in refinement of crystal structures.

The Siemens D5000 Powder Diffractometer

In this thesis, powder diffraction has been used to determine a reliable set of average lattice parameters for $CaMn_7O_{12}$ crystals at several different temperatures. The Siemens D5000 Powder Diffractometer uses a Cu anode x-ray tube with a 2700 W medium frequency high voltage generator. A monochromator crystal is used to select the x-ray wavelength and a collimator and soller slits are used to focus the x-ray beam. The goniometer is large (600 mm), with a single sample stage accommodating powder samples within a 2 mm thick plate. In this thesis an Oxford Cryosystems PheniX low temperature stage was used to achieve temperatures ranging from 295 to 85 K. The sample moves through an angle θ, whilst the detector arm (a scintillator) rotates on an arm through 2θ. The data collected is in the form of a plot of intensity versus 2θ. These theta values can be converted into lattice spacings using Bragg's law, as part of a least squares refinement procedure (see Appendix B).

2.2.2.2 Synchrotron sources

Diamond Light Source

In addition to the higher brilliance that can be obtained from a synchrotron source, there are other advantages over a laboratory source. The x-rays generated from a synchrotron can be significantly higher in energy and shorter in wavelength, enabling greater penetration depth into the sample and allowing the study of finer details of the crystal structure. Additionally, the polarisation and coherence of the x-ray beam can be controlled, enabling a greater variety of experimental conditions.

Synchrotron light is generated through the acceleration of electrons up to relativistic speeds. The electrons are directed through a series of strong magnetic fields, and Lorentz forces cause them to change direction. As they accelerate radially, electrons emit radiation tangentially to their direction of motion, typically in the x-ray range of the electromagnetic spectrum, but with a range of wavelengths, extending into the infrared region in some cases.

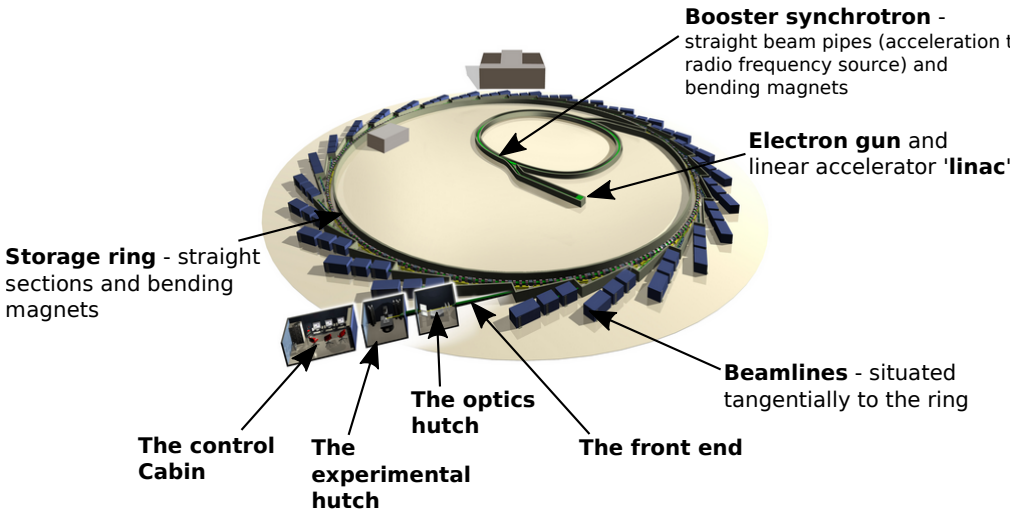
At the Diamond Light Source, electrons are generated by emission from a heated metal cathode, and electrons are drawn towards an anode. Electrons are then accelerated along a linear path (a linac) reaching energies of up to 100 MeV, before entering a booster synchrotron; a series of straight beam pipes held under high vacuum, connected by bending magnets, to form a loop. Electrons traverse the loop, being further accelerated within each straight section by a radio frequency source, up to an energy of 3 GeV. The strength of the bending magnets is varied, coupled to the electron energy in order to ensure the electrons remain on a constant path for each cycle of the loop. In addition to the bending magnets, quadrupoles and sextuple magnets are used to focus the electron beam and hold the electrons in bunches. 3 GeV electrons are released into the storage ring, consisting of 24 straight sections and 48 bending magnets. The entire storage ring is held under vacuum to minimise electrons scattering from air molecules. Electrons orbit within the storage ring at the same nominal energy for a period of several hours, producing x-rays for a wide variety of experi-

ments. A continuous top up system operates, such that every few minutes, electrons are replenished to maintain an approximately constant storage ring current of ∼300 mA. X-rays can either be produced within the bending magnets, or more efficiently by using insertion devices (see below) situated within the straight line sections of the storage ring.

The x-rays are then distributed to the beamlines. Each beamline has four major sections:

- **The Front End**: Where x-rays are extracted from the storage ring. The front end connects to the storage ring at a tangent, and passes through shield walls into the optics hutch. Here, the position of the x-ray beam is monitored and heat is removed.
- **Optics Hutch**: Where specific x-ray wavelengths will be selected and focused. The hutch contains devices such as mirrors and diffraction gratings to filter and focus the beam.
- **Experimental Hutch**: Housing the experimental equipment, where x-rays interact with the sample and are detected.
- **Control Cabin**: The experiment is monitored and controlled from the control cabin.

The layout of the Diamond Light Source is shown in Figure 2.14.



.

Figure 2.14: Adapted from Ref. [52]. The layout that enables synchrotron x-ray generation at the Diamond Light Source. Electrons are accelerated in a circular path and emit x-rays which are distributed to various beamlines.

The I16 Beamline

In this thesis, data obtained from the I16 beamline are presented. This is a single crystal beamline optimised for high incident radiation flux and a wide, tuneable energy range; essential for weak scattering processes, such as diffraction from magnetic, charge or orbital ordering, and for measurements on very small sample volumes [53]. X-rays used in I16 are generated from undulator insertion devices in the storage ring, as described below.

Undulator Radiation

The undulator causes electrons to oscillate in the horizontal plane as they traverse through the straight sections of the storage ring. This is achieved using an array of permanent magnets, that produce alternating north south fields along the path, as shown in Figure 2.15(a). The undulator is constructed such that the radiation emitted by an electron at a given oscillation will be in phase with the radiation from the following oscillations. Thus the amplitudes of the radiated x-rays are added, and the sum is squared to obtain the resulting intensity. The coherent addition of amplitudes should imply a monochromatic spectrum with harmonics. In reality, this is

only quasimonochromatic due to the finite number of periods in the undulator.

The basic parameters for undulator radiation are the cyclic frequency (γ_u), the undulator spatial repeat distance (λ_u) (with associated wavevector $k_u = \frac{2\pi}{\lambda_u}$) and the amplitude of the oscillations (A), as shown in Figure 2.15(b) [46].

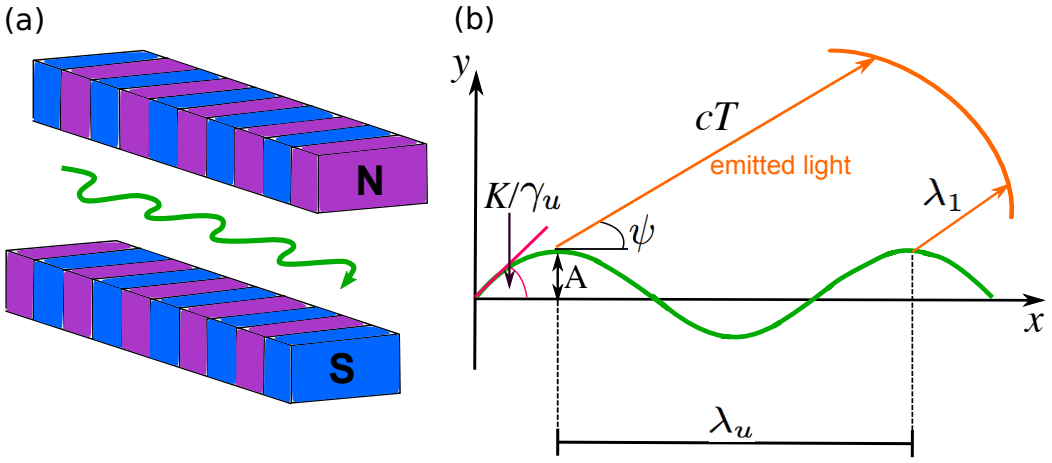


Figure 2.15: (a) An array of permanent bending magnets produces alternating north-south fields, causing electrons to oscillate along the path and generate x-rays as they change direction. (b) The parameters for characterising undulator radiation for an electron traversing the path shown in green, and emitting x-rays in the direction shown in orange.

A non-relativistic electron of momentum $\mathbf{p} = m\boldsymbol{v}$ moving in a constant magnetic field ($\mathbf{B}$), will experience a Lorentz force:

$$\boldsymbol{F} = \frac{d\mathbf{p}}{dt} = -e(\boldsymbol{v} \times \mathbf{B}) \tag{2.2.36}$$

causing the electron to accelerate and move in a circular orbit in a plane perpendicular to $\mathbf{B}$, as shown in Figure 2.16.

The radius of the orbit (r), can be determined from $\mathbf{B}$, because the Lorentz force is equal to the centripetal acceleration ($\frac{v^2}{r}$), multiplied by the electron mass m. For super relativistic particles, $v \approx c$, and $\mathbf{p} = \gamma mv$ where $\frac{1}{\gamma}$ is the opening angle of the electron beam shown in Figure 2.15(b). This yields

$$\gamma mc = re\mathbf{B} \Rightarrow r = \frac{\gamma mc}{e\mathbf{B}}. \tag{2.2.37}$$

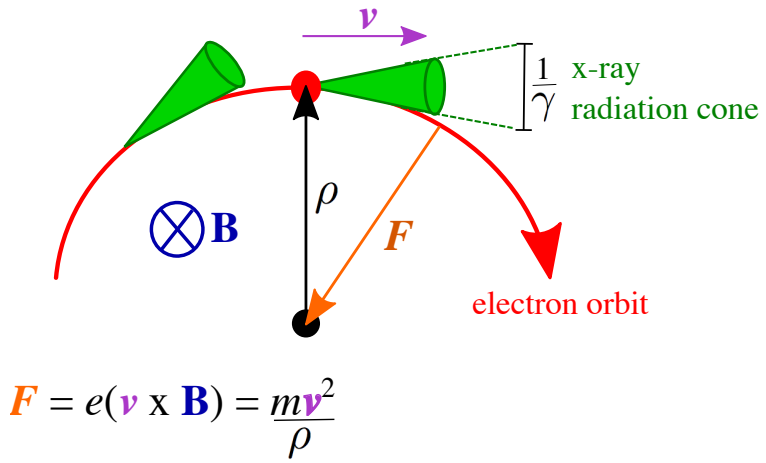


Figure 2.16: Adapted from Ref. [46]. An electron travelling with velocity (v) perpendicular to a magnetic field **B** will experience force (F) perpendicular to the direction of of it's motion. This force will cause the electron go move in a circular path. X-ray radiated will be emitted as a result.

Taking the path of the electron to be a small amplitude sine wave, described by $y \approx A\sin(k_u x)$. Expanding this expression

$$y \approx \mathrm{A}\cos\left[k_u\left(x - \frac{\lambda_u}{4}\right)\right] \Rightarrow y \approx \mathrm{A} - \frac{Ak_u^2}{2}\left(x - \frac{\lambda_u}{4}\right)^2. \tag{2.2.38}$$

Comparing this to the equation of a circle centered at $x = \frac{\lambda_u}{4}, y = \mathrm{A} - r$:

$$(y - \mathrm{A} + r)^2 + \left(x - \frac{\lambda_u}{4}\right)^2 = r^2 \Rightarrow y \approx \mathrm{A} - \frac{1}{2}\left(\frac{x = \frac{\lambda_u}{4}}{r}\right). \tag{2.2.39}$$

Substituting into Eq. 2.2.37, r is given by

$$r \approx \frac{1}{\mathrm{A}k_u^2}. \tag{2.2.40}$$

An undulator characterisation parameter K is commonly defined, where K/γ is the maximum deviation of electrons from the x-axis shown in 2.15. K/γ can be shown to be equivalent to $\mathrm{A}k_u$, and hence

$$K = \frac{e\mathbf{B}}{mck_u} \approx 0.932\lambda_u\mathbf{B}. \tag{2.2.41}$$

If the time taken for the electron to travel one spatial period of the undulator is T, constructive interference occurs if

$$n\lambda_1 = cT - \lambda_u \cos\psi \tag{2.2.42}$$

where λ_1 is the fundamental wavelength emitted by the undulator.

$T = \frac{S}{v}$ where S is the distance travelled by an electron during the period T.

Evaluating this expression:

$$S = \int_0^{\lambda_u} dx \left[1 + \left(\frac{dy}{dx}\right)^2\right]^{1/2} \approx \int_0^{\lambda u} dx \left[1 + \frac{1}{2}\mathrm{A}^2 k_u^2 \cos^2(k_u x)\right] \tag{2.2.43}$$

$$\Rightarrow S = \lambda_u \left(1 + \frac{1}{4}\mathrm{A}^2 k_u^2\right) = \lambda_u \left(1 + \frac{K^2}{4\gamma^2}\right). \tag{2.2.44}$$

The undulator will produce wavelengths given by

$$\lambda_n = \frac{c\lambda_u}{vn}\left(1 + \frac{K^2}{4\gamma_u^2}\right) - \frac{\lambda_u}{n}\cos\psi \tag{2.2.45}$$

$$\Rightarrow \frac{\lambda_u}{2\gamma^2 n}\left(1 + \frac{K^2}{2} + \gamma^2\psi^2\right). \tag{2.2.46}$$

Eq. (2.2.46), known as the undulator equation, shows how emitted x-ray wavelengths can be tuned by varying the parameter K. In practice, this is achieved by changing the undulator gap, which varies with magnetic field $\mathbf{B}$. Electrons in the storage ring at Diamond typically have $\gamma_u \approx 5870$. Taking typical values of $\mathbf{B} = 0.5$ T and $\lambda_u = 0.1$ cm, wavelengths of $\sim$1.8 Å are generated from the undulator.

The theory above would suggest that specific wavelengths exist for which constructive interference occur, and thus we would expect undulator radiation to be monochromatic. In reality, a limit on the number of undulator periods limits the length of the x-ray pulse train and the frequency distribution. An undulator with N magnetic periods will produce a bandwidth of radiation:

$$\frac{\Delta\lambda}{\lambda_n} = \frac{1}{nN}. \tag{2.2.47}$$

Hence for x-rays generated from undulator devices, monochromation of the beam is essential, both to remove unwanted harmonics and to constrain the bandwidth of radiation.

The beamline layout

The undulator generated x-ray beam at I16 can be focused to to $\sim$40 $\times$ 200 μm^2. A continuous, tuneable energy range from 3.3 keV to 25 keV is available, and specific wavelengths can be selected using a silicon monochromator. Data presented in this thesis was obtained using a linearly polarised beam. Experiments can be performed at temperatures of $\sim 6 - 800$ K through the use of cryostats and gas stream coolers. In this thesis, intensities of diffraction peaks were measured from 40-295 K. A range of detectors are available, including a Pilatus 100 K photon-counting detector and point detectors such as scintillators and PIN diodes.

The I19 beamline

In addition to experiments performed at I16, structural studies of $CaMn_7O_{12}$ presented in Chapter 3 required a short experiment using the I19 beamline to collect diffraction peaks corresponding to a structural modulation. This data was used in conjunction with that obtained using the SuperNova laboratory source (see section 2.2.2.1).

Like I16, I19 uses undulator generated x-rays for single crystal scattering measurements. The x-rays are linearly polarised with wavelength 0.6889 Å, and are passed through a monochromator, slits and focusing mirrors to produce a converged beam with a probe size of $\sim$170 $\times$ 85 μm^2 at the sample position. The data used in this thesis was obtained at 150 K, with cooling achieved using a LN_2 cryostream. Single crystal samples are mounted on micro loops, attached to four circle goniometers, and Rigaku Saturn 724 CCD area detectors are used to detect peaks.

The overall set up of the diffractometer at I19 has many similarities to SuperNova, and

the reflection list generated is analysed in the same way using CrysalisPro software. Thus the diffractometer set up is not discussed in detail here (see Ref. [54]).

2.3 Neutron Diffraction

X-ray diffraction is often the preliminary structural characterisation technique used for multiferroic crystals. X-ray sources are readily available in laboratories as well as at national/international facilities and small single crystals or even powders can be used. Neutron diffraction requires reactor or spallation sources, which have higher start up and maintenance costs than x-ray facilities. Additionally, for single crystal studies, large samples (typically mm in dimension) are required, and often experiments need to be performed with powder samples. Despite this added degree of complexity, neutron diffraction studies are of great value, either when used to complement x-ray diffraction, or as a stand alone technique for magnetic structure determination. As described above, x-rays interact with atomic electron clouds, and thus the strength of scattering is dependent upon atomic number (Z). Neutrons interact directly with atomic nuclei. Often, elements that scatter x-rays weakly have strong contributions in neutron scattering, and different isotopes with the same atomic number may have different neutron scattering lengths. Thus neutron scattering can thus be valuable in determining the position of light elements with low atomic number or in differentiating isotopes. Slow (non-relativsitc) neutrons have wavelengths in the range 0.5-10 Å, and hence the wavelength can be similar to typical interatomic distances in crystals, making neutrons suitable for use in crystal diffraction. Although not exploited in this thesis, thermal neutrons have energies suitable for probing collective excitations such as phonons in inelastic scattering studies. Neutrons also posses a magnetic moment and can interact with magnetic moments of atoms to reveal the microscopic magnetic structure of a material, overcoming the shortcomings of weak scattering of x-rays by magnetic moments (see section 2.2.1.5). In this thesis, structural results obtained from elastic neutron scattering are presented. The theory behind this is summarised

briefly below, primarily comparing theory to that for elastic x-ray scattering (see section 2.2.1).

2.3.1 Interaction of neutrons with atoms

The interaction between neutrons and atomic nuclei is both isotope and element specific, and is dependent upon the relative orientation of the neutron and nuclear spins. For neutron diffraction, the coherent scattering amplitude is considered, which is averaged over nuclear spin states.

The coherent scattering amplitude for the neutron nuclear interaction does not incorporate a form factor (in contrast to Eq. (2.2.12) in section 2.2.1.2), and instead, can be expressed as a single number, known as the **Fermi Length**. Fermi lengths can be positive or negative, and are typically of the order of a few fm (10^{-15} m). In contrast to x-ray form factors, Fermi lengths do not vary in a systematic way with atomic number, and do not fall off at high **Q**. A comparison between neutron-nuclear Fermi lengths and atomic form factors for x-ray scattering is given in Figure 2.17.

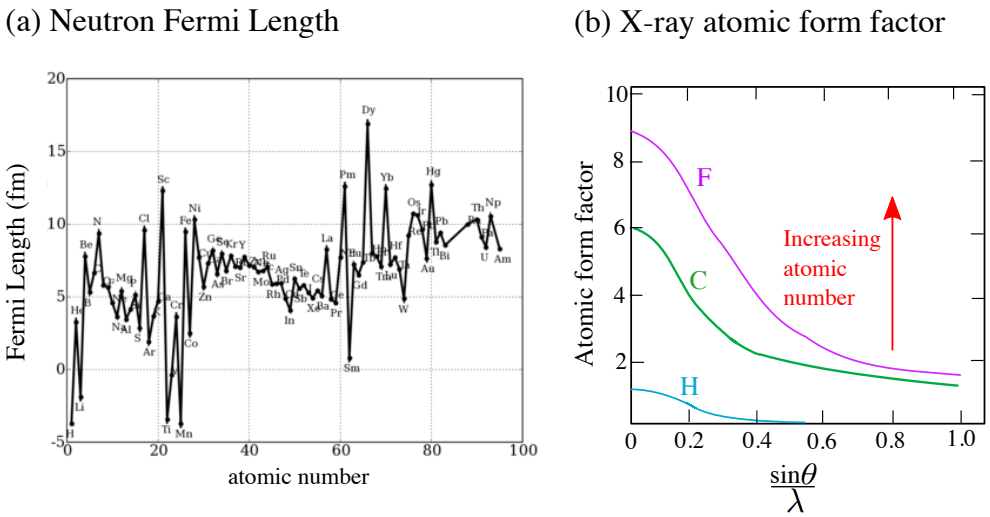


Figure 2.17: (a) Adapted from Ref. [55]. The variation of the neutron Fermi Length with atomic number. Fermi lengths do not vary systematically with atomic number, whereas the corresponding x-ray atomic form factors increase with atomic number, as shown in (b). The x-ray atomic form factors fall off with increasing **Q** ($\propto \frac{sin\theta}{\lambda}$), whereas the corresponding Fermi Lengths would show very little variation with **Q**.

In section 2.2.1.3, an expression was obtained for the x-ray structure factor in the isotropic case (see Eq. (2.2.32)).

In a similar manner, the coherent neutron structure factor for nuclear scattering is given by (following Ref. [56])

$$F^{total}(\mathbf{Q}) = \sum_n b_n \mathrm{e}^{-i\boldsymbol{Q}.\boldsymbol{x_n}} \mathrm{e}^{-iU_n\boldsymbol{Q^2}} \tag{2.3.1}$$

where b_n is the Fermi length.

It can be shown that a differential cross section for elastic, coherent neutron scattering can be calculated, analogously to the x-ray differential cross section (see Eq. (2.2.22)) [57]:

$$\left(\frac{\mathrm{d}\sigma}{\mathrm{d}\Omega \mathrm{d}E_f}\right)_{\text{elastic,nuclear}} = \left|\sum_n b_n e^{i\mathbf{Q}\cdot\mathbf{r}_n}\right|^2 \delta(E_i - E_f) \tag{2.3.2}$$

and considering nuclei that are arranged into a crystal:

$$\left(\frac{\mathrm{d}\sigma}{\mathrm{d}\Omega \mathrm{d}E_f}\right)_{\text{elastic,coherant}} = \frac{(2\pi)^3}{V_{cell}} N_{\text{cell}} \delta(\mathbf{Q} - \mathbf{G}) \left|\sum_n b_n e^{i\mathbf{Q}\cdot\mathbf{R}_n}\right|^2 \delta(E_i - E_f) \tag{2.3.3}$$

where $\mathbf{G}$ is a reciprocal lattice vector. As for x-ray scattering, the cross section is non-zero only when $\mathbf{Q}$ is equal to a reciprocal lattice vector $\mathbf{G}$, and thus diffraction intensity is confined to these points in reciprocal space. It is noted that this is the coherent contribution to scattering. An additional incoherent cross section arises from differences in Fermi scattering lengths, for example, due to different isotopes.

2.3.2 Neutron sources and facilities

Whilst x-rays can be generated using laboratory sources, and are readily available, neutron generation requires either a spallation or reactor source at a national or international facility. Reactor sources, such as the Institut Laue-Langevin (ILL) generate neutrons through nuclear fission of ^{235}U. Reactor sources generate a high neutron

flux, with a broad distribution of energies. Neutrons can be slowed down by passing them through moderators, and are directed along guides to experimental stations. A monochromator crystal can be used to select a single crystal wavelength from the broad distribution of energies. Reactor sources have had great success, providing a spectrum of neutron energies and thus affording great flexibility, similar to that obtained for synchrotron x-ray sources. However, reactor cores generally have high costs associated with them, due to the licensing required for the fissile fuel, the need to remove heat from the reactor, and complex safety and maintenance issues. For this reason, there has been a shift towards using neutrons generated from spallation sources. Neutron diffraction data used in thesis was obtained at the SXD beamline, with neutrons generated from the ISIS spallation source.

2.3.2.1 Spallation source - ISIS

In a spallation source, a beam of high energy protons strike nuclei in a heavy metal target, causing neutrons to be ejected. The energy of these neutrons can be controlled by passing through a moderator material.

ISIS uses an 800 MeV proton accelerator. An ion source produces H^- ions using electronic discharge. These ions are accelerated and separated into pulses using a radio frequency quadrupole accelerator, and then accelerated using a linac, up to ∼37% the speed of light. Acceleration continues in a synchrotron, which operates in a similar manner to that described in section 2.2.2.2. Aluminium foil strips the electrons away from the ions, leaving a beam of protons, and powerful bending magnets and radio frequency electric fields focus and accelerate the beam. After ∼10000 revolutions, the protons separate into two large bunches at ∼84% the speed of light. Each bunch is then extracted from the synchrotron by kicker magnets.

These high energy protons collide with a tungsten target, and drive neutrons from the atomic nuclei, producing an intense neutron pulse. An array of hydrogenous moderators slows the neutrons to speeds/energies useful for experiments, and they

are then directed to beamlines.

2.3.2.2 SXD

SXD is a single crystal diffractometer at ISIS, which exploits a time of flight Laue approach to access large volumes of reciprocal space in a single experiment [58].

ISIS produces a pulsed beam of neutrons (frequency 50 Hz), with a spectrum of wavelengths determined by a moderator. Each pulse of neutrons travels towards the diffractometer, spreading out in space due to the variation in velocity. Each neutron is scattered by the crystal, and as it reaches the detector, time is recorded. The detector is fixed in space, and for each pulse, intensity will be recorded as a function of flight time. Both neutron flight time (t) and total distance travelled (L) can be measured to a high degree of accuracy, and from this, velocity (v) can be calculated; $v = \frac{L}{t}$. The deBroglie equation defines the wavelength of the neutron (λ) as

$$\lambda = \frac{h}{mv} = \frac{ht}{mL}. \tag{2.3.4}$$

Using Bragg's law, for a detector held at a fixed angle θ:

$$\lambda = 2d_{hkl}\sin\theta = \frac{ht}{mL} \tag{2.3.5}$$

$$\Rightarrow d_{hkl} = \frac{ht}{2mL\sin\theta}. \tag{2.3.6}$$

Thus by measuring the time at which neutron pulses arrive at the detector, interplanar spacing for a given set of hkl planes (d_{hkl}) can be calculated.

SXD uses a water moderator to fix neutron energies, resulting in incident wavelengths ranging from 0.2-10 Å. Samples generally need to be at least 1 mm^3 in volume, and are more commonly ∼100 mm^3, requiring 1-2 hours data collection time per sample orientation. Through the use of cryostats and furnaces, temperature ranges of 300 mK to 300 K can be achieved. Eleven 64 × 64 pixel ZnS scintillator detectors are available, each with 192 × 192 mm^2 active area and 3 × 3 mm^2 resolution.

The primary factors limiting the accuracy and resolution of neutron diffraction experiments using spallation sources are the limitations in measuring flight time, distance and the detector angle. Accuracy in detector angle can be reduced by choosing a large scattering angle, whilst accuracy in the measured distance can be optimised by using long flight paths such that the effect of moderator thickness is limited.

2.3.2.3 Data acquisition and analysis

Exploiting the time of flight technique and large area position sensitive detectors, SXD is optimised for experiments requiring continuous coverage of large reciprocal space volumes.

Data may initially be used to make a Laue Plot, integrating the whole time of flight range for each pixel in the detector. SXD has been set up to generate a list of indexed reflections to be used in refinement. A reciprocal space volume collected during a single measurement, sorted in time and space, is referred to as a histogram. For a given stationary crystal and detector arrangement, SXD collects a series of histograms in order to generate a complete structure factor set. Two detectors are typically used simultaneously, subtending a large angle at the sample. Each detector will collect several hundred reflections, leading to relatively straightforward determination and refinement of the **UB** matrix, as described for x-rays in section 2.2.2.1. Peaks are integrated using either a gaussian profile (optimised for time of flight), or using shoebox or line integration methods. Peak intensities are normalised to the incident beam using a vanadium standard. Finally, absorption corrections can be applied, and the resulting corrected intensities can be reduced to structure factors.

For SXD, the above data handling is performed using SXD2001. The resulting structure factors can be used in least squares refinement of crystal structures.

Chapter 3

$CaMn_7O_{12}$

3.1 Introduction

3.1.1 Motivation for studying $CaMn_7O_{12}$

$CaMn_7O_{12}$ belongs to the family of **quadruple perovskite** manganites, derived from a doubling the conventional ABO_3 perovskite cell shown in Figure 3.1, in all three directions.

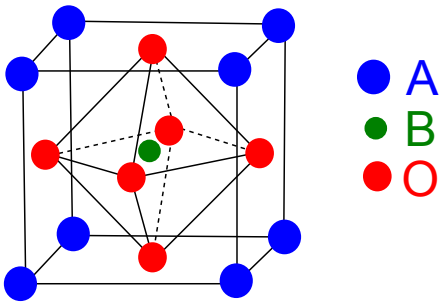


Figure 3.1: The basic perovskite unit cell common to many ferroelectric materials, incorporating B sites (green) octahedrally coordinated by oxygen, and square planar coordinated A sites (blue).

Perovskite crystals frequently undergo ferroelectric phase transitions resulting from displacement of B site cations, for example $BiTiO_3$ undergoes a series of symmetry breaking phase transitions that result in ferroelectric phases, as shown in Figure 3.2 [59, 60, 61].

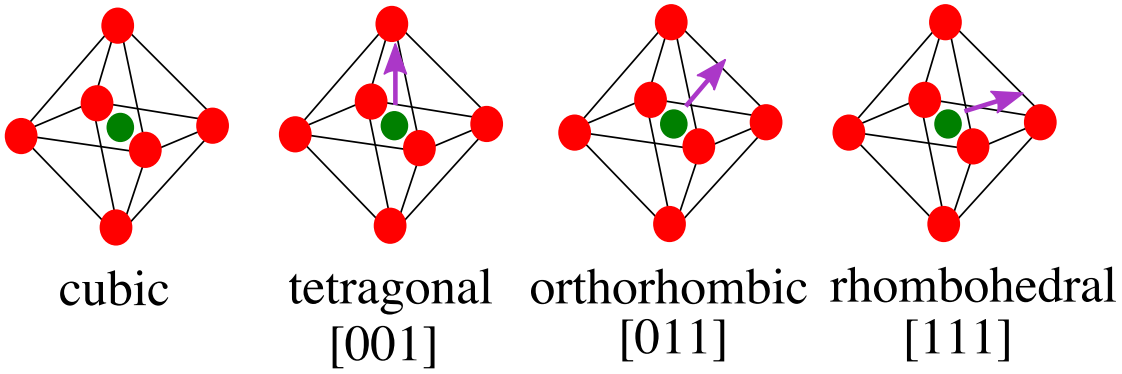


Figure 3.2: A series of symmetry breaking phase transitions in $BiTiO_3$ give rise to the emergence of dipole moments and a net ferroelectric polarisation. The direction of polarisation changes with each phase transition, lying along the direction in which symmetry is broken.

In addition to ferroelectricity, multiferroicity has proven to be prominent in perovskite structures. One of the earliest discovered examples was type I multiferroic $BiFeO_3$ (discussed in section 1.2.5 [13]), in which magnetic behaviour is dominated by partially filled orbitals d orbitals on the perovskite (Fe) B site, and a ferroelectric polarisation arises from A site (Bi^{3+}) lone pairs of electrons. One of the best known type II multiferroics $TbMnO_3$, described in section 1.3.1.1 [14] is part of a broader family of rare earth $RMnO_3$ multiferroics based upon the perovskite structure that show strongly coupled magnetically induced ferroelectric polarisations resulting from symmetric Heisenberg exchange or antisymmetric DM exchange.

The perovskite structure is evidently an important starting structural model for a variety of multiferroics with different coupling mechanisms and magnetic orders, however all known multiferroics based upon the simple perovskite structure have limited technological potential, either due to the strength of their magneto-electric coupling (for type I systems), or due to the magnitude of polarisation and/or the ferroelectric onset temperature (in the case of type II multiferroics). These limitations have prompted investigation into the multiferroic potential of variants on the simple perovskite structure. Speculative and theoretical predictions of multiferroicity in perovskite based structures has been proposed, as outlined below, but experimental realisation of multiferroicity in these systems is yet to be established.

Using density functional theory, Giovannetti *et al.* [62] theoretically predicted multiferroic polarisation of up to several μCm^{-2} in the half doped manganite perovskite $La_{0.5}Ca_{0.5}MnO_3$, based upon early ideas of bond-centred versus site centred charge order [63]. A model proposed by Radaelli *et al.* [64] incorporates Jahn-Teller distortion of octahedra and orbital ordering, that "locks in" to the magnetic structure, with a quasi-commensurate propagation vector below the orbital ordering temperature (T_{OO}), shown in Figure 3.3 . It is predicted that this type of charge/orbital

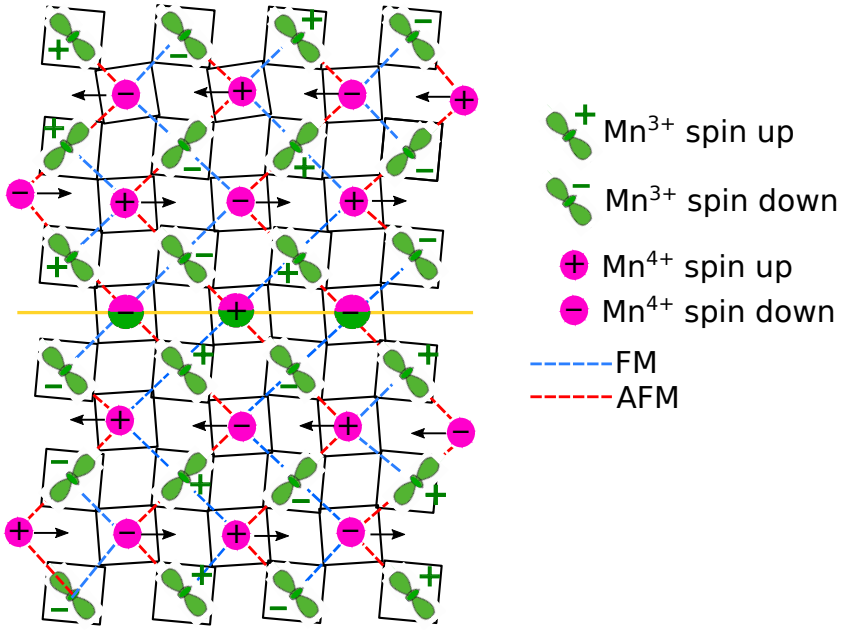


Figure 3.3: Adapted from Ref. [64]. The proposed model for charge, orbital and magnetic ordering below T_N in $La_{0.5}Ca_{0.5}MnO_3$ in the *ac* plane, based upon x-ray and neutron diffraction data. Orbital occupation for Mn^{3+} cations coincides with antiferromagnetic zigzag chains. Displacement of charged cations (as indicated by the black arrows), coupled to the magnetic structure, could give rise to a ferroelectric polarisation. The yellow line indicates a structural domain boundary, highlighting two possible domains that could arise.

ordering, coupled to the magnetic structure, may break inversion symmetry, and may enable the onset of a ferroelectric polarisation [63].

Quarter doped manganite perovskites may also have multiferroic potential. Through Monte Carlo simulations, ferroelectric polarisation in a magnetic "SOS" phase has been predicated in quarter doped manganites [65]. This magnetic phase differs from the more commonly studied CE antiferromagnetic phase in quarter doped manganites

(see Figure 3.4(a) and (b)) [1], and consists of striped blocks, with collinear, E-type antiferromagnetic spins within each block and orthogonal spins across each block (Figure 3.4(c)). This non-collinear spin pattern is a direct consequence of the doping and results from competition between two, strong, nearest neighbour interactions; super exchange and double exchange. It is anticipated that this strong interaction could result in a relatively high onset temperature for inhomogeneous magnetic ordering and hence potential for higher temperature magnetically induced ferroelectricity.

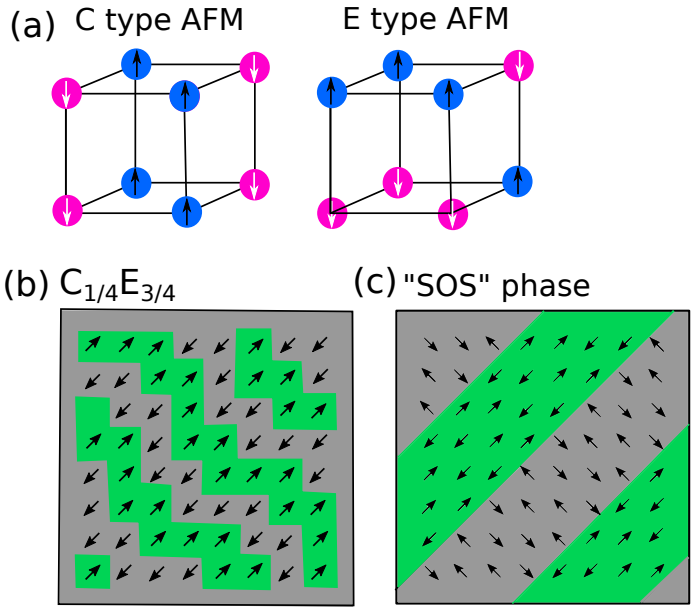


Figure 3.4: (a) C and E type antiferromagnetic orderings depicted for a simple cubic cell. In quarter doped perovskite manganites, these orderings contribute to form zig-zag chains of collinear spins that can be viewed as a superstructure of 1/4 antiferromagnetic C phase and 3/4 antiferromagnetic E phase as shown in (b). In addition to this phase, Dong *et al.* have predicted an "SOS" phase, with non-collinear spins, shown in (c). Adapted from Ref. [65].

Despite predictions for multiferroicity in variants of the perovskite structure, experimental realisation has been limited. Many candidate materials are difficult to synthesise or require extreme pressure/temperatures. For example, to obtain quarter doped manganates predicted to exhibit the "SOS" phase, weak Jahn-Teller distortions but a narrow e_g bandwidth are required. Whilst the bandwidth can be decreased by reducing the A-site cation size, this will simultaneously enhance Jahn-Teller distortions.

Quadruple perovskites may provide a solution to this difficulty. Having the general formula $(AA'_3)B_4O_{12}$, quadruple perovskites consist of a pseudo-cubic, 3-d array of corner sharing BO_6 octahedra, similar to that observed in the normal perovskite cell. There are two inequivalent A sites (A and A'), with A generally occupied by a cation with a relatively large ionic radii, and A' occupied by a transition metal. Jahn Teller distortion of the A' site can lead to significant tilting of the octahedra, and a short, bent, B-O-B bond. This enhances antisymmetric DM exchange, known to be significant in the multiferroic coupling of RMnO$_3$ systems such as TbMnO$_3$ (see section 1.3.1.1).

Research into the multiferroic potential of these systems is already well underway. Coupling between charge, orbital and magnetic orderings in $NaMn_7O_{12}$ has been investigated [66, 67], and will be further explored in Chapter 5. Polarisation arising from helical spin order has been predicted from first principles calculations in $SrMn_7O_{12}$ [68], and magneto-electric coupling resulting from exchange striction has been reported in $BiMn_7O_{12}$ [69].

Here, we investigate and characterise the structural and magnetic properties of $CaMn_7O_{12}$ developing a microscopic model for the multiferroic coupling. Contrast in size between Ca and Mn cations occupying the perovskite A and A' sites results in a highly tilted arrangement of octahedra and a strong multiferroic coupling resulting from antisymmetric DM exchange.

Initially, a summary of the results of previous structural, magnetic studies and polarisation measurements will be presented, describing an incommensurate magnetic modulation and a large polarisation. New single crystal x-ray diffraction data showing an incommensurate structural modulation will then be reported. A model interpreting this structural modulation in terms of orbital occupation is developed, and combined with the known magnetic structure to characterise an unprecedented "magneto-orbital helix".

3.1.2 The crystal structure

At high temperatures, $CaMn_7O_{12}$ crystallises in the body centred, cubic space group $Im\bar{3}$ [70], composed of eight primitive perovskite unit cells. Perovskite A sites are occupied by Ca^{2+} and Mn^{3+} cations in a 1:3 ratio, and all other Mn cations occupy perovskite B sites with an average valence of 3.25 (see Figure 3.5).

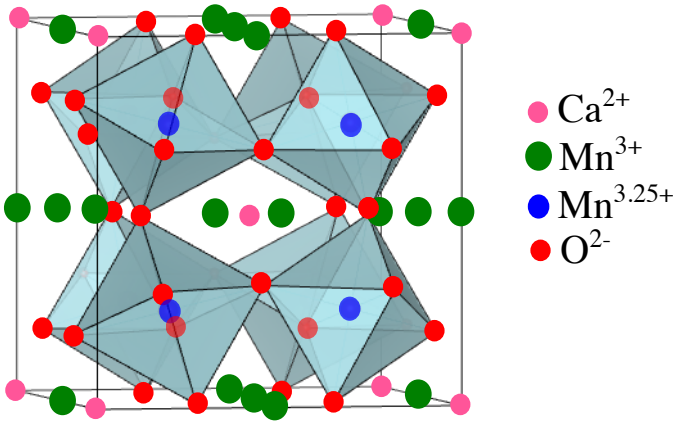


Figure 3.5: The high temperature $Im\bar{3}$ structure of $CaMn_7O_{12}$, comprising eight basic perovskite unit cells with considerable octahedral tilting, and an average B site Mn valence of 3.25, due to disordered occupation of one Mn^{4+} and three Mn^{3+} cations.

Cooling below ~440 K, a first order phase transition to a rhombohedral, $R\bar{3}$ structure occurs, driven by charge ordering on the B sites. The rhombohedral cell is related to the high temperature cubic cell by the reciprocal lattice vectors (-1, 1, 0), (0, -1, 1) and (1/2, 1/2, 1/2) [71, 72]. For the purpose of the results presented in this thesis, it is useful to consider the low temperature phase in both the hexagonal setting, as three inequivalent triangular layers stacked along the c axis, and as a pseudo-cubic perovskite cell. These representations are shown in Figure 3.6.

Three inequivalent Mn sites can be defined with respect to the pseudo-cubic perovskite cell: Mn1 sites are A' sites of symmetry $\bar{1}$, occupied by Mn^{3+}. Mn2 are B sites of symmetry $\bar{1}$ and Mn3 are B sites of symmetry $\bar{3}$. Charge ordering on the Mn2 and Mn3 sites develops gradually upon cooling, and below ~250 K, each formula unit contains three Mn^{3+} cations on Mn2 sites and one Mn^{4+} cation on an Mn3 site [74].

Sławiński *et al.* [75] first reported the emergence of an incommensurate structural

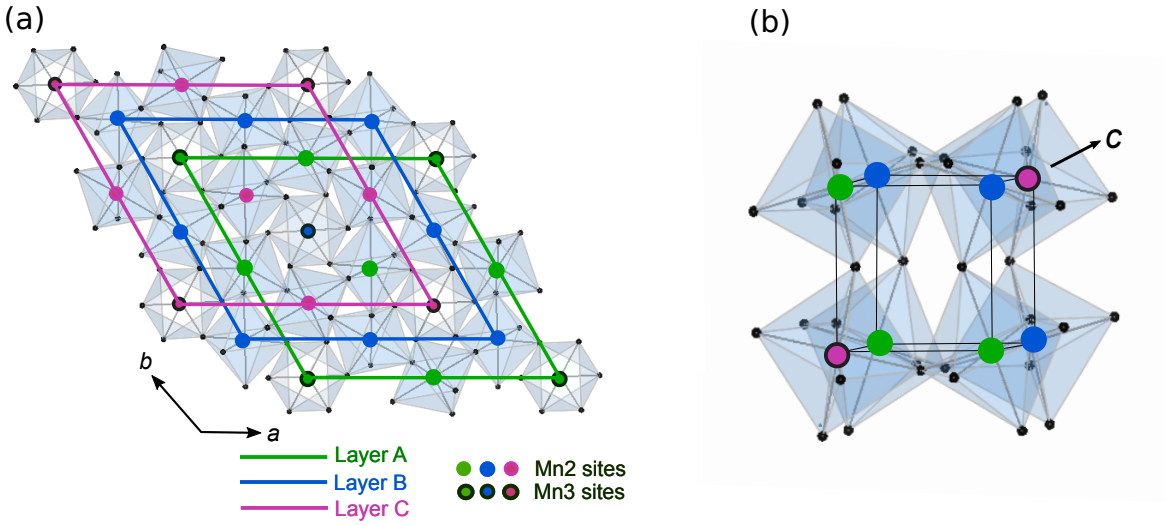


Figure 3.6: Adapted from Ref. [73]. (a) The $R\bar{3}$ structure, highlighting three inequivalent triangular layer (green, blue, pink) stacked along the hexagonal c axis. (b) The $R\bar{3}$ structure in the pseudo-cubic setting. The hexagonal c axis corresponds to the cubic [111], with Mn3 (Mn^{4+}) sites lying along this diagonal

modulation with propagation vector q_c = (0, 0, 0.9213) along the hexagonal c axis below T_{OO}= 250 K and interpreted this in terms of atomic position modulation. A detailed model describing this modulation will be developed in this chapter.

3.1.3 The magnetic structure

$CaMn_7O_{12}$ undergoes two magnetic ordering transitions at T_{N1} = 90 K and T_{N2} = 48 K [76, 77], with T_{N1} coinciding with the onset of a ferroelectric polarisation [78]. Magnetic susceptibility measurements showed a downturn in susceptibility at T_{N1}, suggesting antiferromagnetic ordering of Mn in the hexagonal ab plane [79]. Below T_{N2} a peak in c axis susceptibility may be indicative of ordering along this direction, and this is coupled with an increase in susceptibility in the ab plane.

The magnetic structure between T_{N1} and T_{N2} has been determined through neutron powder diffraction [79]. Magnetic anisotropy constrains Mn spins to lie in the hexagonal ab plane. We can consider the ordering in terms of the triangular layered structure described in section 3.1.2. Within each layer, Mn2 spins are parallel to one another,

whilst Mn3 spins are approximately antiparallel, as shown in Figure 3.7. Spins in adjacent layers are rotated by 124°, giving rise to a helical magnetic structure that propagates along the c axis, with an incommensurate propagation vector q_m = (0, 0, 1.037).

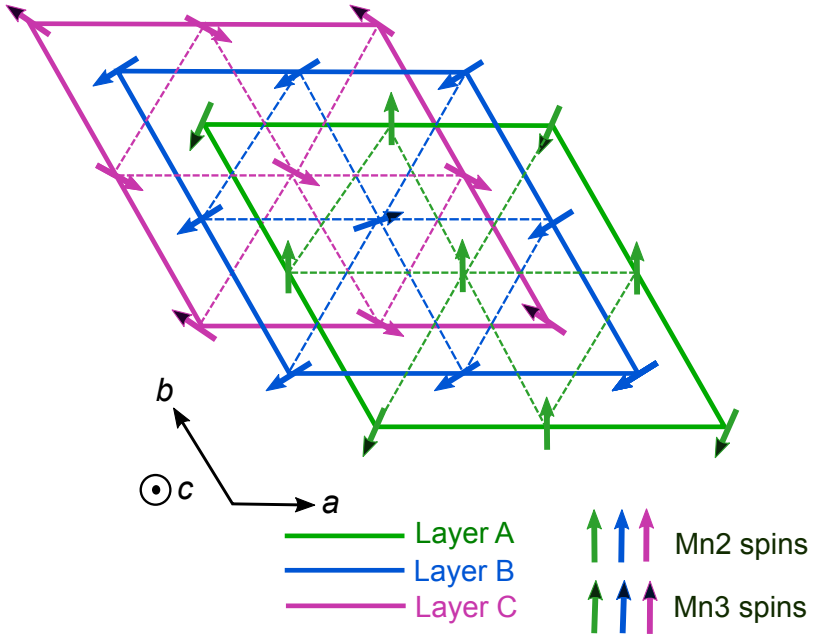


Figure 3.7: Adapted from Ref. [73]. The magnetic structure of $CaMn_7O_{12}$ below T_{N1}, shown as three triangular layers stacked along the c axis (c.f. Figure 3.6(a)). Mn2 spins are approximately parallel whilst Mn3 spins are approximately antiparallel. Adjacent layers along the c axis are rotated by 124°

The magnetic structure below T_{N2} is still under debate. Johnson *et al.* [79] found that magnetic reflections in neutron powder diffraction could no longer be indexed with a single propagation vector, and instead, observed the coexistance of two modulations along the same symmetry line in the Brillouin zone. In fact, q_m appears to split symmetrically below T_{N2}. Sławiński *et al.* [80] have shown that the average propagation vector is constant across T_{N2}, and have fitted neutron data using a model that can be described as a "beating" of the magnetic structure below T_{N1}.

The magnetic structure below T_{N2} will not be discussed in details in this thesis, but it will become clear from the development of the magneto-electric coupling model that its symmetry properties and chirality must be very similar to that of the magnetic

structure below T_{N1}, and the transition itself must have little effect on the electrical properties.

3.1.4 The ferroelectric polarisation

Initial pyroelectric measurements on polycrystalline samples determined that a ferroelectric polarisation develops below T_{N1}[78, 79]. This was followed by single crystal measurements that determined the direction of the polarisation to be parallel to the hexagonal c axis and measured the large saturation value; $P = 2870\ \mu\mathrm{Cm}^{-2}$, at the time, significantly larger than any other recorded magnetically induced ferroelectric polarisation.

Since the ferroelectric polarisation lies parallel to the direction of the magnetic propagation vector, magneto-electric coupling cannot arise purely as a consequence of antisymmetric DM exchange. As described in section 1.3.1.1 the antisymmetric DM interaction displaces anions perpendicular, but within the same plane as a vector connecting two non-collinear spins. Thus in this case the DM interaction would displace oxygen anions perpendicular to the magnetic propagation vector and the axis of the helix. The observed polarisation could be explained through ferroaxial coupling to a global structural or magnetic rotation, as discussed in section 1.3.1.3.

The microscopic coupling mechanism is still under debate, and prompted the structural study presented in this thesis.

With the motivation of gaining insight into the origin of the incommensurate structural modulation, and whether this may be associated with the coupling mechanism between the observed incommensurate magnetic helix and colossal ferroelectric polarisation, a series of x-ray diffraction experiments were performed. Results from single crystal experiments performed using the SuperNova diffractometer were used in conjunction with powder diffraction to assess initial crystal quality and homogeneity. Further single crystal experiments were performed at the I16 and I19 beamlines at the Diamond Light Source, measuring satellite peaks associated with the structural

propagation vector for multiple Bragg peaks, across a range of temperatures. Finally, more detailed diffraction experiments were performed using SuperNova, measuring a very large number of satellite reflections at several temperatures. This data was then used in refinement to produce a model for the modulated structure.

3.2 X-ray Diffraction Experiments

3.2.1 Sample characterisation

The single crystal samples used for x-ray diffraction measurements are cubic in shape, and typically $\sim$150 $\times$ 150 $\times$ 150 μm^3 in volume.[1] These crystals were grown using a flux method: a 5 g mixture of $CaCl_2$:MnO_2 was heated at 850°C for 24 hours in an alumina crucible, and then cooled at a rate of 5°C h^{-1}.

Initial crystal characterisation was performed using the SuperNova single crystal x-ray diffractometer. Between 10 and 15 crystals were tested for to check composition, quality and consistency across the batch. The crystals were mounted on micro loops as shown in Figure 3.8, and short, room temperature measurements were used to collect Bragg peak intensities.

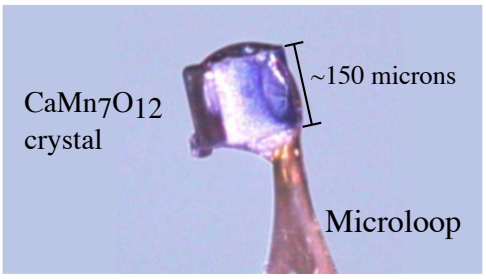


Figure 3.8: A single crystal of $CaMn_7O_{12}$ mounted for a SuperNova x-ray diffraction experiment.

[1] Crystals were grown by C. Martin, Laboratorie CRISMAT, ENSICAEN, France

CrysAlisPRO software [51] was used for peak indexing. For all crystals measured more than 85% of measured diffraction peaks could be indexed using an $R\bar{3}$(obv) lattice with cell parameters of $\sim a$ = 10.4 Å, b = 10.4 Å, c = 6.3 Å, and for the majority of crystals, more than 97% of these peaks could be indexed. These cell parameters are consistent with previous room temperature lattice parameters obtained for $CaMn_7O_{12}$. A representative hk plane is shown in Figure 3.9, with an overlay of the reciprocal lattice grid for the $R\bar{3}$ unit cell. Diffraction peaks are sharp and well defined, with little evidence for impurity phases, modulation or impurity.

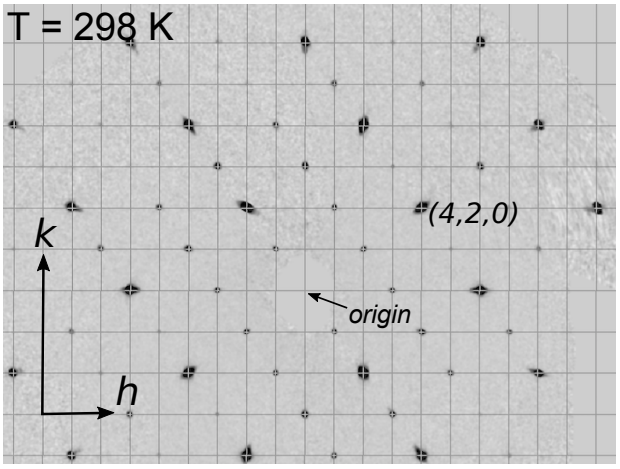


Figure 3.9: Bragg peaks indexed in the $R\bar{3}$ unit cell with $\sim a$ = 10.4 Å, b = 10.4 Å, c = 6.3 Å. This hk plane in reciprocal space, obtained using CrysAlisPRO is indicative of the sharp Bragg peaks observed for all crystals at room temperature.

From the selection of screened crystals, a large, high quality crystal was selected for use in x-ray diffraction experiments to be performed at the I16 and I19 beamlines at the Diamond Light Source.

3.2.2 I16 Diamond Light Source - Observation of the incommensurate structural modulation

This experiment was motivated by the observation of an incommensurate atomic position modulation with propagation vector q_c = (0, 0, 0.9213) below 250 K by Sławiński

et al. [75]. Structural modulations to periodic atomic ordering in crystals give rise to subtle adaptations in crystallographic symmetry, and in the case of diffraction, result in the appearance of satellite peaks, occurring in addition to the Bragg peaks reflecting the average lattice periodicity.

These satellite peaks can be indexed using an extension of h, k, l, indices, as

$$\mathbf{H} = h\mathbf{a}^* + k\mathbf{b}^* + l\mathbf{c}^* + m_1\mathbf{q}_1 + m_2\mathbf{q}_2... + ...m_d\mathbf{q}_d \tag{3.2.1}$$

where a linear combination of basis vectors $\mathbf{q}_i$ describe the positions of the satellites. For a full derivation of the structure factor for modulated crystals, see Appendix A.

Satellite diffraction peaks are typically weaker than Bragg peaks, hence a higher brilliance synchrotron x-ray source has been used for measurement.

In this thesis, in contrast to the previously reported propagation vector q_{c-old} = (0, 0, 0.9213) [75], a propagation vector $\sim q_c$ = (0, 0, 2.077) has been used (obtained from the relationship -q_{c-old} + (0, 0, 3), by the addition of an allowed reciprocal lattice vector).[2] Indexing structural satellite peaks in this convention, the relationship $q_c = 2 \times q_m$ is apparent. This relationship will be discussed further in section 3.3.3.

The single crystal used for this experiment was mounted on a copper puck with the [2 0 1] direction surface normal. A linearly polarised x-ray beam of energy 6.112 keV was used, along with the Pilatus area detector. Following initial refinement of the **UB** matrix, confirmation of crystal orientation and the identification of several strong Bragg peaks, the sample was cooled to 10 K, using a closed tip cryostat. The **UB** refinement was repeated, and the previously observed strong Bragg peaks were located. l scans around the (4, -2, -6) Bragg peak revealed a satellite peak at (4, -2, -3.937), yielding a propagation vector of (0, 0, 2.063). Additionally, a second

[2]The reflection condition for the $R\bar{3}$ cell is $-h + k + l = 3n$.

harmonic of this satellite peak was observed (see Appendix A for explanation) with a propagation vector of (0, 0, 4.124). Centring in the x-ray beam on each of these peaks in turn, the intensity and position was tracked at 2 K increments over a temperature range from 10 - 295 K. The resulting plots are shown below:

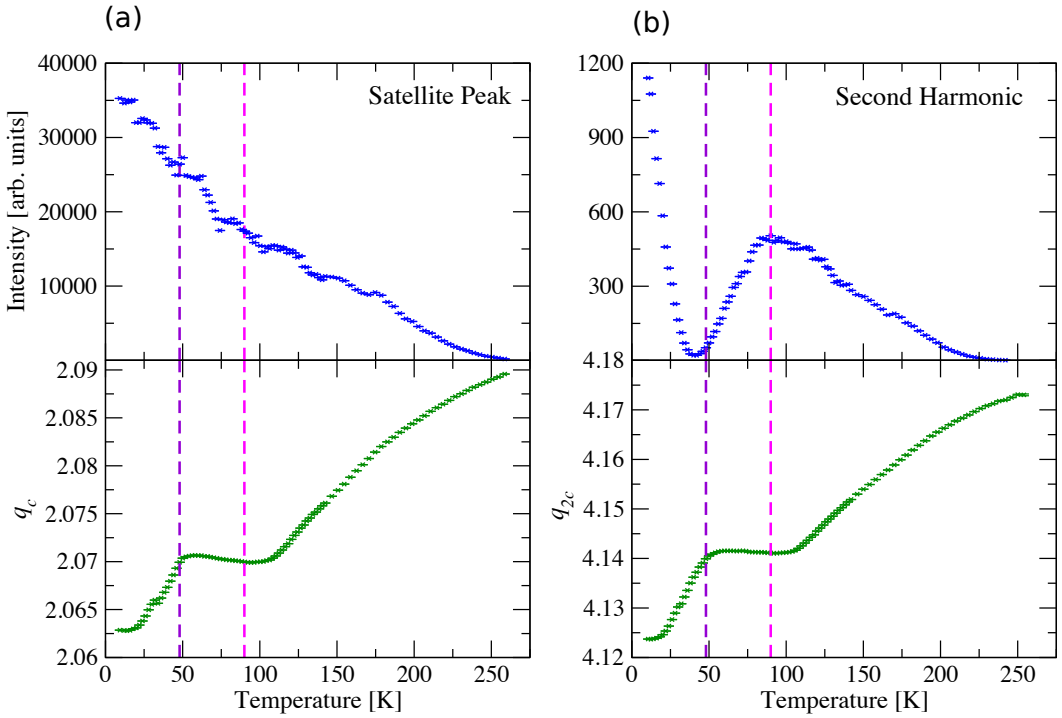


Figure 3.10: (a) Variation in the intensity (upper pane) and propagation vector (lower pane) of the structural satellite of the (4, -2, -6) Bragg peak. Kinks in the variation of q_c coincide approximately with the expected magnetic transitions indicated by the dashed lines. (b) Corresponding variations in intensity and propagation vector of the second harmonic with propagation vector $q_{2c} = 2 \times q_c$.

The variation in both intensity and propagation vector of the satellite peaks are similar to those observed by Sławiński *et al.* [75]. Anomalies in variation of the propagation vector (q_c) and the second harmonic (q_{2c}) coincide approximately with the two magnetic phase transition temperatures; T_{N1} and T_{N2}, indicating likely coupling between the structural modulation and magnetic ordering.

Whilst the primary purpose of the I16 experiment was to identify structural satellites

associated with q_c, a magnetic satellite of the (3, -1, -2) Bragg peak was observed at (3, -1, -0.965), yielding a propagation vector of $q_m = (0, 0, 1.035)$, in good agreement with the previously reported value [79]. Tracking the variation in intensity and propagation vector as a function of temperature, as shown in Figure 3.11 confirmed that this peak could not be detected above T_{N1} and revealed a kink in the intensity temperature dependence coinciding approximately with T_{N2}. The magnetic nature of this peak was confirmed from polarisation analysis. The theory behind this will not be described in detail here, but giving a brief summary: Taking the reference polarisation directions of σ and π defined in Figure 2.8, scattered x-ray intensity can be measured either in the $\sigma \rightarrow \sigma$ channel (σ polarised incident wave, detection of σ polarised scattered intensity), or the $\sigma \rightarrow \pi$ channel (σ polarised incident wave, detection of π polarised scattered intensity). Thomson scattering does not affect the σ polarisation of the incident wave and thus Bragg peaks are suppressed when measuring in $\sigma \rightarrow \pi$. In contrast magnetic peaks show variation in intensity when measured in $\sigma \rightarrow \pi$. The peak show in Figure 3.11, was observable in $\sigma \rightarrow \pi$ and thus is believed to be magnetic in origin.

To summarise, data obtained during this experiment is in good agreement with previous observations of an incommensurate structural modulation emerging below T_{OO}, accompanied by an incommensurate magnetic modulation with $q_m = \frac{1}{2}q_c$ below T_{N1}. Anomalies in variation of intensity and propagation vector of the structural modulation coinciding approximately with the expected magnetic transitions indicate that coupling between the order parameters may exist.

Having established the existence of structural satellite peaks, collection of intensities for a large number of peaks was required to enable refinement of a model for the modulation. Time constraints limited the number of satellite peaks that could be collected at I16, and thus further measurements were made at the I19 beam line, exploiting the rapid data collection capabilities. In conjunction, additional experiments were performed using the SuperNova diffractometer, using long counting times and extensive reciprocal space coverage to measure satellites at several different temperatures:

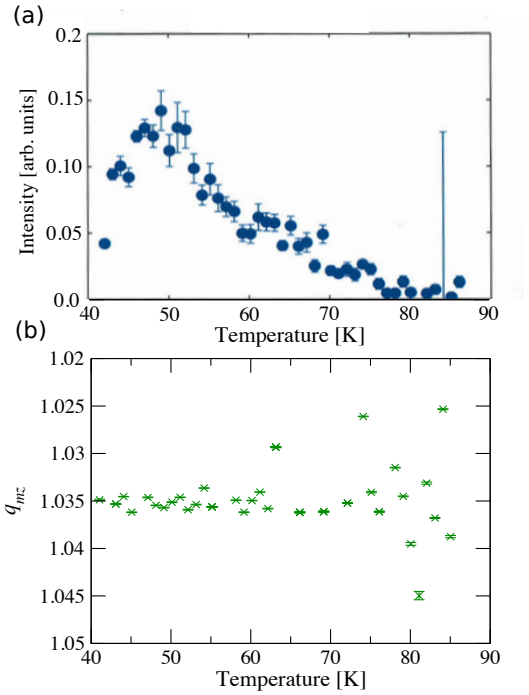


Figure 3.11: Variation in (a) intensity and (b) propagation vector of the magnetic satellite peak. The peak shows a kink in intensity coinciding approximately with T_{N2}, cannot be observed above T_{N1} and has a propagation vector (0, 0, 1.037), in good agreement with the previously reported magnetic propagation vector.

3.2.3 I19 Diamond Light Source and Supernova - Collection of satellite peaks

Experiments using the I19 beam line and SuperNova were performed using different single crystals of $CaMn_7O_{12}$, but both samples had previously been screened for quality using SuperNova, and were of similar size. At I19, Bragg and satellite peaks were measured at 150 K using an area detector to maximise coverage. Using SuperNova, Bragg and satellite peaks were measured at 150, 110 and 85 K.

All data sets were analysed using CrysAlisPRO. Peaks were indexed in $R\bar{3}$ symmetry with cell parameters $a = b = 10.4$ Å, $c = 6.4$ Å and a propagation vector of $q_c = (0, 0, 2.07)$. Data reduction using the constrained unit cell and propagation vector was used to generate a $hkl(m)$ reflection list of intensities peaks that conforming to the reflection condition $-h + k + l = 3n$.

A useful feature of the CrysAlisPRO software is the ability to view reciprocal lattice planes. Visual inspection of these planes confirmed that satellite peaks, whilst weak, were clearly evident in all data sets. The intensity of satellite peaks increased with decreasing temperature, and an example plane taken from 85 K SuperNova data is shown in Figure 3.12.

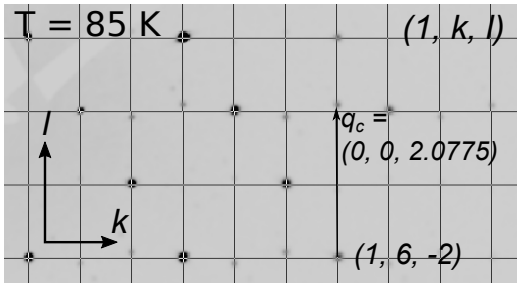


Figure 3.12: The $1kl$ plane in reciprocal space, taken from 85 K SuperNova data. In addition to sharp Bragg peaks indexed in the $R\bar{3}$ cell satellite peaks can be indexed with a propagation vector $q_c = (0, 0, 2.0775(9))$.

The reflection list generated by CrysAlisPRO was used to refine a model for the modulation structure. Lattice parameters for use in this refinement were obtained from a powder x-ray diffraction experiment performed in Oxford.

3.2.4 Powder diffraction - Determination of lattice parameters

A powder sample of $CaMn_7O_{12}$was produced by grinding single crystals described in section 3.2.1 and passing through a 35 μm mesh. Data was collected using a Siemens D5000 powder diffractometer at 150 K, 110 K and 85 K.

Data was refined using the LeBail method [81] in FullProf [82, 83] (see Appendix B - Part 1).

Fits to the powder data are shown in Figure 3.13, and the resulting refined lattice parameters are tabulated and plotted in Figure 3.14.

Having measured reflection intensities for a large number of Bragg and satellite peaks

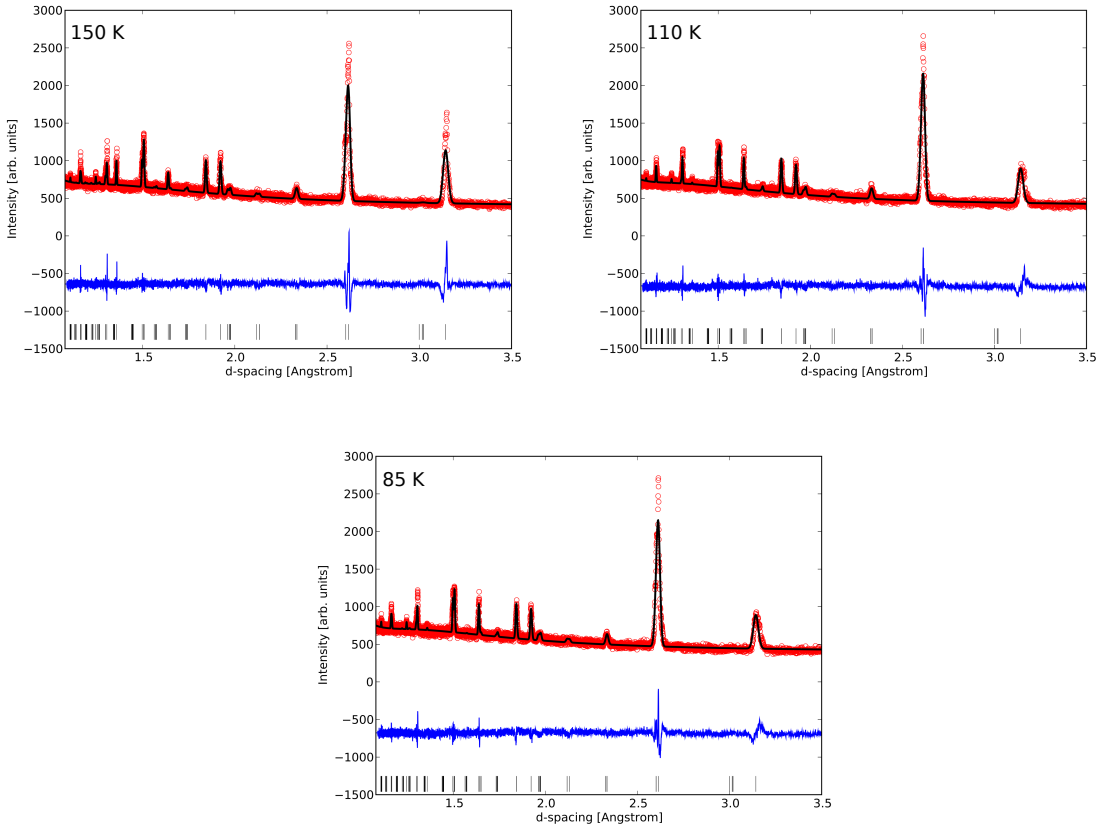


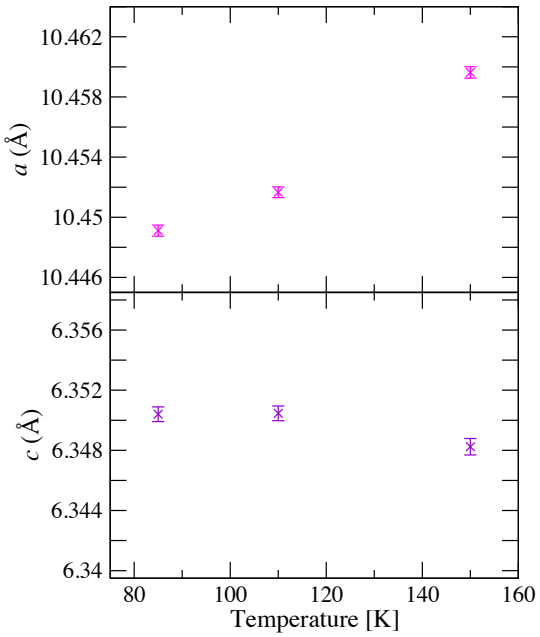
Figure 3.13: Powder diffraction patterns for $CaMn_7O_{12}$ measured at (a) 150 K (b) 100 K and (c) 85 K. The calculated fit to the plot is shown in black, and the difference in blue.

and accurate sets of lattice parameters at each temperature, a structural model was refined against the x-ray diffraction data to reconcile a physical interpretation for the modulation.

3.3 Results

3.3.1 Structural refinement

JANA2006 [84] was used for refinement, employing structural optimisation methods outlined in Appendix B - Part 2. Iterative least squares minimisation was used to fit calculated diffraction intensities from approximate structural models against the



T [K]	a (Å)	c (Å)
150	10.4596(4)	6.3482(6)
110	10.4516(4)	6.3506(5)
85	10.4491(4)	6.3519(5)

Figure 3.14: (a) Plotted and (b) tabulated lattice parameters extracted from the LeBail fits to powder diffraction data.

experimentally measured diffraction intensities. Bragg and satellite peak intensities were taken from the 150 K SuperNova experiment, but the result of the refinement was checked for consistency using 110 K, 85 K and I19 data.

Initially, a model for the average structure was refined against Bragg peak intensities, with the model incorporating $R\bar{3}$ symmetry, lattice parameters obtained in section 3.2.4 and average atomic positions taken from taken from Sławiński *et al.*. Atomic positions and thermal parameters were initially fixed, whilst overall scale and extinction (accounting for multiple diffraction events and x-ray beam attenuation), based upon a type I Lorentzian model, were allowed to refine. Within allowed symmetry constraints, atomic positions and isotropic thermal parameters were then allowed to refine, and a converged fit with R-factor of $\sim$9% was obtained (see Appendix B for an explanation of the R-factor).

The average structure was then fixed, and a model for the incommensurate modulation was included in the refinement. A propagation vector of $q_c = (0, 0, 2.0775(9))$ was used, and the symmetry was adapted from $R\bar{3}$ to the centrosymmetric four dimensional space group $R\bar{3}(00\gamma)0$ (see Appendix C). The model incorporates a sinusoidal

position modulation on each atom, of the form

$$\begin{aligned} x_{mod}(\bar{x}_{qc}) =& x_0 + A_x\sin(2\pi\bar{x}_{qc}) + B_x\cos(2\pi\bar{x}_{qc}) + l_x \\ y_{mod}(\bar{x}_{qc}) =& y_0 + A_y\sin(2\pi\bar{x}_{qc}) + B_y\cos(2\pi\bar{x}_{qc}) + l_y \\ z_{mod}(\bar{x}_{qc}) =& z_0 + A_z\sin(2\pi\bar{x}_{qc}) + B_z\cos(2\pi\bar{x}_{qc}) + l_z, \end{aligned} \tag{3.3.1}$$

where

$$\bar{x}_{qc} = \boldsymbol{q_c} \cdot \boldsymbol{r_0} = q_z \cdot (z_0 + l_z), \tag{3.3.2}$$

$x_{mod}/y_{mod}/z_{mod}$ and $x_0/y_0/z_0$ are the modulated and unmodulated x,y,z coordinates respectively, A and B are the Fourier coefficients of the modulation amplitude and l is an integer value defining the unit cell. Refining this model against satellite reflection intensities, allowing all A and B Fourier coefficients to refine, within symmetry constrains, a converged fit was obtained. Completing a full refinement of the modulated structure against Bragg and satellite reflections produced a converged fit with an R-factor of ∼15% (∼9% for Bragg peaks and ∼17% for satellite peaks). This refinement was checked for repeatability using a range of starting Fourier coefficients for the modulation, and was found to be robust, always converging to the same solution. Tests made using occupancy and charge modulations rather than sinusoidal atomic positions did not produce a converged fit to the data.

The final structural parameters are tabulated below:

Atom	**Occupancy**	$\boldsymbol{x}_0$	$\boldsymbol{y}_0$	$\boldsymbol{z}_0$	$\boldsymbol{U}_{iso}$
Ca	0.166667	0.0	0.0	0.0	0.014(1)
Mn1	0.5	0.5	0.0	0.0	0.0052(8)
Mn2	0.5	0.5	0.5	0.5	0.0023(7)
Mn3	0.166667	0.0	0.0	0.5	0.0029(9)
O1	1	0.2216(6)	0.2714(6)	0.0915(7)	0.015(1)
O2	1	0.3420(6)	0.5142(6)	0.3393(7)	0.012(1)

Table 3.1: Average fractional coordinates, occupancies and isotropic thermal parameters for $CaMn_7O_{12}$, refined using JANA2006 for 150 K SuperNova data.

Atom	$\boldsymbol{A}_x$	$\boldsymbol{A}_y$	$\boldsymbol{A}_z$	$\boldsymbol{B}_x$	$\boldsymbol{B}_y$	$\boldsymbol{B}_z$
Ca	0.0	0.0	-0.0007(6)	0.0	0.0	0.014(1)
Mn1	0.0068(2)	-0.0005(2)	0.0026(2)	0.0	0.0	0.0
Mn2	0.0034(2)	0.0031(2)	0.0005(2)	0.0	0.0	0.0
Mn3	0.0	0.0	0.0011(3)	0.0	0.0	0.0
O1	0.0017(6)	-0.0021(6)	-0.0011(8)	0.0025(7)	-0.0023(6)	-0.0004(8)
O2	0.0028(6)	-0.0004(6)	0.0040(8)	0.0007(6)	0.0009(6)	-0.0034(7)

Table 3.2: Refined Fourier coefficients for the modulation at 150 K

3.3.2 Interpreting the modulation - the orbital helix

Having refined a model for the 150 K x-ray diffraction data in terms of an average structure and a sinusoidal incommensurate position modulation on each atom, a physical interpretation of this modulation can be reconciled. Firstly, considering the impact of the structural modulation on Mn-O bond lengths. In Figure 3.15, Mn-O bond lengths are plotted for adjacent unit cells along the hexagonal c axis.

This bond length variation can be interpreted in terms of orbital occupation, by applying Jahn-Teller theory, as follows:

Mn1 sites are square planar coordinated by oxygen. The two Mn1-O bonds that couple Mn2 octahedra along the c axis chains (shown in Figure 3.17) show very little variation (cyan bonds in Figure 3.15(a)), whilst the remaining two Mn1-O bonds vary predominantly according to displacements of associated oxygen atoms. This small variation implies that the occupied e_g orbital is always oriented perpendicular to the MnO_4 plane. Mn3 sites are occupied by Mn^{4+} and thus the associated octahedra are not expected to be Jahn-Teller active. Variation in bond lengths is again dominated by movement of the oxygen anions, as opposed to the manganese.

The most significant modulation is of Mn2-O bond lengths. The magenta and yellow bonds in the xy plane show significant variation whilst bonds along the z direction vary weakly. The octahedral coordination of Mn2 site by oxygen anions lifts the degeneracy of the Mn $5d$ orbitals, and leads to a high spin arrangement of electrons. Single, unpaired Mn2 electrons may occupy any of the available e_g orbitals, and will

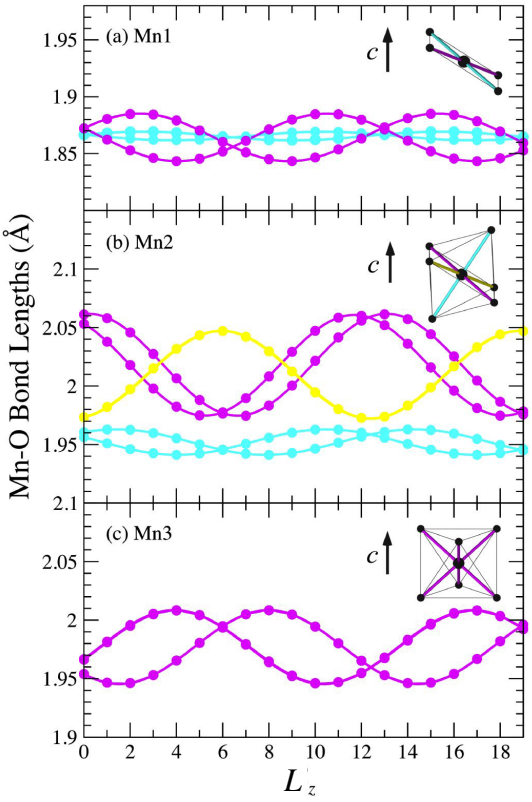


Figure 3.15: Adapted from Ref. [73]. Mn-O bond lengths generated from the refined model for the incommensurately modulated structure, plotted for unit cells (labelled L_z) along the hexagonal c axis. The structural modulation manifests primarily in variation of Mn2-O bonds as shown in (b), whilst Mn1-O (a) and Mn3-O (c) bonds vary predominantly according to oxygen displacements.

elongate the Mn2-O bond that lies parallel to the orbital direction, as shown in Figure 3.16.

Thus, considering the bond length variation shown in Figure 3.15(b), the structural modulation manifests primarily as periodic distortions of the Mn2, Jahn-Teller active octahedra. In the unmodulated, average structure, Mn^{3+} octahedra appear compressed, with two short bonds and four long bonds, implying occupation of the $d_{x^2-y^2}$ orbital. The presence of the structural modulation leads to an incommensurate rotation of a single pair of long Mn2-O bonds in the xy plane, consistent with periodic occupation of the d_{x^2} and d_{y^2} orbitals, passing through $d_{x^2-y^2}$ only at nodal points, as shown below.

This rotating orbital occupation can be characterised using a formalism proposed by

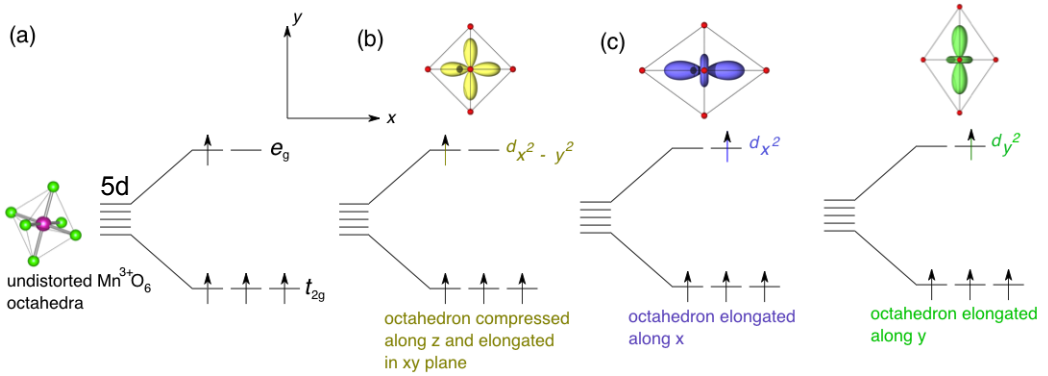


Figure 3.16: For Jahn-Teller active $Mn2(^{3+})O_6$ octahedra, with a high spin arrangement of electrons, a single electron occupies an e_g orbital. Occupation of either the d_{x^2} or d_{y^2} leads to an elongated bond parallel to the occupied orbital.

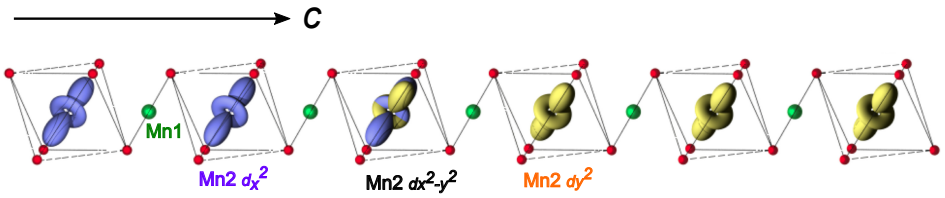


Figure 3.17: Adapted from Ref. [73]. Periodically varying orbital occupation, between d_{x^2} and d_{y^2}, coinciding with the rotation of a single pair of long Mn2-O bonds in the modulated structure. At nodal points, the $d_{x^2-y^2}$ orbital is occupied. Square planar Mn1 sites couple $Mn2O_6$ octahedra along the c axis.

Goodenough [85], which quantifies orbital occupation in terms of a mixing angle:

$$\tan\theta = \frac{\sqrt{3}(x-y)}{(2y-x-z)}. \tag{3.3.3}$$

Following the convention of Wu *et al.* [86], the angular sector $2\pi/3 \leq \theta \leq 4\pi/3$ is considered. Variation in θ for adjacent unit cells along c is plotted in Figure 3.18.

Whilst orbital ordering is a fairly widespread phenomenon in manganese oxides, the orbital ordering observed here is unique in that the preferential occupation direction is not fixed, but rotates around the crystallographic 3-fold axis, perpendicular to the direction of propagation, preserving the overall point group symmetry.

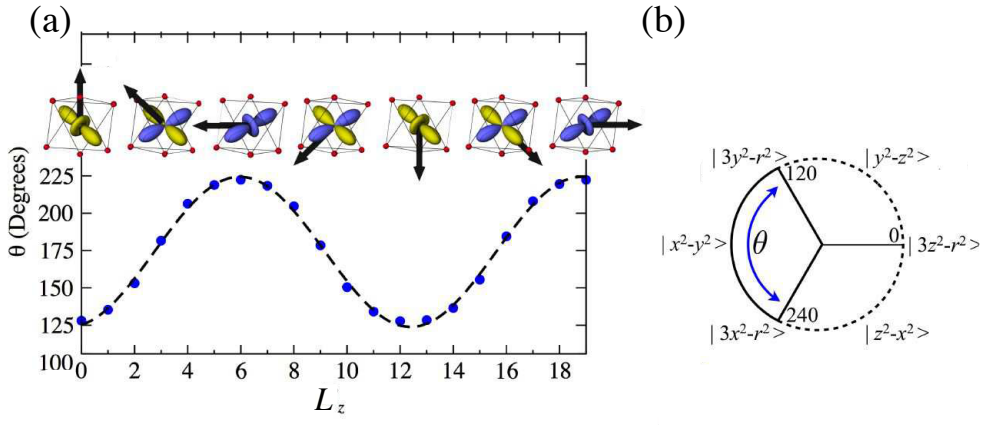


Figure 3.18: (a) Adapted from Ref. [73]. The orbital mixing angle θ, calculated using Eq. (3.3.3) plotted for $Mn2O_6$ octahedra along the c axis. θ correlates directly with orbital occupation, as shown in (b).

For completeness, the charge modulation accompanying this orbital modulation has been calculated using the bond valence sum method [87].

This is a semi-empirical approach developed from Pauling's electron counting rules [88], which estimates oxidation states of atoms based upon observed bond lengths in compounds with localised bonds.

The oxidation state of a six-fold coordinated atom is estimated from the sum of individual bond valences surrounding the atom, calculated as

$$\text{BondValence} = \sum_{i=1}^{6} \exp\left(\frac{(R_0 - R)}{B}\right) \tag{3.3.4}$$

where R_i values are the bond lengths, in this case Mn2-O bond lengths, summed for all bonds in a given octahedra, R_0 is a tabulated parameter giving the bond length when the element i has a valence of exactly 1, and B is an empirical constant, in this case 0.37. In Figure, Mn2 bond valence sums for adjacent cells along the c axis are plotted, and can be directly compared to the variation in bond lengths and orbital occupation shown above.

Mn2 bond valence is closest to the expected value of 3+ at nodal points of the modulation, where the $d_{x^2-y^2}$ orbital is occupied. In Figure 3.19, the bond valences have

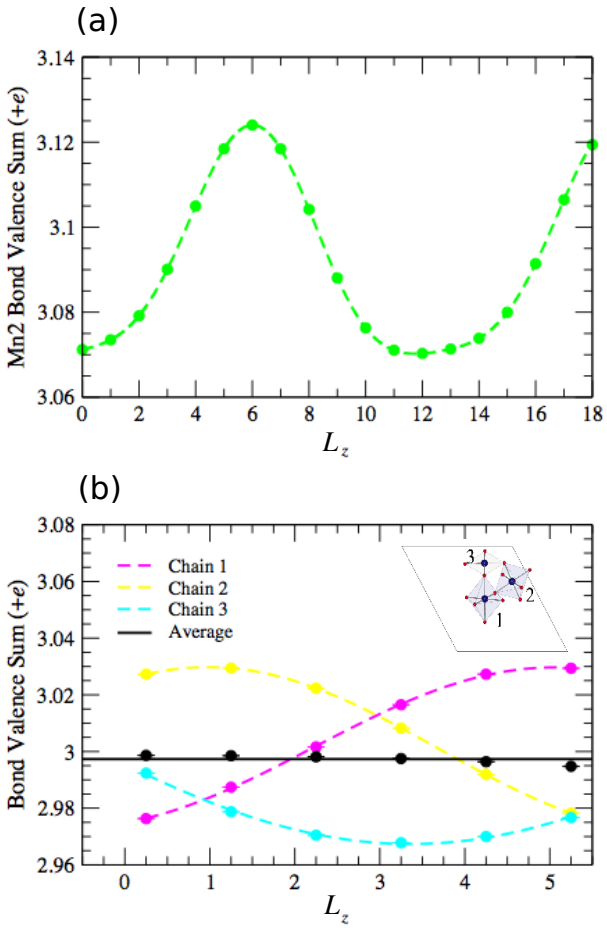


Figure 3.19: Adapted from Ref. [73]. (a) Estimated variation in Mn2 bond valence for a chain along the c axis, calculated using Eq. (3.3.4). (b) Average Mn1/Mn2 bond valence, plotted for three different nearest neighbour c axis chains (yellow, pink and blue), along with the total average charge (black), which is approximately constant at 3+, as expected.

been averaged for successive Mn1/Mn2 pairs along the three symmetrically inequivalent c axis chains, as shown in the Figure inset. Taking the average of these three chains, for any given c value, gives a constant valence of 3+, as expected.

Overall, bond valence fluctuations are small ($\sim 1\%$) and could be an artefact of the refined model not accounting for modulation of thermal parameters. This indicates that the structural modulation primarily manifests as orbital variation, in agreement with refinement tests made to determine whether charge or atomic position modulation produced a better fit to the diffraction data.

3.3.3 Magnetic coupling - the magneto-orbital Helix

Having characterised the structural modulation emerging below T_{OO} as an unprecedented "orbital helix", this section considers how this relates to the incommensurate magnetic modulation [75, 89, 79], that emerges with relationship $q_c = 2q_m$ below T_{N1}. This relationship in not uncommon in magnetically ordered crystals, but in the present case, the structural modulation is also present in the paramagnetic phase, with a "locking in" of the magnetic modulation below T_{N1}.

In fact, the orbital ordering outlined has a profound effect on magnetic ordering below T_{N1}, as explained below:

Goodenough-Kanamori-Anderson (GKA) [39, 40, 41, 42] rules predict the nature of magnetic exchange interactions based upon electron transfer between overlapping orbitals, which is dependent upon the bond length and bond angles between magnetic ions. The key results applicable here for two magnetic (Mn) cations interacting via a non-magnetic (oxygen) ligand are summarised below:

- If both cations have half filled or vacant orbitals exchange will be $antiferromagnetic$.
- If one cation has a filled orbital whilst the other is half filled, exchange will be $ferromagnetic$.
- If one cation has a half filled or filled orbital whilst the other is vacant, exchange can be antiferromagnetic but generally favours ferromagnetism.
- When multiple interactions are present simultaneously, antiferromagnetic exchange is generally dominant.

In the average structure of $CaMn_7O_{12}$, which is heavily distorted, simple GKA rules are complicated by strong deviation of Mn-O-Mn bond angles from 180° which weakens antiferromagnetic interactions. Alternation of half filled and empty $d_{x^2-y^2}$ orbitals on Mn2 and Mn3 sites both within and between triangular A, B and C layers promotes ferromagnetic exchange, and a net ferromagnetic structure is predicted.

This situation changes drastically in the presence of the structural modulation, since the orbitals that mediate magnetic exchange between the A, B and C layers are those that are most affected by the modulation. In Figure 3.20, a region of the crystal in which the modulation amplitude is at its greatest is shown:

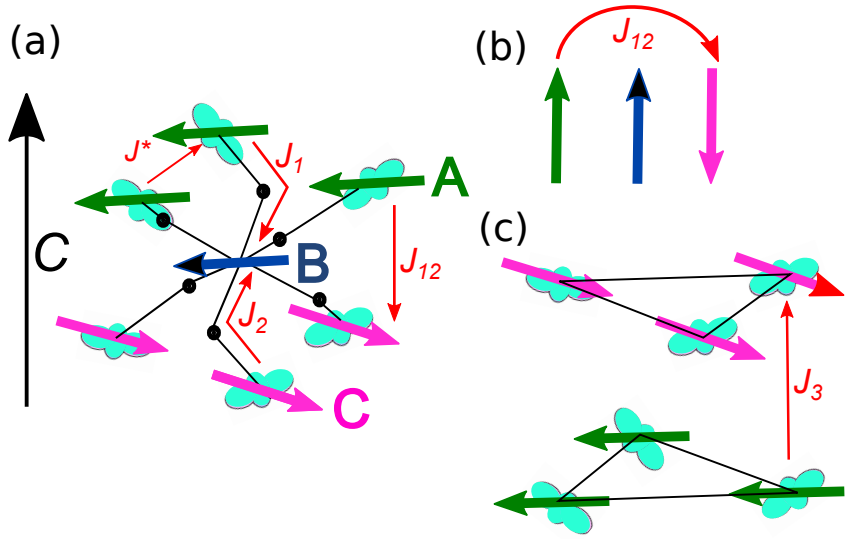


Figure 3.20: (a) The interaction between filled Mn2 orbitals (layer A) and vacant Mn3 orbitals (layer B) leads to ferromagnetic J_1 exchange, whilst interaction between vacant Mn2 (layer C) and Mn3 (layer B) orbitals leads to antiferromagnetic J_2 exchange, thus J_{12} is antiferromagnetic, as shown in (b). The overall nearest neighbour interaction between layers J_3 is experimentally observed to be antiferromagnetic.

Mn3 sites with vacant d orbitals in the B layer are connected to Mn2 sites with filled $d_{x^2-y^2}$ orbitals in the A layer, leading to ferromagnetic exchange (J_1). These same Mn3 sites are also connected to Mn2 sites with vacant $d_{x^2-y^2}$ in the C layer, leading to antiferromagnetic exchange (J_2). Crucially, in the absence of a structural modulation, J_1 and J_2 would be equal. Since all J_1 and J_2 interactions are equivalent by symmetry, an effective ferromagnetic exchange within each of the A, B and C layers is generated. The next-nearest neighbour interaction across layers (J_{12}) is antiferromagnetic, being strongest at the crest of the modulation, but remaining antiferromagnetic everywhere, except possibly at the nodal point. The overall nearest neighbour interaction between layers J_3 results from two competing interactions: ferromagnetic interactions from full-empty $(x-y)$ orbitals, and antiferromagnetic interactions from empty-empty $(y-z)$ orbitals. The sign of J_3 cannot be predicted directly from

Goodenough-Kanamori-Anderson rules, but has been experimentally observed to be positive (antiferromagnetic). The combination of antiferromagnetic nearest neighbour and next nearest neighbour interactions leads to magnetic frustration, and results in a helical magnetic structure propagating along the c axis with spins in adjacent triangular layers rotated with respect to one another. This is in good agreement with the magnetic structure determined from neutron powder diffraction, which found an incommensurate magnetic modulation with an angle of 124° between adjacent layers [79].

To summarise, this analysis, based upon semi-empirical GKA rules, predicts a helical magnetic structure resulting from the orbital helix described in section 3.17. This hypothesis, can be tested using a simple model, which incorporates the average effect of interactions J_1, J_2 and J_3, assumes a magnetic propagation vector (0, 0, q_m) and approximates identical spins S on Mn2 and M3 sites. The magnetic Heisenberg exchange energy for this model per Mn3 site can be written as [73]

$$E = S^2[3J_1\cos\phi + 3J_2\cos(\phi - 2\psi) + 6J_3\cos\psi] \tag{3.3.5}$$

where $\psi = \frac{2}{3}\pi q_m$, and ϕ are the angles between Mn2-Mn2 and Mn3-Mn2 spins in adjacent layers. Minimising this energy as a function of ψ and ϕ for different exchange constants results in the phase diagram shown in Figure 3.21. The two commensurate phases (CM1 and CM2) have $q_m = 1.5$. Within the incommensurate phase (ICM), the yellow line indicates the range of exchange parameters for which q_m is the experimentally observed value of (0, 0, 1.037), and the green dot indicates the magnetic structure determined experimentally from neutron powder diffraction. For this experimentally observed structure, $\frac{J_2}{J_1}$ = -0.85 and $\frac{J_3}{J_1}$ = -0.63, giving good agreement to the qualitative considerations based upon GKA rules described above.

The conclusion from the analysis above is that the helical, incommensurate magnetic structure emerging below T_{N1} results as a direct consequence of orbital ordering. This overall coupled orbital and magnetic ordering can be termed a "magneto-orbital helix".

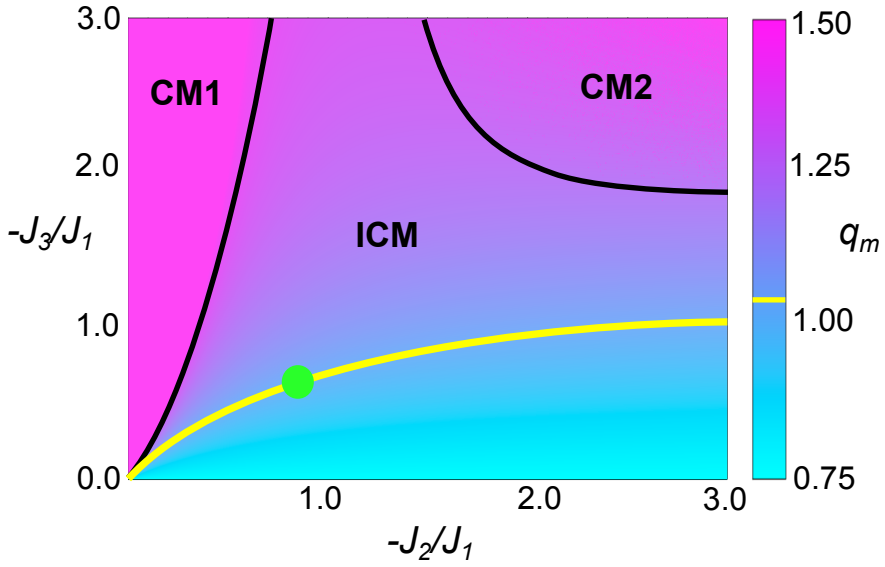


Figure 3.21: Phase diagram for the magnetic structure of $CaMn_7O_{12}$ obtained from minimisation of the Heisenberg exchange energy in Eq. (3.3.5). Two commensurate collinear phases with $q_m = 1.5$ bound the incommensurate phase with a helical magnetic structure. The yellow curve indicates the points for which $q_m = (0, 0, 1.037)$, and the green dot indicates the experimentally determined magnetic structure, corresponding to exchange constants in agreement with those obtained through consideration of GKA rules.

It was discussed in section 1.3.1.3 that helical magnetic structures can give rise to a ferroelectric polarisation through ferroaxial coupling to a global structural rotation [43]. Having characterised the emergence of a magnetic helix below T_{N1} in $CaMn_7O_{12}$, the following section considers why the onset of this magnetic helix coincides with the emergence of a polarisation.

3.3.4 The ferroelectric polarisation

Below T_{N1}, $CaMn_7O_{12}$ acquires a polarisation of $P = 2870\ \mu Cm^{-2}$ [79]. Since the symmetry of $CaMn_7O_{12}$ is the ferroaxial point group $\bar{3}$, this polarisation can result from coupling between the magneto-orbital helix and a global rotation between different elements of the crystal structure (see section 1.3.1.3 [43]).

In the incommensurately modulated crystal structure of $CaMn_7O_{12}$ refined in section 3.3.1, the six oxygen anions that surround a given Mn3 site are all rotated in the same

direction. This rotation can be described by the axial vector **A**, and couples to the spin rotation which is clockwise between layers A and B , and anticlockwise between layers B and C, shown in Figure 3.22.

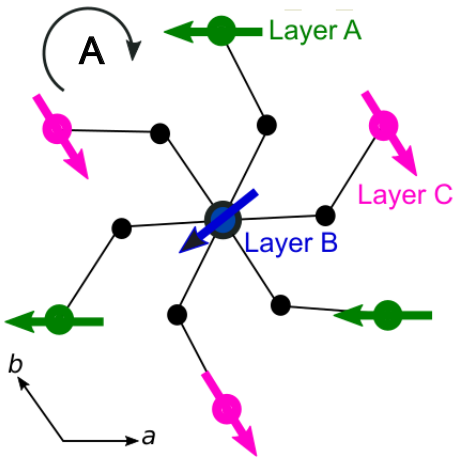


Figure 3.22: Adapted from Ref. [73]. The global structural rotation in $CaMn_7O_{12}$, described by the vector **A**, evident in the rotation of oxygen anions shown in black.

The magnetic helix derived in section 3.3.3 has an associated chirality (σ), and conditions are fulfilled for a phenomenological invariant coupling an electrical polarisation; $\alpha\sigma\mathbf{A}\cdot P$, where α is a coupling constant. The chirality of the magnetic helix can be reversed by a global rotation of all of the spins, and therefore two possible domains with equal symmetric exchange energy exist, related by inversion symmetry.

The microscopic coupling between the magnetic helicity and ferroelectric polarisation can be understood in terms of antisymmetric DM exchange. Both electronic and structural distortions can play a role (see section 1.3.1.1), but here structural distortions are considered. Below T_{N1} non-collinear Mn2 and Mn3 spins ($\boldsymbol{S_i}$ and $\boldsymbol{S_j}$) are connected through oxygen ligands, by a vector $\mathbf{r}_{ij}$, as shown in Figure 3.24. DM exchange favours displacements of these ligands through a vector **u**, resulting in an energy change:

$$\Delta E = \lambda\mathbf{u}\cdot[\mathbf{r}_{ij}\times(\boldsymbol{S_i}\times\boldsymbol{S_j})] = \lambda\mathbf{D}\cdot(\boldsymbol{S_i}\times\boldsymbol{S_j}), \tag{3.3.6}$$

where

$$\mathbf{D} = \mathbf{u} \times \mathbf{r}_{ij}. \tag{3.3.7}$$

In the case of $CaMn_7O_{12}$, energy is minimised by a pattern of local oxygen displacements associated with pairs of spins, either parallel or antiparallel to the vectors $\mathbf{r}_{ij} \times (\boldsymbol{S_i} \times \boldsymbol{S_j})$, depending on the sign of λ. Assuming $\lambda < 0$, the DM interaction will favour oxygen displacements parallel to the red arrows shown in Figure 3.23.

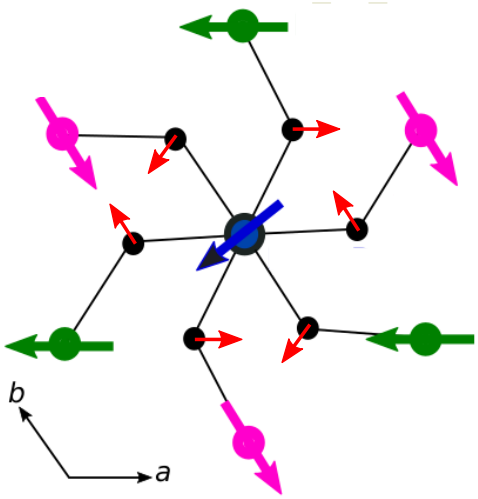


Figure 3.23: The pattern of $\mathbf{r}_{ij} \times (\boldsymbol{S_i} \times \boldsymbol{S_j})$ vectors (red arrows) for Mn2-O-Mn3 bonds. Depending upon the sign of λ the DM interaction will favour displacement of oxygen anions parallel or antiparallel to these vectors.

The combined effects of these displacements is to flatten the bonds between layer B (Mn3 sites) and layer C (Mn2 sites), increasing Mn-O-Mn bond angles closer to 180°. Simultaneously, the Mn-O-Mn bond angles between layer A (Mn2) and layer B (Mn3) decrease. The central Mn3 site in layer B is effectively displaced in the positive c direction by these two effects, creating a local polarisation along c.

Identical consideration for the case of $\lambda > 0$ would lead to a polarisation along the negative c direction. Since the magnetic structure described in section 3.3.3 is globally chiral, local polarisations per Mn3 site will sum to give a net overall polarisation P.

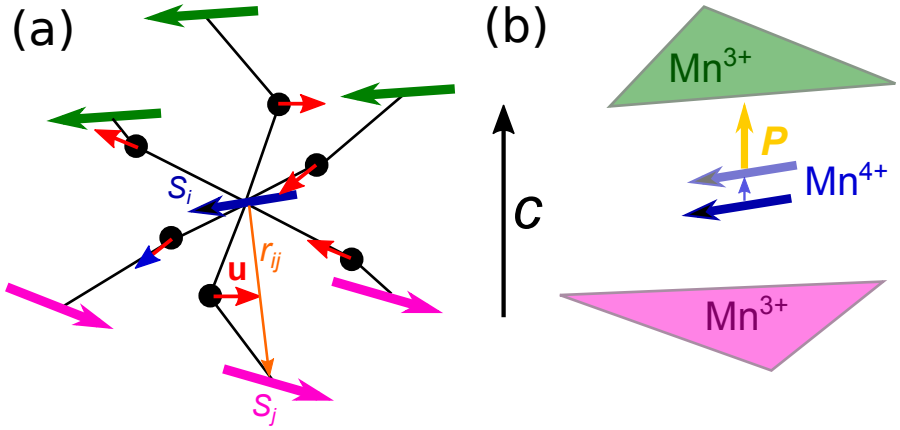


Figure 3.24: (a) The effect of oxygen displacements parallel to $\mathbf{r}_{ij} \times (\boldsymbol{S_i} \times \boldsymbol{S_j})$ vectors. The Mn-O-Mn bond angle between layers A (green) and B (blue) decreases, whilst that between layers B and C increases. (b) This effectively displaces the Mn^{4+} cation leading to a polarisation along c.

In the absence of a global structural rotation, the Mn-O-Mn bonds connecting triangular layers would be 180° and no net polarisation would result. Ferroaxial coupling is thus an essential ingredient for the development of a net polarisation in $CaMn_7O_{12}$. The magnetic chirality determines the direction of P, which can lie in either direction along the high symmetry axial vector, resulting in a switchable 2 domain structure. Under the application of an electric field, the chirality of the magnetic helix will switch, but the axial vector **A** will remain unchanged.

The large magnitude of P observed for $CaMn_7O_{12}$ is explained by considering the angle of rotation (ϕ) between the spins $\boldsymbol{S_i}$ and $\boldsymbol{S_j}$. This angle is determined by competing antiferromagnetic nearest and next nearest neighbour interactions (J_3 and J_{12}) between spins in adjacent layers. As explained in section 3.3.3, this leads to magnetic frustration, and a non-collinear spin arrangement along the c axis. From the experimentally determined magnetic structure, the average angle of rotation is $\langle\phi\rangle = 124°/2 = 62°$ (see section 3.1.3). In contrast, in multiferroic $TbMnO_3$, $\langle\phi\rangle$ between Mn spins is 200°. P is expected to be approximately proportional to $\sin\phi$, and thus it is predicted that the magnitude of P for $CaMn_7O_{12}$will be ∼5 times that of $TbMnO_3$.

It is the rotation angle between spins along the hexagonal c axis that determines

the large value of the magnetically induced polarisation in $CaMn_7O_{12}$. The small deviation from incommensurability in the magnetic propagation vector is not crucial, and the value of P would be almost as large if the magnetic propagation vector was exactly (0, 0, 1).

3.4 Conclusions

To conclude this chapter, combining knowledge of the magnetic structure and polarisation in $CaMn_7O_{12}$ with new x-ray diffraction data, the microscopic coupling mechanism leading to a magnetically induced ferroelectric polarisation has been uncovered. Crucial to understanding this mechanism was the observation and interpretation of satellite peaks in the x-ray diffraction data corresponding to a structural modulation. Whilst it transpires that the incommensurability of this modulation is not a vital ingredient for the development of a polarisation, refinement of modulated atomic displacements and interpretation in terms of orbital ordering is key to understanding how the inhomogeneous magnetic structure in $CaMn_7O_{12}$ develops, and how structural and magnetic parameters couple to generate a magnetically switchable polarisation.

As discussed in section 3.1.1 orbital ordering has theoretically been considered as a promising ingredient for multiferroicity, for example, in quarter and half doped manganites, although this is yet to be experimentally realised. The study presented here is novel in that orbital occupation does not select a fixed orientation, but rotates, leading to an unprecedented "orbital helix" structure. This specific pattern of orbital occupation has strong implications for dictating the magnetic structure, and is crucial in stabilising the chiral magnetic helix, leading to intertwined magnetic and structural modulations in the form of a "magneto-orbital helix".

Whilst the polarisation observed in $CaMn_7O_{12}$ is one of the largest magnetically induced ferroelectric polarisations observed to date, it is still several orders of magnitude smaller than that observed for typical proper ferroelectrics. Similarly, whilst 90 K is a high onset temperature for magnetically induced ferroelectricity, there is

clearly progress to be made to achieve technologically useful multiferroics that will be functional close to ambient conditions. In Chapter 4, the possibilities to tune the multiferroic properties of $CaMn_7O_{12}$ through copper doping are explored.

Chapter 4

$\mathbf{CaCu_{0.15}Mn_{6.85}O_{12}}$

4.1 Introduction

4.1.1 Motivation for studying $\mathbf{CaCu_{0.15}Mn_{6.85}O_{12}}$

As discussed in section 1.3.2, an overriding goal in the characterisation of multiferroic materials is to uncover systems that are not only physically novel and interesting, but that have technological potential, requiring large, strongly coupled polarisations with high onset temperatures. $CaMn_7O_{12}$ improves significantly on many previously discovered systems, and results presented in Chapter 3 highlight an unprecedented rotating orbital occupation as a means of coupling magnetic and structural order parameters, enabling the development of a ferroelectric polarisation with strong magneto-electric coupling. This chapter considers the possibility of tuning physical properties in the $CaCu_xMn_{7-x}O_{12}$ series, specifically focusing on $CaCu_{0.15}Mn_{6.85}O_{12}$. Doping may provide a handle on orbital ordering and magnetic coupling, and may give insight into both the underlying driving force behind the incommensurate structural modulation in $CaMn_7O_{12}$.

4.1.2 The impact of copper doping

Previous studies have already established that low levels of copper doping can have profound effects on the physical properties of the $CaCu_xMn_{7-x}O_{12}$ solid solution, for

example, leading to a substantial increase in magneto-resistance [90].

Cu^{2+} cations substitute on the Mn1 positions up to a potential maximum doping level of $x = 3$. With increasing copper content, the ratio of Mn^{4+} to Mn^{3+} cations increases. Given that the incommensurate modulation in $CaMn_7O_{12}$ manifests primarily as a periodic variation in orbital occupation of Jahn-Teller distorted $Mn^{3+}O_6$ octahedra, it is expected that the introduction of copper may impact the orbital helix, supressing orbital ordering for higher doping levels. This in turn, would have implications for the magnetic modulation.

X-ray powder diffraction studies of $CaCu_xMn_{7-x}O_{12}$ with $x = 0.1$ and $x = 0.23$ found that for $x = 0.1$ a similar structural modulation to that observed for $CaMn_7O_{12}$ emerges below T_{OO}, with a slightly different propagation vector of (0, 0, 0.904) at 150 K, but similar bond length variations to those observed in $CaMn_7O_{12}$, most likely corresponding to the same orbital modulation [75]. For $x = 0.23$, no satellite peaks could be resolved during a synchrotron experiment, suggesting that orbital modulation is indeed suppressed for higher doping levels. In neutron powder diffraction experiments, magnetic satellite peaks have been observed for $x = 0.1$, and conform to the expected relationship of $q_m = \frac{1}{2}q_c$ (see section 3.3.3) [75]. The absence of structural satellites for $x = 0.23$ may be expected to coincide with the absence of a magnetic helix. However, magnetic satellites with the same, q_m propagation vector have been observed below a slightly suppressed Néel temperature of 78.1 K for $x = 0.23$ samples. This raises questions as to how orbital order dictates the magnetic structure and couples the the magnetism to the global structural rotation.

In this chapter, the effect of copper doping has been explored through structural investigations of $CaCu_{0.15}Mn_{6.85}O_{12}$. Compositional studies using SEM and EDX spectroscopy have been used to determine accurate knowledge of crystal composition of a series of doped samples. Satellite peaks corresponding to incommensurate modulations have been identified in single crystal X-ray diffraction experiments, and have prompted the investigation of a series of possible structural models, through analysis of x-ray diffraction data and synchrotron experiments.

4.2 Crystal Characterisation

4.2.1 Preliminary x-ray diffraction

Single crystals of $CaCu_xMn_{7-x}O_{12}$ with nominal compositions $x = 0.1$, 0.2, 0.3, 0.4, 0.5 and 0.6 were grown in Oxford [1] using the flux method described in section 3.2.1.

Single crystal x-ray diffraction measurements using SuperNova were performed at room temperature and 85 K for crystals in each batch. At room temperature, all crystals showed sharp well defined Bragg peaks that could be indexed in the expected $R\bar{3}$ unit cell with lattice parameters similar to those found for $CaMn_7O_{12}$ ($a = b =$ 10.416(14) Å, $c = 6.4(10)$ Å for $x = 0.3$). Example diffraction planes for $x = 0.1$ and $x = 0.6$ are shown in Figure 4.1(a) and (b). No evidence for phase separation or twinning was observed. At 85 K crystals with $x = 0.1$ show satellite peaks bearing close resemblance to those observed for $CaMn_7O_{12}$ (Figure 4.1(c)). These peaks can be indexed with propagation vector $q_c = (0, 0, 2.087)$. In agreement with the results of previous studies (see section 4.1.2), satellites cannot be observed at 85 K for crystals with nominal composition $x = 0.5$ and $x = 0.6$ (Figure 4.1(d)).

For samples with nominal composition $x = 0.3$ - 0.5, room temperature diffraction patterns can be indexed in the $R\bar{3}$ lattice, as shown in Figure 4.2(a) conforming with the expected trend of slightly decreasing lattice parameters with increasing x. Previous studies have found that satellite peaks should not be observed at 85 K for x>0.23. In contrast, as shown in Figure 4.2(b), in addition to sharp Bragg peaks, multiple sets of satellite peaks can be observed in the kl plane, some of which can be indexed with a similar propagation vector to that observed for $CaMn_7O_{12}$, with $q_c =$ (0, 0, 2.087).

Given the contrast in this observation to previous studies of $CaCu_xMn_{7-x}O_{12}$ samples

[1] Crystals were grown by D. Prabhakaran, Clarendon Laboratories, University of Oxford, Oxford

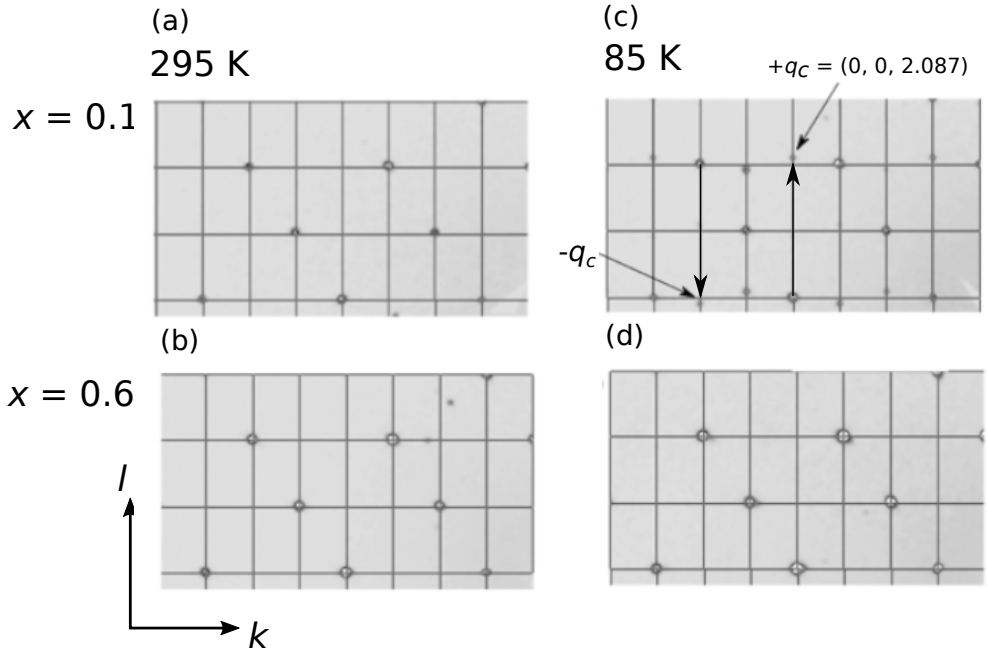


Figure 4.1: kl lattice planes obtained from single crystal x-ray diffraction using SuperNova. (a) Room temperature data for $x = 0.1$ and (b) 0.6, indicating sharp Bragg peaks indexed in the $R\bar{3}$ cell. (c) 85 K data for $x = 0.1$ shows satellite peaks that can be indexed with propagation vector (0, 0, 2.087) (d) for x = 0.6, these satellite peaks cannot be observed.

with $x = 0.23$, this result prompted more thorough analysis of the composition, quality and homogeneity of these samples, using scanning electron microscopy experiments (SEM), as outlined below.

4.2.2 SEM microscopy

SEM experiments were performed using a JEOL6480 SEM equipped with an 80 × 80 mm^2 EDX area detector. For samples with nominal compositions $x = 0.1$, 0.3 and 0.6, several crystals that had been cleaned and polished were mounted on carbon coated pucks.

As described in section 2.1, characteristic x-rays generated from inelastic scattering between the beam and sample were recorded by the detector, and plotted in a spectrum of counts versus x-ray energy. Using these spectra in conjunction with backscattered

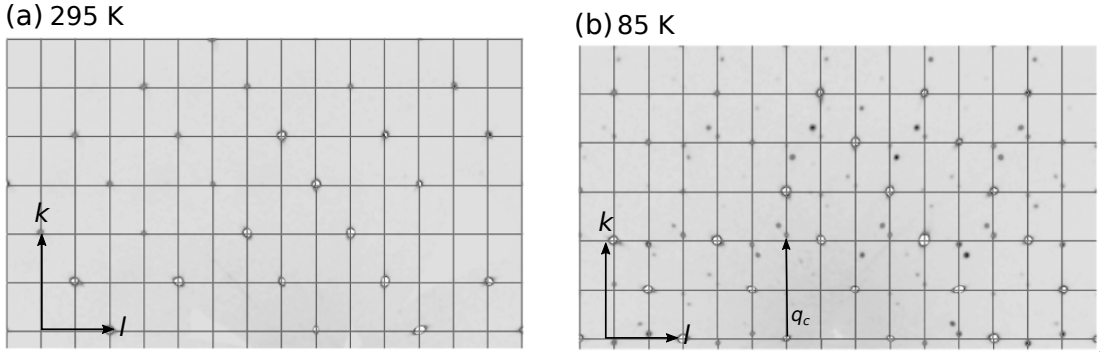


Figure 4.2: (a) Room temperature kl lattice planes for a sample with nominal composition $x = 0.3$, showing sharp Bragg peaks and no evidence of twinning. (b) Upon cooling to 85 K, multiple sets of satellite peaks emerge, some with propagation vector $q_c = (0, 0, 2.087)$, similar to that observed in $CaMn_7O_{12}$.

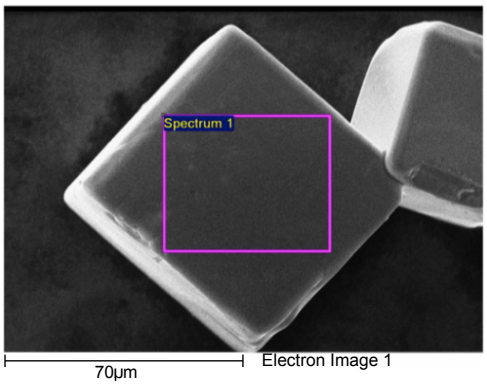
electron signals, the atomic percentage of each element present was recorded for specific points/areas on the sample surface. This gave the relative proportions of each element, which were converted into sample compositions using samples of $CaMn_7O_{12}$ as standards, scaling to obtain a stoichiometric carbon content. Detected carbon was attributed to air impurities and was eliminated from calculations.

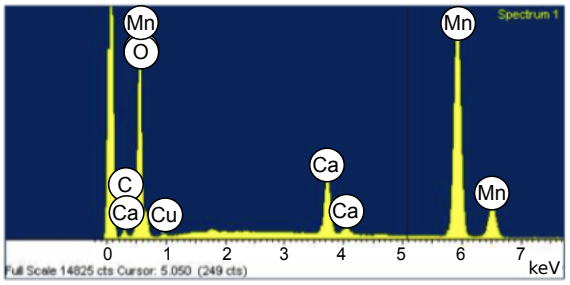
Example measurements for a sample with nominal composition $x = 0.1$ are shown in Figure 4.3. Topographic images of the surface were generated from secondary electron signals, and backscattered electron signals were used to attribute the EDX signals to lateral positions on the sample surface. Figure 4.3(a) shows a spectrum averaged over an area of the crystal, whereas (b) is measured for a specific point on the surface.

For each crystal, the composition was averaged for all points and areas measured on the surface, and at least two crystals were measured for each nominal composition. Results are shown in Table 4.1.

Whilst the calculated compositions for low doped ($x = 0.1$) and high doped ($x = 0.6$) are approximately as expected, crystals that are expected to have moderate doping levels ($x = 0.3$) in fact have a significantly lower doping, approximately $x = 0.15$. This compositional difference could explain the observation of structural satellites at 85 K for these crystals. Sławiński *et al.* observed structural satellites for crystals $x = 0.1$, and found that satellites could not be observed for samples with $x = 0.23$, but

(a) $x = 0.1$ Area signal (b)

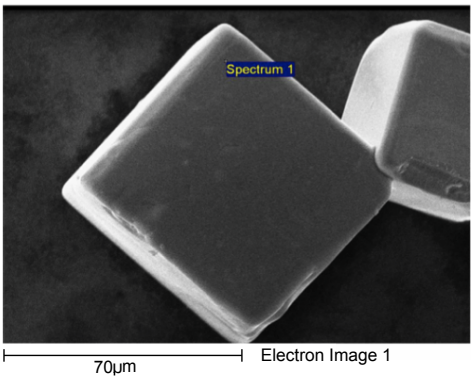


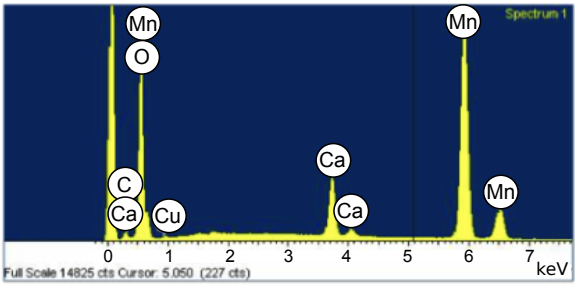


Element	Weight %	Atomic %
C K	2.96	6.88
O K	34.73	60.46
Ca K	6.00	4.17
Mn K	55.39	28.09
Cu K	0.92	0.40
Totals	100.00	

$Ca_1Cu_{0.096}Mn_{6.736}O_{14.499}$

(c) $x = 0.1$ Point signal (d)





Element	Weight %	Atomic %
C K	4.06	9.24
O K	34.74	59.31
Ca K	5.88	4.01
Mn K	54.45	27.07
Cu K	0.87	0.38
Totals	100.00	

$Ca_1Cu_{0.095}Mn_{6.751}O_{14.790}$

Figure 4.3: Compositional analysis of a $CaCu_xMn_{7-x}O_{12}$ sample with nominal composition $x = 0.1$. Two EDX spectrums were recorded, one averaged over an area (a) and (b) and one for a specific point on the surface (c) and (d). The region of the crystal being measured is indicated on the secondary electron topographic maps shown in (a) and (c).

did not measure a crystal with $x = 0.15$.

Closer examination of backscattered electron signals and secondary electron topographic images of samples with $x = 0.15$ highlighted small impurity regions, as shown in Figure 4.4. Backscattered electron signals indicated that these may be low calcium regions. These impurity regions occupy a very small proportion of the overall crystal

Expected x	Sample no.	Ca	Cu	Mn	O
0	1	1	0	6.796	16.264
	2	1	0	6.674	17.972
0.1	1	1	0.096	6.736	14.499
	2	1	0.095	6.751	14.790
0.3	1	1	0.142	6.634	14.499
	2	1	0.156	7.363	16.921
0.6	1	1	0.596	5.877	15.590
	2	1	0.529	6.262	11.240

Table 4.1: Calculated compositions for $CaMn_7O_{12}$ and $CaCu_xMn_{7-x}O_{12}$ samples with nominal compositions of $x = 0$, 0.1, 0.3, and 0.6. Compositions were calculated assuming stochiometric calcium content. For each sample, the composition given is taken from the average of several points/surfaces on the sample surface. Significant deviation from nominal composition is observed for $x = 0.3$ samples.

volume and are unlikely to have a significant impact on x-ray diffraction results. Apart from these small impurity regions, all samples measured appeared homogenous.

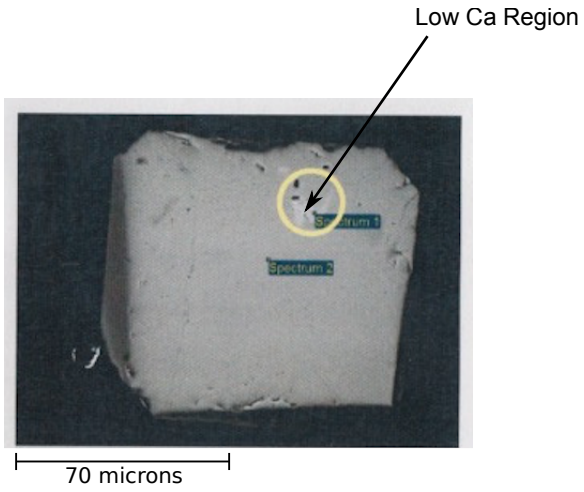


Figure 4.4: A possible low Ca impurity region in a crystal of $CaCu_{0.15}Mn_{6.85}O_{12}$, discovered through analysis of backscattered electron signals combined secondary electron topographic imaging.

From this batch, two specific crystals were selected for use in further X-ray diffraction studies. The composition of both of these crystals was analysed in detail using point scans at 5μm intervals, in addition to square area scans. On this length scale, both crystals appeared homogeneous, with no evidence of phase separation. The compositions for the two crystals, averaged over the point and areas scans, were measured as $x = 0.149 \pm 0.007$ (crystal 1) and $x = 0.140 \pm 0.009$ (crystal 2).

The appearance of multiple sets of satellite peaks in preliminary x-ray diffraction data for these samples prompted further x-ray diffraction studies, which will be outlined below.

4.3 Results

4.3.1 Single crystal x-ray diffraction on $CaCu_{0.15}Mn_{6.85}O_{12}$ SuperNova experiment

4.3.1.1 Collection of satellite peak intensities

Using SuperNova, a room temperature, single crystal x-ray diffraction experiment was performed using Crystal 1. As expected, more than 98% of Bragg peaks could be indexed in the hexagonal $R\bar{3}$ cell with $a = b = 10.421(2)$ Å, $c = 6.3811(12)$ Å, and satellite peaks could not be observed. Measurements made at 150 K and 85 K, collecting over a large region in reciprocal space, revealed multiple sets of satellite peaks, as observed in section 4.2.1. Tests at temperatures just below and above T_{OO} = 250 K revealed that satellite peaks could be weakly observed below T_{OO} but could not be detected above T_{OO}

Four sets of satellites can be indexed, as shown in Figure 4.5 below. The satellites labelled q_c in Figure 4.5(a) bear close resemblance to those observed for $CaMn_7O_{12}$, whilst the remaining three sets appear to be related by 3-fold symmetry. This can be seen more clearly by taking a hk slice in reciprocal space at an l value of 0.698, as shown in Figure 4.5(b).

Using CrysAlisPRO, the four sets of satellites were indexed, constraining q_1, q_2 and

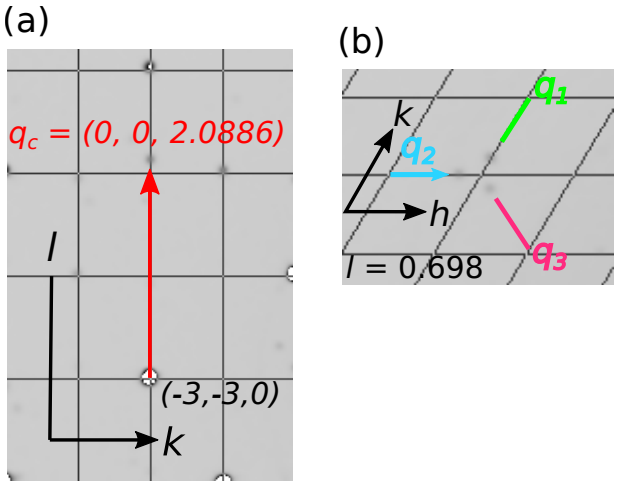


Figure 4.5: (a) A satellite peak with propagation vector q_c in $CaCu_{0.15}Mn_{6.85}O_{12}$, bearing a strong resemblance to satellite peaks corresponding to an orbital modulation in $CaMn_7O_{12}$. b) Three additional sets of satellites, related by 3-fold symmetry, evident in a reciprocal space slice taken at $l = 0.698$.

q_3 to be related by 3-fold symmetry:

$$\begin{aligned} q_c &= (0, 0, 2.0886 \pm 0.0019), \\ q_1 &= (0, \delta, \tau), \\ q_2 &= (-\delta, 0, \tau), \\ q_3 &= (\delta, -\delta, \tau), \end{aligned} \tag{4.3.1}$$

where $\delta = 0.206 \pm 0.002$ and $\tau = 0.698 \pm 0.002$.

Whilst the satellites indexed by q_c appear to correspond to a very similar modulation as that developed for $CaMn_7O_{12}$ in Chapter 3, the physical interpretation of satellites corresponding to q_1, q_2 or q_3 is not immediately apparent. The four propagation vectors may be related, with $q_c = q_1 + q_2 + q_3$. Four different scenarios could explain the appearance of four families of satellites, outlined as four structural models below:

1. The 1-q model: Crystals of $CaCu_{0.15}Mn_{6.85}O_{12}$ become multi-domain below T_{OO}. A single propagation vector q_c exists in some parts of the crystal whilst either q_1, q_2 or q_3 exist in three additional domains, giving rise to the appearance of four propagation vectors.

2. The 2-q model: Three domains exist in the crystal below T_{OO}, each domain simultaneously incorporating two modulations, described by q_c and one of the $q_1/q_2/q_3$ propagation vectors.

3. The 1+ 3-q model: Two domains exist below T_{OO}, one with a modulation described by q_c, and the other with three simultaneous modulations described by q_1, q_2 and q_3.

4. The 4-q model: Below T_{OO} $CaCu_{0.15}Mn_{6.85}O_{12}$ remains single domain, and incorporates four modulations described by q_c, q_1, q_2 and q_3.

As will be explored in section 4.3.3.4, the 1-q model provides the simplest explanation for the observed satellites, incorporating four twins in the $R\bar{3}$ phase with c axes corresponding to the four cubic diagonals in the high temperature $Im3$ phase. This model provides the best fit to SuperNova X-ray diffraction data. However, this result was not immediately apparent, and was not automatically assumed given the absence of evidence for twinning in samples of $CaMn_7O_{12}$, and difficulty in observing twins in the diffraction data, due to the very small rhombohedral distortion in the crystal. As discussed in section 4.3.2.1, synchrotron single crystal x-ray diffraction data obtained at I16 indicated a distinction between q_c satellites and those indexed by q_1, q_2 and q_3 and did not show evidence for a domain structure. Thus in the analysis below, all four models are tested against experimental data.

Firstly, satellite peaks indexed with propagation vector q_c are analysed.

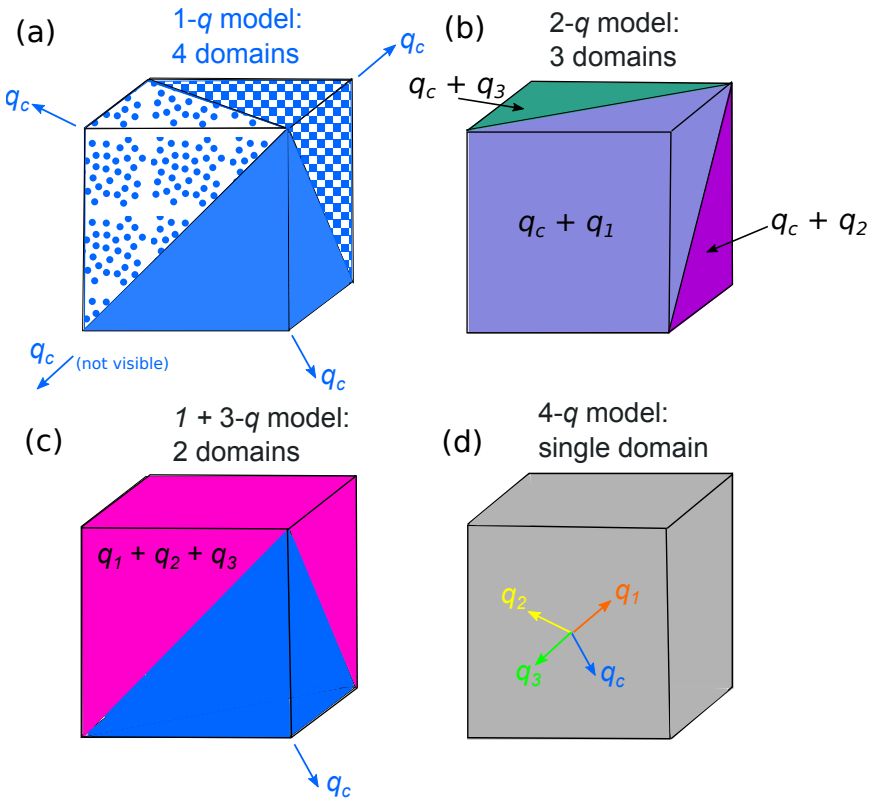


Figure 4.6: (a) In the 1-q model, each domain encompasses the same propagation vector in a different orientation. (b) in the 2-q model each domain encompasses q_c and one additional new propagation vector (c) Two domains exist, one encompassing q_c as observed for $CaMn_7O_{12}$, and the other incorporating three new modulations (d) an unprecedented 4-q, single domain model.

4.3.1.2 Refinement of the q_c propagation vector

The strong similarity of these satellite peaks to those observed for $CaMn_7O_{12}$ suggest that these satellites are likely to correspond to the same incommensurate structural modulation, which manifests as a rotating orbital occupation. For completeness, a model has been refined using JANA2006 [84].

85 K diffraction data for crystal 1 was used for refinement, using lattice parameters of $a = b = 10.416(14)$ Å, $c = 6.400(10)$ Å obtained from CrysAlis PRO. Using the same refinement procedure as for $CaMn_7O_{12}$ (see section 3.3.1), initially a model for the average structure was refined against the Bragg peak intensities, with the model incorporating $R\bar{3}$ symmetry atomic positions, occupancies and unit cell parameters. The

average structure was based upon $CaMn_7O_{12}$, but with 5% Cu^{2+} cations substituted on the Mn1 site. Allowing average oxygen positions, extinction (type I Lorentzian), isotropic thermal parameters and overall scale to refine, a converged fit with an R-factor of ∼9% was obtained. Fixing the average structure, a model for the modulation was included in the refinement, using a propagation vector of q_c = (0, 0, 2.0886 ± 0.0019) obtained from CrysAlis PRO, and adapting the symmetry to space group $R\bar{3}(00\gamma)00$ (see section 3.3.1 and Appendix C).

Given the similarities of these satellite peaks to those observed for $CaMn_7O_{12}$, the initial model for the modulation was based upon the same sinusoidal position modulation on each atomic site, with modulated fractional coordinates defined by

$$\begin{aligned} x_{mod}(\bar{x}_{qc}) &= x_0 + A_x\sin(2\pi\bar{x}_{qc}) + B_x\cos(2\pi\bar{x}_{qc}) + l_x, \\ y_{mod}(\bar{x}_{qc}) &= y_0 + A_y\sin(2\pi\bar{x}_{qc}) + B_y\cos(2\pi\bar{x}_{qc}) + l_y, \\ z_{mod}(\bar{x}_{qc}) &= z_0 + A_z\sin(2\pi\bar{x}_{qc}) + B_z\cos(2\pi\bar{x}_{qc}) + l_z, \end{aligned} \tag{4.3.2}$$

where

$$\bar{x}_{qc} = \mathbf{q}_c \cdot \mathbf{r}_0 = q_z \cdot (z_0 + l_z), \tag{4.3.3}$$

x_{mod}, y_{mod}, z_{mod} and x_0, y_0, z_0 are the modulated and unmodulated x, y, z coordinates respectively, A and B are the Fourier coefficients of the modulation amplitude and l is an integer value defining the unit cell. Initially, the parameters x_0, y_0, z_0,A and B were taken from the refinement of $CaMn_7O_{12}$, but all values were then allowed to freely refine within symmetry constraints. A stable, reproducible refinement converged, and it was found that repeatable results could be produced using random starting coefficients for A and B. A slight improvement in the refinement was obtained through the use of anisotropic thermal parameters. Completing a full refinement of Bragg and satellite peaks against the modulated structure produced a converged refinement with an R-factor of ∼17% (∼9% for Bragg peaks and ∼23% for satellite peaks). As with $CaMn_7O_{12}$, a stable refinement could not be generated by incorporating occupancy or charge modulations.

The structural parameters for the modulation are tabulated below:

Atom	**Occupancy**	x_0	y_0	z_0
Ca	0.166667	0.0	0.0	0.0
Mn1/Cu	0.5	0.5	0.0	0.0
Mn2	0.5	0.5	0.5	0.5
Mn3	0.166667	0.0	0.0	0.5
O1	1	0.222(1)	0.269(1)	0.0894(1)
O2	1	0.348(9)	0.517(1)	0.339(1)

Table 4.2: Occupancies and average fractional coordinates for $CaCu_{0.15}Mn_{6.85}O_{12}$ at 85 K.

Atom	U_{11}	U_{22}	U_{33}	U_{12}	U_{13}	U_{23}
Ca	0.0092(5)	0.0092(5)	0.007(2)	0.0046(1)	0	0
Mn1/Cu	0.0052(4)	0.0068(4)	0.005(1)	0.0008(2)	0.0032(2)	-0.0014(2)
Mn2	0.0038(3)	0.0031(3)	0.001(1)	0.0020(2)	-0.0002(2)	0.00002(2)
Mn3	0.0036(4)	0.0036(4)	0.001(1)	0.0018(2)	0	0
O1	0.0129(7)	0.0091(7)	0.014(2)	0.0028(6)	-0.0030(8)	0.0029(8)
O2	0.0183(8)	0.0158(8)	0.007(1)	0.0127(7)	-0.0028(8)	-0.0036(8)

Table 4.3: Refined anisotropic thermal parameters for $CaCu_{0.15}Mn_{6.85}O_{12}$ at 85 K

Atom	A_x	A_y	A_z	B_x	B_y	B_z
Ca	0	0	-0.0005(4)	0	0	0
Mn1/Cu	0.0043(1)	-0.0005(1)	0.0017(2)	0	0	0
Mn2	0.0021(2)	0.0019(1)	0.0002(2)	0	0	0
Mn3	0	0	0.0010(2)	0	0	0
O1	0.0015(4)	0.0018(1)	-0.0007(2)	0.0012(4)	-0.0013(2)	-0.0001(2)
O2	0.0021(4)	-0.0002(4)	0.0028(3)	0.0006(2)	0.0008(1)	-0.0024(3)

Table 4.4: Refined Fourier coefficients associated with the q_c modulation in $CaCu_{0.15}Mn_{6.85}O_{12}$ at 85 K.

Using the refined atomic positions and Fourier coefficients tabulated above, Mn-O bond lengths for Mn1, Mn2 and Mn3 have been calculated and plotted for adjacent unit cells along the hexagonal c axis. These are compared to the corresponding bond lengths for $CaMn_7O_{12}$ in Figure 4.7.

Comparing the bond lengths for the square planar Mn1 site, which accommodates both Cu^{2+} and Mn^{3+} in $CaCu_{0.15}Mn_{6.85}O_{12}$, similar, weak modulations are observed for $CaCu_{0.15}Mn_{6.85}O_{12}$ and $CaMn_7O_{12}$. The average cation-oxygen bond lengths are longer in $CaCu_{0.15}Mn_{6.85}O_{12}$, in order to accommodate the larger Cu^{2+} ion. Based on

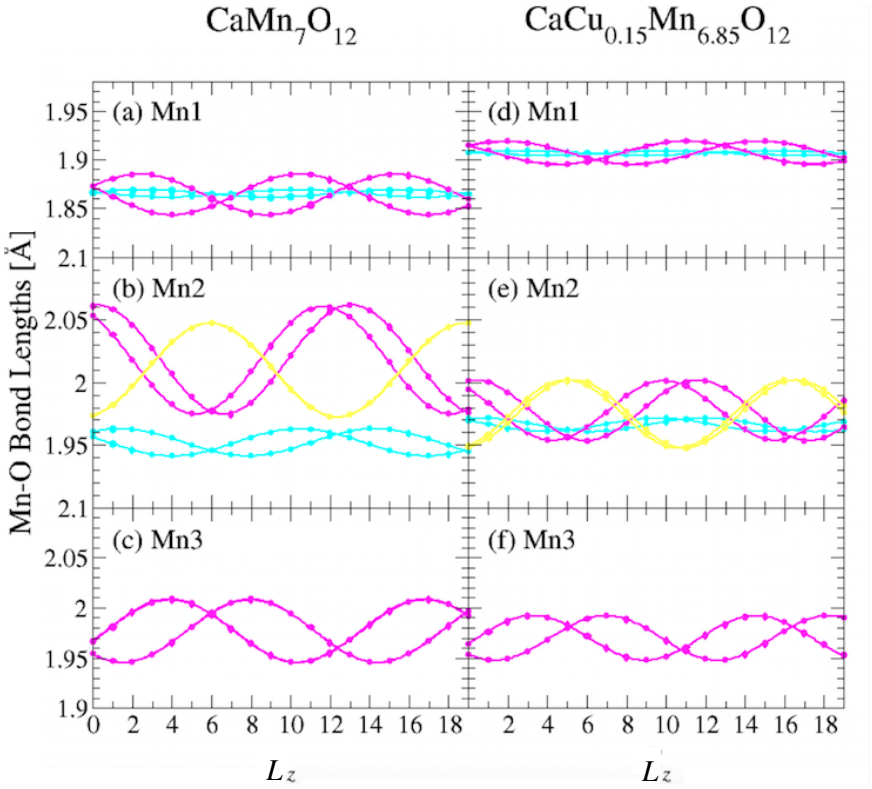


Figure 4.7: Comparison of the incommensurately modulated Mn-O bond lengths along the hexagonal c axis, associated with the q_c propagation vectors in the $CaMn_7O_{12}$ (a - c) and $CaCu_{0.15}Mn_{6.85}O_{12}$ (d - f) structures respectively.

the copper stoichiometry and the ionic radii of the other relevant species, a bond length increase of ∼1% is expected, in good agreement with the results shown here. The average Mn2-O bond length decreases by ∼1% in $CaCu_{0.15}Mn_{6.85}O_{12}$, which again, is in good agreement with calculations based upon atomic radii, considering that copper doping results in 15% substitution of Mn^{3+} for Mn^{4+}. More significantly, the modulation amplitude of Mn2 sites is reduced by ∼40% in $CaCu_{0.15}Mn_{6.85}O_{12}$ compared to $CaMn_7O_{12}$. It may be that this "missing amplitude" is accounted for by the additional families of satellites in $CaCu_{0.15}Mn_{6.85}O_{12}$. In both $CaCu_{0.15}Mn_{6.85}O_{12}$ and $CaMn_7O_{12}$, Mn3 sites are exclusively occupied by Mn^{4+} and as expected, both the average bond length and amplitude for modulation are comparable for both cases.

It can be concluded that there are strong similarities between the q_c modulations for $CaCu_{0.15}Mn_{6.85}O_{12}$ and $CaMn_7O_{12}$, with most discrepancies being understood through consideration of the impact on the geometry of the crystal structure when Mn^{3+} is sub-

stituted by Cu^{2+}. This indicates that the satellites indexed by q_c in $CaCu_{0.15}Mn_{6.85}O_{12}$ correspond to the same "orbital helix" discovered for $CaMn_7O_{12}$.

Having established a physical interpretation of the q_c modulation in $CaCu_{0.15}Mn_{6.85}O_{12}$, the following sections explore interpretations of q_1, q_2 and q_3, testing the viability of the four proposed models outlined in section 4.3.1.1.

4.3.2 Testing the models

4.3.2.1 Synchrotron single crystal x-ray diffraction of $CaCu_{0.15}Mn_{6.85}O_{12}$ I16 experiment

A synchrotron single crystal x-ray diffraction experiment at I16, Diamond Light Source was performed to collect intensity data for all four families of satellites as a function of temperature, and to identify any variation in relative satellite intensities for different regions of the crystal, as this may reveal evidence for domains.

The sample used for this experiment was crystal 2, characterised using SEM in section 4.2.2. Preliminary SuperNova experiments on this crystal at room temperature and 85 K confirmed the appearance of all four families of satellites and lattice parameters in agreement with those obtained for crystal 1.

The crystal was mounted on a flat copper puck with the (0, 0, 1) reflection surface normal, using SuperNova to determine the orientation of the family of <0 0 1> planes. At room temperature, the sample was centred in the x-ray beam, which was tuned to an energy of 6.4 keV. The (0, 4, 2) and (1, 2 , 2) Bragg reflections were identified and used to determine the **UB** matrix and precise sample orientation.

The sample was then cooled to 85 K, and realigned in the x-ray beam. q_c, q_1, q_2, and q_3 satellites corresponding to two strong Bragg peaks ((0, 6, 3) and (0, 4, 2)) were identified. For the (0, 4, 2) Bragg peak, satellites corresponding to the negative propagation vectors and second harmonic peaks with intensities $\sim$2% of the first order satellites (see Appendix A) were also observed for q_c, q_1, q_2, and q_3.

The propagation vectors measured for the first order satellites of the (0, 4, 2) Bragg peak are tabulated below.

Propagation Vector	q_x	q_y	q_z
q_c	0	0	2.092
q_1	0	0.216	0.687
q_2	-0.203	0.0	0.692
q_3	0.204	-0.200	0.692

Table 4.5: Propagation vectors q_c, q_1, q_2 and q_3 measured for the (0, 4, 2) Bragg peak at I16.

4.3.2.2 Investigating possible domain structure

If a 1-q, multi domain model exists in $CaCu_{0.15}Mn_{6.85}O_{12}$, focusing on a region of the crystal below a certain "maximum domain size", all four sets of satellites should not be observable simultaneously. For different regions of the crystal domains may be present in different proportions, and the relative intensities of the satellite peaks may change.

Exploiting variable focusing of the x-ray beam at I16, two tests were performed in an attempt to gain insight into possible domain distribution for a 1-q model:

Test 1 - Systematic reduction in x-ray beam probe size

The x-ray beam was focused on each of the satellites around the (0, 4, 2) Bragg peak in turn. Using an initial beam probe size 500 $\times$ 500 μm^2, the intensity of each of the satellites was measured, integrating over a cubic volume centred on the peak maximum. Parallel slits and mirrors were then used to systematically reduce the beam probe size, and the intensity was remeasured. in Figure 4.8(a), the (0, 4, 2) + q_c Bragg peaks is shown for different beam probe sizes, and in (b), variation in intensity is plotted as a function of probe size. In Figure 4.8(c) intensity variation with slit size has been plotted for all four propagation vectors, scaled to the maximum intensity in each case. Similarities in intensity variation indicate that if the satellites are associated with different domains, the domains are spanned in the same proportions as the beam size is reduced. This is possible, but perhaps indicates that a multi-q model is likely.

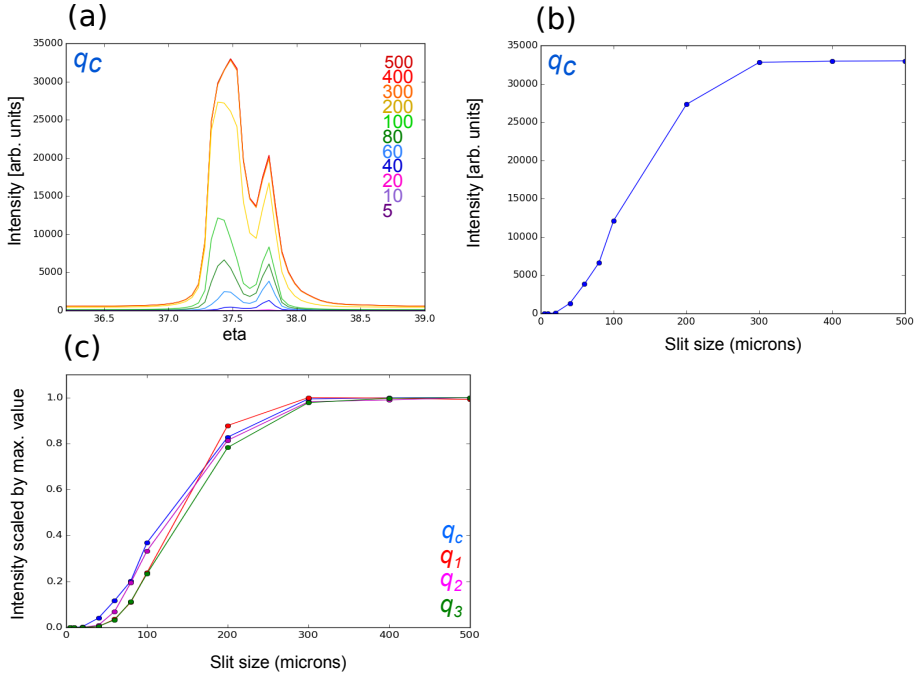


Figure 4.8: (a) Variation in intensity of the q_c satellite of the (0, 4, 2) Bragg peak for a range of different x-ray beam probe sizes. (b) Integrated intensity as a function of slit size, for the q_c satellite and (c) comparing the variation in intensity with slit size for all four families of satellites around the (0, 4, 2) Bragg peak.

Test 2 - Rastering across the sample surface

Using the minimum possible beam probe size of 5 × 5 μm^2, the four satellites surrounding the (0, 4, 2) Bragg peak were located. The intensity of the satellites is weak for this probe size, but they are still clearly visible, as shown in Figure 4.9.

The 5 × 5 μm^2 x-ray beam was then rastered across the crystal surface. The intensity of each satellite was recorded at 5μm increments, for a distance of 50 μm. At each point measured, all four satellites could be observed, with similar relative intensities in each case. This suggests that if each satellite is associated with a different domain, domains are spanned in the same proportions in each measurement. Additionally, domains must be smaller than the probe size of 5 μm. This is possible, but again, indicates that a multi-q model is likely.

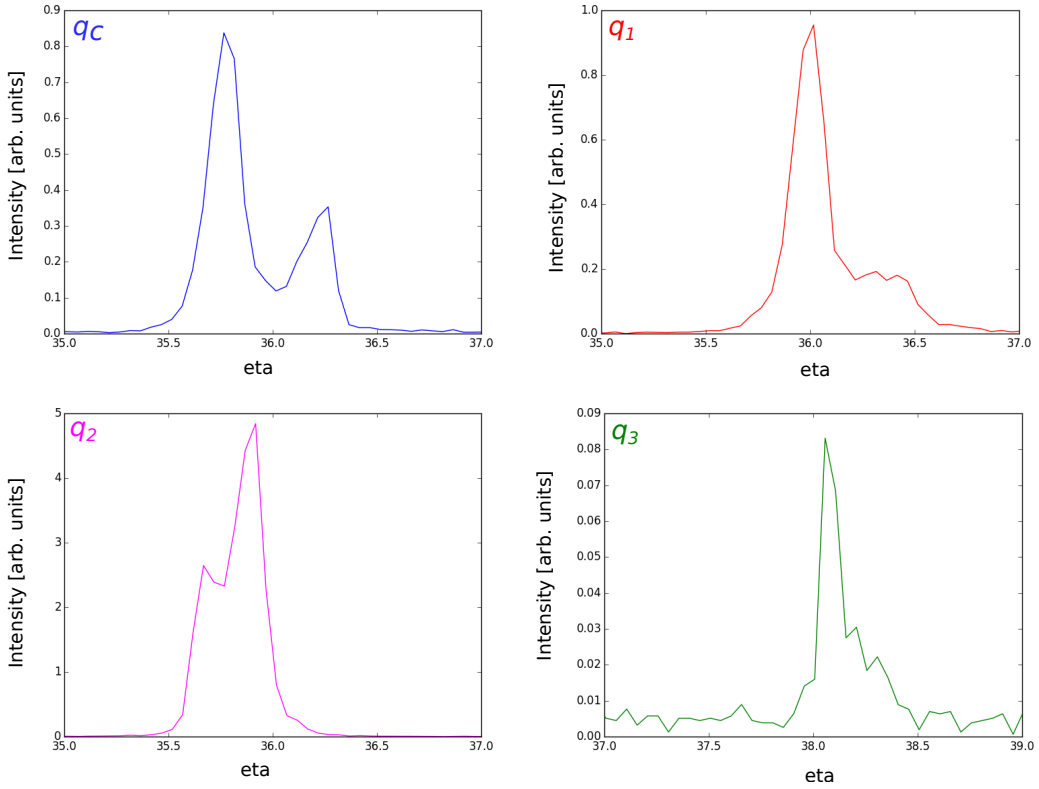


Figure 4.9: The intensities of all four satellites around the (0,4,2) Bragg peak, for an x-ray probe size of 5 × 5 μm^2. All intensities are scaled by the intensity of the Bragg peak.

4.3.2.3 Temperature dependencies of the satellite peaks

Using a closed-cycle cryostat, the intensity of all four satellites was measured between 60 and 260 K at 10 K intervals. To ensure consistency, satellites of both the (0, 4, 2) and (0, 6, 3) Bragg peaks were measured, and repeated on warming and cooling to check for hysteresis. Results for the for the (0, 4, 2) Bragg peak in Figure 4.10. All intensities have been scaled to the Bragg peak intensity and scaled to the same maximum intensity to enable direct comparison of the variation in intensity with temperature.

Between 60 and ∼210 K, intensities of all four satellite scale with linear, identical temperature dependencies. Closer inspection of data above ∼180 K (shown in the inset to Figure 4.10(a)) reveals a discrepancy between the satellites associated with q_c

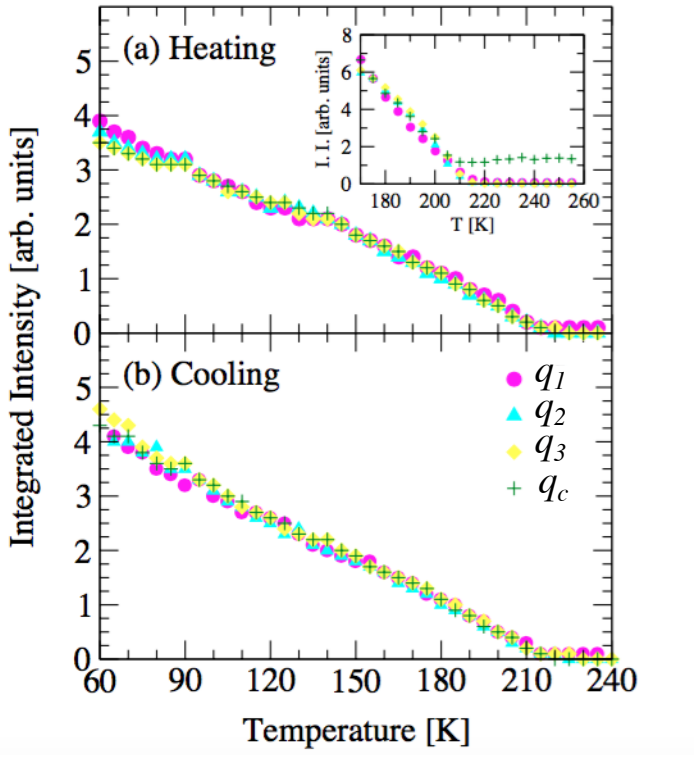


Figure 4.10: Temperature dependencies of the four satellites of the (0,4,2) Bragg peak, scaled to the Bragg peak intensity and to the maximum intensity for each satellite. Above $\sim$ 210 K, only the q_c satellites can be observed.

and those indexed by q_1, q_2 and q_3. Satellites associated with q_1, q_2 and q_3 cannot be observed above $\sim$210 K, whilst those associated with q_c are weakly observable up to 260 K, most likely evolving from a higher temperature. A sharp increase in intensity of the q_c satellites coincides with the emergence of the additional three satellites at $\sim$210 K.

This relationship between the families of satellites is consistent on both heating and cooling, and the same result is obtained for satellites of the (0, 6, 3) Bragg peak.

This distinction between the modulations associated with q_c and $q_1/q_2/q_3$ is inconsistent with the 1-q model (for which all four satellites would correspond to the same modulation). The q_1, q_2 and q_3 satellites have very similar temperature dependencies, indicating that they may well be related. The abrupt change in the temperature de-

pendence of the q_c satellites coinciding with the emergence of q_1, q_2 and q_3 could be indicative of a "lock in" of the q_c modulation at 210 K. This would be inconsistent with the 1 + 3-q model described in section 4.3.1.1, for which the domains incorporating q_c and $q_1/q_2/q_3$ would be distinct and unrelated.

To summarise, results obtained at I16 indicate that a 4-q model, incorporating four distinct modulations seems likely, but does not rule out a 1-q, multi domain model.

4.3.3 Analysis of SuperNova data

4.3.3.1 Comparing equivalent satellite intensities

Returning to the SuperNova data collected in section 4.3.1.1, intensities for a large number of q_1, q_2 and q_3 satellite reflections were collected for crystal 1 at 85 K, indexed in $R\bar{3}$ symmetry by propagation vectors related by 3-fold symmetry: $q_1 = (0, \delta, \tau), q_2 = (-\delta, 0, \tau), q_3 = (\delta, -\delta, \tau)$ with $\delta = 0.206 \pm 0.002$ and $\tau = 0.698 \pm 0.002$. Transforming the h, k and l indices for q_2 and q_3 satellites by 3-fold rotation, intensities of equivalent satellites can be plotted against each other, as shown in Figure 4.11.

In each case, equivalent pairs of satellite peaks scale linearly with gradients approximately equal to one, meaning that the overall 3-fold symmetry of the crystal is preserved. This would be a natural result in a 4-q model, with q_1, q_2 and q_3 corresponding to distinct modulations. In 2-q and and 1q-models, for which q_1, q_2 and q_3 correspond to the same modulation, intensity gradients would correspond to the relative proportion of the domains related by three fold rotation. Gradients of one, as observed in Figure 4.11 would imply three equally populated domains. This is possible, but not necessary, given random effects such as pinning that tend to influence domain formation in single crystals. This analysis was repeated with SuperNova experiments on several different crystals of $CaCu_{0.15}Mn_{6.85}O_{12}$, and the same result was obtained.

This analysis again indicates that a 4-q model is likely, but does not rule out a 1-q

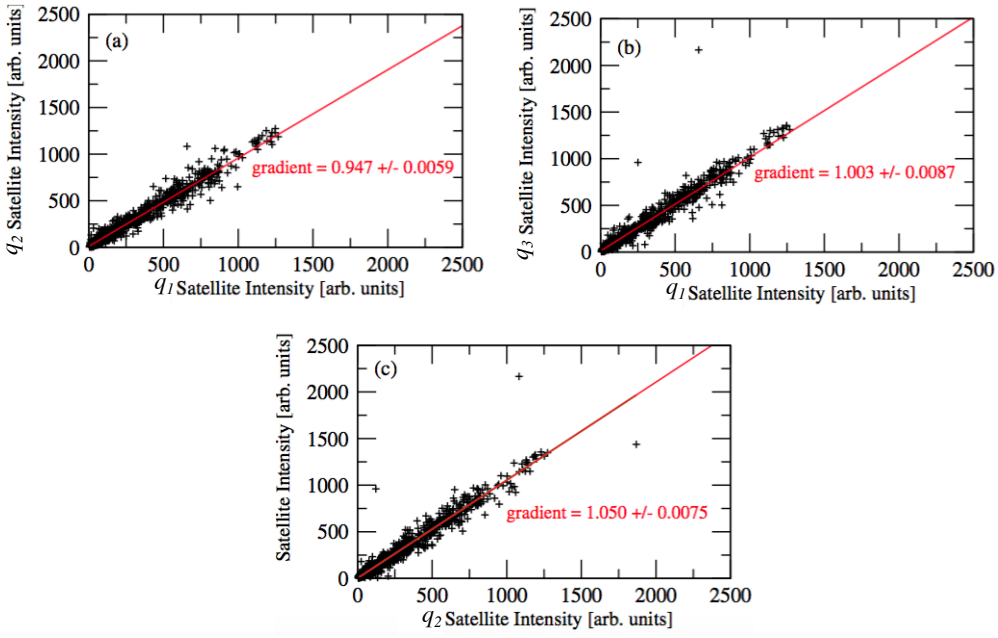


Figure 4.11: Pairs of equivalent q_1, q_2 and q_3 satellites related by 3-fold symmetry. Intensities for each pair scale linearly with gradients approximately equal to one.

model. Given the interesting physics associated with an unprecedented 4-q structure, this model has been developed below and tested against experimental data.

4.3.3.2 Refinement of a model for the q_1, q_2 and q_3 modulations

Results of the test above do not give give conclusive evidence for a simple 1-q twinned model, and I16 data indicates a possible distinction between the q_c and q_1, q_2 and q_3 satellites.

Whilst it will be shown in section 4.3.3.4 that the 1-q model produces an improved fit to the available data, a viable model incorporating charge and orbital modulations can be constructed, as outlined below:

Having refined a model for the incommensurate modulation associated with q_c (see section 4.3.1.2), in the following section, a model is constructed that incorporates the three modulations associated with q_1, q_2 and q_3 simultaneously.

Using a reflection file incorporating Bragg peaks (indexed in R$\bar{3}$ with $a = 10.421(2)$ Å,

$b = 10.421(2)$ Å, $c = 6.3811(12)$ Å), and the three sets of satellites indexed with q_1, q_2 and q_3 propagation vectors, a model has been refined using JANA2006, using similar methods to those outlined in section 4.3.1.2. Using the Bragg peaks, and refining against the same average structure used in section 4.3.1.2, allowing average oxygen positions, thermal parameters, overall scale and extinction to refine, convergence with an R-factor of ∼9% was obtained, generating an identical structure to that obtained in section 4.3.1.2.

Fixing the average structure, the three sets of satellite peaks were then simultaneously incorporated into the refinement. As an initial model for the modulated structure, three atomic position modulations of the same sinusoidal form as q_c (see section 4.3.1.2) were incorporated on each atomic site.

Within symmetry constraints of the four dimensional space group $R\bar{3}(00\gamma)$, simultaneously allowing all A and B Fourier coefficients to refine did not produce a stable, converged global minimum. This is most likely due to the large number of free parameters associated with the refinement. An approximation was made to reduce the number of free parameters, constraining the shape of Mn3 octahedra by fixing the unmodulated fractional coordinates of Mn3 and specific oxygen atoms. This assumes that Mn3 sites are neither charge or orbitally modulated, and is a reasonable approximation given that these sites are nominally Mn^{4+} and are not expected to be Jahn-Teller active.

Invoking this constraint, a stable refinement, incorporating three atomic position modulations on Mn1, Mn2 and specific oxygen sites converged. Completing a full refinement, incorporating Bragg and satellite peaks, a converged minima with an R factor of ∼24% (∼9% for Bragg peaks and ∼30% for satellite peaks) was obtained. Atomic positions and Fourier coefficients were found to be reproducible from a wide range of starting parameters and several local minima with higher R-factors were identified, suggesting that the model is a global minimum solution.

Parameters obtained from the refinement are tabulated below, and in Figure 4.12(a) and (b), observed and calculated structure factors for the refined model are plotted,

giving an indication of the goodness of fit for the model. Refined Mn2-O bond lengths incorporating the effects of q_1, q_3 and q_3 are shown in Figure 4.12(c).

Atom	**Occupancy**	$\boldsymbol{x}_0$	$\boldsymbol{y}_0$	$\boldsymbol{z}_0$
Ca	0.166667	0.0	0.0	0.0
Mn1/Cu	0.5	0.5	0.0	0.0
Mn2	0.5	0.5	0.5	0.5
Mn3	0.166667	0.0	0.0	0.5
O1	1	0.222(1)	0.268(1)	0.0894(1)
O2	1	0.348(9)	0.518(1)	0.339(1)

Table 4.6: Occupancies and fractional coordinates obtained from refining 85 K SuperNova data for $CaCu_{0.15}Mn_{6.85}O_{12}$ incorporating three atomic position modulations on Mn1, Mn2 and O sites.

Atom	$\boldsymbol{U}_{11}$	$\boldsymbol{U}_{22}$	$\boldsymbol{U}_{33}$	$\boldsymbol{U}_{12}$	$\boldsymbol{U}_{13}$	$\boldsymbol{U}_{23}$
Ca	0.0085(4)	0.0086(3)	0.008(2)	0.0042(3)	0	0
Mn1/Cu	0.0052(4)	0.0066(3)	0.006(2)	0.0006(2)	0.0032(2)	-0.0014(1)
Mn2	0.0025(4)	0.0034(3)	0.002(1)	0.002(1)	0.0003(2)	0.0003(2)
Mn3	0.0032(3)	0.0032(3)	0.002(1)	0.0016(2)	0	0
O1	0.0129(6)	0.0088(7)	0.015(2)	0.0028(6)	-0.0033(8)	0.0026(8)
O2	0.0186(8)	0.0154(8)	0.008(2)	0.0127(7)	-0.0029(7)	-0.0037(7)

Table 4.7: Refined anisotropic thermal parameters for $CaCu_{0.15}Mn_{6.85}O_{12}$ at 85 K.

Atom	$\boldsymbol{A}_x$	$\boldsymbol{A}_y$	$\boldsymbol{A}_z$	$\boldsymbol{B}_x$	$\boldsymbol{B}_y$	$\boldsymbol{B}_z$
Ca	0	0	0	0	0	0
Mn1/Cu	0.00474(10)	-0.00065(10)	0.00125(16)	0	0	0
Mn2	0.00243(10)	0.00132(9)	0.00308(15)	0	0	0
Mn3	0	0	0	0	0	0
O1	0	-0.0011(3)	-0.0005(5)	0	-0.0028(3)	0.0017(5)
O2	0	0	0	0	0	0

Table 4.8: Refined Fourier coefficients for q_1.

Atom	$\boldsymbol{A}_x$	$\boldsymbol{A}_y$	$\boldsymbol{A}_z$	$\boldsymbol{B}_x$	$\boldsymbol{B}_y$	$\boldsymbol{B}_z$
Ca	0	0	0	0	0	0
Mn1/Cu	0.00093(10)	0.00301(10)	-0.00611(16)	0	0	0
Mn2	0.00035(9)	0.00234(10)	-0.00287(15)	0	0	0
Mn3	0	0	0	0	0	0
O1	-0.0011(3)	0.0002(3)	-0.0015(5)	0.0001(3)	0.0009(3)	-0.0034(5)
O2	0	0	0	0	0	0

Table 4.9: Refined Fourier coefficients for q_2.

Atom	A_x	A_y	A_z	B_x	B_y	B_z
Ca	0	0	0	0	0	0
Mn1/Cu	-0.00071(10)	0.00603(16)	-0.00611(16)	0	0	0
Mn2	0.00098(10)	0.00049(10)	-0.00061(15)	0	0	0
Mn3	0	0	0	0	0	0
O1	0.0016(3)	0.0006(3)	0.0032(5)	-0.0007(3)	-0.0008(3)	0.0029(5)
O2	0	0	0	0	0	0

Table 4.10: Refined Fourier coefficients for q_3.

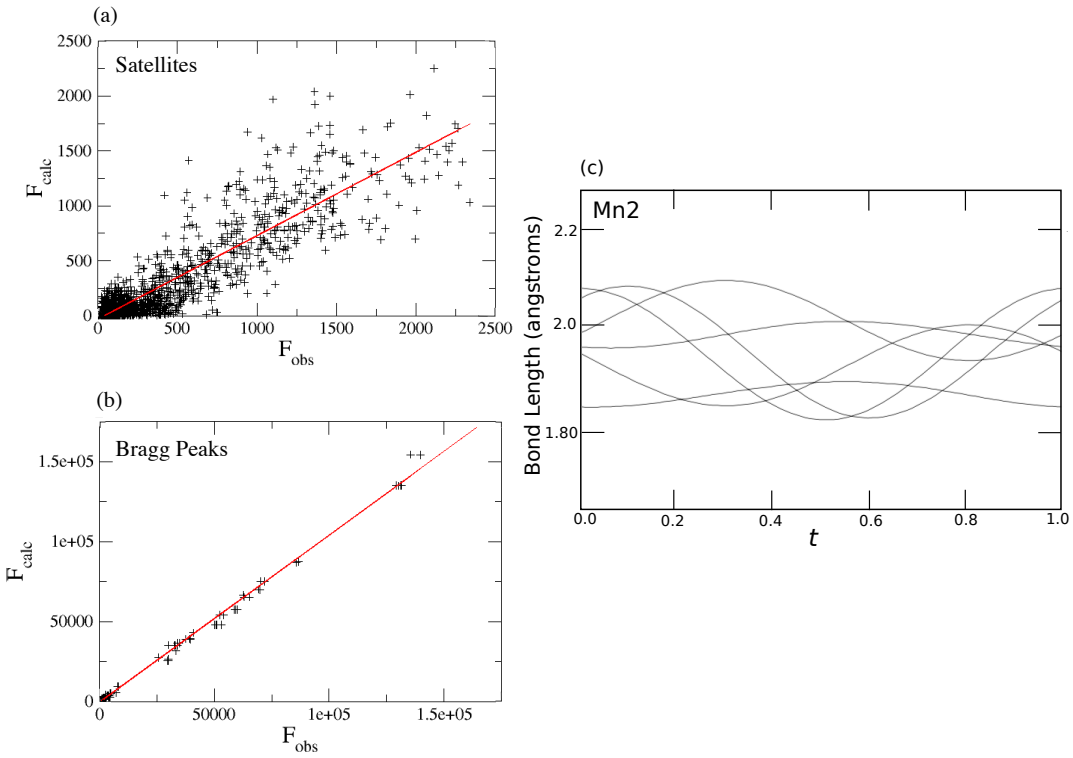


Figure 4.12: (a) and (b) F_{obs} versus F_{calc} plots Bragg peaks and q_1 q_2 and q_3 satellite peaks, indicating the quality of the quality of fit for the model. (c) Refined Mn2-O bond lengths plotted as a function the scaled parameter $t = \bar{x}_q = \boldsymbol{q} \cdot \boldsymbol{r}_0$, incorporating the effect of q_1, q_2 and q_3 simultaneously.

4.3.3.3 Interpreting the refined model for the q_1, q_2 and q_3 modulations

In contrast to the model for q_c, refined Mn-O bond lengths do not not appear to manifest as orbital ordering. This has prompted consideration of alternative physical manifestations of the modulations associated with q_1, q_2 and q_3. These modulations could correspond to charge ordering, and this can be explored through the calculation of bond valence sums, as introduced in section 3.3.1:

Based upon the refined bond lengths from section 4.3.3.2, in the figures below, bond valence sums are calculated for hexagonal ab planes at a height $l_z = 0$ along the c axis.

Within a given unit cell nine distinct Mn2 sites exist. Initially, bond valence variation is shown for one of these sites in Figure 4.13.

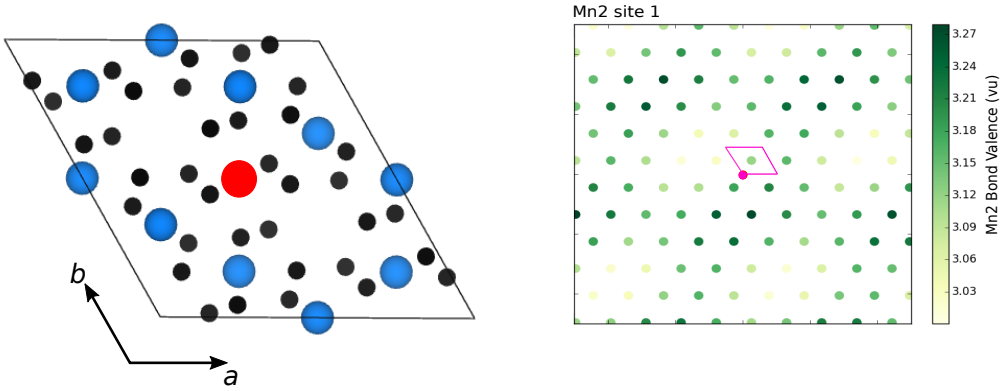


Figure 4.13: Bond valence values for a single Mn2 site per unit cell, plotted in the hexagonal ab plane. Each point in the plot corresponds to an equivalent Mn2 site, with one unit cell outlined in pink.

Each point in the plot corresponds to an inequivalent Mn2 site, with a single unit cell marked in pink.

Incorporating contributions from Mn2 sites related by 3-fold symmetry (Figure 4.14) and then by R-centring: (Figure 4.15)

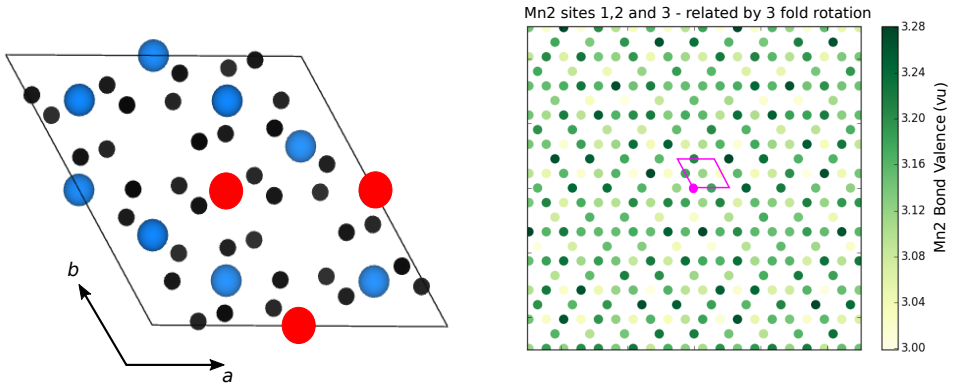


Figure 4.14: Bond valence variation for Mn2 sites related by 3-fold symmetry in the ab plane.

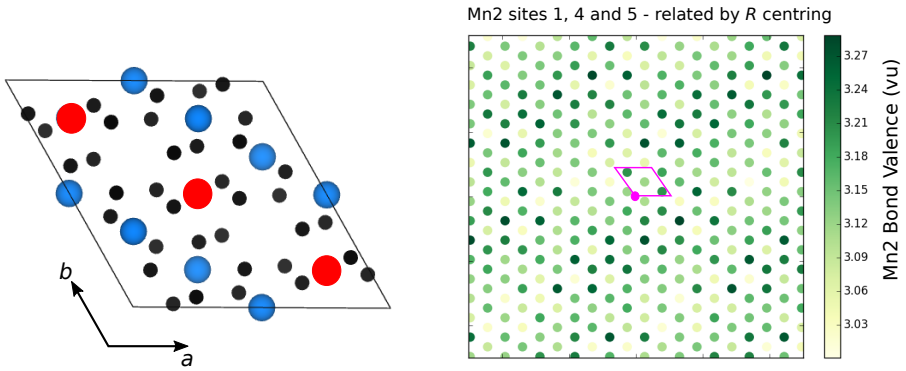


Figure 4.15: Bond valence variation for Mn2 sites related by R-centring in the ab plane.

Finally, all inequivalent Mn2 sites are incorporated into the plot, which is shown in Figure 4.16:

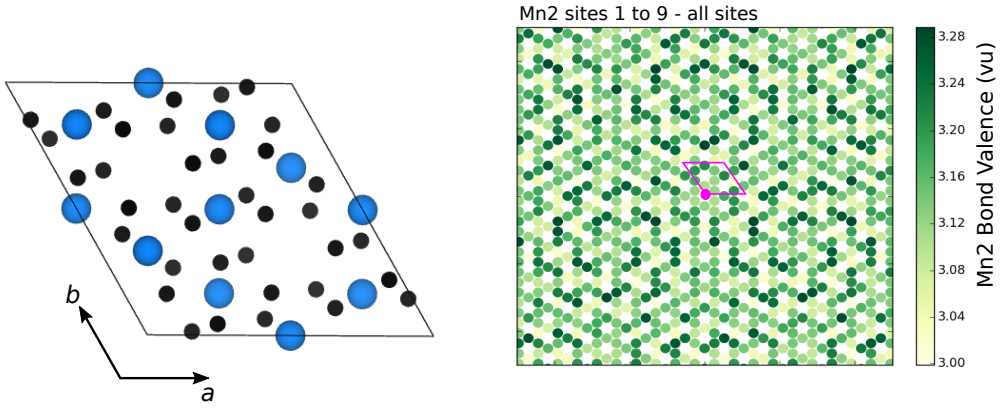


Figure 4.16: Summing bond valence contributions from all inequivalent Mn2 sites in the hexagonal ab plane, generating a 3-fold symmetric pattern.

The absolute values of charge obtained are somewhat empirical, since they are based upon the choice of R_0 and B (in this case taking tabulated values from Ref. [87]), however, they are sufficient to compare relative charge variation across the Mn2 sites.

Incorporating the bond valence variations for all nine inequivalent Mn2 sites in a given unit cell leads to a pattern that preserves the overall 3-fold symmetry of the system. For comparative purposes, a plot has also been calculated for the 7^{th} unit cell along the c axis, and is shown below.

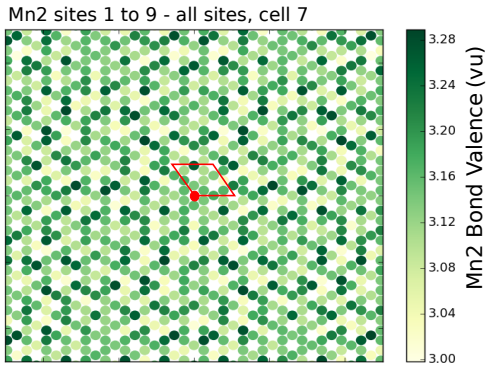


Figure 4.17: Comparing bond valence variation in the ab plane for the 7^{th} unit cell along the hexagonal c axis. The 3-fold symmetric pattern is preserved, with small shifts in the absolute bond valence values.

Small shifts in the bond valence values are observed, but the overall 3-fold preserving pattern is similar.

As might be anticipated from the bond valence calculations in section 3.3.1, tests made incorporating bond valence variations associated with q_c had little impact on the relative variation in charge within a given ab plane.

In the bond valence calculations above, the phases between the three modulations have been arbitrarily set to zero. The full effect of varying these phases is beyond the scope of this thesis, but an analogy to skyrmion phases can be considered [91]. Taking a simple model, these naturally chiral, stable magnetic states can be visualized as a simple superposition of three helical states under applied magnetic field. The lowest energy state can be viewed as a lattice of antiskyrmion lines (that is, magnetic vortices for which the magnetisation in the center is antiparallel to the applied field). Phases exist between these helical states with two phase parameters between controlling the position of the pattern within the hexagonal ab plane. In the case of a 4-q model, a phase would also exist between q_c and the charge pattern generated by q_1, q_2 and q_3, controlling the lock in between the orbital and charge modulations. This phase could be set such that the pattern of charge modulation reinforces the orbital ordering. Finally, a global phase exists, which controls the overall nature of the charge modulations. In the case of skyrmions, this global phase controls the overall chirality,

which can go from right handed to left handed, through a mixture of skyrmions and antiskyrmions. In the case here, it is expected that this global phase would be a maximum value, coinciding with the overall structural chirality.

Charge modulation provides a viable physical interpretation of the three related modulations with propagation vectors q_1, q_2 and q_3. In conjunction with the interpretation of q_c in terms of a modulated orbital occupation, this could provide a complete description for a 4-q model, incorporating four distinct modulations.

The development of a 4-q model was prompted by I16 data, showing a lack of evidence for domain formation and a distinction between q_c and q_1, q_2, q_3. In fact, developing a twin model (the 1-q model outlined in section 4.3.1.1) provides a better fit to SuperNova x-ray diffraction data, as discussed below.

4.3.3.4 Development of a twin model

The theory of the model

The twin model is derived from the choice in defining the hexgagonal c axis in relation to the high temperature $Im\bar{3}$ cubic phase. Cooling through the cubic to $R\bar{3}$ transition, the hexagonal c axis could lie along any of the four equivalent cubic diagonals [111], [-111], [1-11] or [-1-11], as shown in Figure 4.18. This leads to four possible hexagonal twins.

For **twin 1**, the $R\bar{3}$ lattice vectors (a_h, b_h, c_h) are related to the cubic $Im\bar{3}$ lattice vectors by

$$\begin{aligned} a_h &= -a_c + b_c, \\ b_h &= -b_c + c_c, \\ c_h &= \frac{1}{2}a_c + \frac{1}{2}b_c + \frac{1}{2}c_c. \end{aligned} \tag{4.3.4}$$

The corresponding lattice vectors for twin 2, twin 3 and twin 4 are generated through

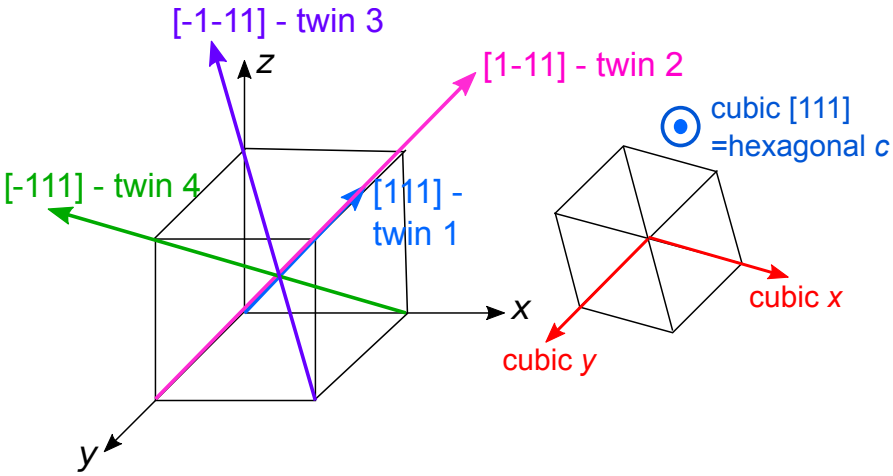


Figure 4.18: Four possible hexagonal c axes (pink, green, blue, purple) corresponding to the four cubic diagonals in the parent cell.

90° rotations around the cubic z axis:

Twin 2:

$$\begin{aligned} a'_h &= a_c + b_c, \\ b'_h &= -a_c + c_c, \\ c'_h &= \frac{1}{2}a_c - \frac{1}{2}b_c + \frac{1}{2}c_c. \end{aligned} \tag{4.3.5}$$

Twin 3:

$$\begin{aligned} a''_h &= a_c - b_c, \\ b''_h &= b_c + c_c, \\ c''_h &= -\frac{1}{2}a_c - \frac{1}{2}b_c + \frac{1}{2}c_c. \end{aligned} \tag{4.3.6}$$

Twin 4:

$$\begin{aligned} a'_h &= -a_c - b_c, \\ b'_h &= a_c + c_c, \\ c'_h &= -\frac{1}{2}a_c + \frac{1}{2}b_c + \frac{1}{2}c_c. \end{aligned} \tag{4.3.7}$$

The $R\bar{3}$ twins derived from a parent cubic cell can either be *obverse* or *reverse*, as shown in Figure 4.19.

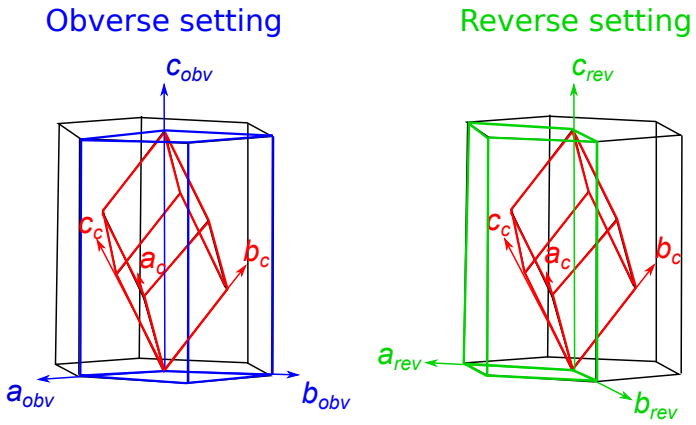


Figure 4.19: Adapted Ref. [92]. Distinct obverse and reverse settings of the hexagonal unit cell (applicable to rhombohedral $R\bar{3}$ symmetry in this model), derived from the parent cell, which in this case is cubic $Im3$.

The equations above are consistent for four *obverse* twins.

For a body centred cubic, $Im\bar{3}$ parent cell, the matrix $\mathbf{T}$ that transforms lattice vectors to the hexagonal setting is given in Ref. [92]

$$\begin{pmatrix} a_c \\ b_c \\ c_c \end{pmatrix} = \begin{pmatrix} -\frac{2}{3} & -\frac{1}{3} & \frac{2}{3} \\ \frac{1}{3} & -\frac{1}{3} & \frac{2}{3} \\ \frac{1}{3} & \frac{1}{3} & \frac{2}{3} \end{pmatrix} \begin{pmatrix} a_h \\ b_h \\ c_h \end{pmatrix}. \tag{4.3.8}$$

For diffraction data indexed in the $R\bar{3}$ cell for a given obverse twin, transformations can be made to reindex peaks with respect to the other three obverse twins using the following matrices.

Transforming from the $R\bar{3}$ cell for **Twin 1** to the $R\bar{3}$ cell for **Twin 2**:

$$\begin{pmatrix} a_{\mathbf{t2}} \\ b_{\mathbf{t2}} \\ c_{\mathbf{t2}} \end{pmatrix} = \begin{pmatrix} -\frac{1}{3} & -\frac{2}{3} & \frac{4}{3} \\ 1 & 1 & 0 \\ -\frac{1}{3} & \frac{1}{3} & \frac{1}{3} \end{pmatrix} \begin{pmatrix} a_{\mathbf{t1}} \\ b_{\mathbf{t1}} \\ c_{\mathbf{t1}} \end{pmatrix}. \tag{4.3.9}$$

Transforming from the $R\bar{3}$ cell for **Twin 1** to the $R\bar{3}$ cell for **Twin 3**:

$$\begin{pmatrix} a_{\mathbf{t3}} \\ b_{\mathbf{t3}} \\ c_{\mathbf{t3}} \end{pmatrix} = \begin{pmatrix} -1 & 0 & 0 \\ \frac{2}{3} & \frac{1}{3} & \frac{4}{3} \\ \frac{1}{3} & \frac{2}{3} & -\frac{1}{3} \end{pmatrix} \begin{pmatrix} a_{\mathbf{t1}} \\ b_{\mathbf{t1}} \\ c_{\mathbf{t1}} \end{pmatrix}. \tag{4.3.10}$$

Transforming from the $R\bar{3}$ cell for **Twin 1** to the $R\bar{3}$ cell for **Twin 4**:

$$\begin{pmatrix} a_{\mathbf{t4}} \\ b_{\mathbf{t4}} \\ c_{\mathbf{t4}} \end{pmatrix} = \begin{pmatrix} \frac{1}{3} & \frac{2}{3} & -\frac{4}{3} \\ -\frac{1}{3} & \frac{1}{3} & \frac{4}{3} \\ \frac{2}{3} & \frac{1}{3} & \frac{1}{3} \end{pmatrix} \begin{pmatrix} a_{\mathbf{t1}} \\ b_{\mathbf{t1}} \\ c_{\mathbf{t1}} \end{pmatrix}. \tag{4.3.11}$$

Applying the model to SuperNova data

Taking the SuperNova diffraction data for crystal 1 measured at 85 K, Bragg peaks were indexed in $R\bar{3}$ *obverse* symmetry, with cell parameters a = 10.421(2) Å, b = 10.421(2) Å, c = 6.3811(12) Å, and satellite peaks were indexed with a single propagation vector of q_c = (0, 0, 2.09).

The unit cell used for peak indexation was then transformed using the matrices for each of the twins (Eq. (4.3.9), Eq. (4.3.10) and Eq. (4.3.11)) in turn. In each case, diffraction peaks were reindexed using the same unit cell and propagation vector (q_c).

From the indexed reflection lists for Bragg and satellite peaks generated for each twin, in Figure 4.20 below, intensities of equivalent satellites for each twin are plotted against each other :

The gradients of ∼1 obtained for all plots suggest equal fractions for all four twins are likely.

This twin model was then tested by refining against the x-ray diffraction data, using JANA2006 [84]. initially a model for the average structure was refined against the Bragg peak intensities for a single twin, using the same method described in section 4.3.1.2. The refinement converged with an R-factor of ∼9%, generating an identical

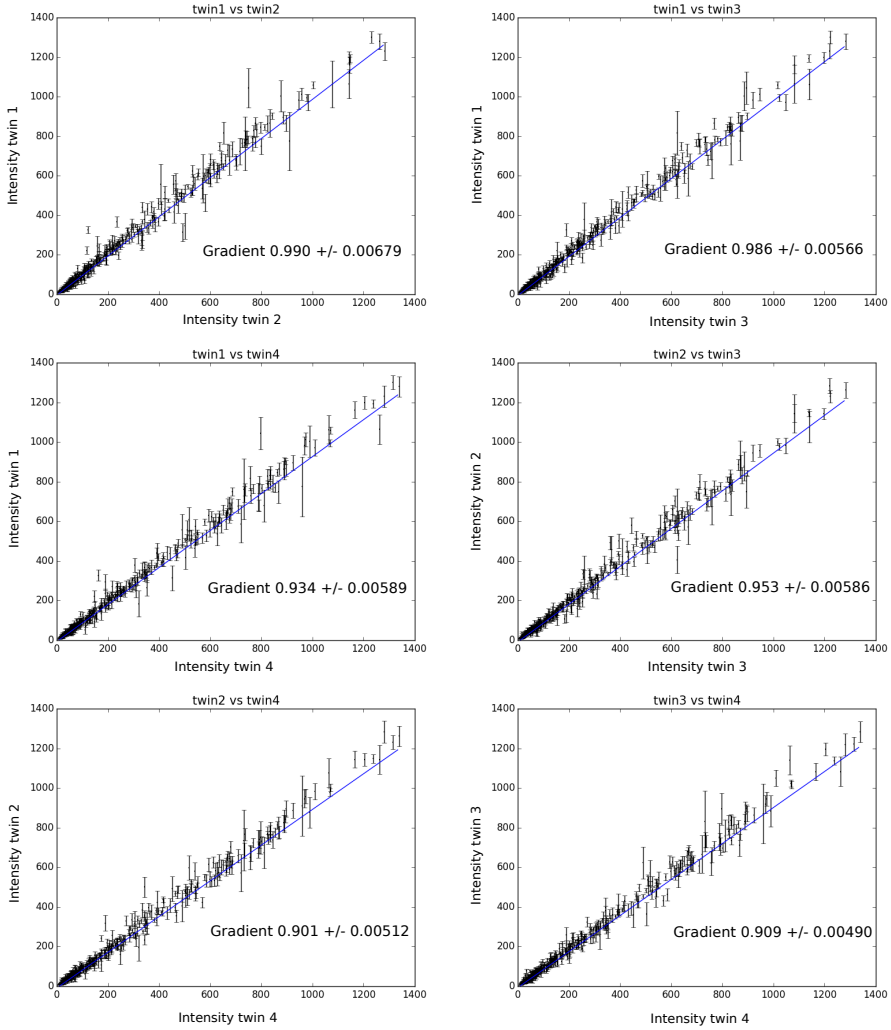


Figure 4.20: Comparing intensities of equivalent satellites associated with all four twins, indexed using CrysAlisPRO. Linear scaling with a gradient of $\sim$1 obtained for all pairs of twins indicates four approximately equal twin fractions.

structure to the obtained in section 4.3.1.2, as expected.

A model for the four twins was then incorporated into the refinement, using the matrices given in Eq. (4.3.9), Eq. (4.3.10) and Eq. (4.3.11). Incorporating the reflection files for all four twins, refining the average structure against all of the Bragg peaks, and allowing twin fractions to refine, a converged fit was obtained with an R-factor of $\sim$3 was obtained; a significantly better fit to the average structure than was obtained in section 4.3.3.2.

The average structure was then fixed and a single sinusoidal atomic position modu-

lation on each atom, used in section 4.3.1.2 was incorporated into the model for each twin. Refining this model against satellite peaks associated with all fourtwins, freely refining all Fourier coefficients from random starting values, with no constraints other than those imposed by the $R\bar{3}(00\gamma)0$ space group, a converged fit with an R-factor of $\sim$20% was obtained for the satellite peaks.

Completing a full refinement of the Bragg and satellite peaks associated with all four twins produced a converged fit with an overall R-factor of 5.93% (16.93% for satellite peaks, and 3.5% for Bragg peaks). Refined Mn-O bond lengths bear close resemblance to those observed in $CaMn_7O_{12}$, as shown in Figure 4.21.

A summary of the refined model is shown below:

Atom	**Occupancy**	$\mathbf{x}_0$	$\mathbf{y}_0$	$\mathbf{z}_0$
Ca	0.166667	0.0	0.0	0.0
Mn1/Cu	0.5	0.5	0.0	0.0
Mn2	0.5	0.5	0.5	0.5
Mn3	0.166667	0.0	0.0	0.5
O1	1	0.3783(2)	0.4455(3)	0.7488(4)
O2	1	0.3467(2)	0.5172(2)	0.3417(4)

Table 4.11: Occupancies and average fractional coordinates for $CaCu_{0.15}Mn_{6.85}O_{12}$ at 85 K.

Atom	$\mathbf{A}_x$	$\mathbf{A}_y$	$\mathbf{A}_z$	$\mathbf{B}_x$	$\mathbf{B}_y$	$\mathbf{B}_z$
Ca	0	0	0	0	0	-0.0017(8)
Mn1/Cu	0.0037(1)	-0.00095(10)	0.00110(16)	0	0	0
Mn2	0.00921(10)	0.0088(9)	0.002539(15)	0	0	0
Mn3	0	0	0.0047(5)	0	0	0
O1	0.000869(10)	-0.00085(13)	-0.0017(5)	-0.0033(3)	-0.0012(3)	-0.0010(5)
O2	0.0023(3)	-0.0010(4)	0.0035(3)	0.0010(5)	0.0013(6)	-0.00040(10)

Table 4.12: Refined Fourier coefficients for the q_c modulation in $CaCu_{0.15}Mn_{6.85}O_{12}$ at 85 K, incorporating a twin model into the refinement.

Twin 1	**Twin 2**	**Twin 3**	**Twin 4**
0.269(7)	0.232(4)	0.262(4)	0.230(4)

Table 4.13: Refined twin fractions for $CaCu_{0.15}Mn_{6.85}O_{12}$.

The R-factor for the average structure is improved significantly by implementing the twin model, and the R-factor factor for satellite peaks compared to the that obtained

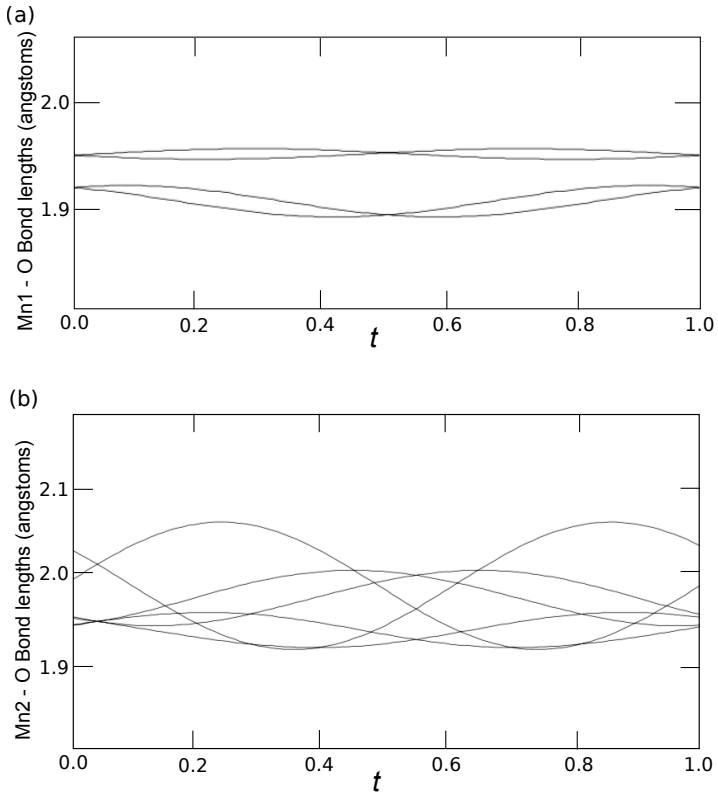


Figure 4.21: Refined Mn-O bond lengths for $CaCu_{0.15}Mn_{6.85}O_{12}$ incorporating a twin model and a single propagation vector q_c, plotted as a function of plotted as a function the scaled parameter $t = \bar{x}_{qc} = \boldsymbol{q}_c \cdot \boldsymbol{r}_0$. Variation in both the (a) Mn1-O and (b) Mn2-O bond lengths bears close resemblance those observed for $CaMn_7O_{12}$.

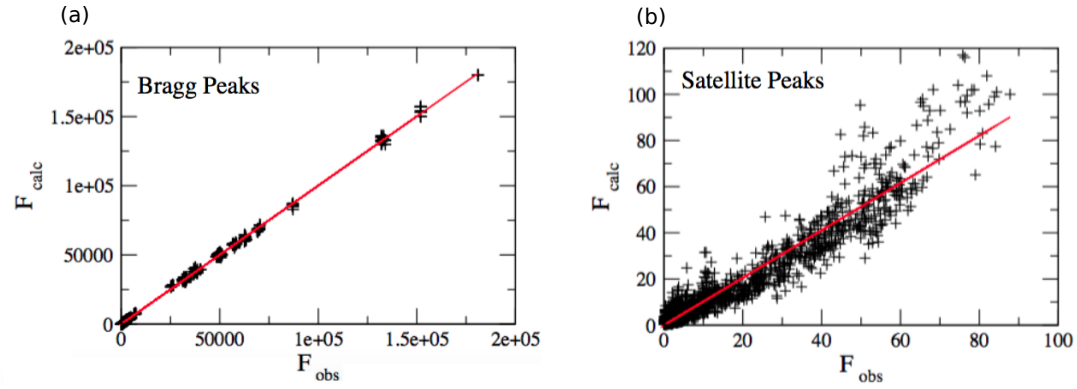


Figure 4.22: Correlation between calculated and observed structure factors of the (a) Bragg and (b) satellite peaks in the twin model. Correlation is significantly better than that obtained for the 4-q model.

for the 4-q model (see section 4.3.3.2) is also lower. The improved correlation between the observed and calculated structure factors for both the Bragg and satellite peaks compared to that obtained for the 4-q model indicates that the 1-q, multi-domain model is the most likely explanation for the appearance of four families of satellite peaks,.

4.4 Conclusions and Further Investigations

The initial aim of this study was to investigate whether the multiferroic properties of $CaMn_7O_{12}$ could be tuned through copper doping across the $CaCu_xMn_{7-x}O_{12}$ solid solution, manipulating charge and orbital ordering by varying the average manganese valence. Complications arising from initial uncertainty in precise crystal composition and the appearance of multiple sets of satellite peaks have limited studies to a single composition of $CaCu_{0.15}Mn_{6.85}O_{12}$. However, this structural study has opened up many possibilities for further investigation, exploring the domain structure of samples and establishing the multiferroic potential. Ideas for further study are outlined below.

4.4.1 The role of twinning

Evidence presented in this chapter has indicated that twinning in $CaCu_{0.15}Mn_{6.85}O_{12}$ crystals may give rise to the appearance of multiple families of satellite peaks, however visualisation of the twin structure has not yet been realised. An interesting avenue to explore would be the possibility of observing twins through optical microscopy and manipulating the twinning pattern through application of stress.

If twins of the form outlined in section 4.3.3.4 exist in crystals of $CaCu_{0.15}Mn_{6.85}O_{12}$, application of stress along one of the cubic diagonals may alter the twin distribution, favouring twins with the hexagonal c axis parallel to the direction of applied stress, and allowing these twins to grow, whilst minimising other sets of twins, as shown in Figure

4.23. Optical observation during this process may provide insight into twin growth and twin wall motion. Under application of sufficient stress, complete detwinning of the crystal may be possible.

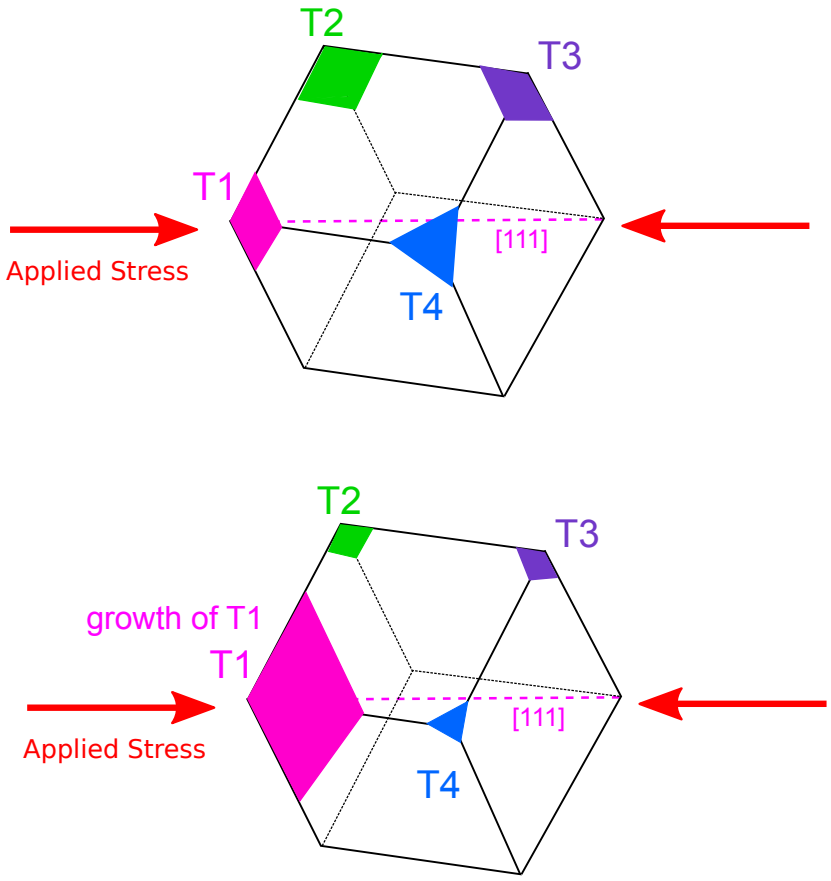


Figure 4.23: Assuming a twin model based upon four obverse twins with c axes along the four cubic diagonals, application of stress along a cubic diagonal may enable preferential growth of specific twin domains (T1 in this case), at the expense of other twins.

For $CaCu_xMn_{7-x}O_{12}$ crystals, lack of crystal transparency limits the use of optical microscopy methods for twin observation, as transmission techniques are not possible. Optical contrast in reflection may allow for twin observation, resulting from differences in surface topography, however, it may be necessary to use diffraction techniques for observation of twins and twin motion, studying variation in intensity of families of satellites associated with the different twins to gain insight into the twin proportions and distribution.

4.4.2 The magnetic structure

Analogously to $CaMn_7O_{12}$, it may be expected that an incommensurate magnetic modulation will accompany structural modulations in $CaCu_{0.15}Mn_{6.85}O_{12}$. The magnetic structure has not been studied here, but a reasonable starting point would be to look for magnetic diffraction peaks at a propagation vector $\frac{1}{2}q_c$, as observed for $CaMn_7O_{12}$. The difference in cation size and average valence on Mn1 sites due to copper doping will influence geometry and may impact the exchange constants predicted from GKA rules, as well as altering the magnitude of magnetic moments in the structure.

4.4.3 Ferroelectric polarisation and multiferroicity

Based upon the similarity of the modulation to $CaMn_7O_{12}$ and anticipated similarities in the magnetic structure, it is likely that the ferroelectric properties and multiferroicity in $CaCu_{0.15}Mn_{6.85}O_{12}$ will be similar to those outlined in Chapter 3, although as commented in section 4.4.2, it will be interesting to explore the impact that copper doping will have on the geometry of the magneto-orbital helix, and in turn on both the strength of magneto-electric coupling and the magnitude of the resulting polarisation.

Chapter 5

$NaMn_7O_{12}$

5.1 Introduction

5.1.1 Motivation for studying $NaMn_7O_{12}$

In section 3.1.1, the multiferroic potential of variants of the basic perovskite structure were discussed. Quadruple perovskites were pinpointed as promising structures, since the two inequivalent perovskite A sites can lead to structural distortions that may enhance antisymmetric DM exchange interactions and lead to multiferroicity. Experimental realisation of multiferroicity in the quadruple perovskite $CaMn_7O_{12}$ was discussed in Chapter 3. In Chapter 4, the impact of manipulating average manganese valence on physical properties was considered through the use of copper doping. Common to both these systems is an important role of charge and orbital ordering in influencing structural and magnetic properties. This chapter continues to explore charge/orbital ordering in manganite perovskite systems, here considering a different average Mn valence to that of $CaMn_7O_{12}$. Often A site doping is used to manipulate the average Mn valence in perovskites, however, a disordered distribution of dopant A site cations, often with a different size to the parent A site cations leads to local distortions in the system, and may give rise to difficulties in characterising the physical properties. $NaMn_7O_{12}$ has the same average B site Mn valence as the half doped simple perovskite $La_{0.5}Ca_{0.5}MnO_3$, ($Mn^{3.5+}$), but avoids complications of disorder related to A site doping. Thus $NaMn_7O_{12}$ is a good candidate for unambiguously studying

symmetry and Mn^{3+}/Mn^{4+} charge and orbital ordering [93, 94]. The weak insulating properties of $NaMn_7O_{12}$ mean it may also be a candidate multiferroic system, since a ferroelectric polarisation could arise from intermediate site centred/bond centred charge ordering as proposed by Efremov *et al.* [63].

5.1.2 The crystal structure

Prodi *et al.* determined the room temperature crystal structure of $NaMn_7O_{12}$ through refinement of powder x-ray diffraction data [67]. The room temperature space group is cubic $Im\bar{3}$, with lattice parameters $a = b = c = 7.3043(3)$ Å, as shown in Figure 5.1.

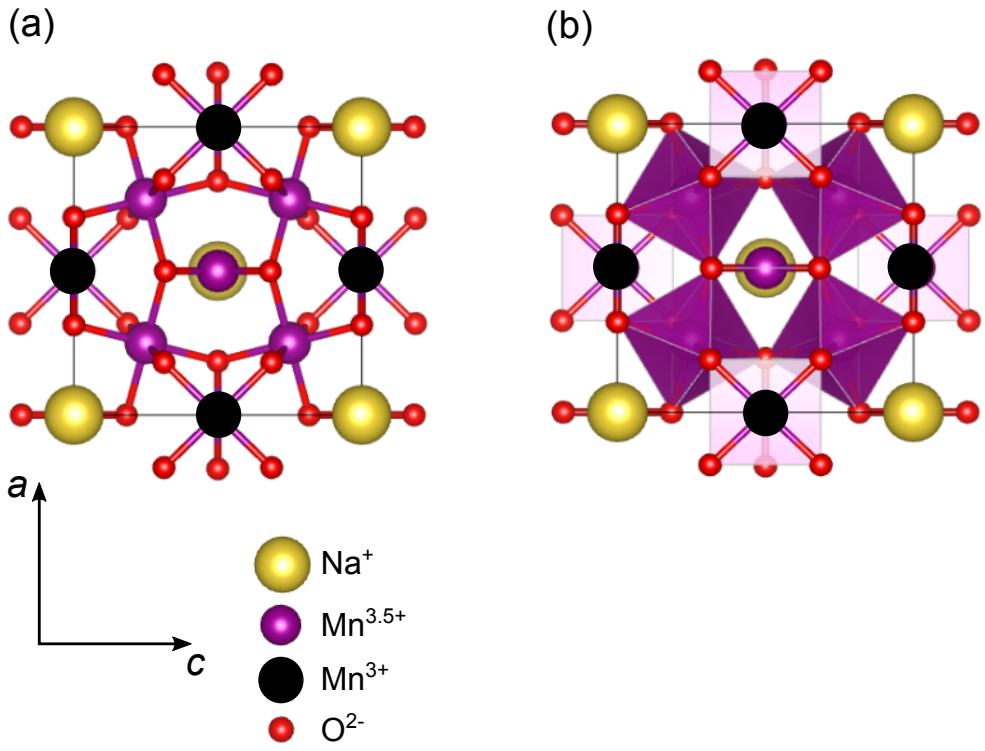


Figure 5.1: (a) The $Im\bar{3}$ room temperature crystal structure of $NaMn_7O_{12}$. Perovskite A sites are occupied by Na^+/Mn^{3+} in a 1:3 ratio. Disorder of Mn^{3+} and Mn^{4+} on perovskite B sites leads to an average valence of $Mn^{3.5+}$. In (b), coordination polyhedra; square planar for A sites and octahedral for B sites are shown.

Rewriting as $(NaMn_3^{3+})(Mn_4^{3.5+})O_{12}$, it is apparent how the crystal structure relates to the perovskite unit cell. Square planar perovskite A sites are occupied by Na^+ and

Mn^{3+}, whilst the remaining Mn cations occupy octahedrally coordinated B sites.

Lattice parameters show little variation with decreasing temperature, but below 176 K, new diffraction peaks indicate the emergence of a new phase. Two-phase coexistence has been observed between 168 and 176 K. Prodi *et al.* determined the low temperature phase to be monoclinic $12/m$ with lattice parameters at 150 K of $a = 7.3527$ Å, $b = 7.1986$ Å, $c = 7.3493$ Å, $\beta = 90.558°$. This phase transition is accompanied by checkerboard charge ordering on the octahedrally coordinated perovskite B sites within the monoclinic ac plane, such that the structure can be written as $(NaMn_3^{3+})(Mn_2^{3+}Mn_2^{4+})O_{12}$. Chains of the same Mn valence exist along the monoclinic b axis. The Mn_A^{3+} sites split over the $12/m$ $2b$, $2c$ and $2d$ sites whilst Mn_B sites split over the $4e$ and $4f$ positions. Oxygen atoms are split over 4 symmetrically distinct sites (O1-O4) with O1 and O4 occupying $8j$ positions and O2 and O3 occupying $4i$ positions. The monoclinic, charge ordered structure, with Na cations deleted for simplicity, is shown viewed down the b axis in Figure 5.2.

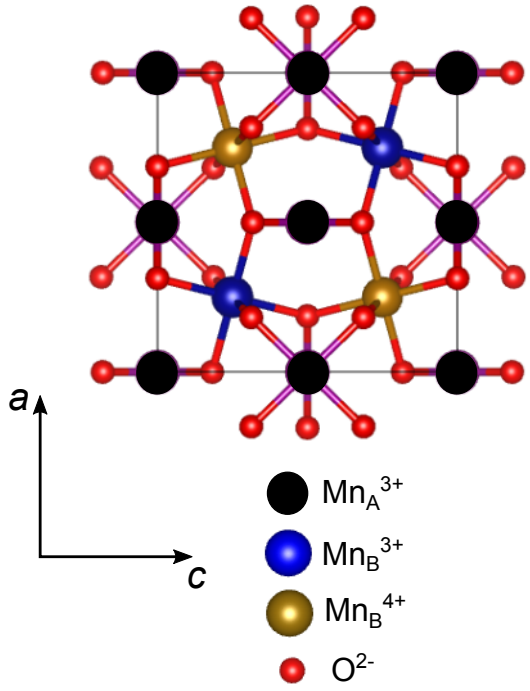


Figure 5.2: Charge ordering on the perovskite B sites of $NaMn_7O_{12}$ in the $I2/m$ phase, forming a checkerboard of Mn^{3+} (blue) and Mn^{4+} (gold) in the ac plane.

5.1.3 The magnetic structure

Using neutron powder diffraction, Prodi *et al.* [67] have determined that antiferromagnetic ordering exists below 168 K, coinciding with the onset of the single phase $I2/m$ structural ordering. The antiferromagnetic neutron diffraction peaks can be accounted for by CE ordering (see section motivationundoped) of the magnetic moments on octahedrally coordinated Mn sites, as shown in Figure 5.3.

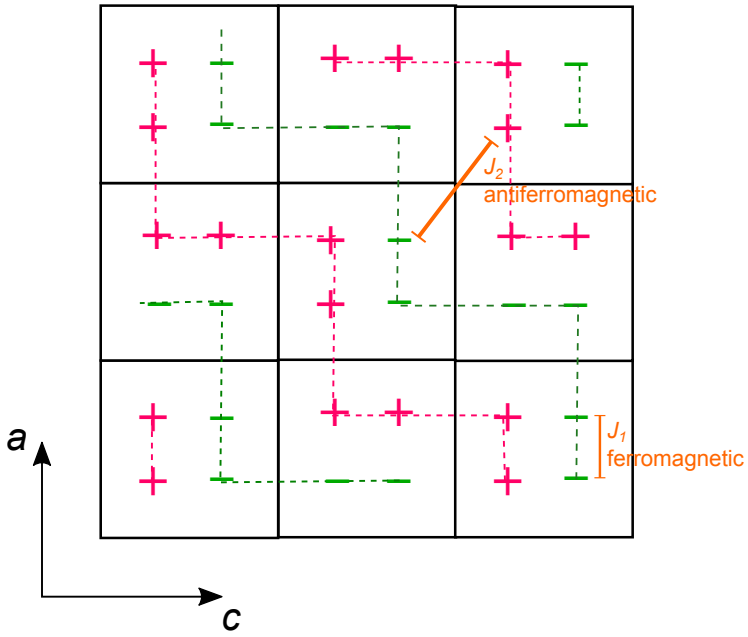


Figure 5.3: The CE antiferromagnetic structure of $NaMn_7O_{12}$, with ferromagnetic zigzag chains and antiferromagnetic interactions across the chains.

In addition to this ordering, below 90 K, Mn A sites order antiferromagnetically.

The CE ordering is the same as that found in $La_{0.5}Ca_{0.5}MnO_3$ [64]. Refined magnetic moments for Mn^{3+} and Mn^{4+} of 2.85 and 2.04 μ_B respectively are lower than those expected for a fully ordered arrangement of cations, and are in fact comparable to those obtained for $La_{0.5}Ca_{0.5}MnO_3$ at 1.5 K [95]. This indicates that structural fluctuations in $La_{0.5}Ca_{0.5}MnO_3$ do not significantly affect the behaviour of the magnetic moment in the CE structure. The reduced Mn magnetic moment may result from spin transfer onto oxygen anions.

5.1.4 Orbital ordering

From refinement of low temperature neutron diffraction data, and calculation of Mn-O bond lengths, Prodi *et al.* concluded that Jahn-Teller distortion occurs on both Mn_B sites, corresponding to apical compression of $Mn^{3+}O_6$ octahedra and elongation of $Mn^{4+}O_6$. At 150 K, the degree of Jahn-Teller distortion, defined by [96]:

$$\sigma_{JT} = \sqrt{\frac{1}{3}\sum_i [(\mathrm{Mn-O})_\mathrm{i} - <\mathrm{Mn-O}>]^2} \tag{5.1.1}$$

where $<\mathrm{Mn-O}>$ is the average Mn-O bond lengths for a given octahedron and the sum i is over all bond lengths for the octahedron, was found to be 4.2×10^{-2}Å. This indicates that for the $Mn^{3+}O_6$ octahedra the occupied $3d$ orbitals are of $x^2 - y^2$ symmetry.

This result would contrast to orbital occupation observed in the half doped manganites, in which Jahn-Teller distortions correspond to occupation of the $3z^2 - r^2$ orbital, and to the rotating pattern of orbital ordering established for $CaMn_7O_{12}$ (see Chapter 3), in which the $x^2 - y^2$ orbital is occupied only at nodal points of the modulation.

Ab initio band structure calculations performed by Streltsov and Khomskii [66] demonstrated that the orbital ordering proposed by Prodi *et al.* is inconsistent with the proposed magnetic ordering below 176 K. Exchange constant calculations, performed using the LIEP formalism [97], indicated that the orbital occupation proposed by Prodi *et al.*, with a single electron occupying the $x^2 - y^2$ orbital for $Mn^{3+}O_6$ octahedra, should stabilise ferromagnetic ordering, in contrast to the experimentally observed CE antiferromagnetic order. Additional calculations, using the experimentally observed magnetic structure, with antiferromagnetic CE ordering on all Mn_B sites, found that even in the absence of Jahn-Teller distortion, orbital ordering with alternating occupation of $3x^2 - r^2$ and $3y^2 - r^2$ was energetically favoured.

Streltsov and Khomskii concluded that orbital occupation in the low temperature crystal structure is in fact alternating occupation of $3x^2 - r^2$ and $3y^2 - r^2$ orbitals

for $Mn^{3+}O_6$ octahedra, forming stripes in the *ac* plane, as this would stabilise the experimentally observed magnetic structure

5.1.5 The purpose of this work

The studies of Prodi *et al.* and Streltsov and Khomskii agree that the high temperature $Im3$ structure undergoes a charge ordering phase transition between 168 and 176 K, forming a checkerboard of octahedrally coordinated Mn^{3+} and Mn^{4+} cations in the *ac* plane, with chains of the same valence along the *b* axis. The magnetic structure between 125 and 90 K is also agreed upon, with an antiferromagnetic CE structure. Within a given *ac* plane, ferromagnetic coupling exists within zig zag chains of MnO_6 octahedra, whilst antiferromagnetic coupling exists between the chains.

However, orbital ordering in the low temperature phase has caused debate, with Streltsov and Khomskii suggesting that the $x^2 - y^2$ orbital occupation proposed by Prodi *et al.* is inconsistent with an antiferromagnetic CE structure. Their alternative orbital ordering of alternating $3x^2 - r^2$ and $3y^2 - r^2$ orbitals is consistent with the experimentally observed magnetic structure, but has not been experimentally tested. If this pattern of orbital ordering is correct, the space group of the low temperature structure may not necessarily be consistent with that proposed by Prodi *et al.*.

In this chapter, the structure and symmetry of the low temperature phase is explored. A model is developed, based upon the orbital ordering patterns proposed above, and built within ISODISTORT. This model has then been tested against previously obtained single crystal neutron diffraction data from SXD, ISIS.

5.2 Building a Model for the Low Temperature Structure

5.2.1 Constructing the model using ISODISTORT

As a starting point, a model will be developed here that incorporates $I2/m$ symmetry along with a pattern of orbital ordering in agreement with that proposed by Streltsov and Khomski. In section 5.2.3, tests considering alternative space groups will be considered.

Five inequivalent Mn sites per unit cell are assigned: Mn1, Mn2, and Mn3 sites are square planar coordinated and occupied by Mn^{3+}, whilst Mn4 and Mn5 sites are octahedrally coordinated. As shown in Figure 5.4, here, Mn4 has been assigned as Mn^{4+} (shown in gold) and Mn5 has been assigned as Mn^{3+} (shown in blue).

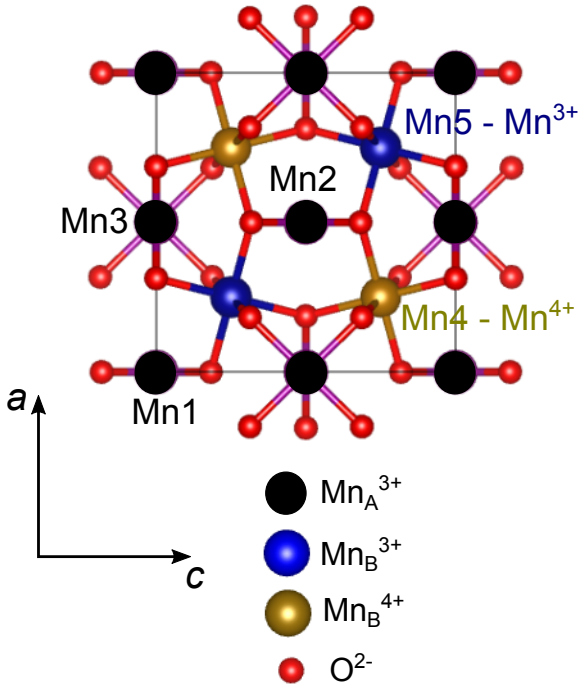


Figure 5.4: Assigning five inequivalent Mn sites in the low temperature $I2/m$ structure of $NaMn_7O_{12}$. Mn1, Mn2 and Mn3 are square planar coordinated, Mn^{3+} sites. Assuming checkerboard charge ordering in the ac plane, octahedrally coordinated Mn5 has been assigned as Mn^{3+} (blue), whilst Mn4 has been assigned as Mn^{4+} (gold).

Our model incorporates a pattern of orbital ordering consistent with that suggested by Streltsov and Khomskii. Mn5 octahedra are Jahn-Teller distorted (elongated) in the ac plane with the long axis of the octahedra alternating between the x and y directions, giving rise to an average crystal structure that appears to be compressed along the b axis. Mn4 sites are displaced in a an alternating striped pattern along the pseudocubic [110] directions (at 45° to the direction of octahedral elongation), as shown in Figure 5.5(a) and (b). The Mn4 octahedra as a whole remain undistorted.

This pattern of displacements leads to a doubling of the pseudo-cubic unit cell in the a and c directions, resulting in a supercell approximately four times larger than the parent $Im3$ cell, as shown in Figure 5.5(c).

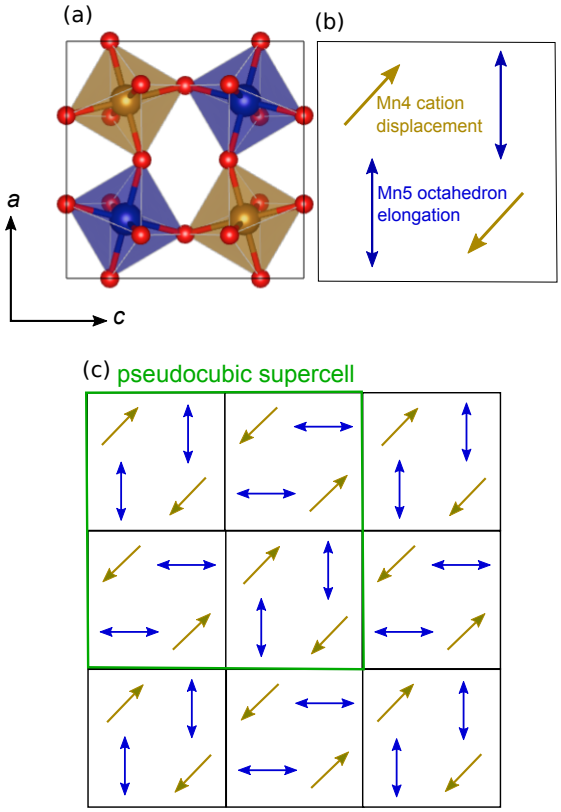


Figure 5.5: (a) and (b) Jahn-Teller active $Mn5O_6$ octahedra are elongated in the ac plane, with the long axis alternating between the a and c directions in adjacent unit cells. $Mn4O_6$ octahedra are not expected to be Jahn-Teller active, but Mn4 cations displace along psuedocubic [110] directions. This overall pattern leads to a doubling of the quadruple perovskite cell in both the a and c directions, as shown (c).

Distortions in the model can be described by a propagation vector $q = (\frac{1}{2}, 0, -\frac{1}{2})$ with

respect to the undistorted $I2/m$ cell, and the new primitive cell is the monoclinic cell shown in Figure 5.6.

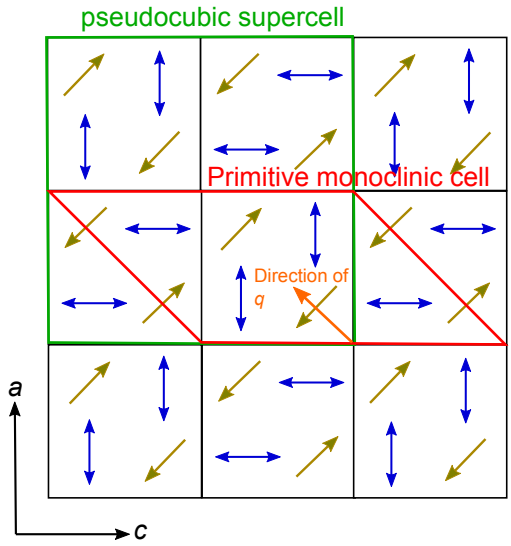


Figure 5.6: Incorporating Jahn-Teller distortions of $Mn5O_6$ and Mn4 cation displacements leads to a pseudo-cubic supercell, encompassing four quadruple perovskite cells. This corresponds to a primitive monoclinic cell, indicated in red.

The viability of this model can be tested using ISODISTORT, a programme that enables determination of allowed distortion modes based upon irreducible representations for a given crystal structure and symmetry [98, 99].

Starting from an undistorted, $I2/m$ charge ordered structure (shown in Figure 5.4 - based upon the low temperature structure proposed by Prodi *et al.* [67]) as the parent structure for ISODISTORT, atomic displacements of Mn4 (Mn^{4+}) sites and oxygens forming the surrounding octahedron were allowed, as shown in Figure 5.7. In accordance with the supercell defined in Figure 5.6(c), a constraint was imposed to consider distortions with a propagation vector $q = (\frac{1}{2},0,-\frac{1}{2})$ (corresponding to A point distortions in the first Brillouin zone as shown in Figure 5.7(b)).

For the Mn4 site, there are three modes (within a single irreducible representation), that can displace the Mn4 site whilst preserving $I2/m$ symmetry. Two of these modes involve the Mn4 cations sliding along one of the family of <100> directions of the parent cubic cell, and are inconsistent with the proposed model. The third mode, shown in Figure 5.8, involves sliding of the two Mn4 cations within a given unit cell,

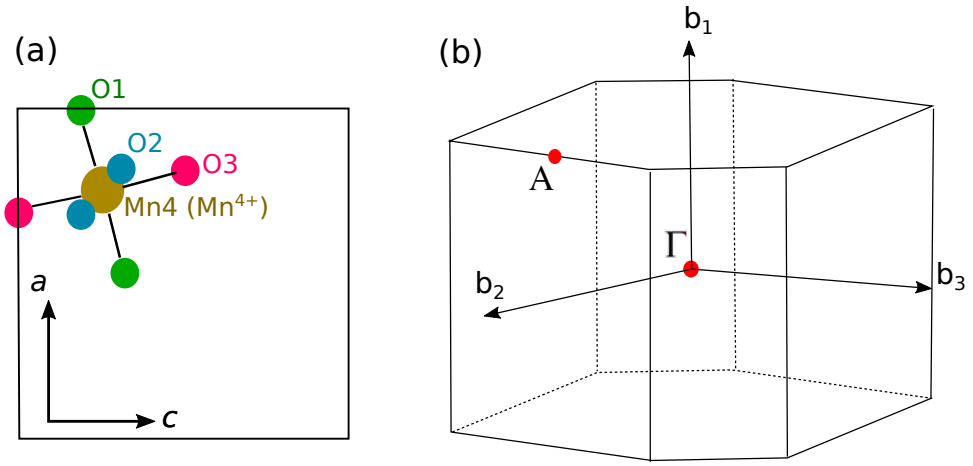


Figure 5.7: (a) The Mn4 sites and the surrounding oxygens forming an octahedron that are allowed to displace within the ISODISTORT model. (b) The model was constrained to consider A point distortions within the first Brillouin zone, as shown.

along opposite <110> type directions, consistent with the pattern of displacements shown in Figure 5.5.

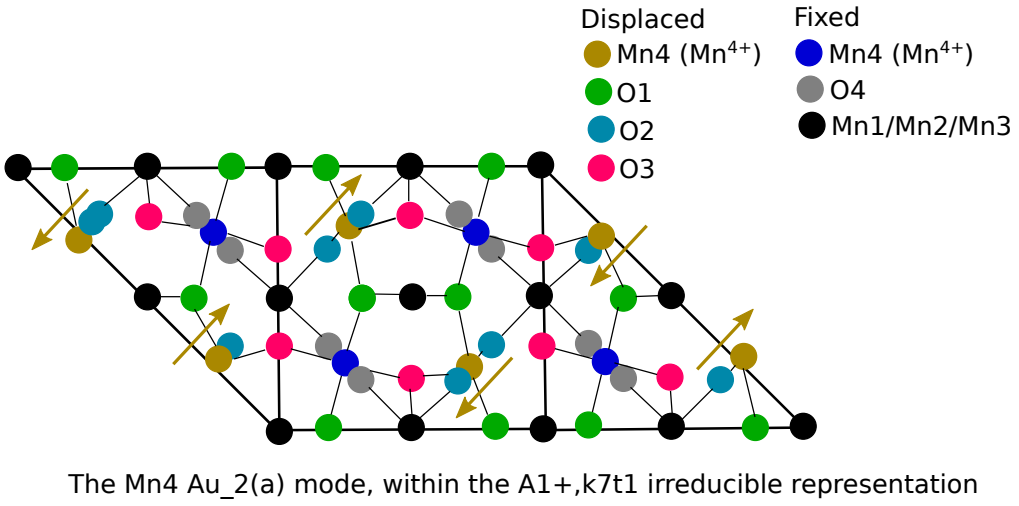


Figure 5.8: The symmetry allowed displacement mode for Mn4 that is consistent with the proposed model. Mn4 sites slide along alternating pseudo-cubic <110> directions.

Similarly, for each of the inequivalent oxygen sites forming an octahedron surrounding Mn4, (two O1 sites, two O2 sites and two O3 sites as defined in Figure 5.7(a)) there is a single mode that generates displacements consistent with the proposed model. These modes are shown in Figure 5.9.

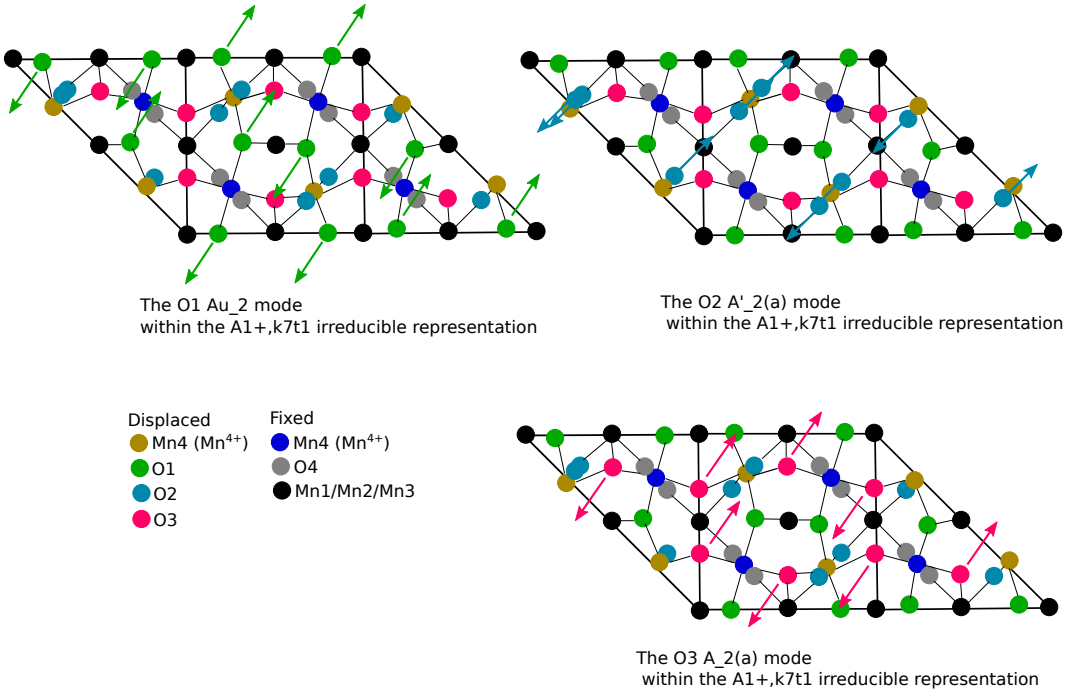


Figure 5.9: Symmetry allowed displacement modes for the oxygen anions forming the $Mn4O_6$ octahedra. These modes are consistent with the proposed model and preserve undistorted Mn4 octahedra.

Having established which modes are consistent with our proposed model, the amplitudes of each of these modes have been varied to determine the combination that best constrains the $Mn4O_6$ octahedra to be rigid and undistorted. A combination of amplitudes that successfully reproduce our model is given in Table 5.1: As shown in Figure 5.10 combining the oxygen displacements associated with these modes generates an overall distortion pattern that also results in the expected elongation of $Mn5O_6$ octahedra, shown in blue.

Atom	**Mode Label**	**Distortion Amplitude** (Å)
Mn4 (Mn^{4+})	Au2(a)	0.15
O1	A2(a)	0.25
O2	A'2(a)	-0.2
O3	A2(a)	-0.2

Table 5.1: The combination of symmetry allowed distortion modes for Mn4 and oxygen anions forming the surrounding octahedra that best reproduces our model. The amplitudes of these modes are approximate, obtained from inspection of the distorted structure generated by ISODISTORT.

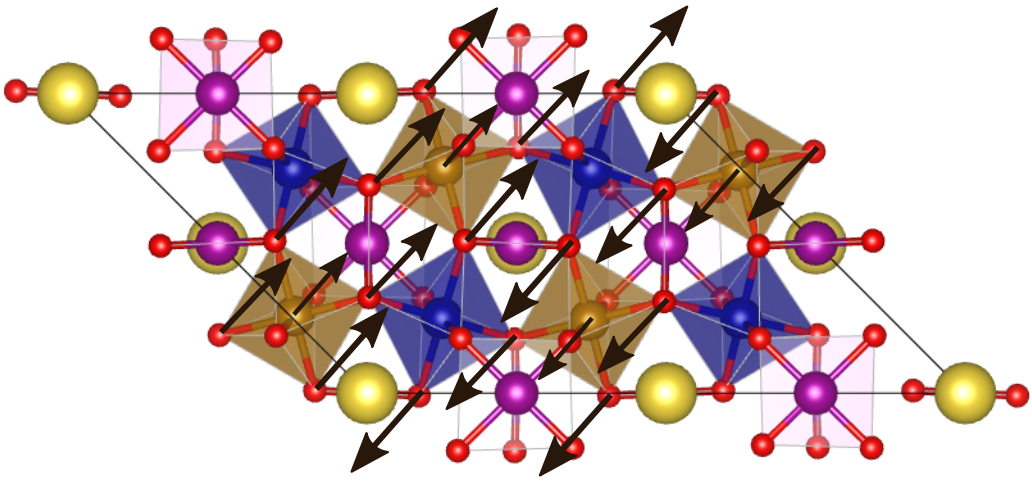


Figure 5.10: Combining the distortion modes from ISODISTORT (as indicated by the black arrows) generates a distorted low temperature structure in $I2/m$ symmetry showing Jahn-Teller elongation of the $Mn5O_6$ (blue) octahedra.

5.2.2 Testing consistency with the magnetic structure

In sections 5.1.4 and 5.1.5, a discrepancy between the orbital ordering pattern proposed by Prodi *et al.* and their experimentally determined CE antiferromagnetic structure was highlighted. Thus it is important to consider whether the model developed here is consistent with the low temperature magnetic structure.

The pattern of Jahn-Teller elongated octahedra described in section 5.2.1 manifests as the pattern of orbital occupation on Mn5 site shown in Figure 5.11(a), with long Mn5-O bonds corresponding to occupied $3d$ orbitals. The experimentally observed magnetic structure determined by Prodi *et al.* can be overlaid onto this pattern of orbital occupation, as shown in Figure 5.11(b). Checking for consistency, applying Goodenough-Kanamori-Anderson rules (as described in section 3.3.3) within a given zig-zag chain, interaction between the Mn5 $3d$ orbitals occupied by a single electron, and vacant Mn4 $3d$ orbitals leads to ferromagnetic exchange. Across zig-zag chains, interaction between two half filled Mn5 $3d$ orbitals or two vacant Mn4 $3d$ orbitals leads to antiferromagnetic exchange. These results are both consistent with the experimentally determined magnetic structure.

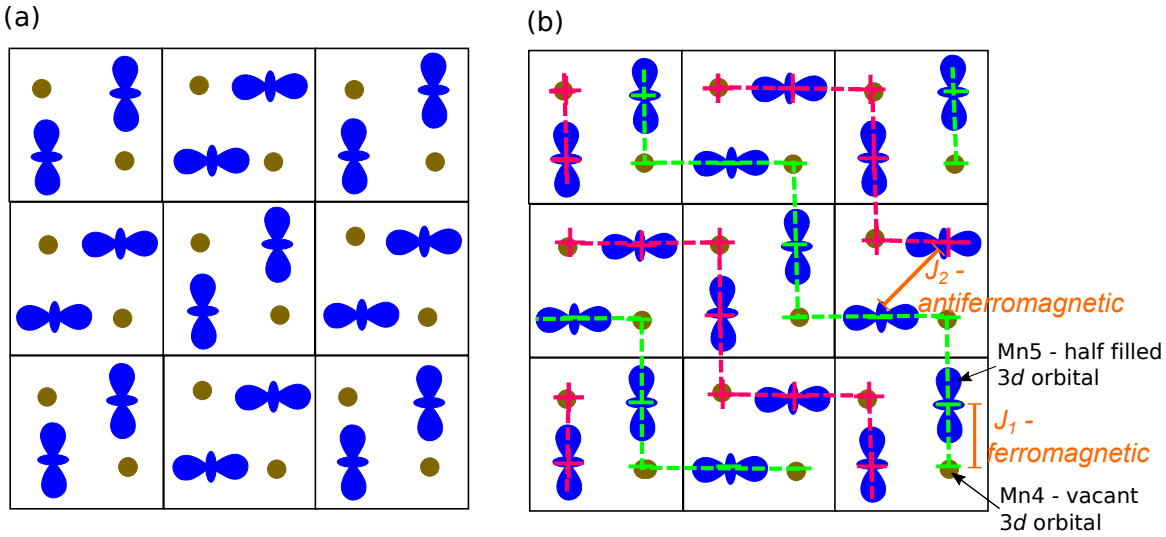


Figure 5.11: Comparing the pattern of orbital ordering generated from our model (a), incorporating Jahn-Teller elongated $Mn5O_6$ octahedra with the long axis alternating in the *ac* plane, with the experimentally determined magnetic structure of Prodi *et al.* (b). Occupied 3*d* orbitals for the Mn5 sites are shown in blue, whilst ferromagnetic zig-zag chains in the magnetic structure are indicated by green and pink dashed lines. Application of Goodenough-Kanamori-Anderson rules confirms consistency between the two structures.

5.2.3 Alternative models for the low temperature structure

Our model built within ISODISTORT above is consistent with both the pattern of orbital occupation proposed by Streltsov and Khomskii and the experimentally determined magnetic structure of Prodi *et al.*. However, this model is limited in that it does not incorporate effects of lattice strain associated with the distortion modes, and it may not be the only possible solution to the low temperature structure of $NaMn_7O_{12}$. In the development of our model, $I2/m$ symmetry has been assumed. Whilst breaking I centring in the distorted phase would require consideration of a different propagation vector, there may be alternative distortion modes that preserve I centring.

Returning to ISODISTORT, this possibility has been considered. An alternative irreducible representation gives rise to a distorted phase with symmetry $I2/a$. This symmetry still allows for checkerboard charge ordering of Mn cations in the *ac* plane, however within this irreducible representation there is no combination of distortion

modes that simultaneously gives rise to undistorted Mn4 octahedra and elongated Mn5 octahedra simultaneously.

Our model, developed in section 5.2.1 is the simplest solution, incorporating only single mode A point distortions associated with a one irreducible representation. Streltsov has independently developed a more complex model, using $C2/m$ symmetry, incorporating both Γ and A point distortions and accounting for effects of lattice strain [100].

Whilst Streltsov's model is significantly more complex, amplitudes for the modes that are common to both models are very similar, as shown in Tables 5.2 and 5.3 (modes common to both models are in bold). In fact, it is the modes that are common to both models that have the largest amplitude and dominate the overall pattern of distortions.

Atom	**Γ Mode**	**Amplitude** (Å)
O1	A-1(a)	0.17635
O1	A-2(a)	0.01456
O1	A-3(a)	-0.06728
O2	A'-1(a)	0.01088
O2	A'-2(a)	0.12343
O3	A'-1(a)	0.11117
O3	A'-2(a)	0.07923
O4	A-1(a)	-0.11916
O4	A-2(a)	-0.19867
O4	A-3(a)	0.05948

Table 5.2: Gamma Point distortion modes in Streltsov's model.

The modes common to both models are directly compared in Table 5.4.

Despite the added complexity in Streltsov's model, the resulting structure obtained is in agreement with that produced here. Both models generate equivalent patterns of Jahn-Teller elongated $Mn^{3+}O_6$ octahedra. Our model is a simplified version, considering only the displacive distortions of Mn^{4+} cations and oxygens forming the surrounding octahedra, and produced using single distortion modes for each atom.

Having developed a model for the low temperature structure, consistent with the experimentally determined magnetic structure determined by Prodi *et al.* and with

Atom	**A Mode**	**Amplitude** (Å)
Na	Bu-1(a)	-0.03889
Na	Bu-2(a)	-0.19485
Mn1	Bu-1(a)	0.15556
Mn1	Bu-2(a)	-0.10456
Mn5	Au-1(a)	0.03088
Mn5 (Mn^{4+})	**Au-2(a)**	**-0.15348**
Mn5	Au-3(a)	0.001765
O1	A-1(a)	0.10357
O1	**A-2(a)**	**-0.22426**
O1	A-3(a)	0.04586
O2	A'-1(a)	0.01765
O2	**A'-2(a)**	**-0.16668**
O3	A-1(a)	-0.14162
O3	**A-2(a)**	**-0.29014**
O3	A-3(a)	0.01685
O4	A'-1(a)	0.14970
O4	A'-2(a)	0.11521

Table 5.3: A Point distortion modes in Streltsov's model - modes consistent with our model are in bold.

Atom	**Distortion Mode**	**Amplitude** (Å) - **Our model**	**Streltsov's Model**
Mn5 (Mn^{4+})	Au-2(a)	0.15	-0.15348
O1	A-2(a)	0.25	-0.22426
O2	A'-2(a)	0.2	-0.16668
O3	A-2(a)	0.2	-0.29014

Table 5.4: Comparison of the amplitudes for distortion modes common to our model and Streltsov's model.

orbital ordering proposed by Streltsov and Khomskii [66], the natural progression is to test this model against experimental data.

A single crystal of $NaMn_7O_{12}$ was not available for this study, however in the section below, previously existing single crystal neutron diffraction data has been analysed and used to test our model.

5.3 Testing the Model - Refinement Against Experimental Data

5.3.1 Analysis of the single crystal neutron diffraction data

Single crystal neutron diffraction experiments at room temperature and 150 K had previously been performed using a large crystal of $NaMn_7O_{12}$ at SXD, ISIS (see section 2.3). In this section, this data is analysed using SXD2001 software [101, 102] to generate reflection files suitable for refinement of our structural model.

Initially, room temperature data is analysed. Diffraction peaks were collected from all 11 detector banks, and scaled using a vanadium standard. Ten strong reflections were used to determine the crystal orientation and **UB** matrix, and the **UB** matrix was then refined. Initial lattice parameters of $a = b = c = 7.3043(3)$ Å were taken from the powder x-ray diffraction refinement of Prodi *et al.* [67].

Peak integration was performed using the shoebox method with a variable box size. Visual checks were made to ensure accurate peak fitting and peaks were integrated manually where necessary. This process generated a reflection list of Bragg peaks indexed in the $Im3$ cell.

This data analysis was then repeated for the low temperature data measured at 150 K. In accordance with the model proposed in section 5.2.1, satellite peaks were indexed by a propagation $q = (1/2, 0, -1/2)$. In fact, three monoclinic domains exist in the low temperature structure, depending on the orientation of the unique axis with respect to the high temperature cubic structure. This gives rise to the appearance of three propagation vectors:

$$
\begin{aligned}
q_1 &= \left(\frac{1}{2}, \frac{1}{2}, 0\right), \\
q_2 &= \left(\frac{1}{2}, 0, -\frac{1}{2}\right), \\
q_3 &= \left(0, \frac{1}{2}, -\frac{1}{2}\right),
\end{aligned}
\tag{5.3.1}
$$

each associated with a single domain.

In the refinement below, satellites associated with a single domain have been considered.

5.3.2 Refinement of the single crystal neutron diffraction data

5.3.2.1 The room temperature structure

Reflection files generated for the room temperature and 150 K SXD data have been used to refine structural models in JANA2006 [84].

Initially, an $Im\bar{3}$ model based upon that generated by Prodi *et al.* from x-ray powder diffraction data was refined against the room temperature data. Allowing oxygen fractional coordinates, harmonic thermal parameters, a type I Lorentzian extinction model and overall scale to refine, a converged fit with an R-factor of 7.34% was obtained. A summary of the refined model is given below:

Atom	u	x	y	z	$\mathbf{U}_{iso}$
Na	0.041667	0	0	0	0.013(4)
Mn1	0.125	0	0.5	0.5	0.007(1)
Mn2	0.166667	0.25	0.25	0.25	0.003(1)
O1	0.5	0.3133(4)	0.1836(4)	0	0.0088(5)

Table 5.5: Refined oxygen fractional coordinates and thermal parameters for the room temperature $NaMn_7O_{12}$ structure.

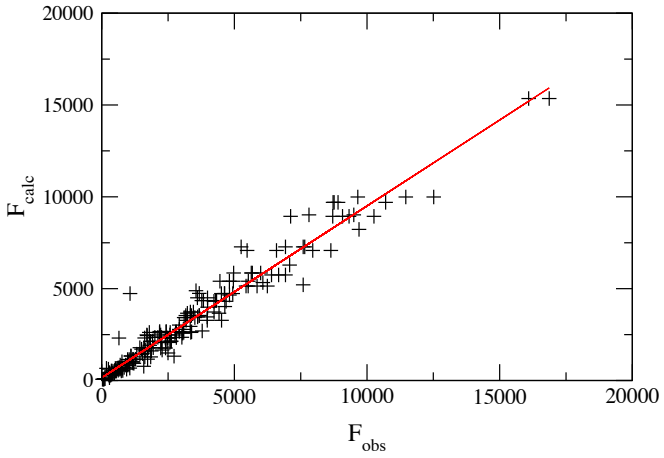


Figure 5.12: Comparison of calculated and observed structure factors for the room temperature $NaMn_7O_{12}$ structure - the refined model provides a good fit to the data.

5.3.2.2 The 150 K structure

Having confirmed the high temperature structure of the $NaMn_7O_{12}$ crystal to be consistent with that observed previously, 150 K data analysed in section 5.3.1 was used to refine a model for the low temperature structure.

The model was refined with a propagation vector $q = (\frac{1}{2}, \frac{1}{2}, 0)$, in a supercell related to the $I2/m$ cell used in data analysis by the following transformation of reciprocal lattice vectors:

$$\begin{aligned} \boldsymbol{a}^{*'} &= 1\boldsymbol{a}^* + 1\boldsymbol{b}^* + 0\boldsymbol{c}^*, \\ \boldsymbol{b}^{*'} &= -1\boldsymbol{a}^* + 1\boldsymbol{b}^* + 0\boldsymbol{c}^*, \\ \boldsymbol{c}^{*'} &= 0\boldsymbol{a}^* + 0\boldsymbol{b}^* + 1\boldsymbol{c}^*. \end{aligned} \tag{5.3.2}$$

The symmetry of the supercell is $I2/m$(ab0)00 (see Appendix C).

Initially, Bragg peaks were used to refine the average structure, in $I2/m$ symmetry with lattice parameters $a = 7.3493$ Å, $b = 7.3528$ Å, $c = 7.1986$ Å, $\gamma = 90.558°$ (taken from the refinement of Prodi *et al.*). In section 5.3.1 it was noted that three distinct monoclinic domains exist with respect to the high temperature cubic structure. Since

only a single domain is being refined here, Bragg peak intensities were scaled, assuming equal proportions of all three domains. Allowing scale, extinction, isotropic thermal parameters and average oxygen positions refine, a converged fit with R factor 10.75% was obtained.

Satellite peaks were then used to refine the model for the low temperature structure, based upon that proposed in section 5.2.1. A single atomic position modulation was allowed on each Mn4 site and the oxygen anions forming the surrounding octahedra (O1, O2 and O3 sites as defined in section 5.2.1.)

Atomic position modulations were of the form

$$\begin{aligned} x_{mod}(\bar{x}_q) &= x_0 + A_x \sin(2\pi\bar{x}_q) + l_x, \\ y_{mod}(\bar{x}_q) &= y_0 + A_y \sin(2\pi\bar{x}_q) + l_y, \\ z_{mod}(\bar{x}_q) &= z_0 + A_z \sin(2\pi\bar{x}_q) + l_z, \end{aligned} \tag{5.3.3}$$

where

$$x_q = \boldsymbol{q} \cdot \boldsymbol{r_0}. \tag{5.3.4}$$

In accordance with the model proposed in section 5.2.1, the Mn4 site was constrained to be modulated in the xy plane, fixing Fourier coefficients such that x_{mod}[Mn4] = -2×y_{mod}[Mn4]. Fourier coefficients for the oxygen modulations were freely fined within the constraints imposed by the space group. Refining the against the satellite peaks, keeping the average structure fixed, a converged refinement with an R-factor of 19.12% was obtained.

Completing a full refinement, incorporating Bragg and satellite peaks, a converged fit was obtained with an R-factor of 11.11%. An improved fit to the experimental data could not be obtained by allowing for modulations on Mn1, Mn2 and Mn3 sites, or by reversing the Mn5 and Mn4 site assignment.

The refined model is summarised below.

Refining our model proposed in section 5.2.1 against experimental data does produce a

Atom	**Occupation**	x	y	z	$\mathbf{U}_{iso}$
Na	0.25	0.0	0.0	0.0	0.007(2)
Mn1	0.25	0.0	0.0	0.5	0.007(2)
Mn2	0.25	0.5	0.0	0.0	0.008(3)
Mn3	0.25	0.5	0.0	0.5	0.016(4)
Mn4	0.5	0.25	0.25	0.25	0.006(2)
Mn5	0.5	0.25	0.75	0.25	0.008(2)
O1	1	0	0.81721	0.3136(5)	0.009(1)
O2	0.5	0.1845(9)	0.687(1)	0	0.011(1)
O3	0.5	0.1828(9)	0.315(1)	0	0.010(2)
O4	0.5	0.3135(6)	0	0.1833(5)	0.007(1)

Table 5.6: Refined oxygen fractional coordinates and isotropic thermal parameters for the low temperature structure of $NaMn_7O_{12}$.

Atom	$\mathbf{A}_x$	$\mathbf{A}_y$	$\mathbf{A}_z$
Mn4	0.007(1)	-0.0035	0.0
O1	0.015(4)	0.0014(6)	0.0
O2	0.017(9)	0.0	0.0
O3	0.006(2)	-0.006(3)	0.0
O4	0.008(2)	-0.0027(9)	0.011(1)

Table 5.7: Refined Fourier coefficients for the low temperature distorted structure of $NaMn_7O_{12}$.

reasonable fit. Jahn-Teller elongated octahedra with alternating long Mn5-O axes are generated, as shown in Figure 5.13(b). The two inequivalent Mn5 sites are indicated by the blue and green dotted lines and for each site, four short and two long Mn-O bonds exist, with the long pair of bonds switching between the two sites. The expected pattern of Mn4 cations is also produced, indicated by the orange arrows in Figure 5.13(c). However, there are some clear limitations in the refinement of this model. If the Fourier coefficients of the Mn4 site are not constrained, a repeatable converged fit to the experimental data cannot be reproduced. This is most likely due to a low number of satellite peaks available for fitting (a consequence of the low reciprocal space coverage of the SXD data), coupled with the weak intensity of the satellite peaks compared to the Bragg peaks. As shown in Figure 5.13(a), there is also some deviation from the expected ideal Mn4-O bond lengths. Whilst this may due to the quality of data available, it may also be indicative of an issue with our proposed model.

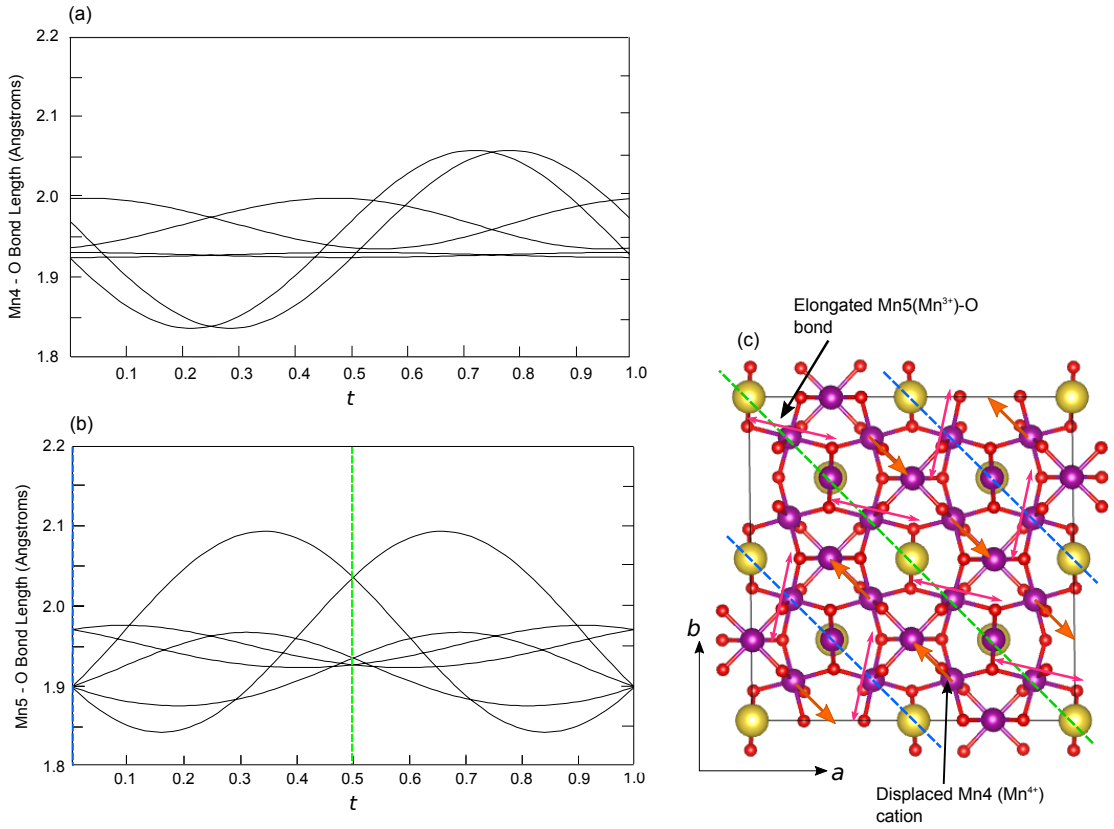


Figure 5.13: The refined low temperature model for $NaMn_7O_{12}$. Bond lengths are plotted as a function the scaled parameter $t = \bar{x}_q = \boldsymbol{q} \cdot \boldsymbol{r}_0$ with values of 0 and 0.5 corresponding to actual atomic positions. (a) Refined Mn4-O bond lengths. Deviation from ideal, undistorted $Mn4O_6$ octahedra expected from our model is evident, and may be due to a inaccuracy in the model, or due to the quality of experimental data. (b) Refined Mn5-O bond lengths. For the two inequivalent Mn5 sites indicated by the green and blue lines (also shown in (c)), one long pair of Mn-O bonds indicates Jahn-Teller elongated octahedra. (c) The refined structure, highlighting displacements of the Mn4 sites (orange arrows) and Jahn-Teller elongated $Mn5O_6$ octahedra (pink arrows).

To conclude, given the limited experimental data available, it is difficult to conclusively determine whether our model proposed in section 5.2.1 is correct. A structure with $I2/m$ symmetry incorporating Jahn-Teller elongated $Mn5O_6$ octahedra and displaced Mn4 cations appears to be consistent with the experimental data, but subtleties of the model cannot be established. Further experimental work is required, as discussed below.

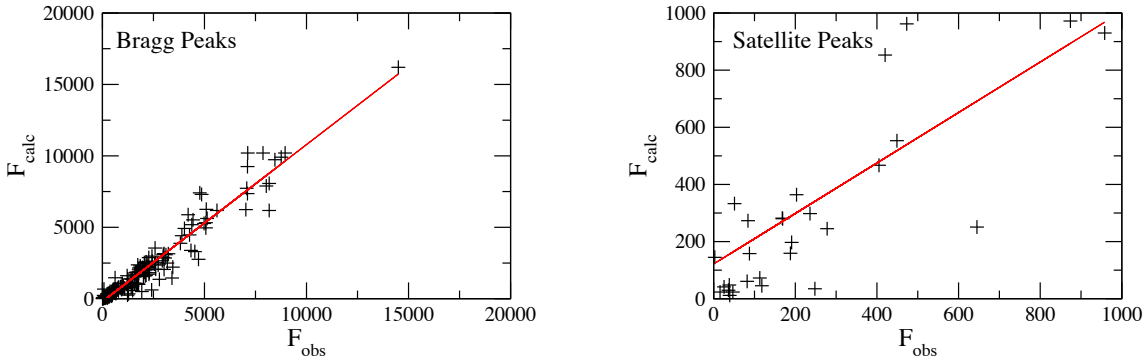


Figure 5.14: Comparing observed and calculated structure factors for (a) Bragg peaks and (b) satellite peaks in the low temperature $NaMn_7O_{12}$ structure. Good agreement is observed for the Bragg peaks, but a low number of satellite peaks makes it difficult to assess the quality of our model for the distorted structure.

5.4 Further Work

If a single crystal of $NaMn_7O_{12}$ were available, performing an x-ray diffraction experiment using SuperNova would be beneficial to determination the low temperature structure, as greater coverage of reciprocal space could be obtained, and twins may be observable in reciprocal lattice planes. This x-ray data would be used in conjunction with SXD data analysed in this study, as neutron diffraction data is beneficial in determining oxygen position, owing to the strong neutron scattering length.

In addition to the three monoclinic domains described in section 5.3.1, monoclinic structures commonly form twins related by a 180° rotation about one of the two non-unique axes. Tests incorporating a twin model of this type were made when refining the 150 K SXD data here, but did not significantly improve the fit. However, due to the low number of satellite peaks and poor reciprocal space coverage of the data used in this study, it cannot be ruled out that twinning of this type may exist in $NaMn_7O_{12}$ crystals. As discussed in Chapter 4, observation of twins may be possible through optical microscopy techniques, and if twins are found to exist, detwinning and manipulation of twin distribution may be possible, in order to simplify the data analysis.

If the low temperature structure of $NaMn_7O_{12}$ can be conclusively determined, further investigation could consider whether coupling may exist between the orbital ordering and magnetic structure, and whether this might result in a ferroelectric polarisation. As discussed in section 5.1.1, Efremov *et al.*, have proposed an intermediate bond centred/site centred state in doped simple perovskite manganites such as $La_{0.5}Ca_{0.5}MnO_3$. Based on dielectric constant measurements, this phase could be ferroelectric, but this is difficult to measure in the poorly insulating structures that have been investigated so far. $NaMn_7O_{12}$ has better insulating properties, and thus could be a good candidate system for exploring this possible ferroelectric phase.

Chapter 6

Concluding Remarks

Work presented in this thesis highlights the powerful influence orbital order can have over magnetic structures and magneto-electric coupling in quadruple perovskite structures.

Establishing the microscopic mechanism for multiferroicity in $CaMn_7O_{12}$ is an important breakthrough, firstly as an experimental realisation of orbital order in a multiferroic system, and also because of the novel and interesting physics associated with the "orbital helix".

Exploring the multiferroic potential of the $CaCu_xMn_{7-x}O_{12}$ series and $NaMn_7O_{12}$ is still a challenge for the future, but given the promising results obtained for $CaMn_7O_{12}$, and the progress made in understanding the modulated structure of $CaCu_{0.15}Mn_{6.85}O_{12}$, this is an avenue worth pursuing. Progress is likely to be aided by combining experimental magnetic and polarisation studies with theoretical predictions, such as those made by Efremov *et al.* [63], Streltsov and Khomskii [66], developing models for orbitally ordered structures and identifying potential ferroelectric phases.

Results presented in Chapter 4 and Chapter 5 highlight the the importance of considering bulk crystal formation when characterising physical properties. In this thesis, twinning in the low temperature phases of $CaCu_{0.15}Mn_{6.85}O_{12}$ and $NaMn_7O_{12}$ significantly impacts x-ray diffraction data. In future studies of quadruple perovskite structures, knowledge of twin models and crystal inhomogeneities may be crucial for correct interpretation of experimental results. Development of optical microscopy

techniques to observe twin structures may be beneficial, and beyond this, it would be interesting to explore the possibility of manipulating twin formation, through the application of stress, magnetic fields or electric fields. This could provide a means of ensuring the growth of single domain synthetic crystals, which would simplify structural analysis, and may also open up opportunities to tune directions and magnitudes of magnetic and ferroelectric properties, through control of domain structure.

Overall, results presented here provide evidence for continuing improvement in the search for multiferroic systems with technological potential; uncovering the microscopic mechanism for a large, magnetically induced ferroelectric polarisation in $CaMn_7O_{12}$. Promising avenues for future investigation have been highlighted, and it is hoped that the work presented in the later chapters will provide grounding for successful development of many more orbitally ordered systems and multiferroics.

References

[1] Hotta, T. *Rep. Prog. Phys.* **69**, 2061 (2006).

[2] Beale, T. A. W., Bland, S. R., Johnson, R. D., Hatton, P. D., Cezar, J. C., Dhesi, S. S., Zimmermann, M. V., Prabhakaran, D., and Boothroyd, A. T. *Phys. Rev. B* **79**, 054433 (2009).

[3] den Brink, J. V. and Khomskii, D. I. *J. Phys.-Condens. Mat.* **20**, 434217 (2008).

[4] Salje, E. K. H. *Chem. Phys. Chem.* **11**, 940 (2010).

[5] Blundell, S. *Magnetism in Condensed Matter.* Oxford University Press, (2001).

[6] Spaldin, N. A. *J. Solid State Chem.* **195**, 2 (2012).

[7] Cheong, S. W. and Mostovoy, M. *Nat. Mater.* **6**, 13 (2007).

[8] Aken, B. V., Rivera, J., Schmid, H., and Fiebig, M. *Nature* **449**, 702 (2007).

[9] Gorbatsevich, A. and Kopaev, Y. *Ferroelectrics* **449**, 702 (1994).

[10] Scott, J. F. *ISRN Materials Science* **2013**, 187313 (2013).

[11] Salje, E. K. H. *Ann. Rev. Mater. Res.* **42**, 265 (2012).

[12] Spaldin, N., Fiebig, M., and Mostovoy, M. *J. Phys.-Condens. Mat.* **20**, 434203 (2008).

[13] Wang, J., Neaton, J. B., Zheng, H., , Nagarajan, V., Ogale, S. B., Liu, B., Viehland, D., Vaithyanathan, V., Schlom, D. G., and Waghmare, U. V. *Science* **299**, 5613 (2003).

[14] Kimura, T., Goto, T., Shintani, H., Ishizaka, K., Arima, T., and Tokura, Y. *Nature* **426**, 55 (2003).

[15] Baryachtar, V. G., Lvov, V. A., and Jaoblonskii, D. A. *JETP Lett+.* **37**, 673 (1983).

[16] Stefanovskii, E. P. and Jaoblonskii, D. A. *Sov. J. Low Temp. Phys.* **12**, 478 (1986).

[17] Mostovoy, M. *Phys. Rev. Lett.* **96**, 067601 (2006).

[18] Maxwell, J. C. *Philos. T. R. Soc. Lond.* **155**, 459 (1865).

[19] Dzyaloshinskii, I. E. *Sov. Phys. JEPT-USSR* **10**, 628 (1960).

[20] Astrov, D. *Sov. Phys. JETP-USSR* **11**, 708 (1960).

[21] Schmid, H. *Ferroelectrics* **162**, 317 (1994).

[22] Hill, N. A. *J. Phys. Chem. B* **104**, 6694 (2000).

[23] Khomskii, D. I. *J. Mag. Mag. Mat.* **306**, 1.

[24] Zhao, T., Scholl, A., Zavaliche, F., Lee, K., Barry, M., Doran, A., Cruz, M. P., Chu, Y. H., Ederer, C., Spaldin, N. A., Das, R. R., Kim, D. M., Baek, S. H., Eon, C. B., and Ramesh, R. *Nat. Mater.* **5**, 823 (2006).

[25] Johnson, R. D., Barone, P., Bombardi, A., Bean, R. J., Picozzi, S., Radaelli, P. G., Oh, Y. S., Cheong, S. W., and Chapon, L. C. *Phys. Rev. Lett.* **110**, 217206 (2013).

[26] Quezel, S., Tcheou, F., Rossat-Mignod, J., Quezel, G., and Roudaut, E. *Physica B* **86**, 916 (1977).

[27] Dzyaloshinskii, I. *J. Phys. Chem. Solids* **4**, 241 (1958).

[28] Moriya, T. *Phys. Rev.* **120**, 91 (1960).

[29] Katsura, H., Nagaosa, N., and Balatsky, A. V. *Phys. Rev. Lett.* **95**, 057205 (2005).

[30] Baier, J., Meier, D., Berggold, K., Hemberger, J., Balbashov, A., Mydosh, J. A., and Lorenz, T. *Phys. Rev. B* **73**, 100402 (2006).

[31] Prokhnenko, O., Feyerherm, R., Dudzik, E., , Landsgesell, S., Aliouane, N., Hapon, L. C., and Argyriou, D. N. *Phys. Rev. Lett.* **98**, 05720 (2007).

[32] Feyerherm, R., Dudzik, E., Aliouane, N., and Argyriou, D. N. *Phys. Rev. B* **73**, 180401 (2006).

[33] Feyerherm, R., Dudzik, E., Wolter, A. U. B., Valencia, S., Prokhnenko, O., Maljuk, A., Landsgesell, S., Aliouane, N., Bouchenoire, L., Brown, S., and Argyriou, D. N. *Phys. Rev. B* **79**, 134426 (2009).

[34] Schierle, E., Soltwisch, V., Schmitz, D., Feyerherm, R., Maljuk, A., Yokaichiya, F., Argyriou, D. N., and Weschke, E. *Phys. Rev. Lett.* **105**, 167207 (2010).

[35] Blake, G. R., Chapon, L. C., Radaelli, P. G., Park, S., Hur, N., Cheong, S. W., and Rodriguez-Carvajal, J. *J. Phys.-Condens. Mat.* **21**, 5653 (2005).

[36] Brinks, H. W., Rodriguez-Carvajal, J., Fjellvag, H., Kjekshus, A., and Hauback, B. C. *Phys. Rev. B* **63**, 094411 (2001).

[37] Munoz, A., Casais, M. T., Alonso, J. A., Martinez-Lope, M. J., Martinez, J. L., and Fernandez-Diaz, M. T. *Inorg. Chem.* **40**, 1020 (2001).

[38] Lorenz, B., Wang, Y. Q., and Chu, C. W. *Phys. Rev. B* **76**, 104405 (2007).

[39] Anderson, P. W. *Phys. Rev.* **79**, 350 (1950).

[40] Kanamori, J. *Prog. Theor. Phys.* **17**, 177 (1957).

[41] Kanamori, J. *Prog. Theor. Phys.* **17**, 197 (1957).

[42] Goodenough, J. B. *J. Phys. Chem. Solids* **6**, 287 (1958).

[43] Hearmon, A. J., Fabrizi, F., Chapon, L. C., , Johnson, R. D., Prabhakaran, D., Streltsov, S. V., Brown, P. J., and Radaelli, P. G. *Phys. Rev. Lett.* **108**, 237201 (2012).

[44] Inami, T. *J. Solid State Chem.* **180**, 2075 (2007).

[45] of Technology Zurich, S. F. I. ETH Zurich - Electron Microscopy. `http://www.microscopy.ethz.ch/se.htm`, (2006). [Online; accessed 1-July-2015].

[46] McMorrow, D., Nielsen, J. A., and Nielsen, A. *Elements of Modern X-ray Physics*. Wiley, (2011).

[47] Jackson, J. D. *Classical Electrodynamics*. John Wiley & Sons, (1975).

[48] Radaelli, P. G. *Lecture notes distributed in Crystal Structure and Dynamics, University of Oxford* **Lectures 6-8**, pg. 4 (October 2014).

[49] Kittel, C. *Introduction to Solid State Physics*. John Wiley & Sons, (1976).

[50] Busing, W. R. and Levy, H. A. *Acta Crystallogr.* **22**, 457 (1967).

[51] CrysAlis PRO. Developed by Agilent Technologies Ltd., Yarnton, UK.

[52] Source, D. L. Birds eye view of the synchrotron. `http://www.diamond.ac.uk/Science/Machine/Components.html`, (2003). [Online; accessed 1-July-2015].

[53] Collins, S. P., Bombardi, A., Marshall, A., Williams, J. H., Barlow, G., Day, A. G., Pearson, M. R., Woolliscroft, R. J., Walton, R. D., and Beutier, G. *AIP Conference Proceedings* **1234**, 303 (2010).

[54] Nowell, H., Barnett, S. A., Christensen, K. E., Teat, S. J., and Allan, D. R. *J. Synchrotron. Radiat.* **19**, 435 (2012).

[55] Sears, V. F. *Neutron News* **3**, 26 (1992).

[56] Dove, M. T. *Introduction to Lattice Dynamics*. Cambridge University Press, (1993).

[57] Squires, G. L. *Introduction to the Theory of Thermal Neutron Scattering*. Cambridge University Press, (2012).

[58] Keen, D. A., Gutmann, M. J., and Wilson, C. C. *J. Appl. Crystallogr.* **39**, 714 (2006).

[59] Megaw, H. D. *Nature* **155**, 484 (1945).

[60] Miyake, S. and Ueda, R. *J. Phys. Soc. Jpn.* **1**, 32 (1946).

[61] Kay, H. F. and Vousden, P. *Philos. Mag.* **40**, 1019 (1949).

[62] Giovannetti, G., Kumar, S., den Brink, J. V., and Picozzi, S. *Phys. Rev. Lett* **103**, 037601 (2009).

[63] Efremov, D. V., den Brink, J. V., and Khomskii, D. I. *Nat. Mater.* **3**, 853 (2004).

[64] Radaelli, P. G., Cox, D. E., Marezio, M., and Cheong, S. W. *Phys. Rev. B.* **55**, 3015 (1997).

[65] Dong, S., Yu, R., Liu, J. M., and Dagotto, E. *Phys. Rev. Lett.* **103**, 107204 (2009).

[66] Streltsov, S. V. and Khomskii, D. I. *Phys. Rev. B.* **89**, 201115 (2014).

[67] Prodi, A., Gilioli, E., Gauzzi, A., Licci, F., Marezio, M., Bolzoni, F., Huang, Q., Santoro, A., and Lynn, J. W. *Nat. Mater.* **3**, 48 (2004).

[68] Liu, H., Dong, M., Du, Z. Z., Chu, P., and Liu, J. M. *EPL-Europhys. Lett.* **108**, 67012 (2014).

[69] Mezzadri, F., Calestani, G., Calicchio, M., Gilioli, E., Bolzoni, F., Cabassi, R., Marezio, M., and Migliori, A. *Phys. Rev. B.* **79**, 100106 (2009).

[70] Troyanchuk, I. O. and Chobot, A. N. *Crystallogr. Rep* **42**, 983 (1997).

[71] Bochu, B., Buevoz, J. L., Chenavas, J., Collomb, A., Joubert, J. C., and Marezio, M. *Solid State Commun.* **36**, 133 (1980).

[72] Przenioslo, R., Sosnowska, I., Suard, E., Hewat, A., and Fitch, A. N. *J. Phys.-Condens. Mat.* **14**, 5747 (2002).

[73] Perks, N. J., Johnson, R. D., Martin, C., Chapon, L. C., and Radaelli, P. G. *Nat. Commun.* **3**, 1277 (2012).

[74] Przenioslo, R., Sosnowska, I., Suard, E., Hewat, A., and Fitch, A. N. *Physica* **344B**, 358 (2002).

[75] Sławiński, W., Przenioslo, R., Sosnowska, I., Bieringer, M., Margiolaki, I., and Suard, E. *Acta. Crystallogr. A* **65**, 535 (2009).

[76] Przenioslo, R., Sosnowska, I., Suard, E., Hewat, A., and Fitch, A. N. *Solid State Commun.* **111**, 687 (1999).

[77] Sánchez-Andújar, M., Yáñez-Vilar, S., Biskup, N., Castro-García, S., Mira, J., Rivas, J., and Señarís-Rodríguez, M. A. *J. Magn. Magn. Mater.* **321**, 1739 (2009).

[78] Zhang, G., Dong, S., Yan, Z., Guo, Y. Y., Zhang, Q. F., Yunoki, S., Dagotto, E., and Liu, J. M. *Phys. Rev. B.* **84**, 174413 (2011).

[79] Johnson, R. D., Chapon, L. C., Khalyavin, D. D., Manuel, P., Radaelli, P. G., and Martin, C. *Phys. Rev. Lett.* **108**, 067201 (2012).

[80] Sławiński, W., Przenioslo, R., Sosnowska, I., and Chrobak, A. *J. Phys. Soc. Jpn.* **81**, 094708 (2012).

[81] LeBail, A., Duroy, H., and Fourquet, J. L. *Mater. Res. Bull.* **23**, 447 (1988).

[82] Rodriguez-Carvajal, J. *Physica B* **192**, 55 (1993).

[83] Rodriguez-Carvajal, J. *IUCr Newsletter* **26**, 12 (2001).

[84] Patrick, V., Dusek, M., and Palatines, L. *Z. Kristallogr.* **199**, 345 (2014).

[85] Goodenough, J. B. and Cooper, S. L. *Localised to Intinerant: Electronic Transition in Perovskite Oxide.* Springer, (2001).

[86] Wu, H., Chang, C. F., Schumann, O., Hu, Z., Cezar, J. C., Burnus, T., Hollmann, N., Brookes, N. B., Tanaka, A., Braden, M., Tjeng, L. H., and Khomskii, D. *Phys. Rev. B.* **84**, 115126 (2011).

[87] Brown, I. D. and Altermatt, D. *Acta. Crystallogr.* **B41**, 244 (1985).

[88] Pauling, L. *The Nature of the Chemical Bond and the Structure of Molecules and Crystals; an Introduction to Modern Structural Chemistry.* Cornell University Press, (1960).

[89] Sławiński, W., Przenioslo, R., Sosnowska, I., and Bieringer, M. *J Phys.-Condens. Mat.* **22**, 186001 (2010).

[90] Vasilev, A. N. and Volkova, O. S. *Low. Temp. Phys.* **33**, 11 (2007).

[91] Mühlbauer, S., Binz, B., Jonietz, F., Pfleiderer, C., Rosch, A., Neubauer, A., Georgii, R., and Böni, P. *Science* **323**, 915 (2009).

[92] Hahn, T. and Paufler, P. *International Tables for Crystallography, Volume A, Chapter 4.3.* Wiley Online Library, (2006).

[93] Gilioli, E., Calestani, G., Licci, F., Gauzzi, A., Bolzoni, F., Prodi, A., and Marezio, M. *J. Cryst. Growth.* **275**, 877 (2005).

[94] Gilioli, E., Calestani, G., Licci, F., Gauzzi, A., Bolzoni, F., Prodi, A., and Marezio, M. *Solid State Sci.* **7**, 746 (2005).

[95] Huang, Q., Lynn, J. W., Erwin, R. W., Santoro, A., Dender, D. C., Smolyaninova, V. N., Ghosh, K., and Greene, R. L. *Phys. Rev. B.* **61**, 8895 (2000).

[96] Radaelli, P. G., Iannone, G., Marezio, M., Hwang, H. Y., Cheong, S. W., Jorgensen, J. D., and Argyriou, D. N. *Phys. Rev. B.* **56**, 8265 (1997).

[97] Liechtenstein, A., Gubanov, V., Katsnelson, M., and Anisimov, V. *J. Magn. Magn. Mat.* **36**, 125 (1983).

[98] ISOTROPY Software Suite. Available from iso.byu.edu.

[99] Campbell, B. J., Stokes, H. T., Tanner, D. E., and Hatch, D. M. *J. Appl. Crystallogr.* **39**, 607 (2006).

[100] Discussed in a personal communication.

[101] Gutmann, M. J. *Acta Crystallogr. A* **61**, 164 (2005).

[102] SXD2001. M J Gutmann, ISIS Facility, Rutherford Appleton Laboratory, Oxfordshire, UK.

[103] deWolff, P., Janssen, T., and Janner, A. *Acta Crystallogr. A* **37**, 625 (1981).

Appendix A

The Structure Factor for Modulated Crystals

In section 2.2.1.3, the structure factor for elastic x-ray scattering from a periodic crystal was derived, based upon the classical Thomson scattering formalism. Here, this formalism is extended to the case of modulated crystals.

Figure A.1 shows a 1-d sinusoidal modulation to a 2-d lattice of atoms. The modulation can be described by a propagation vector of the form $\mathbf{q} = (0, 0, q_z)$, where q_z is related to the period of the modulation (T) by $\mathrm{T} = 1/q_z$.

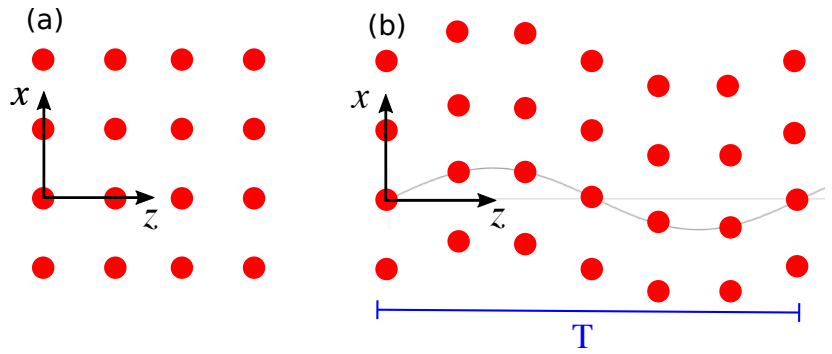


Figure A.1: (a) A primitive 2-d square lattice with one atom per unit cell (b) this simple square lattice with 1-d sinusoidal modulation of period T, along z.

Each atom is associated with a unit cell (n) with lattice vector $\mathbf{R}_n$. Hence, for the case of a primitive lattice, the displacement of the nth atom can be described by the vector

$$\mathbf{d}_n = \begin{pmatrix} 0 \\ 0 \\ d(e^{i\mathbf{R}_n\cdot\mathbf{q}} + e^{-i\mathbf{R}_n\cdot\mathbf{q}}) \end{pmatrix} \tag{A.0.1}$$

where d parameterises the size of the displacement. For an unmodulated primitive lattice, atomic positions are given by $\mathbf{r}_n = \mathbf{R}_n$, and for the modulated structure shown in Figure A.1, the atomic positions are given by $\mathbf{r}_n = \mathbf{R}_n + \mathbf{d}_n$.

The structure factor then becomes

$$F(\mathbf{Q}) = \sum_n f_n(\mathbf{Q}) e^{i\mathbf{q}\cdot(\mathbf{R}_n+\mathbf{d}_n)} \tag{A.0.2}$$

$$\rightarrow F(\mathbf{Q}) = \sum_n f_n(\mathbf{Q}) e^{i\mathbf{Q}\cdot\mathbf{R}_n} e^{iQ_z d[\exp(i\mathbf{R}_n\cdot\mathbf{q}+\exp(-i\mathbf{R}_n\cdot\mathbf{q})]}. \tag{A.0.3}$$

Expanding the second exponential term:

$$F(\mathbf{Q}) = \sum_n f_n(\mathbf{Q}) e^{i\mathbf{Q}\cdot\mathbf{R}_n} \left(1 + iQ_z d(e^{i\mathbf{R}_n\cdot\mathbf{q}} + e^{-i\mathbf{R}_n\cdot\mathbf{q}}) + \frac{i^2 Q_z^2 d^2 (e^{i\mathbf{R}_n\cdot\mathbf{q}} + e^{-i\mathbf{R}_n\cdot\mathbf{q}})^2}{2!} + ...\right). \tag{A.0.4}$$

Since the displacements associated with the modulation are expected to be small, the series can be truncated at the quadratic term, giving

$$\begin{aligned} F(\mathbf{Q}) \approx \sum_n f_n(\mathbf{q}) e^{i\mathbf{Q}\cdot\mathbf{R}_n} \\ + \sum_n f_n(\mathbf{Q}) iQ_z d(e^{i\mathbf{R}_n\cdot\mathbf{q}} + e^{-i\mathbf{R}_n\cdot\mathbf{q}}) \\ - \frac{1}{2}\sum_n f_n(\mathbf{Q}) Q_z^2 d^2 (e^{i\mathbf{R}_n\cdot 2\mathbf{q}} + e^{-i\mathbf{R}_n\cdot 2\mathbf{q}} + 2). \end{aligned} \tag{A.0.5}$$

Rewriting this expression:

$$F(\mathbf{Q}) \approx (1 - Q_z^2 d^2) \sum_n f_n(\mathbf{Q}) e^{i\mathbf{Q}\cdot\mathbf{R}_n} + iQ_z d \sum_n f_n(\mathbf{Q}) e^{i(\mathbf{Q}+\mathbf{q})\cdot\mathbf{R}_n} + iQ_z d \sum_n f_n(\mathbf{Q}) e^{i(\mathbf{Q}-\mathbf{q})\cdot\mathbf{R}_n} - \frac{1}{2} Q_z^2 d^2 \sum_n f_n(\mathbf{Q}) e^{i(\mathbf{Q}+2\mathbf{q})\cdot\mathbf{R}_n} - \frac{1}{2} Q_z^2 d^2 \sum_n f_n(\mathbf{Q}) e^{i(\mathbf{Q}-2\mathbf{q})\cdot\mathbf{R}_n}. \quad \text{(A.0.6)}$$

The phase factor given by

$$\sum_n f_n(\mathbf{Q}) e^{i\mathbf{Q}\cdot\mathbf{R}_n} \quad \text{(A.0.7)}$$

is only non-zero for the case where $\mathbf{Q}$ is equal to a reciprocal lattice vector $\mathbf{G}$ (see section 2.2.1.3), and writing this condition as a delta function:

$$F(\mathbf{Q}) \approx (1 - Q_z^2 d^2) f(\mathbf{Q}) \delta(\mathbf{Q} - \mathbf{G}) + iQ_z d f(\mathbf{Q}) \delta(\mathbf{Q} + \mathbf{q} - \mathbf{G}) + iQ_z d f(\mathbf{Q}) \delta(\mathbf{Q} - \mathbf{q} - \mathbf{G}) - \frac{1}{2} Q_z^2 d^2 f(\mathbf{Q}) \delta(\mathbf{Q} + 2\mathbf{q} - \mathbf{G}) - \frac{1}{2} i Q_z^2 d^2 f(\mathbf{Q}) \delta(\mathbf{Q} - 2\mathbf{q} - \mathbf{G}). \quad \text{(A.0.8)}$$

Diffraction intensity is proportional to the square of the structure factor ($|F(\mathbf{Q})|^2$). Thus, for each Bragg peak, satellites are expected to be located at $\mathbf{G} \pm \mathbf{q}$, with intensity proportional to d^2, and second order satellite peaks at $\mathbf{G} \pm 2\mathbf{q}$, with intensity proportional to d^4.

Appendix B

Refinement of X-ray Diffraction Data

B.1 Powder Diffraction Data

Rietveld Refinement and the LeBail Method

As explained in section 2.2.1.4, in an ideal powder sample, all crystal orientations exist simultaneously in equal proportions. Orientational averaging means that measurements of 3-dimensional reciprocal space are projected onto a single dimension in a diffraction pattern. In theory, all diffraction peaks should be observed simultaneously, with contributions from an equal number of crystallites (in practice only a small number of crystallites will be in the correct orientation to diffract).

As discussed in section 2.2.1.3, the intensity of diffraction peaks is proportional to the square of the structure factor, and hence from analysis of a large number of diffracted peaks, atomic positions of atoms within the unit cell can be determined.

In a powder diffraction pattern peak intensities are complicated by a number of factors, relating to the quality of the powder, and to the projection of 3-dimensional space onto one dimension which results in families of {hkl} planes being associated with a single peak. Diffraction intensity for a position i in the pattern is calculated as

$$y_i = s \sum \mathbf{L}_{hkl} |\mathbf{F}_{hkl}|^2 \phi(2\theta_i - \theta_{hkl}) \mathbf{P}_{hkl} \mathbf{A} + y_{bi}, \tag{B.1.1}$$

where

- s is a scale factor.
- $\mathbf{L}_{hkl}$ incorporates peak multiplicity (dependent upon crystal symmetry), Lorentz factor (a measure of the amount of time that a point of reciprocal lattice remains on the sphere of reflection during the measuring process), and a polarisation factor.
- $\mathbf{F}_{hkl}$ is the structure factor for a given hkl Bragg peak.
- ϕ is a profile function (incorporating both sample and instrumental contributions to peak profiles).
- $\mathbf{P}_{hkl}$ is a factor accounting for preferred crystallite orientation within the powder.
- $\mathbf{A}$ is an absorption factor.
- y_{bi} is the background intensity for the i^{th} step.

Starting from a reasonable initial "guess" structural model, incorporating space group symmetry, approximate lattice parameters and approximate atomic positions, a predicted powder diffraction can be calculated. Through use of the **Rietveld method**, the difference between the experimentally observed and calculated diffraction pattern is minimised by refining the structural model.

In this thesis, a simpler approach is used, since powder diffraction is used to calculate lattice parameters, and not atomic positions. Peak positions, rather than peak intensities are dependent upon lattice parameters and the crystal symmetry. Diffraction peak positions are determined from the average unit cell parameters of many crystallites, and hence powder diffraction is a valuable tool for determination of lattice parameters.

Using a similar, but simplified version of the Rietveld method, in the **LeBail method** $\mathbf{F}_{hkl}$ values are fixed, and an initial model incorporating approximate lattice parameters and symmetry is built. The background to the diffraction pattern is fitted, and lattice parameters and peak shape profile parameters are iteratively refined to produce

the best fit to the experimentally observed diffraction pattern. The function that is minimised in the refinement process is

$$\chi^2 = \sum_{i=1}^{n} w_i \left(y_i - y_{c,i}\right)^2, \tag{B.1.2}$$

where w_i is a weighting parameter, and y_i and $y_{c,i}$ are the observed and calculated intensities for the ith point in the diffraction pattern.

Various "goodness of fit" parameters can be calculated as an indication of the quality of the model and hence the accuracy of the parameters derived from the refinement.

B.2 Single Crystal Diffraction Data Structural Optimisation and Refinement

B.2.1 The phase problem

Determination of atomic positions within a crystal unit cell using single crystal x-ray diffraction should be more simple than through powder diffraction. For a given x-ray wavelength and scattering angle, a diffraction peak corresponds to a specific set of lattice planes defined by *hkl* Miller indices, rather than a projection of a family of planes in 3-d reciprocal space onto a single dimension.

However, complications arise in determining absolute atomic positions from the crystal structure factor.

In section 2.2.1.3 it was established that the crystal structure factor, given by

$$F(\mathbf{Q}) = r_0 \sum_i \int_{Unitcell} f(\mathbf{r}) \mathrm{e}^{-i\mathbf{Q}\cdot\mathbf{r}} d\mathbf{r}, \tag{B.2.1}$$

(for a scattering vector $\mathbf{Q}$ and atoms with position vectors $\mathbf{r}$) is proportional to the

Fourier transform of electron charge density, integrated over the crystal unit cell. The quantity actually measured in an x-ray diffraction experiment, the scattering cross section, is proportional to the square of the crystal structure factor. This leads to problem directly reconstructing charge density maps from x-ray diffraction data, in order to determine atomic positions. Whilst the amplitudes of the structure factors are known, the phase information is lost. This is the "phase problem".

Solving a crystal structure from x-ray diffraction data is therefore effectively a process of phasing reflections.

Whilst scattering density cannot be obtained without phasing the reflections, it is possible to gain some information about the scattering density in a crystal without knowledge of the phases.

B.2.2 The Patterson function

Taking the square of the crystal structure factor (as measured in a scattering experiment):

$$|F(\mathbf{q})|^2 = r_0^2 \sum_i \int \int_{Unitcell} d\mathbf{r} d\mathbf{r'} f(\mathbf{r}) f(\mathbf{r'}) e^{-i\mathbf{q}\cdot(\mathbf{r}-\mathbf{r'})} \tag{B.2.2}$$

.

Through a change of variable, it can be shown that

$$\frac{1}{r_0^2 v_0^2} \sum_\tau |F(\tau)|^2 e^{\tau\cdot\mathbf{r}} = \int_{Unitcell} d\mathbf{r} d\mathbf{r'} f(\mathbf{r}) f(\mathbf{r}+\mathbf{r'}) = P(\mathbf{r}). \tag{B.2.3}$$

The function P($\mathbf{r}$) is the **Patterson function**.

Since atomic scattering densities are zero except at atomic positions, the Patterson function will be zero except at the origin ($\mathbf{r} = 0$), and for values of $\mathbf{r}$ corresponding to vectors joining two atoms. At these vectors, the Patterson function will have peaks,

with the height of the peak being proportional to $Z_i Z_j$ (where Z is the atomic number) for atoms of different species i and j.

In simple cases, the Patterson function can be uniquely interpreted to yield exact positions of atoms in the unit cell, but this method is of more limited use in solving complex crystal structures.

B.2.3 Direct methods

If no prior knowledge of the crystal structure is available, **Direct methods** can be employed to solve moderately complex crystal structures. Exploiting inequalities between terms in the Fourier series for positive definite functions, probable phase relations between reflections can be obtained based on intensity ratios. After initial phasing of reflections, Fourier maps are calculated and attempts are made to locate atoms. Phasing is then modified in an iterative manner to determine atomic positions from Fourier maps.

In general, at least some degree of prior knowledge is available when solving a crystal structure from x-ray diffraction data, for example, the number of formula units per unit cell and the stoichiometry are nearly always known. If information available is limited and fragmented, it may be incorporated using the direct methods outlined above.

B.2.4 Structural optimisation

For the structural problems in this thesis, the atomic structures being solved are variants of known structures. In this case, **Structural Optimisation** is employed; minimising the agreement between observed and calculated squared structure factors, as a function of the free parameters that are being determined.

JANA2006 has been used for structure determination in this thesis. A least squares refinement procedure is used to minimise the agreement between observed structural

parameters and those of an initial model:

We can define a model f^* that operates on a set of parameters n_i to make a prediction $f^*(n_i)$. In the case of a crystal structure refinement, the crystallographic model is a function $f^*(hkl, \lambda x_i, y_i, z_i...)$ (where x_i, y_i and z_i are fractional coordindates), which predicts diffraction peak intensities I_{hkl} for a given set of atomic planes; hence

$$I^*_{hkl} = f^*(hkl, \lambda x_i, y_i, z_i...). \tag{B.2.4}$$

For a given set of parameters hkl, $\lambda x_i, y_i, z_i...$, the predicted Bragg intensity (I^*_{hkl}) can be calculated.

Refining the parameters n_i to improve the model $f^*(n_i)$, requires a corresponding set of observations, in this case, experimentally observed diffraction peak intensities. The function $f(n_i)$ returns these observations.

A quantity called the residual describes how closely the calculated model matches observations, and in the case of a least squares refinement, the residual is defined as

$$R_{lsq} = \sum |f(n_i) - f^*(n_i)|^2. \tag{B.2.5}$$

Least squares refinement varies the values of n_i to make R_{lsq} as small as possible. The location of the minimum is not changed by taking the square root of the residual, or by normalising. Generally, in crystal structure studies, and in JANA2006 the square root of the normalised residual is used, and defined in terms of I_{hkl} rather than F_{hkl}.

$$R = \left(\frac{\sum [I_{hkl} - I^*_{hkl}]^2}{\sum [I_{hkl}]^2} \right)^{\frac{1}{2}} \tag{B.2.6}$$

$$\Rightarrow R(F^2) = \frac{\sum |F^2obs_{hkl} - F^2calc_{hkl}|}{\sum |F^2obs_{hkl}|}. \tag{B.2.7}$$

This expression yields the R-factor which is used throughout this thesis to indicate the quality of structural refinements.

The R-factor is not the only quantity calculated to indicate refinement quality. For

example, weighted R-factors are commonly used, which weight the functions that are being minimised according to estimates of the precision of the measured quantity. The weighted R-factor is given as

$$wR(F^2) = \frac{\sum w|F^2obs_{hkl} - F^2calc_{hkl}|}{\sum |wF^2obs_{hkl}|}. \tag{B.2.8}$$

Appendix C

Four Dimensional Space Group Analysis

In this thesis, incommensurately modulated crystal structures are studied. These crystal structures can be described as an average structure with three dimensional space group symmetry, periodically displaced according to a modulation wave. For a one dimensional sinusoidal modulation wave, if the position of the jth particle in unit cell n of the average structure is defined by the vector

$$\mathbf{r}_0(\mathbf{n}, j) = \mathbf{n} + \mathbf{r}_j. \tag{C.0.1}$$

The position of the same particle in the modulated structure will be defined by

$$\mathbf{r}(\mathbf{n}, j) = \mathbf{n} + \mathbf{r}_j + \mathbf{U}_j \sin[2\pi\mathbf{q} \cdot (\mathbf{n} + \mathbf{r}_j)], \tag{C.0.2}$$

where $\mathbf{q}$ is the propagation vector for the modulation, and $\mathbf{U}$ is a polarisation vector for the jth particles modulation.

In this thesis, in accordance with the convention used in JANA2006, the modulated crystal structure is considered within the enlarged class of symmetry transformations developed by DeWolff and Janner & Jansen [103].

If a lattice translation of the average structure acts upon the modulated structure, it will give rise to a shift of the phase. If this translation is combined with a compensating

phase shift, a transformation is obtained that leaves both the average structure and the modulation invariant. This transformation corresponds to a lattice translation in four dimensions.

Taking the approach of "embedding" the modulated structure, the phase of the modulation can be considered as an additional coordinate (t). Three dimensional atomic positions are then given by the intersection of lines of atomic positions (parameterised by t), with the hyperplane $t = 0$.

The lines of atomic position can be expressed as

$$\mathbf{r}(\mathbf{n}, j) = \mathbf{n} + \mathbf{r}_j + \mathbf{U}_j \sin[2\pi\{\mathbf{q} \cdot (\mathbf{n} + \mathbf{r}_j) + t\}], t). \tag{C.0.3}$$

This pattern of lines has lattice periodicity, and is left invariant under the combination of a lattice translation from the average structure ($\mathbf{n}$) and a phase shift $t \rightarrow t - \mathbf{q} \cdot \mathbf{n}$.

It should be emphasised that the variable t takes the double role of a parameter and as an additional coordinate. In the latter case, it is implicit that t assumes a choice of 4th basis vector $\mathbf{d}$, perpendicular to the physical space of the crystal, so that the following four dimensional vector notations describing atomic positions are equivalent:

$$\mathbf{r}_s = (\mathbf{r}, \mathbf{t}) = (\mathbf{r}, t\mathbf{d}) = (\mathbf{r}, t). \tag{C.0.4}$$

Equation (C.0.3), is invariant under translation from a four dimensional lattice with basis

$$\begin{aligned} a_1 &= (\mathbf{a}, -\mathbf{q} \cdot \mathbf{a}), \\ a_2 &= (\mathbf{b}, -\mathbf{q} \cdot \mathbf{b}), \\ a_3 &= (\mathbf{c}, -\mathbf{q} \cdot \mathbf{c}), \\ a_4 &= (0, 1). \end{aligned} \tag{C.0.5}$$

The concept of three dimensional space groups can be extended to describe an incom-

mensurately modulated crystal structure within a four dimensional basis. Some, or all of the symmetry transformations of the space group of the three dimensional average structure will give rise to a symmetry transformation for the modulated structure if combined with an appropriate phase shift (and possible phase inversion).

If $\{R|v\}$ is a symmetry element of the space group of the average structure, Δ is a phase shift, and $\epsilon = \pm 1$ (indicating phase inversion), then a position vector $(\mathbf{r}, t)$ in the average structure becomes $(R\mathbf{r}+\mathbf{v}, \epsilon t+\Delta)$ in the modulated structure. The space group in four dimensions will comprise elements $\{R|\mathbf{v}\}, \{\epsilon|\Delta\}$, that satisfy

$$(R\mathbf{n}+R\mathbf{r}_j+\mathbf{v}+R\mathbf{u}_j[\mathbf{q}\cdot(\mathbf{n}+\mathbf{r}_j)+\epsilon t-\epsilon\Delta], t) = (\mathbf{n'}+\mathbf{r}_j+\mathbf{v}+\mathbf{u}_j[\mathbf{q}\cdot(\mathbf{n'}+\mathbf{r}_j)+t], t), \quad \text{(C.0.6)}$$

where the position vector $\mathbf{n'} + \mathbf{r}_j$ is the transform of $\mathbf{n} + \mathbf{r}_j$ in the average structure.

The process for determining the four dimensional space group for a modulated crystal will not be outlined here, but explaining the notation for the four dimensional space group of $CaMn_7O_{12}$ below T_{OO}:

$R\bar{3}(00\gamma)0$

- $R\bar{3}$ is the space group of the average structure in three dimensions.
- (00γ) represents the indices of the propagation vector $\mathbf{q} = \alpha\mathbf{a}^* + \beta\mathbf{b}^* + \gamma\mathbf{c}^*$. For $CaMn_7O_{12}$, the propagation vector is parallel to $\mathbf{c}^*$, hence α and β are 0.
- The final index, 0, relates to the phase shift when $\mathbf{q}$ is transformed by the symmetry operators of the space group. For the case of $CaMn_7O_{12}$ this is a single index, representing the phase shift of γ. For systems with non-zero α and β values, additional indices would be required, and non-zero phase shifts, are represented by letter s, t,q, and h.

For further details of the notation of four dimensional space groups see Ref. [103].